

ab4962 / 5112800

PHOTODETECTION WITH NOVEL MATERIALS:

**COLLOIDAL QUANTUM DOTS
NANORIBBONS AND LAYERED MATERIALS**

**PHOTODETECTION WITH NOVEL MATERIALS:
COLLOIDAL QUANTUM DOTS
NANORIBBONS AND LAYERED MATERIALS**

TU Delft Library
Prometheusplein 1
2628 ZC Delft

Proefschrift

ter verkrijging van de graad van doctor
aan de Technische Universiteit Delft,
op gezag van de Rector Magnificus prof. ir. K. C. A. M. Luyben,
voorzitter van het College voor Promoties,
in het openbaar te verdedigen op 10 april 2015 om 12:30 uur

door

Michele BUSCEMA

Materials Engineer
geboren te La Spezia, Italië

Dit proefschrift is goedgekeurd door de promotor:

Prof. dr. Ir. H.S.J. van der Zant

Samenstelling promotiecommissie:

Rector Magnificus,	voorzitter
Prof. dr. Ir. H.S.J. van der Zant,	Technische Universiteit Delft, promotor
dr. A. Castellanos-Gomez,	Technische Universiteit Delft & IMDEA Nanoscience, Madrid
Prof. dr. M. Terrones,	Penn State University, Pennsylvania
Prof. dr. ir. F. Koppens,	ICFO, Barcellona
Prof. dr. R. Bratschitsch,	Westfälische Wilhelms-Universität Münster, Münster
Prof. dr. Y.M. Blanter,	Technische Universiteit Delft
Prof. dr. L.D.A. Siebbeles,	Technische Universiteit Delft

Dr. A. Castellanos-Gomez heeft als begeleider in belangrijke mate aan de totstandkoming van het proefschrift bijgedragen.



Keywords: Photodetection, semiconducting colloidal quantum dots, semiconducting layered materials, single layer MoS₂, TiS₃ nanoribbons, black phosphorus, PN junctions defined by local electrostatic gating...

Printed by: Gildeprint - Enschede

Front & Back: Photograph of the laser beams in one of the setups used for the measurements in this Thesis. Photograph and cover design by Michele Buscema

Copyright © 2015 by M. Buscema All rights reserved. No part of this book may be reproduced, stored in a retrieval system, or transmitted, in any form or by any means, without prior permission from the copyright owner.

Casimir PhD Series, Delft-Leiden 2015-7

ISBN 978-90-8593-215-4

An electronic version of this dissertation is available at
<http://repository.tudelft.nl/>.

CONTENTS

1 Introduction	1
1.1 Opto-electronics	1
1.2 Photodetectors	2
1.3 Silicon-based opto-electronic devices.	3
1.4 Non-silicon based opto-electronic devices	4
1.5 Need for new materials	4
1.6 This Thesis	4
References	5
2 Photodetection mechanisms	7
2.1 Typical device architecture	8
2.2 Photon absorption processes	9
2.3 Photocurrent generation driven by electron-hole separation	11
2.3.1 Photoconductive effect	11
2.3.2 Photovoltaic effect	12
2.3.3 Simplified photocurrent generation phenomenological description	14
2.4 Photocurrent generation driven by thermal mechanisms	15
2.4.1 Photo-thermoelectric effect	15
2.4.2 Photo-bolometric effect	18
2.5 Photodetectors figures-of-merit.	19
References	21
3 Two-dimensional materials for photodetection	23
3.1 Introduction	24
3.2 Graphene-based photodetectors	24
3.3 Photodetectors based on transition metal dichalcogenides	27
3.3.1 Photodetection with molybdenum disulphide.	28
3.3.2 Molybdenum diselenide	34
3.3.3 Tungsten disulfide	35
3.3.4 Tungsten diselenide	35

3.4	Semiconducting transition metal trichalcogenides.	37
3.5	III-VI and IV-VI layered compounds.	38
3.6	Few-layer black phosphorus	40
3.7	Device comparison	43
3.8	Future directions	45
3.8.1	Artificial van-der-Waals heterostructures.	46
3.9	Summary and outlook	50
3.10	Acknowledgments	51
3.11	Appendix: Tables	51
	References	55
4	Fast and efficient photodetection in nanoscale quantum-dot junctions	63
4.1	Introduction	64
4.2	Fabrication and electrical characterization	64
4.3	Photoresponse	65
4.4	Power dependence	66
4.5	Conclusion and outlook.	69
4.6	Acknowledgments	69
4.7	Supporting information.	70
4.7.1	Fabrication of the self-aligned QD devices	70
4.7.2	Photoresponse spatial extension.	71
4.7.3	Quantum efficiency calculations.	71
	References	72
5	Ultrahigh photoresponse of few-layer TiS_3 nanoribbon transistors	75
5.1	Introduction	76
5.2	Growth and characterization	76
5.3	FET fabrication	77
5.4	Electrical characterization	77
5.5	Photoresponse	79
5.6	Time response	82
5.7	Comparison with literature	82
5.8	Conclusions.	83
	References	84
6	Photo-thermoelectric effect in single-layer MoS_2	87
6.1	Introduction	88
6.2	Fabrication and electrical characterization	88
6.3	Scanning photocurrent microscopy.	90
6.4	Photothermoelectric effect	93
6.5	Conclusion and outlook.	97

6.6	Supporting information.	97
6.6.1	Materials and Methods.	97
6.6.2	Raman spectroscopy data	98
6.6.3	Laser-induced temperature increase estimation	98
	References	100
7	Fast and broadband photoresponse of few-layer black phosphorous photo transistors	103
7.1	Introduction	104
7.2	Fabrication and electrical characterization	104
7.3	Photoresponse	107
7.4	Time response	109
7.5	Comparison with literature	110
7.6	Conclusion and outlook.	112
	References	112
8	Photovoltaic effect in few-layer black phosphorus PN junctions defined by local electrostatic gating	115
8.1	Introduction	116
8.2	Fabrication of locally gated devices	116
8.3	Transistor operation	117
8.4	PN junction operation	118
8.5	Photovoltaic effect	120
8.6	Discussion	124
8.7	Supporting information.	124
8.7.1	Two other fabricated devices.	124
8.7.2	Determination of the diode parameters with Shockley model	125
	References	127
A	Experimental Methods	131
A.1	Fabrication techniques	132
A.1.1	Electron Beam Lithography	132
A.1.2	Exfoliation	133
A.1.3	Fabrication of electrical devices based on 2D materials	134
A.1.4	All dry, deterministic transfer method	135
A.2	Characterization Techniques	139
A.2.1	Atomic Force Microscopy	139
A.2.2	Raman Microscopy	139
A.2.3	Opto-electronic characterization setup	141
	References	144

Summary	145
Samenvatting	147
Curriculum Vitæ	149
List of Publications	151
Patents	152
Acknowledgments	153

CHAPTER 1

INTRODUCTION

1.1. OPTO-ELECTRONICS

The field of opto-electronics bridges electronics and optics by using electronic signals to generate, detect and control light. Opto-electronic devices transduce information between electronic signals and photons via photon absorption and emission in semiconductors. An electrically biased semiconductor can generate current upon photon absorption and, conversely, can emit photons under electrical excitation. The bandgap of the semiconductor influences the wavelength range of operation and the strength (or efficiency) of the absorption/emission of photons.

State-of-the-art opto-electronic devices can address the entire electromagnetic spectrum. Starting from high-energy photons, such as γ and X-rays (used in medicine and material science) and ultraviolet (UV) radiation that is used to fabricate and inspect electronic components.

Moving to the visible part of the spectrum, opto-electronic devices that operate with visible light are at the heart of modern consumer society. In 2014, the Nobel prize for physics has been jointly awarded to Isamu Akasaki, Hiroshi Amano and Shuji Nakamura for

*the invention of efficient blue light-emitting diodes which has enabled bright and energy-saving white light sources.**

This testifies the impact that opto-electronics has on modern society.

A few examples of visible opto-electronic devices are presented in Figure 1.1: light emitting diodes (LEDs) of various colors (Figure 1.1a), a solid-state laser (SSL) (Figure 1.1b), solar cells (Figure 1.1c) and the image sensor of a digital single-lens reflex (DSLR) camera (Figure 1.1d). LEDs generate light that can be used for illumination while SSLs emit laser light that can be used to provide optical excitation for scientific purposes or generate high power for industrial applications. Solar cells are widespread generators

*Quote from the press release of the Royal Swedish Academy of Sciences, 7 October 2014.

of electrical power. Image sensors are used in microscopy, photography, medical and industrial applications.

Moving on to devices that operate with infrared (IR) radiation, they comprise ultrafast lasers and ultrafast receivers at telecommunication wavelengths (from 1260 to 1675 nm), used both for fundamental studies[1–3] and for broadband communications. Infrared photodetection is the base for optical communication and night-vision devices, of importance for both civil and military applications.

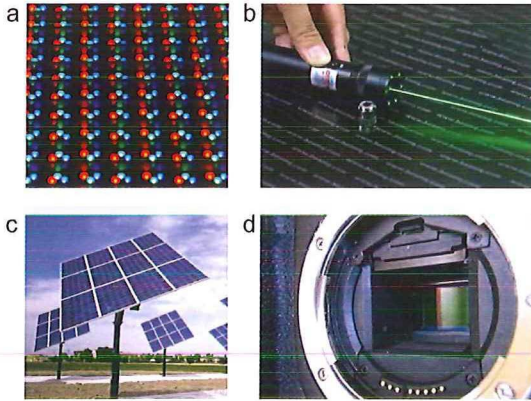


FIGURE 1.1: Opto-electronic macroscopic devices (a) Light emitting diodes (LEDs) array converting electrical current in incoherent photons. (b) Green laser pointer converting electrical current in coherent photons. (c) Solar cell, converting light in electrical power. (d) Image sensor, converting light into electrical signal.

1.2. PHOTODETECTORS

Photodetectors are key components for spectroscopy, optical communication and imaging. Under illumination, these devices convert photons into a measurable electrical signal.

Typical device architectures include field-effect transistors (FETs) and diodes, both with the semiconducting channel or junction exposed to the incoming light. Such a photo-FET entails a semiconductor channel that is contacted by two metallic electrodes (source and drain electrodes). A gate electrode, separated from the channel by an insulating layer, can be used to control the resistance of the device via the field-effect. An external source drain bias (V_{ds}) drives current through the device and separates the photogenerated electron-hole pairs.

A photodiode is based on a junction between a p-doped and an n-doped semiconductor. At the junction, an internal electric field develops due to the equilibrium between the diffusion of electrons and the static charge of the lattice ions. This internal electric field separates the electron-hole pairs generated by the absorption of the impinging photons, giving rise to a current without any applied bias.

1.3. SILICON-BASED OPTO-ELECTRONIC DEVICES

Most photodetectors that operate in the visible or near-IR (NIR) are based on silicon as semiconductor material, allowing for a seamless integration with conventional electronics (CMOS technology). Device miniaturization and fabrication scalability are responsible for the success of Si-based photodetectors. Silicon photodiodes can achieve a responsivity of about 0.6 A W^{-1} , coupled with fast, low-noise and multiplexed readout, as exemplified by the CMOS image sensor of many DSLRs (see Figure 1.2).

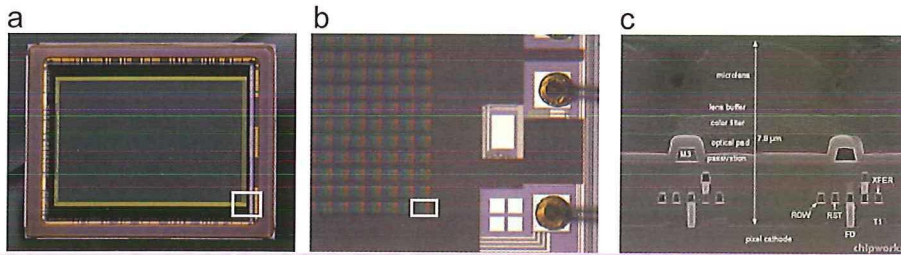


FIGURE 1.2: (a) Si-based image sensor (from Nikon D800, imaging.nikon.com). (b) Zoom-in Si-based image sensor in panel (a), white box (from Nikon D800, chipworks.com). (c) SEM image of Si-based image sensor in panel (b), white box (from chipworks.com).

However, silicon technology has its limitations. Crystalline silicon has an indirect bandgap of about 1.13 eV. Therefore, Si photodetectors can detect photons up to about 1100 nm. This precludes the absorption of most IR photons, hampering the use of silicon photodetectors for optical telecommunications and night vision. The indirect nature of the bandgap represents also a strong limitation of silicon as it reduces the amount of charge carriers generated per impinging photon (absorption efficiency). This reduces the responsivity of the Si photodiodes, that remains weak across the entire visible part of the spectrum.

Furthermore, photons of short wavelengths (below $\sim 500 \text{ nm}$) are absorbed very close (within $1 \mu\text{m}$) to the surface of the detector. Thus, the generated electron-hole pairs will be affected by surface states, reducing the amount of charge carriers available for electrical detection or power generation. The short photon penetration length makes silicon, limiting its application in transparent devices. Finally, silicon is also brittle, allowing for tensile strains below 1% before rupture. This reduces its applicability in wearable and flexible device concepts.

1.4. NON-SILICON BASED OPTO-ELECTRONIC DEVICES

Exotic materials have been studied and implemented to increase absorption efficiency and to extend the wavelength operation range towards the infrared and, especially, telecommunication wavelengths (1300 nm to 1550 nm). As an example, germanium photodetectors have recently been explored[4] due to their sizable absorption coefficient up to telecommunication wavelengths and the possible integration with Si fabrication technology.

Also, alloys of elements belonging to the III and V groups of the periodic table have been investigated in the past decades and are nowadays implemented in photodetectors for specialized applications, like night vision.

Also II-VI and IV-VI compounds have been studied and present some advantages compared to both Si and III-V compounds. A limitation of these compounds is the growth process, usually performed via Molecular Beam Epitaxy (MBE). MBE growth delivers stoichiometric compounds with clean and atomically sharp interfaces, enabling the engineering of structures where layers of different compounds are periodically alternated (heterostructures). These heterostructures exploit quantum confinement effects to increase the efficiency of photon emission and detection (quantum wells). However, MBE growth is limited by the small lattice mismatch that is allowed between two compounds to preserve epitaxial growth. Moreover, it is not a continuous process as it requires high vacuum and the uniformity over large surfaces is poor, requiring selection of the devices after fabrication.

1.5. NEED FOR NEW MATERIALS

The intrinsic limitations of silicon and the technological challenges of exotic compounds motivate the study of the opto-electronic properties of novel compounds that can achieve a larger responsivity in the visible or an extended wavelength range or that can be implemented in novel device concepts, such as transparent and flexible devices.

1.6. THIS THESIS

This Thesis describes an experimental study of photodetection based on new materials. Throughout the entire Thesis, the dimensionality of the materials plays an important role: we start with zero-dimension (colloidal quantum dots) and one-dimension (nanoribbons) and then move on to two dimensions (exfoliated flakes). After this Introduction, Chapter 2 deals with the theoretical aspects of photodetection that are relevant for the remainder of this Thesis. Chapter 3 reviews the current state-of-the-art for photodetection with novel materials. In Chapter 4, we present a novel photodetector architecture based on PbSe colloidal quantum dots that allowed us to achieve high-gain and high-speed detection. In Chapter 5 we present a study of the photoresponse of TiS_3 nanoribbons in nanostructured devices. Chapter 6 deals

with the interplay between optical and thermal effects in single and few-layer MoS₂. Chapter 7 shows the fast and broadband photoresponse of photodetectors based on few-layer black phosphorus. At last, Chapter 8 builds on the results presented in Chapter 7 by fabricating a versatile device based on a locally gated few-layer black phosphorus flake. In Appendix A we describe in detail the experimental methods used to fabricate and characterize the studied devices.

REFERENCES

- [1] M. Wagner, Z. Fei, A. S. McLeod, A. S. Rodin *et al.*, *Ultrafast and Nanoscale Plasmonic Phenomena in Exfoliated Graphene Revealed by Infrared Pump-Probe Nanoscopy*, *Nano letters* **14** 894 (2014).
- [2] M. Aerts, T. Bielewicz, C. Klinke, F. C. Grozema *et al.*, *Highly efficient carrier multiplication in PbS nanosheets*, *Nature communications* **5** (2014).
- [3] Y. Li, Y. Rao, K. F. Mak, Y. You *et al.*, *Probing Symmetry Properties of Few-Layer MoS₂ and h-BN by Optical Second-Harmonic Generation*, *Nano Lett.* **13** 3329 (2013).
- [4] J. M. Hartmann, A. Abbadie, A. M. Papon, P. Holliger *et al.*, *Reduced pressure-chemical vapor deposition of Ge thick layers on Si(001) for 1.3 μm photodetection*, *Journal of Applied Physics* **95** 5905 (2004).

CHAPTER 2

PHOTODETECTION MECHANISMS

This Chapter introduces some fundamental aspects of photodetection that are relevant for the interpretation of the data in the rest of this Thesis. We start by briefly introducing the typical device architecture and photon absorption processes in semiconductors. We then move on to treat photocurrent generation mechanisms driven by electron-hole separation that are relevant for Chapters 5, 7 and 8. Next, we introduce thermal processes that are responsible for photocurrent generation, especially focusing on the photo-thermoelectric effect of interest for Chapter 6. At last, we summarize the relevant figures-of-merit for photodetectors to facilitate comparison among devices working with different principles.

2.1. TYPICAL DEVICE ARCHITECTURE

Figure 2.1 shows the schematics of typical devices used for photodetection: a field-effect transistor (FET, Figure 2.1a) and a photodiode based on a PN junction (Figure 2.1c). In both device architectures, a semiconductor (SC, channel) is contacted by two metal electrodes (M, source and drain). In the case of a photo-transistor, a third electrode (gate) is present, which controls the carrier density in the semiconductor via the field-effect. The gate electrode is separated from the channel by an insulating material (dielectric) to prevent leakage currents. The corresponding band diagram has been sketched in Figure 2.1b. An applied source-drain bias (V_{ds}) of either polarity generates a current (I_{ds}) whose magnitude is controlled by the voltage applied on the gate electrode (V_g). At low applied V_{ds} the $I_{ds}-V_{ds}$ curve is usually linear. The applied V_{ds} is also responsible for the separation of the photo-generated electron-hole (e-h) pairs.

For a PN junction (Figure 2.1c), the doping profile in the semiconductor channel varies from hole doping to electron doping. At the interface between the two areas of the semiconductor with different doping, an electric field builds up. This internal electric field stems from the equilibrium between electron diffusion driven by the difference in electrochemical potential between the two channel regions with opposite doping and the static electric field of the ions in the semiconductor lattice.

A schematic band diagram is sketched in Figure 2.1d, showing the conduction band minimum (CBM) and valence band maximum (VBM) energy as a function of the position along the device. The red (blue) shaded areas correspond to the p-(n-)doped regions, as evident from the location of the Fermi energy (E_F) with respect to the CBM and VBM. An internal electric field, due to the lattice ions, develops at the junction region. This internal electric field reduces charge accumulation in the region between the p- and n-type semiconductor (depletion region) and separates the electron-hole pairs generated by impinging photons, giving rise to a photocurrent under illumination.

For a diode, the relationship between V_{ds} and I_{ds} is no longer linear. A current only flows when the bias polarity is aligned with the junction polarity (*forward bias*) and has an exponential dependence on the applied forward V_{ds} . In *reverse bias*, the current is negligible until electrons can start tunneling across the depletion region (junction breakdown).

For both device geometries, the metal contacts to the semiconductor channel play an important role in the electrical behavior. In a metal-semiconductor contact at equilibrium, the E_F of the metal and of the Fermi level of the semiconductor need to be at the same energy. Any misalignment is balanced by charge diffusion between the semiconductor and the metal, resulting in a depletion region in the semiconductor localized at the metal/semiconductor interface. In turn, this local depletion region results in an electric field at the interface, giving rise to band bending, known as Schottky barrier (SB, see Figure 2.1b). The electric field at the SB introduces non-

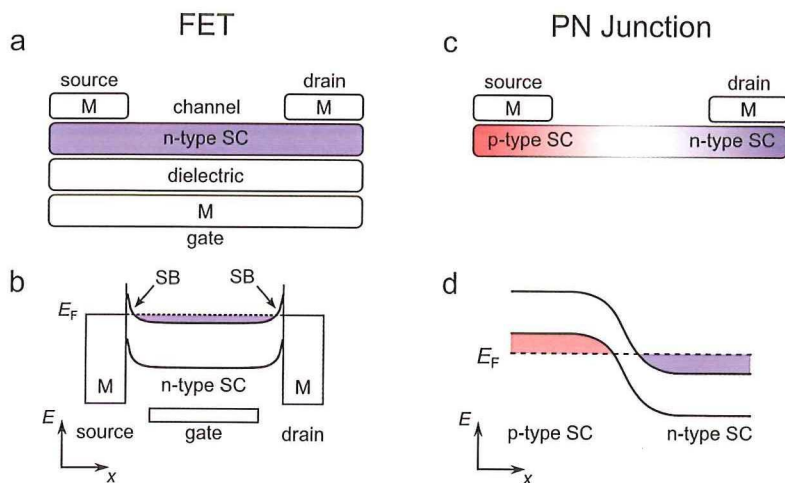


FIGURE 2.1: Device schematics and band diagram for a field-effect transistor (FET) and a PN junction. (a) FET device schematics. A channel of an n-type semiconductor (SC) is contacted by two metals (M), forming the source and drain electrodes. A dielectric separates the channel from the gate metallic electrode. (b) Band alignment for the device in panel (a), highlighting the presence of Schottky barriers (SB) at the metal-semiconductor interface. E_F is the Fermi energy. (c) PN-junction device schematics. A channel of a semiconducting material has a gradual change in the doping profile from p-type (red shade) to n-type (blue shade), resulting in a PN junction. (d) Band diagram for the device in panel (c). The E_F is equal on both sides as a result of charge diffusion. The internal electric field provided by the lattice ions bends the bands and sustains a region where the density of charge carriers is reduced – depletion region.

linearities in the $I_{ds} - V_{ds}$ curves and can separate e-h pairs, generating photocurrent without externally applied bias. A detailed and comprehensive discussion over SB is beyond the scope of this Thesis; we refer the reader to refs. [1, 2]

2.2. PHOTON ABSORPTION PROCESSES

Photon absorption by semiconductors is the mechanisms underpinning photodetection. An incoming photon can deliver its energy to an electron in the valence band, promoting it to an empty state in the conduction band. The electron will not change momentum, since the momentum of the photon is negligible compared to the electron momentum. Thus, this transition is allowed if the energy of the photon is large enough to bring the electron to an empty state in the conduction band while preserving the total momentum. This is the typical description of a direct absorption process, dominating absorption in direct bandgap semiconductors (see Figure 2.2a). [3, 4]

In the case of indirect bandgap semiconductors, the electron receiving the energy

of the incoming photon usually needs to change its momentum to find available states in the conduction band (indirect transition). Lattice phonons provide the momentum difference by electron-phonon interaction (see Figure 2.2b). This process involves three particles and, thus, it is less efficient compared to direct absorption processes.

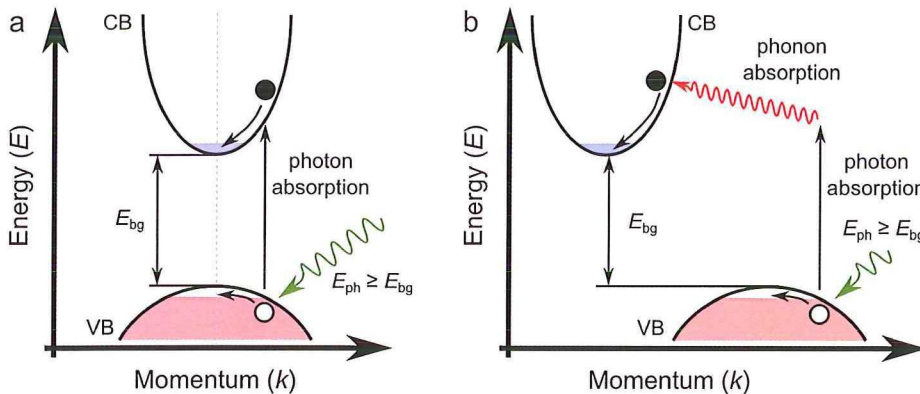


FIGURE 2.2: Schematics of photon absorption processes in semiconductors. (a) Photon absorption process for direct bandgap semiconductors. A photon with energy (E_{ph}) larger than the bandgap (E_{bg}) delivers its energy to an electron in the valence band (VB). The electron undergoes a vertical transition, since the momentum of the photon is much smaller than the momentum of the electron itself $k_{photon} \ll k_e$. The promoted electron then thermalizes to the conduction band (CB) edge by intra-band phonon scattering. In the VB, a hole is left behind, which also thermalizes to the valence band edge. (b) Photon absorption process for indirect bandgap semiconductors. A photon with $E_{ph} > E_{bg}$ delivers its energy to an electron in the VB. The electron undergoes a vertical transition and, to find available states in the CB, absorbs a lattice phonon (phonon emission is also possible). The promoted electron then thermalizes to the CB edge by intra-band phonon scattering. In the VB, a hole is left behind, which also thermalizes to the VB edge.

Both direct and indirect absorption processes lead to the formation of an e-h pair, the electron being promoted into the conduction band and the hole left behind in the valence band. The electron and hole interact electrostatically and may form bound neutral particles, excitons. The corresponding excitonic states have a lower energy than the band gap (exciton binding energy) and present large absorption and emission efficiency. They play a major role in the optical properties of quantum-confined systems, such as (colloidal) quantum dots and two-dimensional semiconductors.[5–8]

2.3. PHOTOCURRENT GENERATION DRIVEN BY ELECTRON-HOLE SEPARATION

Photodetectors produce electrical signal by separating the photo-generated e-h pairs and collecting the resulting current/voltage. The underlying mechanisms are usually categorized as the photoconductive and the photovoltaic effect, discussed in the next subsections.

2

2.3.1. PHOTOCONDUCTIVE EFFECT

In the photoconductive effect, photon absorption generates extra free carriers, reducing the electrical resistance of the semiconductor (see Figure 2.3). [9–11] Figure 2.3a sketches the band diagram of an FET device. In dark and under an applied bias (V_{ds}), a small source-drain current can flow (I_{dark}). Under illumination, the absorption of photons with energy higher than the bandgap ($E_{ph} > E_{bg}$) generates a e-h pairs which are separated by the applied V_{ds} (Figure 2.3b). The photogenerated free electrons and holes drift in opposite directions towards the metal leads, resulting in a current (I_{photo}). This photogenerated current adds to the dark current, reducing the electrical resistance of the device, as measured via $I_{ds} - V_g$ or $I_{ds} - V_{ds}$ traces (Figure 2.3c and d).

It is instructive to consider the case of a large difference between the electron and hole mobilities. This will result in a large difference in the electron/hole transit time ($\tau_{transit}$): [11]

$$\tau_{transit} = \frac{L^2}{\mu \cdot V_{ds}}, \quad (2.1)$$

where L is the length of the transistor channel, μ the charge carrier mobility and V_{ds} the source-drain bias. If the hole mobility is much lower than the electron mobility, the photogenerated electrons can leave the semiconductor much faster than the photogenerated holes. Due to charge neutrality, an electron from a metallic contact is injected into the semiconductor channel and can be extracted at the opposite contact, according to the external bias direction. Until recombination or hole extraction, many electrons can participate in the photocurrent, leading to the photoconductive gain (G). [11] Effectively, this means that more electrons can be extracted from a single photon, resulting in a quantum efficiency larger than one. The photoc

$$G = \frac{\tau_{photocarriers}}{\tau_{transit}} = \frac{\tau_{photocarriers} \cdot \mu \cdot V}{L^2}. \quad (2.2)$$

Hence, large recombination times and large mismatch in the electron/hole mobility yield large G .

Photogating is a particular example of the photoconductive effect. If holes/electrons are *trapped* in localized states, they act as a local gate, effectively modulating the resistance of the material. In this case, $\tau_{photocarriers}$ is only limited by the recombination lifetime of the localized *trap* states, leading to larger G . [11] The trap states where

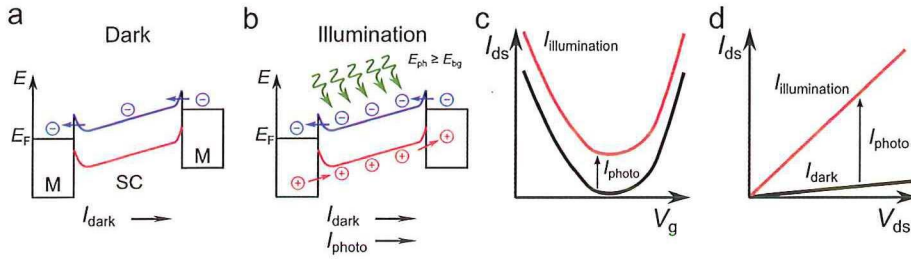


FIGURE 2.3: Schematic of the photoconductive effect. (a) Band alignment for a semiconductor (SC) channel contacted with two metals (M) under external bias in dark. A small current flows through the device (I_{dark}). (b) Band alignment under illumination with photons of energy higher (E_{ph}) than the bandgap (E_{bg}). The absorption of a photon generates an e-h pair that is separated by the external applied bias, resulting in a photocurrent (I_{photo}) which adds to the I_{dark} . (c) $I_{\text{ds}}-V_{\text{g}}$ traces in dark (solid black line) and under illumination (solid red line). Illumination results in an increase in the conductivity (vertical shift) and a positive photocurrent across the entire gate voltage range. (d) $I_{\text{ds}}-V_{\text{ds}}$ curves in dark (solid black line) and under illumination (solid red line). Illumination results in an increase in the conductivity and a positive photocurrent.

carriers can reside for long times are usually located at defects or at the surface of the semiconducting material. This effect is of particular importance for nanostructured materials, like colloidal quantum dots, nanowires and two dimensional semiconductors, where the large surface and reduced screening play a major role in the electrical properties.

Photogating can be seen as a horizontal shift in the $I_{\text{ds}}-V_{\text{g}}$ traces under illumination. Figure 2.4 schematically shows the photogating effect. Under illumination, the absorption of a photon generates an e-h pair. One carrier type (holes in Figure 2.4b) is then trapped in localized states with energy near the VB band edge. The electric field-effect of the trapped holes shifts the Fermi level which induces more electrons. The increased electron density reduces the resistance of the device, allowing more current to flow (I_{photo}). Under illumination, the $I_{\text{ds}}-V_{\text{g}}$ trace will be horizontally shifted (ΔV_{g}) with respect to the dark trace due to the effective gate electric field of the trapped charges. The sign of ΔV_{g} indicates the polarity of the trapped carrier. Photogating can also result in negative I_{photo} , as sketched in Figure 2.4c,d.

In practice, this clear distinction between photoconductive and photogating effect is faded, since both effects can take place in the same device. However, the difference in their time scales can be used to disentangle their signatures, as shown by Furchi *et al.*[12]

2.3.2. PHOTOVOLTAIC EFFECT

In the photovoltaic effect, the photogenerated e-h pairs are separated by an internal electric field. The origin of the internal electric field could be a PN junction or a Schot-

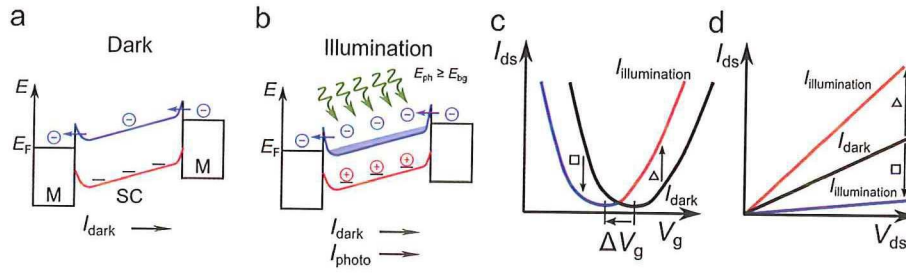


FIGURE 2.4: Photogating schematics. (a) Band alignment for a semiconductor (SC) channel contacted with two metals (M) under external bias in dark. A small current flows through the device (I_{dark}). The solid dark line segments represent trap states at the valence band edge. (b) Band alignment under illumination with photons of energy higher (E_{ph}) than the bandgap (E_{bg}). The absorption of a photon generates an electron-hole pair. Holes are trapped at the band edge and act as a local gate. The field-effect induces more electrons in the channel, generating a photocurrent (I_{photo}) which adds to the I_{dark} . (c) $I_{\text{ds}}-V_{\text{g}}$ traces in dark (solid black line) and under illumination (solid blue/red line). Illumination results in a horizontal shift (ΔV_{g}) of the traces, due to the trapped charges that act as an additional gate electric field. (d) $I_{\text{ds}}-V_{\text{ds}}$ curves in dark (solid black line) and under illumination at the gate value marked by a triangle in panel c (solid blue line) and at the gate voltage marked by a square in panel c (solid blue line). Illumination results in positive photocurrent for one gate value (triangle marker) and negative photocurrent for another gate value (square marker).

tky barrier at a metal/semiconductor interface (see Figure 2.5a).[11] In both cases, the devices present nonlinear $I_{\text{ds}}-V_{\text{ds}}$ characteristics. In the case of PN junctions, the forward source-drain current I_{ds} scales exponentially with the source-drain voltage V_{ds} as $I_{\text{ds}} \propto \exp(V_{\text{ds}}) - 1$; the reverse current, on the other hand, is negligibly small until junction breakdown.[1] Under illumination and zero external bias ($V_{\text{ds}} = 0$), the internal electric field separates the photoexcited e-h pairs thereby generating a sizable photocurrent (short-circuit current, I_{sc}). Keeping the circuit open leads to the accumulation of carrier of opposite polarities in distinct parts of the device, generating a voltage (open circuit voltage, V_{oc}). Under illumination and reverse bias, the magnitude of the reverse current increases since the photoexcited carriers are swept in opposite directions by the junction electric field. An additional forward-bias is required to compensate the photogenerated reverse-current, giving rise to a non-zero V_{oc} .

Figure 2.5b plots the $I_{\text{ds}}-V_{\text{ds}}$ characteristics of a PN junction in dark (black solid line) and under illumination (red line). Since the photocurrent has the same sign as the reverse current, the $I_{\text{ds}}-V_{\text{ds}}$ under illumination appears shifted downwards, with respect to the dark curve. The part of the $I_{\text{ds}}-V_{\text{ds}}$ curve that lays in the fourth quadrant is used in solar cells to generate electrical power ($P_{\text{el}}^{\text{max}}$).

Photodetectors based on the photovoltaic effect are usually PN diodes and are used at zero bias (photovoltaic mode) or under reverse bias (photoconductive mode).

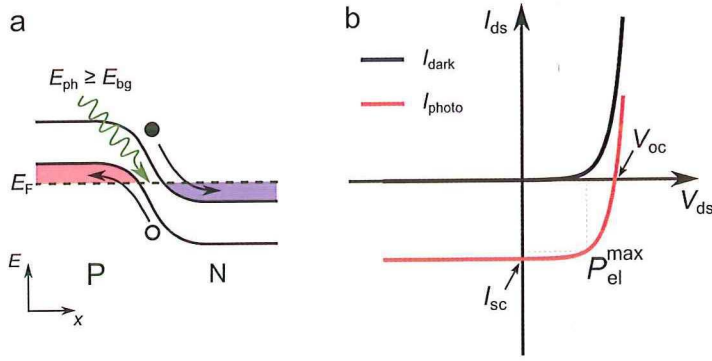


FIGURE 2.5: Photovoltaic effect schematics. (a) Band alignment in a PN junction. The dashed line represents the common Fermi energy E_F for the P-doped and N-doped semiconductor. The absorption of a photon with $E_{ph} > E_{bg}$ generates an electron-hole (black dot and white dot respectively) pair. The electron-hole pair is then separated and accelerated by the built-in electric field at the junction. (b) $I_{ds} - V_{ds}$ curves in dark (solid black line) and under illumination (solid red line). The illumination results in a short-circuit current I_{sc} and an open-circuit voltage V_{oc} . The device produces electrical power when operated in the fourth quadrant. The point of maximum power generation is indicated as P_{el}^{max} .

In the photovoltaic mode, the dark current is the lowest, improving the detectivity (see Section 2.5) of the detector. However, the absolute responsivity (see Section 2.5) is usually smaller than a photodetector working with the photoconductive or photogating mechanism, since there is no internal gain. The advantage of reverse-bias operation (the photoconductive mode) is the reduction of the junction capacitance, increasing the speed of the photodiode. Under large reverse bias, the strong junction electric field can give enough energy the photogenerated electrons to initiate impact ionization multiplications, or avalanching (avalanche photodiode - APD). This mechanism provide large internal gain, so that light of extremely low power can be detected.

2.3.3. SIMPLIFIED PHOTOCURRENT GENERATION PHENOMENOLOGICAL DESCRIPTION

The generated *photocurrent*, I_{photo} , in a photoconductive detector can be estimated with the following formula:

$$I_{photo} = I_{illumination} - I_{dark} = \Gamma \cdot \eta \cdot e \cdot G, \quad (2.3)$$

where Γ is the number of absorbed photons per unit time, η the efficiency of the conversion of the absorbed photons to electrons and e the electron charge. The parameter η is the internal quantum efficiency of the detector, without considering gain mechanisms.

With the help of equation 2.2, we can now rewrite equation 2.3 as:[13]

$$I_{\text{photo}} = \Gamma \cdot \eta \cdot e \cdot G \cdot \frac{\tau_{\text{photocarriers}} \cdot \mu \cdot V}{L^2}. \quad (2.4)$$

From Equation 2.4 we see that I_{photo} is linearly dependent on the photon flux (i.e., the excitation power), the photogenerated carrier lifetime, the electron mobility and the applied bias, following simple physical intuition.

This simplified model, however, does not take into account the presence of a finite number of trap states. These trap states strongly affect the dependence of the photocurrent on the excitation power (usually it becomes sub-linear) and the carrier lifetime (usually it increases). Engineering trap states is a viable way to achieve ultra high gain, usually at the expense of a slower time response of the detector.

2.4. PHOTOCURRENT GENERATION DRIVEN BY THERMAL MECHANISMS

Temperature *gradients* induced by non-uniform heating under illumination can also generate a photocurrent or photovoltage through the photo-thermoelectric effect. On the other hand, a *homogeneous* temperature change affects the resistivity of a material (photo-bolometric effect), which can be detected by electrical means.

2.4.1. PHOTO-THERMOELECTRIC EFFECT

In the photo-thermoelectric effect (PTE), a heat gradient from light-induced heating results in a temperature gradient across a semiconductor channel. As a result, the two ends of the semiconductor channel display a temperature difference ΔT . This ΔT is converted into a voltage difference (ΔV) via the Seebeck (or thermoelectric) effect (see Figure 2.6). The magnitude of ∇V is linearly proportional to the temperature gradient via the Seebeck coefficient (S):[14]

$$\Delta V = S \cdot \Delta T. \quad (2.5)$$

The heat gradient can stem from either localized illumination, as with a focused laser spot with dimensions much smaller than those of the measured device,[15, 16] or from a strong difference in the absorption in distinct parts of the device under global illumination.[17]

The Seebeck effect can be divided into three main microscopic processes, in dynamic equilibrium with each other.[14, 18] The first process is the diffusion of electrons due to a steady state temperature gradient along a conductor. As electrons carry a charge, their diffusive flux will generate an electric field in an open conductor; in turn, this electric field will exert a force on the electrons in the opposite direction, balancing the diffusion induced by the temperature gradient. This process will result

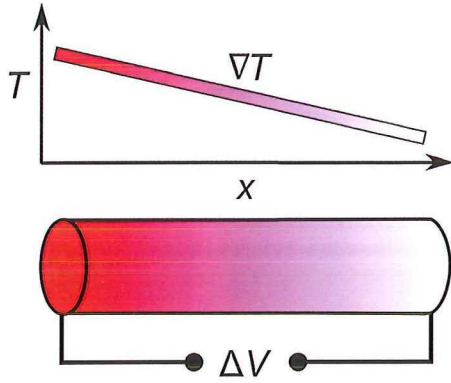


FIGURE 2.6: Thermoelectric effect. A steady-state temperature gradient ∇T is converted into a voltage difference ΔV at the end of a conductor.

in a component of the Seebeck coefficient (S_e) which is proportional to the specific heat capacity of the electrons in the conductor :

$$S_e \propto \frac{dE_e}{dT} \propto c_e, \quad (2.6)$$

where E_e is the electron energy, T the temperature and c_e the specific heat of the electrons.

The second process is the variation of the chemical potential μ with temperature: this variation affects the concentration of electrons along the temperature gradient and, therefore, induces electron diffusion. Assuming that μ diminishes with temperature, the diffusion of electrons induced by this term is in the opposite direction compared to the mechanism discussed in the previous paragraph. This process gives rise to a Seebeck coefficient component (S_μ) proportional to the change of the chemical potential with temperature:

$$S_\mu = \frac{1}{e} \frac{d\mu}{dT}, \quad (2.7)$$

where e is the electron charge.

The third process is the phonon drag: as phonons diffuse from the warm side of the conductor to the cold side, they can scatter and drag along electrons. This process gives rise to a component of the Seebeck coefficient (S_{lattice}) which is proportional to the electron-phonon coupling and the specific heat of phonons:

$$S_{\text{lattice}} \propto \alpha \frac{c_{\text{lattice}}}{eN}, \quad (2.8)$$

where α is the electron-phonon coupling, c_{lattice} the specific heat of the phonons and N the electron concentration.

As it is difficult to experimentally determine microscopic properties such as the energy dependent density of states in a given sample, the Seebeck coefficient is often parameterized in terms of the conductivity of the sample using the Mott relation: [19–22]

$$S = \frac{\pi^2 k_B^2 T}{3e} \left. \frac{d \ln(\sigma(E))}{dE} \right|_{E=E_F}, \quad (2.9)$$

where k_B is the Boltzmann constant and $\sigma(E)$ the conductivity as a function of energy (E), and where the derivative is evaluated at the Fermi energy E_F . The sign of the Seebeck coefficient is determined by the majority charge carrier polarity in the semiconductor.

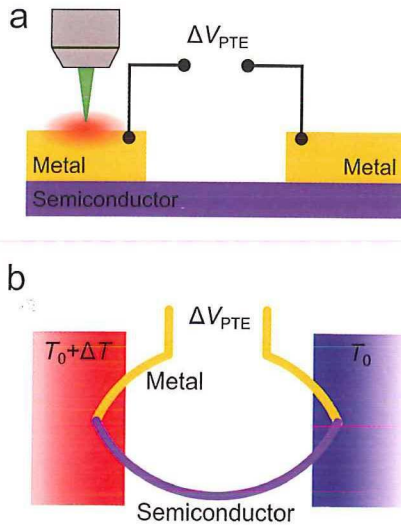


FIGURE 2.7: Photo-thermoelectric effect. (a) Schematic of a field-effect transistor locally illuminated by a focused laser spot on one of the metal contacts to the semiconducting channel. The circuit is open and a thermoelectric voltage ΔV_{PTE} develops across the contacts. (b) Thermal circuit corresponding to the device depicted in (a). The two metal/semiconductor junctions are kept at a steady-state temperature difference ΔT , generating a photo-thermoelectric voltage ΔV_{PTE} .

The photo-thermoelectric effect (PTE) generates a voltage difference that can drive a current through a device at zero V_{ds} . As sketched in Figure 2.7, a device which is illuminated by a focused laser spot can be modeled as two junctions between the contact metal and the semiconductor channel. In this example, a focused illumination keeps a steady-state ΔT between the two junctions, leading to a voltage difference across them (ΔV_{PTE}):

$$\Delta V_{PTE} = (S_{\text{semiconductor}} - S_{\text{metal}}) \cdot \Delta T \approx S_{\text{semiconductor}} \cdot \Delta T. \quad (2.10)$$

In this equation, the term $S_{\text{metal}} \cdot \Delta T$ can usually be neglected because the Seebeck coefficients of pure metals are in the order of $1 \mu\text{VK}^{-1}$, smaller than typical values for semiconductors. ΔT can be estimated via finite element simulations [16, 23, 24]

or measured with on-chip thermometers.[24, 25] Once ΔT is known, it is possible to estimate the Seebeck coefficient of the semiconductor material. The magnitude of ΔV_{PTE} typically ranges from tens of μV to tens of mV . In order to drive current through a metal-semiconductor contact, ΔV_{PTE} should be larger than the height of the Schottky barrier (E_{SB}).

Figure 2.8 shows a typical $I_{\text{ds}}-V_{\text{ds}}$ curve of a device where the photoresponse is dominated by the photo-thermoelectric effect. In dark, I_{ds} is linear with V_{ds} indicating that the Schottky barriers are small. Under illumination, the photo-thermoelectric effect generates a current at zero bias, without changing the resistance of the device. ΔV_{PTE} can be read off from the intersection with the zero-current axis, as illustrated in Figure 2.8.

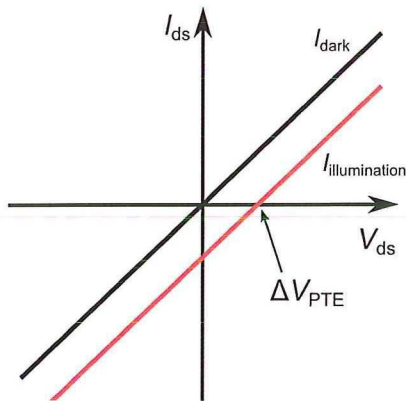


FIGURE 2.8: $I_{\text{ds}}-V_{\text{ds}}$ characteristics in dark (black solid line) and under illumination (red solid line) of a device whose photoresponse is dominated by the photo-thermoelectric effect. Illumination results in a current at zero bias and a thermoelectric voltage ΔV_{PTE} develop across the contacts when the circuit is kept open.

2.4.2. PHOTO-BOLOMETRIC EFFECT

The photo-bolometric effect (PBE) is based on the change of resistivity of a material due to uniform heating induced by photon absorption. The magnitude of this effect is proportional to the conductance variation of a material with temperature (dG/dT) and the homogeneous temperature increase (ΔT) induced by laser heating. The bolometric effect underpins many detectors for mid and far-IR.[26] Detectors working on this principle are usually measured in a four-wire configuration to increase the accuracy in the determination of the conductance change. Recent reports have also demonstrated the importance of the photo-bolometric effect for graphene-based detectors, where electron cooldown is limited by the available phonons,[27, 28] and for photodetectors based on ~ 100 nm thick black phosphorus.[29, 30]

COMPARISON BETWEEN PHOTO-THERMOELECTRIC AND BOLOMETRIC EFFECTS

The main difference between the PTE and the PBE is that the PBE cannot drive currents in a device. Since the PBE is related to a change in the conductivity of the material with temperature, it will only modify the magnitude of the current flowing under external bias and illumination.

The sign of the photoresponse is also very different between the two mechanisms. In the PTE the sign of the photocurrent is related to the difference in Seebeck coefficients between the components of the junction and, ultimately, to the type of charge carriers in the material. For the PBE, the sign of the photocurrent is related to the change in the material conductivity with temperature.[26]

From a device architecture perspective, the photo-thermoelectric effect requires a temperature difference between two junctions of materials with different Seebeck coefficients. In contrast, the photo-bolometric effect will be present in a homogeneous material, with a homogeneous temperature profile, and under external bias.

2.5. PHOTODETECTORS FIGURES-OF-MERIT

To facilitate comparison between photodetectors working with different principles and realized with different materials and geometries, it is customary to use a set of figures-of-merit. In the following discussion, we will briefly introduce the general meaning of each figure of merit and give a reference to commercial silicon and recent graphene-based detectors, as a benchmark.

Responsivity, \mathfrak{R} , measured in A W^{-1} . The responsivity is the ratio between the photocurrent and the incident optical power on the photodetector. It is an indication of the achievable electrical signal under a certain illumination power: a large responsivity indicates a large electrical output signal for a defined optical excitation power. With the help of Equation 2.4, we can define the responsivity as:

$$\begin{aligned}\mathfrak{R} &= \frac{I_{\text{photo}}}{P} = \Gamma \eta e \cdot G \cdot \frac{\tau_{\text{photocarriers}} \mu V}{L^2} \cdot \frac{\lambda}{\Gamma h c} = \\ &= \frac{e \lambda}{h c} \cdot \eta \cdot G \cdot \tau_{\text{photocarriers}} \cdot \frac{\mu V}{L^2},\end{aligned}\quad (2.11)$$

where λ is the photon wavelength, h Planck's constant and c the speed of light in vacuum. Equation 2.11 shows that the responsivity still depends on the external bias (V) or geometrical factors, at least in the simplified model presented here. For commercial silicon photodiodes, the responsivity is in the order of 500 mA W^{-1} at a wavelength of 880 nm and becomes negligible for wavelengths shorter than 405 nm and larger than 1100 nm. For graphene photodetectors, the responsivity is about 10 mA W^{-1} across the visible and telecommunication wavelengths.[31] Recently, more complex graphene detectors based on photogating either with quantum dots[32] or

with another graphene sheet separated by a tunnel barrier[33] have achieved much larger responsivities: $1 \cdot 10^7 \text{ A W}^{-1}$ and $1 \cdot 10^3 \text{ A W}^{-1}$, respectively.

External quantum efficiency, EQE . The external quantum efficiency is the ratio of the number of the charge carriers in the photocurrent n_e and the total number of impinging excitation photons $n_{\text{photon}}^{\text{total}}$. It is closely related to the responsivity \mathfrak{R} :

$$EQE = \frac{n_e}{n_{\text{photon}}^{\text{total}}} = \mathfrak{R} \cdot \frac{hc}{e\lambda}, \quad (2.12)$$

The EQE is a measure of the optical gain G in the photodetector: $EQE > 1$ effectively means that more than one charge carrier per impinging photon is measured. It is usually a lower bound for the internal quantum efficiency since it assumes that all the incident photons are absorbed. For a silicon photodiode the EQE is in the order of $6 \cdot 10^5$ and for a graphene detector is about $1 \cdot 10^{-2}$. [31, 34]

Internal quantum efficiency, $IQE = \eta$. The internal quantum efficiency is number of measured charge carriers n_e divided by the number of *absorbed* photons $n_{\text{photon}}^{\text{abs}}$. Accounting for the reflectance r and using Lambert-Beer law for the absorption, we can express the number of absorbed photons per unit area and per unit time (n_{abs}) as:

$$n_{\text{photon}}^{\text{abs}} = n_{\text{photon}}^{\text{total}} \cdot (1 - r) \cdot \exp^{-\alpha(\lambda) \cdot z}, \quad (2.13)$$

where $\alpha(\lambda)$ is the wavelength-dependent absorption coefficient and z is the *optical* thickness. The optical thickness can be enhanced by substrate-induced optical interference effects. [35–37] The IQE can be expressed as $EQE \cdot \frac{\exp^{\alpha(\lambda) \cdot z}}{1 - r}$.

Noise equivalent power, NEP , measured in $\text{W Hz}^{-\frac{1}{2}}$. The noise equivalent power is the minimum illumination power that delivers a unity signal-to-noise ratio at 1 Hz bandwidth. It is similar to the *sensitivity* figure-of-merit for other type of detectors. It is a measure of the minimum detectable illumination power; thus a low NEP is a desirable property of a photodetector. It can be estimated by:

$$NEP = \frac{PSD}{\mathfrak{R}}, \quad (2.14)$$

where the PSD is the current noise power spectral density in dark (in $\text{A Hz}^{-\frac{1}{2}}$) at 1 Hz bandwidth. Under the assumption of a shot-noise limited detector, the PSD is proportional to the square root of the dark current. Thus a detector with a small dark current and large responsivity will have a small NEP . Commercial silicon photodiodes have a NEP in the order of $1 \cdot 10^{-14} \text{ A Hz}^{-\frac{1}{2}}$ while graphene detectors reach values about $1 \cdot 10^{-12} \text{ A Hz}^{-\frac{1}{2}}$, being limited by the high dark current.

Time response, measured in s. The time response of a photodetector is usually measured between 10% and 90% of the generated signal under modulated excitation intensity, either on the raising or falling edge. A photodetector with a small response time is usually desired to allow for certain applications, like video-rate imaging. Commercial silicon photodiodes show rise times of about 50 ps while graphene detectors can already reach hundreds of picoseconds.[31, 34]

Bandwidth, B , measured in Hz. The bandwidth of a photodetector is defined as the modulation frequency ($f_{\text{modulation}}$) of the incoming light excitation at which the intensity of the detector signal is 3 dB less than under continuous illumination. A photodetector with a large bandwidth is desirable for high-rate optical information transfer. As for the response time, the bandwidth of commercial silicon and graphene detectors is similar and reaches a few tens GHz.[31, 34] Using optical correlation techniques, the intrinsic bandwidth of graphene has been estimated to be about 260 GHz.[38]

Detectivity, D^* , measured in $\frac{\text{cm}\sqrt{\text{Hz}}}{\text{W}}$. The detectivity (D^*) is a figure-of-merit derived from the NEP that enables comparison between photodetectors of different geometries: a higher detectivity indicates a better photodetector performance. It is defined as:

$$D^* = \frac{\sqrt{AB}}{NEP} \quad (2.15)$$

where A is the area of the photodetector and B is its bandwidth. The detectivity of silicon photodiodes is in the order of $1 \cdot 10^{12} \frac{\text{cm}\sqrt{\text{Hz}}}{\text{W}}$ while for hybrid graphene-PbS systems can reach about $1 \cdot 10^{13} \frac{\text{cm}\sqrt{\text{Hz}}}{\text{W}}$, similar to commercial detectors based on III-V materials.[32]

REFERENCES

- [1] S. M. Sze and K. K. Ng, *Physics of semiconductor devices*, John Wiley & Sons (2006).
- [2] R. T. Tung, *The physics and chemistry of the Schottky barrier height*, Applied Physics Reviews **1** 011304 (2014).
- [3] J. Ziman, *Principles of the Theory of Solids*, Cambridge University Press (1972).
- [4] M. Fox, *Optical Properties of Solids*, Oxford Master Series in Physics, OUP Oxford (2010).
- [5] J. Finley, A. Ashmore, A. Lemaître, D. Mowbray *et al.*, *Charged and neutral exciton complexes in individual self-assembled In (Ga)As quantum dots*, Physical Review B **63** 073307 (2001).
- [6] R. J. Ellingson, M. C. Beard, J. C. Johnson, P. Yu *et al.*, *Highly efficient multiple exciton generation in colloidal PbSe and PbS quantum dots*, Nano letters **5** 865 (2005).
- [7] D. Dalacu, K. Mnaymneh, J. Lapointe, X. Wu *et al.*, *Ultraclean Emission from InAsP Quantum Dots in Defect-Free Wurtzite InP Nanowires*, Nano Lett. **12** 5919 (2012).
- [8] K. E. Mak, K. He, C. Lee, G. H. Lee *et al.*, *Tightly bound trions in monolayer MoS₂*, Nat. Mater. **12** 207 (2013).
- [9] A. Rose, *Concepts in photoconductivity and allied problems*, Interscience Publishers (1963).
- [10] R. Bube, *Photoelectronic Properties of Semiconductors*, Cambridge University Press (1992).

- [11] B. Saleh and M. Teich, *Fundamentals of photonics*, Wiley series in pure and applied optics, Wiley (1991).
- [12] M. M. Furchi, D. K. Polyushkin, A. Pospischil and T. Mueller, *Mechanisms of Photoconductivity in Atomically Thin MoS₂*, Nano Lett. – (2014).
- [13] F. H. L. Koppens, T. Mueller, P. Avouris, A. C. Ferrari *et al.*, *Photodetectors based on graphene, other two-dimensional materials and hybrid systems*, Nat Nano 9 780 (2014).
- [14] N. Ashcroft and N. Mermin, *Solid state physics*, Saunders College (1976).
- [15] J. Park, Y. H. Ahn and C. Ruiz-Vargas, *Imaging of Photocurrent Generation and Collection in Single-Layer Graphene*, Nano Lett. 9 1742 (2009).
- [16] M. Buscema, M. Barkelid, V. Zwiller, H. S. J. van der Zant *et al.*, *Large and Tunable Photothermoelectric Effect in Single-Layer MoS₂*, Nano Lett. 13 358 (2013).
- [17] D. J. Groenendijk, M. Buscema, G. A. Steele, S. Michaelis de Vasconcellos *et al.*, *Photovoltaic and Photothermoelectric Effect in a Double-Gated WSe₂ Device*, Nano Lett. 14 5846 (2014).
- [18] D. Mac Donald, *Thermoelectricity: An Introduction to the Principles*, John Wiley & Sons (1962).
- [19] N. Mott and H. Jones, *The theory of the properties of metals and alloys*, The Clarendon Press (1936).
- [20] G. Nolas, J. Sharp and H. Goldsmid, *Thermoelectrics: Basic Principles and New Materials Developments*, Springer (2001).
- [21] Bhushan, *Springer Handbook of Nanotechnology* – (2007).
- [22] J. P. Heremans, V. Jovic, E. S. Toberer, A. Saramat *et al.*, *Enhancement of Thermoelectric Efficiency in PbTe by Distortion of the Electronic Density of States*, Science 321 554 (2008).
- [23] A. Slachter, F. L. Bakker, J.-P. Adam and B. J. van Wees, *Thermally driven spin injection from a ferromagnet into a non-magnetic metal*, Nat. Phys. 6 879 (2010).
- [24] Z. Li, M.-H. Bae and E. Pop, *Substrate-supported thermometry platform for nanomaterials like graphene, nanotubes, and nanowires*, Applied Physics Letters 105 (2014).
- [25] J. Wu, H. Schmidt, K. K. Amara, X. Xu *et al.*, *Large Thermoelectricity via Variable Range Hopping in Chemical Vapor Deposition Grown Single-Layer MoS₂*, Nano Lett. 14 2730 (2014).
- [26] P. L. Richards, *Bolometers for infrared and millimeter waves*, Journal of Applied Physics 76 1 (1994).
- [27] M. Freitag, T. Low, F. Xia and P. Avouris, *Photoconductivity of biased graphene*, Nat. Photon. 7 53 (2013).
- [28] L. Vicarelli, M. Vitiello, D. Coquillat, A. Lombardo *et al.*, *Graphene field-effect transistors as room-temperature terahertz detectors*, Nature Materials 11 865 (2012).
- [29] M. Engel, M. Steiner and P. Avouris, *Black Phosphorus Photodetector for Multispectral, High-Resolution Imaging*, Nano Lett. – (2014).
- [30] T. Low, A. S. Rodin, A. Carvalho, Y. Jiang *et al.*, *Tunable optical properties of multilayer black phosphorus thin films*, Phys. Rev. B 90 075434 (2014).
- [31] F. Xia, T. Mueller, Y.-m. Lin, A. Valdes-Garcia *et al.*, *Ultrafast graphene photodetector*, Nat Nano 4 839 (2009).
- [32] G. Konstantatos, M. Badioli, L. Gaudreau, J. Osmond *et al.*, *Hybrid graphene-quantum dot phototransistors with ultrahigh gain*, Nature nanotechnology 7 363 (2012).
- [33] C.-H. Liu, Y.-C. Chang, T. B. Norris and Z. Zhong, *Graphene photodetectors with ultra-broadband and high responsivity at room temperature*, Nat Nano 9 273 (2014).
- [34] T. Mueller, F. Xia, M. Freitag, J. Tsang *et al.*, *Role of contacts in graphene transistors: A scanning photocurrent study*, Phys. Rev. B 79 245430 (2009).
- [35] P. Blake, E. W. Hill, A. H. C. Neto, K. S. Novoselov *et al.*, *Making graphene visible*, Appl. Phys. Lett. 91 063124 (2007).
- [36] C. Casiraghi, A. Hartschuh, E. Lidorikis, H. Qian *et al.*, *Rayleigh Imaging of Graphene and Graphene Layers*, Nano Lett. 7 2711 (2007).
- [37] M. M. Furchi, A. Pospischil, F. Libisch, J. Burgdörfer *et al.*, *Photovoltaic Effect in an Electrically Tunable van der Waals Heterojunction*, Nano Lett. 14 4785 (2014).
- [38] A. Urich, K. Unterrainer and T. Mueller, *Intrinsic Response Time of Graphene Photodetectors*, Nano Lett. 11 2804 (2011).

CHAPTER 3

TWO-DIMENSIONAL MATERIALS FOR PHOTODETECTION

Michele Buscema, Joshua O. Island, Dirk J. Groenendijk, Sofya I. Blanter, Gary A. Steele, Herre S.J. van der Zant and Andres Castellanos-Gomez

Two-dimensional (2D) layered two-dimensional materials have attracted a great deal of interest in recent years. This family of materials allows for the realization of versatile electronic devices and hold promise for next-generation (opto)electronics. The electronic properties of 2D materials strongly depend on their number of layers, making them interesting from a fundamental standpoint. For electronic applications, semiconducting 2D materials benefit from sizable mobilities and large on/off ratios, due to the large achievable field effect. Moreover, being mechanically strong and flexible, these materials can withstand large strain (> 10%) before rupture, making them interesting for strain engineering and flexible devices. Even in their single layer form, semiconducting 2D materials have demonstrated efficient light absorption, enabling large responsivity in photodetectors. Therefore, semiconducting layered 2D materials are strong potential candidates for optoelectronic applications, especially for photodetection. Here, we review the state-of-the-art in photodetectors based on semiconducting 2D materials, especially focusing on the transition metal dichalcogenides, black phosphorus, novel van-der-Waals materials and heterostructures.

3.1. INTRODUCTION

The isolation of graphene in 2004,[1, 2] rapidly followed by the discovery of its amazing properties,[3–10] has generated an intense research effort on the large family of layered materials.[3, 11] In these materials, the atoms forming the compound are arranged into planes (layers) that are held together by strong in-plane bonds, usually covalent. To form a 3D crystal, the atomic layers are stacked in the out-of-plane direction with weak van-der-Waals (vdW) interactions. This vdW stacking allows to cleave bulk crystals and fabricate thinner *flakes*, down to the single layer limit.[2] For photodetection, flakes of layered materials present several advantages over conventional 3D materials, from both a practical and a fundamental standpoint. The atomic thickness makes layered materials almost transparent (and yet present strong light-matter interaction), which is of high interest for novel applications, e.g. photovoltaics integrated in façades or wearable electronics. Their atomic thickness is also responsible for quantum confinement effects in the out-of-plane direction. These effects are strong in the semiconducting transition metal dichalcogenides - TMDCs - where the reduced thickness results in strongly bound excitons.[12–14] Another effect of the vertical confinement is the modulation of the bandgap as a function of the number of layers, particularly evident in TMDCs.[12, 15–19]

Layered materials have also demonstrated elastic moduli larger than hundreds of GPa[6, 20, 21] and ultimate strain larger than 10% before rupture.[6, 22, 23] Large strains have a strong effect on the electronic and optical behavior of these materials.[6, 19, 24–27] Thus, strain-engineering can be used to tune the optical properties and realize novel device architectures (wearable, bendable devices) and devices with novel functionalities, like exciton funnelling.[28, 29]

THIS CHAPTER

This Chapter is a review of the state-of-art in photodetection with layered materials, especially focusing on the semiconducting materials that are going to be addressed in Chapters 6, 7 and 8. We start with a very brief overview of graphene-based photodetectors, then move on to review the main results for photodetectors based on the TMDCs, especially the molybdenum and tungsten compounds. Next, we describe the recent experimental findings for the novel compound black phosphorus. Last we review the recent advances in artificially stacked van der Waals heterostructures.

3.2. GRAPHENE-BASED PHOTODETECTORS

Graphene-based photodetectors have shown several photocurrent generation mechanisms due to the peculiar properties of graphene, especially its large mobility,[10] the high transparency[30] and the absence of an energy gap.[31–33] The gapless energy dispersion relationship of graphene carriers allows the absorption of photons of very small energy: recent reports show photodetection for $E_{\text{photon}} \sim 10 \text{ meV}$, correspond-

ing to a wavelength of about 120 μm . [34, 35]

The metal contacts to graphene play a major role in its photodetection properties. [7, 36, 37] Figure 3.1a shows a micrograph of a graphene FET (gFET) from reference [37]. Scanning photocurrent microscopy (SPCM) measurements on the gFET in Figure 3.1a reveal that the photocurrent is generated when the focused laser spot is illuminating the graphene/metal interface (see Figure 3.1b). The alternating photocurrent sign is an indication of the direction of the electric field at each interface. [37]

Xia *et al.* performed gate-dependent SPCM measurements on a similar graphene device. [7] The reflectance image of the gFET in Figure 3.1c allows one to locate the electrodes. The white dashed line corresponds to the location where the linecuts in Figure 3.1d were collected. While applying a gate voltage, the peaks in the photocurrent shift away from the center of the flake and get closer to the electrodes edges with respect to their position at the flatband condition ($V_g = 15\text{ V}$). Moreover, the intensity of the peaks increases when the gate voltage is far from the flatband condition. Both the shift in position and the increase in magnitude are consistent with a photocurrent generation dominated by the electric field at the Schottky Barriers (SBs): applying a gate bias changes the slope of the bands at the metal/graphene interface, changing the location of the maximum electric field. A larger gate voltage results in steeper bands at the interface, pushing the SBs electric field maximum towards the metal edge. [7] At the highest gate voltage ($V_g = 45\text{ V}$), the doping in the bulk graphene is opposite to the local doping induced by the electrodes, giving rise to a localized PN junction. [7]

The photo-thermoelectric effect can also drive photocurrents in a gFET, competing with the photovoltaic effect induced by the SBs. [37] Figure 3.2a shows a micrograph of the same gFET from Figure 3.1a. In their study, the authors report photocurrent driven by the electric field at the SBs by illuminating with $\lambda = 780\text{ nm}$, see Figure 3.1b. Figure 3.2b plots an SPCM map collected by scanning with $\lambda = 410\text{ nm}$ in hole-doping regime. Interestingly, there is a strong photocurrent generated from the *inside* of electrodes A and E, several microns away from the electrodes edges. This current can be attributed to the photo-thermoelectric effect. As schematically depicted in Figure 3.2c, the local illumination provides a temperature difference between the two contacts ΔT that can generate a thermoelectric current in the device (for more details, see Section 2.4.1).

Contacts also play a major role when the devices are globally illuminated. Mueller *et al.* [8] contacted a single-layer graphene flake with interdigitated electrodes made of titanium and palladium (see inset of Figure 3.3a). The $I_{\text{ds}} - V_{\text{ds}}$ are linear both in dark and under illumination and intersect at the point where the external V_{ds} bias is equal to the built-in electric field induced by the different metals. This built-in electric field separates the photogenerated electron-hole pairs and drives photocurrent at zero V_{ds} . Figure 3.3b shows the band diagrams as a function of the applied V_{ds} . The different contact metals locally induce a slightly different doping in the graphene,

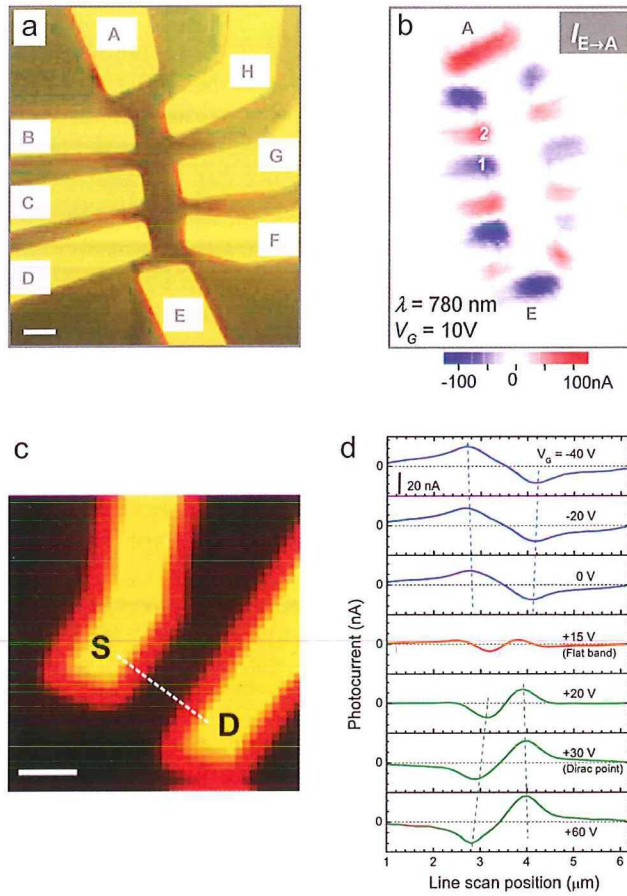


FIGURE 3.1: (a) Optical micrograph of a graphene FET used to perform SPCM measurements by Park *et al.* [37]. The scale bar is $2\ \mu\text{m}$. (b) Scanning photocurrent map. The colorscale represents the measured photocurrent while a focused laser ($\lambda = 780\ \text{nm}$, $P = 0.34\ \text{mW}$) spot is scanned over the surface. The intensity of the reflection is collected simultaneously and used to locate the edges of the electrodes (gray shapes). (c) Reflectance image of the gFET measured in ref. [7]. The source and drain electrodes are identified by S and D respectively. The scale bar is $2\ \mu\text{m}$. The dashed white line indicates the location where the gate dependent linecut shown in panel (d) are taken. (d) Gate-dependent SPCM linecuts ($\lambda = 632.8\ \text{nm}$, $P_{\text{incident}} = 30\ \mu\text{W}$.) Panels a,b are adapted from ref. [37] Panels c,d are adapted from ref. [7]

due to their difference in workfunction. The local difference in doping shifts the charge neutrality point by $\Delta\phi$ which, in turn, promotes band bending, giving rise to the internal electric field. This photodetector reaches a responsivity of $6.1\ \text{mA W}^{-1}$ and can be operated at zero external bias (photovoltaic mode), decreasing the noise

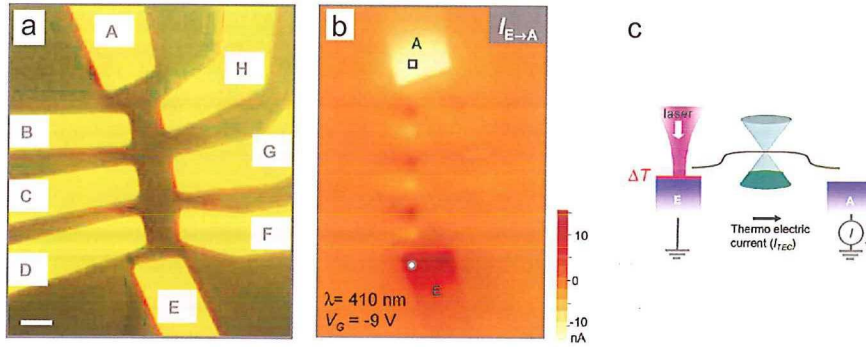


FIGURE 3.2: (a) Optical micrograph of a graphene FET used to perform SPCM measurements by Park *et al.*[37]. The scale bar is $2 \mu\text{m}$. (b) SPCM map of the device presented in panel a collected with $\lambda = 410 \text{ nm}$, $P = 1 \text{ mW}$, $V_g = -9 \text{ V}$ and lock-in detection. (c) Band schematics of the device under localized illumination highlighting the temperature difference ΔT that drives the thermoelectric current. All panels from ref. [37]

equivalent power (NEP). At telecommunication wavelengths, this graphene-metal detector reaches a bandwidth of 16 GHz allowing for 10 Gbits^{-1} data exchange rate (Figure 3.3c and inset).

Graphene photodetectors demonstrate a variety of photocurrent generation mechanisms, owing to the interaction with the metallic contacts. While operation wavelengths can be up to $120 \mu\text{m}$ and operation frequencies can be as high as 40 GHz , the absolute responsivity is low, limited to a few mA W^{-1} . For more in-depth reviews about photodetection in graphene and graphene oxide, we refer the reader to refs.[38, 39]

3.3. PHOTODETECTORS BASED ON TRANSITION METAL DICHALCOGENIDES

Transition metal dichalcogenides (TMDCs) are layered compounds with general formula MX_2 where M is a metal from group IV, V or VI of the transition metals and X is a chalcogen atom (group VI, e.g., S, Se or Te).[9] In every layer, the metal atoms form a plane in between two planes of chalcogen atoms. Every metal atom is covalently bonded to the chalcogen atoms on either side. This covalent bond provides the structural integrity to a single-layer. To form a bulk crystal, the layers are held together by weak van der Waals interactions (see Figure 3.4a). The weak out-of-plane interaction facilitates micromechanical exfoliation, allowing isolation of single-layers (see Figure 3.4b). The mechanical exfoliation of these materials has opened the door to the fabrication of FETs based on single- and few-layer TMDCs and to the study of

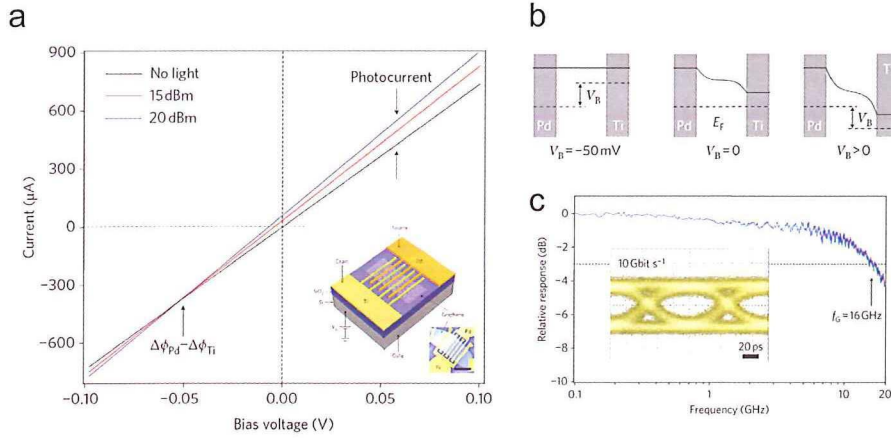


FIGURE 3.3: (a) $I_{ds} - V_{ds}$ characteristics in dark (black solid line) and under laser illumination with λ 1550 nm and $P = 15\text{dBm} \sim 32\text{ mW}$ (red solid line) and $P = 20\text{dBm} = 100\text{ mW}$ (blue solid line). Inset: device schematics and optical micrograph - scale bar is $5\text{ }\mu\text{m}$ (b) Band diagrams as a function of applied bias. The dark solid line represents the charge neutrality point. (c) Relative response as a function of modulation frequency. Inset: superposition of the electrical response to repeated pulses at a rate of 10Gbits^{-1} (eye diagram). The empty region between the high and low signal level indicates that the detector can work well at this data rate. All panels from ref. [8]

their (opto)electronic properties.

3.3.1. PHOTODETECTION WITH MOLYBDENUM DISULPHIDE

MoS_2 is the most studied semiconducting TMDC, especially in its single-layer form. Its large and direct bandgap (1.8 eV)[12, 15, 17, 18], its mobility[16, 40] above $100\text{ cm}^2\text{ V}^{-1}\text{ s}^{-1}$ and its remarkable mechanical properties[22, 24] make single and few-layer MoS_2 an interesting material for optoelectronic and flexible devices.[41–52]

TMDCs show a variety of electronic transport phases: metallic, superconducting, charge density wave and semiconducting. We refer the reader to ref.[9] for an overview. In the remainder of this Chapter we will focus on the semiconductors and especially on MoS_2 , MoSe_2 , WS_2 and WSe_2 given their large and direct bandgap, useful for detection in the visible part of the electromagnetic spectrum (see Table 3.1).

The number of layers dramatically affects the bandgap, both in magnitude and in nature. MoS_2 shows a transition from a direct, 1.89 eV bandgap in single layer to an indirect 1.6 eV bandgap in two layers. [12–18] In the single-layer form, the direct bandgap is located at the K point of the Brillouin zone while in a few-layer sample the fundamental transition is indirect from the Γ point to an intermediate point in the $K - \Gamma$ direction (see Figure 3.5a). This shift can be explained by a change in the confinement of the carriers.[12, 17] This direct-to-indirect bandgap transition

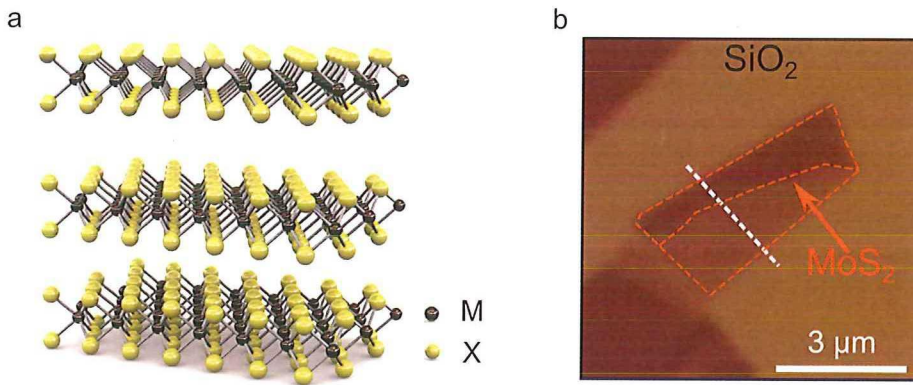


FIGURE 3.4: (a) Artist impression of a layered transition metal dichalcogenide in its 2H phase. The black dots are the metallic atoms; the yellow dots are the chalcogen atoms. (b) Typical micrograph of an MoS₂ flake exfoliated in SiO₂/Si substrate. The arrow points at the single-layer part. Panel (a) is adapted from [9]

	Bandgap 1L (eV)	Bandgap bulk (eV)	Ref
MoS ₂	1.89	1.20	[12–18]
MoSe ₂	1.51	1.10	[53]
WS ₂	1.90	1.40	[54]
WSe ₂	1.65	1.30	[53]

TABLE 3.1: Bandgap of Mo and W based TMDCs

drastically reduces the luminescence intensity for multilayer samples (see Figure 3.5b).[17] This effect is found to be common for MoS₂, MoSe₂, WS₂ and WSe₂. [17, 53]. The change in bandgap magnitude with the number of layers has been proposed as a method to engineer the spectral response of photodetectors by using different thicknesses of MoS₂ flakes.[44]

The symmetry of the unit cell (i.e. the crystalline phase) has also a large influence on the electronic properties.[18, 55] Figure 3.6a,b shows the 1T and the 2H phase for MoS₂. [18] The 1T phase has a octahedral symmetry and makes MoS₂ metallic while the 2H phase is trigonal prismatic and makes MoS₂ a semiconductor with a 1.89 eV bandgap.[18, 55] The absence of a bandgap in the metallic (1T) phase results in a suppressed photoluminescence intensity (see Figure 3.6c).[18, 55] It was recently shown that a chemical treatment can induce the phase transformation.[55] The region where the phase transition takes place can be defined by means of electron-beam lithography, allowing for on-demand realization of metallic patches in a semiconducting flake.[55] These metallic patches were recently exploited to drastically reduce

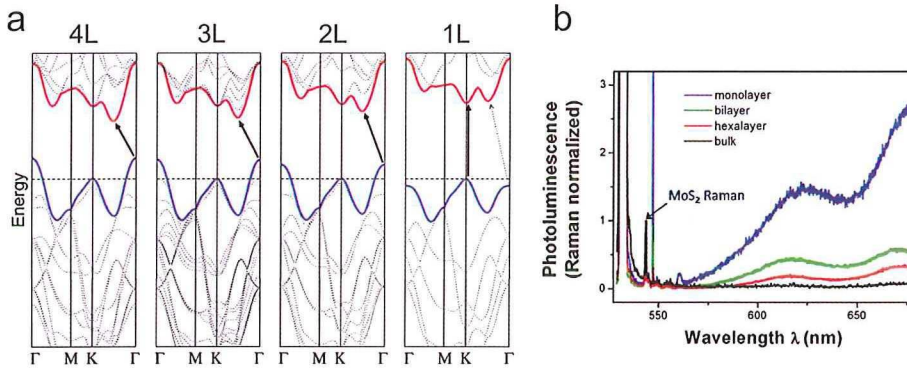


FIGURE 3.5: (a) Band structure of 4 layers (4L), 3 layers (3L), 2 layers (2L) and 1 layer (1L) MoS₂. The red (blue) solid line highlights the conduction (valence) band edge. Arrows indicate the lowest-energy transition. (b) Luminescence spectra for 1L (blue solid line), 2L (green solid line), 6L (red solid line) and bulk (black solid line) MoS₂. The intensity is normalized to the A_{1g} Raman mode. Both panels are modified from ref. [17]

(-60%) the contact resistance of FETs based on single layer MoS₂. [55]

We will now turn our attention to the photodetectors based on TMDCs, starting from biased and unbiased detectors based on MoS₂. We will briefly describe the recent results on MoSe₂ and WS₂.

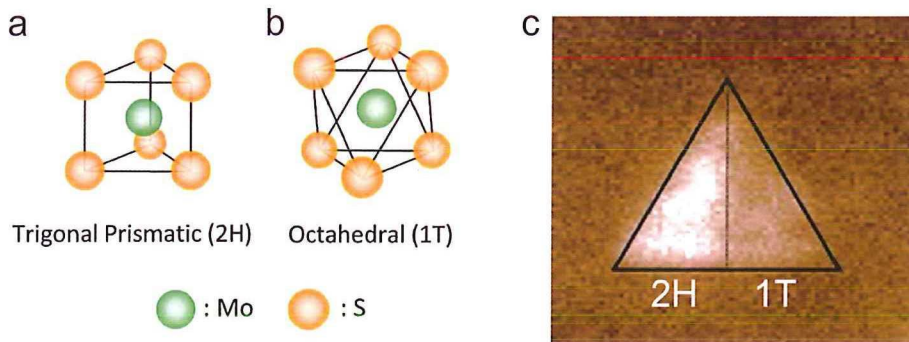


FIGURE 3.6: (a) Trigonal prismatic symmetry of the 2H unit cell. (b) Octahedral symmetry of the 1T unit cell. In both (a) and (b) panels the green dot is the Mo atom and the orange dot is the S atom. (c) Spatially resolved photoluminescence of single layer MoS₂ composed of 2H phase and 1T phase. The 2H phase appears brighter due to the higher luminescence efficiency of the 2H-semiconducting phase. Panels (a) and (b) are modified from ref. [18]. Panel c is adapted from ref. [55]

EXTERNALLY BIASED PHOTODETECTORS.

Photodetectors based on single- and few-layer MoS₂ are usually in the form of photo-FETs (see Figure 3.7a). Yin *et al.*[43] first reported a photo-FET based on single layer MoS₂ (Figure 3.7a) reaching a responsivity of about 7.5 mA W⁻¹ in electron accumulation, measurable photoresponse up to about 750 nm and a response time in the order of 50 ms (see Figure 3.7b).[43]

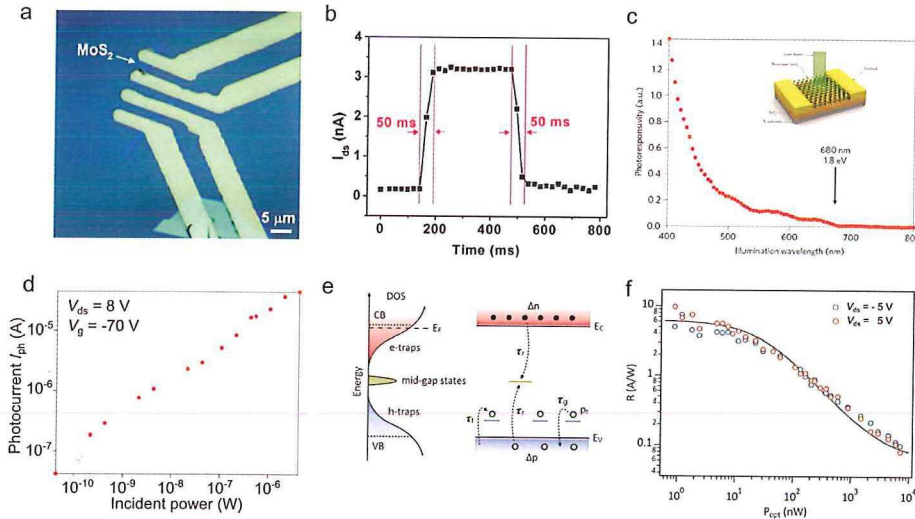


FIGURE 3.7: (a) Optical image of a typical device based on single layer MoS₂. (b) Time response of the device in panel (a). (c) Photoresponsivity as a function of illumination wavelength, evidencing the cut-off wavelength at 680 nm. Inset: device schematics. (d) Photocurrent as a function of incident optical power. (e) Energy and relevant rates for the trap-assisted recombination model. Hole traps are the only relevant traps due to the large effective mass of the holes (open dots) compared to the electrons (closed dots) (f) Responsivity as a function of excitation power for V_{ds} = -5 V (blue dots) and V_{ds} = 5 V (red dots). Panels a,b are adapted from ref. [43]. Panels c,d are adapted from ref. [46]. Panels e,f adapted from ref. [52].

Recently, a similar study by Lopez-Sanchez *et al.*[46] reported a low-bound responsivity for exfoliated 1L MoS₂ photo-FET 880 A W⁻¹ in depletion and a cut-off wavelength of 680 nm (see Figure 3.7c).[46] The reported responsivity is a lower bound since it is estimated in the OFF state of the photo-FET, where the photocurrent magnitude is the lowest.[46] With increasing power, the photocurrent raises sublinearly (Figure 3.7d). The time response is in the order of 4 s and it could be reduced to 600 ms with the help of a gate pulse to reset the dark conductivity of the FET.[46] Both the sublinear behavior of the photocurrent with power and the need of a gate pulse to reset the conductivity are symptomatic of a photocurrent generation mechanism where trap states play a dominant role.

The NEP reached by the photodetector presented by Lopez-Sanchez *et al.* is

$1.8 \cdot 10^{-15} \text{ WHz}^{-\frac{1}{2}}$. [46] This remarkably low NEP stems from the low magnitude of the dark current in electron depletion, achievable due to efficient field-effect tunability in single-layer MoS_2 and the 1.8 eV bandgap of 1L MoS_2 that suppresses thermally activated carriers. [16]

In case of 1L MoS_2 grown by chemical vapor deposition (CVD), Zhang *et al.* reported responsivities in the order of 2200 A W^{-1} in vacuum and 780 A W^{-1} in air, highlighting the importance of the environment for both the electronic and the optoelectronic properties. [51] Given the large surface-to-volume ratio, adsorbates play a major role in the properties of layered materials. [56–59] Charged adsorbates also reduce the photoresponse as they suppress the lifetime of trapped carriers by acting as recombination centers. [51]

Both exfoliated and CVD-grown MoS_2 display large responsivity (large optical gain), sub-linear I_{photo} with incident optical power and ms-to-s response times; all these properties point to a photogeneration mechanism in which trap states play a major role. In particular, the photocurrent generation mechanism is a combination of both photoconductance (PC) and photogating (PG), as recently reported in ref [52]. Furchi *et al.* [52] study the photoresponse of single and bilayer MoS_2 photo-FETs by varying the incident optical power and the modulation frequency of the optical excitation. The large difference in time scales between PC (fast) and PG (slow) facilitates disentangling the two effects. The proposed model, based on mid-gap states and hole-trap states (Figure 3.7e), allows the authors to fit the measured data (Figure 3.7f) and extract relevant parameters, such as the density and energy of the trap states involved in the photoconduction process. [52]

MULTILAYER MoS_2 PHOTODETECTORS.

Multilayer MoS_2 photodetectors benefit from the decrease in bandgap, allowing for extended detection range, [44, 45] larger absorption due to increased thickness, [50] and achieve responsivity similar to single-layer photodetectors, even if their bandgap is indirect. [52, 60] The photodetection mechanism in multilayer MoS_2 is still dominated by trap states.

HYBRID MoS_2 –PbS QUANTUM DOTS PHOTODETECTORS.

Very recently, Kufer *et al.* [61] have realized hybrid photodetectors based on bilayer MoS_2 and lead sulfide (PbS) quantum dots. The final device was fabricated in two steps; first the bilayer MoS_2 was patterned into an FET and, second, the PbS quantum dots were deposited on top via a layer-by-layer and ligand exchange process. The ligand exchange step is crucial to improve the charge transport properties of the quantum dot film and the charge transfer to the MoS_2 bilayer. The deposition of the QDs affects the $I_{\text{ds}}-V_{\text{g}}$ characteristics of the bilayer MoS_2 , reducing the ON/OFF ratio and mobility. This is a strong indication that the QD deposition increases the charge carrier concentration in the MoS_2 flake by charge transfer and makes it more metallic.

This hybrid photodetector shows high responsivity ($6 \cdot 10^3 \text{ A W}^{-1}$), detection up to $\lambda = 1500 \text{ nm}$ and a time response in the order of 350 ms. Moreover, by tuning the MoS₂ in the OFF state, the dark current can be suppressed, decreasing the NEP and increasing the detectivity of the detector. The low dark current and large detectivity are a major improvement with respect to a similar hybrid device based on single-layer graphene, where the large dark current of the graphene FETs reduces the detectivity.[62]

The photodetection mechanisms are a combination of photovoltaic and photogating. The electric field at the interface between the n-type MoS₂ and the p-type PbS quantum dot film separates the electron hole pairs that are generated by photon absorption in either of the two materials (photovoltaic). Next, the holes are trapped in the quantum dot film, increasing the photocarrier lifetime and yielding the large responsivity and long response time (photogating).

In conclusion, biased photodectors based on single- and few-layer MoS₂ routinely achieve high responsivity, indicating high photogain, originating from the long lifetime of photogenerated carriers, boosted by trap states. Table 3.2 summarizes the main figures-of-merit of this type of photodetectors.

PHOTOVOLTAIC AND PHOTO-THERMOELECTRIC EFFECTS IN MoS₂.

In a recent study, Fontana *et al.*[48] reported PV effect in a photo-FET based on a thin ($\sim 50 \text{ nm}$) MoS₂ flake where the source/drain contacts were made from gold and palladium, respectively.[48] The workfunction difference between Au and Pd promotes a small difference in local doping of the MoS₂ flake, giving rise to an asymmetry in the SBs at the two contacts, as in the case of graphene phototransistors.[48, 63] The SBs asymmetry effectively acts as an internal electric field and generates a photocurrent under global illumination ($r_{\text{spot}} \gg L_{\text{device}}$). An independent study on a similar device based on single-layer MoS₂ with Au and Pd contacts has demonstrated that the SB height for Pd contacts is larger than for Au.[64]

Figure 3.8a shows a micrograph of the device by Fontana *et al.*,[48] highlighting the asymmetric metalization of the contacts. The measured $I_{\text{ds}} - V_{\text{ds}}$ characteristics are plotted in Figure 3.8b and show diode-like behavior in the dark and a clear PV photocurrent generation under illumination. For different devices, the short-circuit current I_{sc} ranges from 0.2 to 2 nA and the open-circuit voltage V_{oc} from about 30 to 100 mV. The large current in reverse bias indicates non-ideal diode behavior.

In Chapter 6 of this Thesis, we present an SPCM study of a single-layer MoS₂ photo-FET.[47] We find that, unlike in many other semiconductors, the photocurrent generation in single-layer MoS₂ is dominated by the photo-thermoelectric effect and not by the separation of photoexcited electron-hole pairs across the Schottky barriers at the MoS₂/electrode interfaces. We observe a large value for the Seebeck coefficient for single-layer MoS₂ that, by means of an external electric field, can be tuned between $-4 \cdot 10^4$ and $-1 \cdot 10^5 \mu\text{V K}^{-1}$. This value is in reasonable agreement with recent estimates made with electrical measurements.[65] We finally note that, under

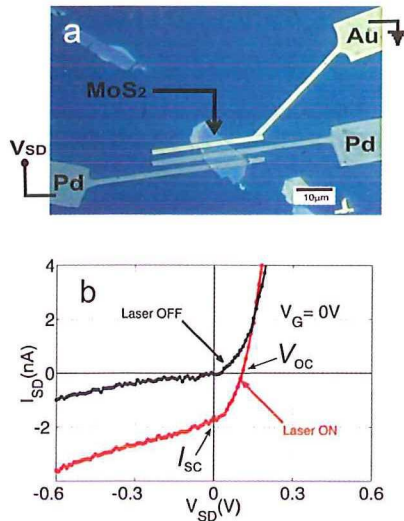


FIGURE 3.8: (a) Optical image and circuit schematic of a typical ultrathin MoS₂ device contacted with different metals (Au and Pd). (b) $I_{ds}-V_{ds}$ characteristics of the device in panel a, in dark (solid black line) and under illumination (solid red line). Both panels are adapted from ref. [48]

focused illumination and external bias, also the PV effect at the Schottky barriers (SBs) could play a role, as reported in multilayer MoS₂ devices.[50]

In summary, devices based on MoS₂ demonstrate the possibility of photocurrent generation with no external bias via both the photo-thermoelectric effect and SB-driven photovoltaics. The large and gate-tunable Seebeck coefficient of single-layer MoS₂ drives current under focused illumination while, for devices based on multilayer MoS₂ under blanket illumination, the electrode material can induce SB-driven photocurrent generation.

We now turn our attention to other semiconducting TMDCs that have recently attracted a great deal of attention for photodetection.

3.3.2. MOLYBDENUM DISELENIDE

Molybdenum diselenide (MoSe₂) has been grown via CVD techniques by several groups,[66–73] yielding large-area triangular flakes or continuous films on a variety of substrates. Photodetectors were patterned on the as-grown films or flakes were transferred to an oxidized silicon wafer to fabricate photo-FETs.

Typical CVD grown MoSe₂ photodetectors show responsivity between 0.26 mA W⁻¹ [67] and 13 mA W⁻¹. [73] Recently, a photo-detector based on a ~ 20 nm MoSe₂ exfoliated flake, deterministically stamped on Ti electrodes, demonstrated a responsivity up to 97.1 A W⁻¹. [74] The response time is in the order of few tens of milliseconds for all the studied devices.

3.3.3. TUNGSTEN DISULFIDE

Tungsten disulfide (WS_2) has also been employed for photodetection.[75, 76] In their recent study, Huo *et al.*[76] show a significant dependence of the photoresponse on the gaseous environment in which the measurements were performed. [76] At low excitation powers, the responsivity ranges from $\sim 13 \text{ A W}^{-1}$ in vacuum to 884 A W^{-1} in a NH_3 atmosphere. The increase of responsivity in the NH_3 atmosphere was attributed charge transfer from the absorbed molecules to the WS_2 flake, which affects the WS_2 doping level, as seen in luminescence experiments.[59] As a result of the charge transfer, the lifetime of (one of the) photogenerated carriers can be extended, leading to an enhancement in the responsivity.

The relevant figures-of-merit for MoSe_2 and WS_2 photodetectors are summarized in Table 3.2 to facilitate a direct comparison between photodetectors based on MoS_2 , MoSe_2 and WS_2 .

3.3.4. TUNGSTEN DISELENIDE

Photodetectors. Zhang *et al.*[77] demonstrate the large impact of the metal contacts to a tungsten diselenide (WSe_2) flake on the photoresponse. The responsivity reaches 180 A W^{-1} with Pd contacts and decreases by a factor ~ 30 with Ti contacts. Conversely, the time response for the devices with Ti contacts is less than 23 ms while for the Pd contacts it is in the order of tens of seconds. The large variation in responsivity is attributed to the large difference in SBs induced by Pd and Ti, which is of general importance for photodetectors based on 2D materials.

Electrostatically defined PN junctions. In contrast to MoS_2 , MoSe_2 and WS_2 , devices based on WSe_2 readily demonstrate ambipolar transport via electrostatic gating.[81–86] Exploiting this property, locally-gated PN junctions have been realized with single-layer WSe_2 . [78–80, 87] In the following, we will review the recent studies concerning such PN junctions. We refer the reader to Table 3.2 for a synthetic presentation of the photodetection performance of both the photodetector of ref.[77] and the PN junctions.

The schematics of the locally-gated PN junction devices in references [78–80] are presented in Figures 3.9a,b,c. The fabrication of these PN junctions relies on the deterministic transfer of single-layer WSe_2 on top of two local gates covered with a dielectric, which can be made from a conventional (HfO_2 [78] or Si_3N_4 [79]) or layered (hBN)[80, 87] material. The single-layer WSe_2 is then contacted with electrodes providing low Schottky barriers, usually a Cr/Au stack.[78, 80]

The local gates allow effective control of the charge carrier type and density in the WSe_2 channel and, thus, can induce different carrier types in adjacent parts of the channel, giving rise to a PN junction. Looking at the $I_{\text{ds}} - V_{\text{ds}}$ characteristics highlights the effect of the local gates on the electrical transport, as Figures 3.9d,e,f illustrate. As a function of the gate configuration, the $I_{\text{ds}} - V_{\text{ds}}$ curves range from metallic (PP or

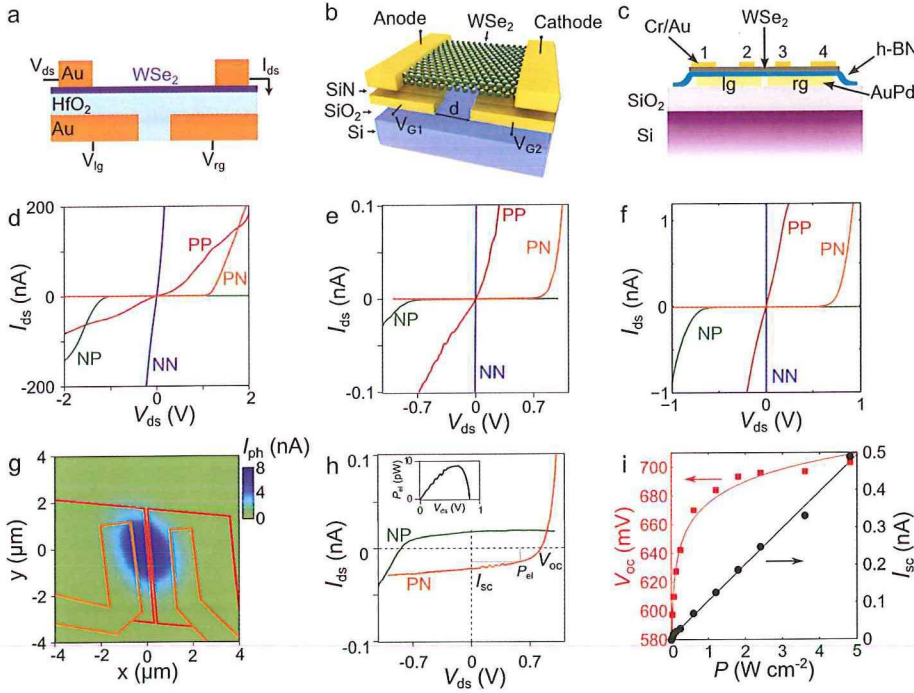


FIGURE 3.9: (a) to (c) Device schematics: panel (a) from ref.[78], panel (b) from [79] and panel (c) from ref. [80]. (d) to (f) $I_{ds}-V_{ds}$ characteristics measured in different gate configurations; (d) from ref.[78], (e) from [79] and (f) from ref. [80]. (g) SPCM map of the photocurrent of the device in (a) in PN configuration. (h) $I_{ds}-V_{ds}$ characteristics measured in PN and NP configuration under white light illumination for the device in (b). Inset: electrical power (P_{el}) extracted from the device. (i) V_{oc} (left axis) and I_{sc} (right axis) as a function of excitation power for the device in (c). Panels (a), (d) and (g) are adapted from reference [78]. Panel (b),(e) and (h) are adapted from ref [79]. Panels (c),(f) and (i) are adapted from ref. [80]. For the $I_{ds}-V_{ds}$ in panels (d) to (f) the gate configurations are as follows: PP (both gates with negative bias), PN and NP (gate at opposite bias), NN (both gates at positive bias). The specific values of the gates voltages differ per device.

NN) to rectifying with opposite direction (PN or NP).

Consistently across three independent studies, the $I_{ds}-V_{ds}$ curves in PN and NP configuration present a high resistance in parallel to the device (R_{par}) and a low saturation current (I_{sat}), both indicating nearly ideal diode behavior. This favorable behavior can be attributed to the large bandgap of single-layer WSe_2 which reduces parallel pathways for current flow, such as thermally-activated carriers and field emission. The devices are also less resistive in the NN configuration than in the PP configuration. This may indicate a larger SB for hole injection resulting from the Cr/Au contacts. The difference in the absolute magnitude of I_{ds} between these studies

may be attributed to differences in device fabrication, gate-induced carrier density or measurement conditions.

We now turn our attention to the response to light excitation of such locally gated PN junctions. Figure 3.9g shows a false-color map of the photocurrent obtained by SPCM on the device in Figure 3.9a in NP gate configuration.[78] Even though the spatial resolution is limited by the long wavelength of the excitation laser, the photocurrent peaks at the depletion region (separation between the gates), suggesting that the photocurrent generation is indeed dominated by the PN junction electric field.

In Figure 3.9h we show the $I_{ds} - V_{ds}$ in PN and NP configuration under illumination for the device in Figure 3.9b. In both curves, the reverse current increases, giving rise to a short-circuit current I_{sc} and an open-circuit voltage V_{oc} . These signatures clearly indicate that the photocurrent generation is driven by the photovoltaic effect, as expected in a PN junction. The extracted electrical power is between tens of pW[79] and hundreds of pW (see inset of Figure 3.9h for a representative plot).[78, 80]

Figure 3.9i plots the V_{oc} (left axis) and I_{sc} (right axis) for increasing excitation power. The I_{sc} increases linearly while the V_{oc} increases logarithmically, confirming the ideal diode behavior, observed in the three independent studies.[78–80] As a zero-biased photodetector, the external quantum efficiency (EQE) can be estimated from I_{sc} and it is in the order of $0.1 \sim 0.2\%$ at $\lambda = 532$ nm (see Figure 3.9f, left axis).[78, 80] The NEP of detectors based on locally gated single-layer WSe_2 is expected to be low in photovoltaic operation, due to the negligible dark current. The time response is in the order of 10 ms and reduces in reverse bias.[80]

3.4. SEMICONDUCTING TRANSITION METAL TRICHALCOGENIDES.

In the previous Section, we reviewed the state-of-art in photodetection with layered semiconducting TMDCs which demonstrate large responsivities in the visible range and have shown the possibility of realizing versatile devices through local gating. However, there are more semiconducting chalcogenide compounds whose electronic properties in the ultra-thin limit are not yet explored.

Materials from the transition metal *trichalcogenides* family (general formula MX_3) present a layered, chain-like structure. Each chain is formed by the repetition of the trigonal-prismatic unit cell along the direction of the b crystallographic axis. The chains extend in one preferential direction, resulting in elongated, ribbon-like sheets. In bulk crystals, these sheets are held together by van der Waals interaction in the out-of-plane direction, facilitating mechanical exfoliation.[88]

In this Section, we review the latest literature on photodetectors based on transition metal *trichalcogenides* materials: TiS_3 (Chapter 5)[88] HfS_3 ,[89] and ZrS_3 . [90] In Chapter 5 we present the photoresponse of ultrathin TiS_3 nanoribbons (NR). Devices

made with ultrathin TiS_3 NR achieved responsivity up to 2910 A W^{-1} at 640 nm illumination wavelength, photoresponse to wavelengths up to 940 nm and short response times (fall time $\sim 5 \text{ ms}$).

To obtain single HfS_3 ribbons, Xiong *et al.*[89] dispersed part of the as-grown material in ethanol and drop-cast it onto a 300 nm SiO_2/Si substrate. Next, photolithography and metal evaporation were used to contact the randomly dispersed nanoribbons. The fabricated devices showed p-type behavior with ON currents in the order of few pA. Under illumination, the current reached up to 200 pA; the responsivity is about 110 mA W^{-1} and the time response is about 0.4 s. The measured light absorbance extends up to about 650 nm.[89]

Tao *et al.*[90] studied the photoresponse of a network of ZrS_3 ribbons transferred onto flexible substrates, polypropylene and paper. Electrical devices were fabricated by shadow-mask evaporation and, under illumination, demonstrate a responsivity of about $5 \cdot 10^{-2} \text{ mA W}^{-1}$, a photoresponse to excitation wavelengths up to 850 nm and a time response of 13 s.[90]

In summary, from the available data, we conclude that photodetectors based on a single nanoribbon of a trichalcogenide compound can achieve responsivity comparable or larger than single layer chalcogenides ($R_{\text{MoS}_2} \sim 1000 \text{ A W}^{-1}$) and faster response times ($\tau_{\text{MoS}_2} \sim 50 \text{ ms}$). Table 3.3 summarizes the main figures of merit of photodetectors based on these materials. The large responsivity and fast response make TiS_3 a material promising for nanoscale photodetection, highlighting the need for further studies.

3.5. III-VI AND IV-VI LAYERED COMPOUNDS.

Besides the transition metal dichalcogenides, also III-VI and IV-VI compounds are interesting for application as photodetectors.[91–98] They are usually stoichiometric compounds between elements from group III (e.g. Ga and In) or IV (usually Sn) and a chalcogen (S, Se or Te). Similarly to the TMDCs, the layers are held together with van-der-Waals forces. However, the structure of a single layer is different from single-layered TMDCs. In the layered III-VI compounds with 1:1 stoichiometry, like GaS, the atoms in each layer have the following repeating unit: S–Ga–Ga–S (Figure 3.10a, top part).

The schematic in Figure 3.10a represents the crystal structure of a GaS nanosheet from a direction perpendicular to the layer plane, showing that the atoms are arranged in a graphene-like honeycomb lattice.[94] For GaS and GaSe, this crystal structure leads to a band structure with dominant indirect transitions (indirect: 2.59 eV, direct 3.05 eV for GaS; indirect: 2.11 eV, direct 2.13 eV for GaSe).[99–103] The structure of GaTe is slightly different, leading to a dominant direct transition (1.7 eV). [104] Compounds with different stoichiometry (like In_2Se_3) have a more complex layer structure and a variety of structural phases influencing their electrical properties (The α -phase has a direct bandgap of 1.3 eV). [105–107]

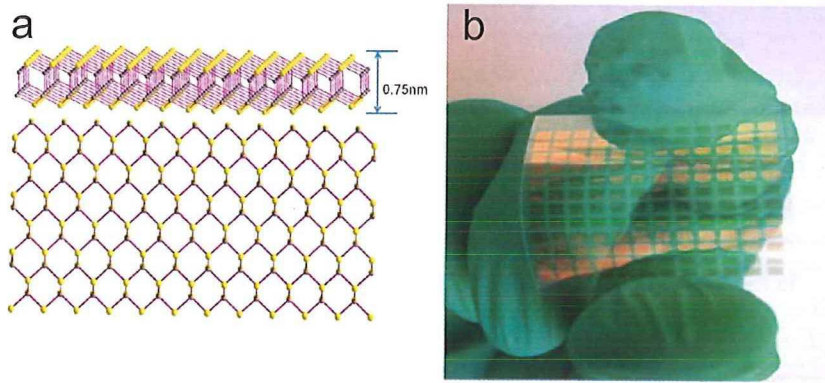


FIGURE 3.10: (a) Atomic structure schematics of GaS. (b) Photograph of flexible photodetector based on GaS flakes. Panels c and d are adapted from ref. [94]

Photodetectors in the form of photoFET have been realized with multilayer flakes of these materials on regular SiO_2/Si substrates and on flexible substrates (see Figure 3.10b), showing similar performances. Direct bandgap materials (GaTe and In_2Se_3) [95, 108] show responsivities of about $1 \cdot 10^4 \text{ A W}^{-1}$ while GaSe and GaS [91, 94] reach about 4 A W^{-1} , in the UV-visible range. The photocurrent raises sublinearly as a function of excitation power, indicating that trap states play an important role in the photoconduction mechanism. [91, 94, 95, 108] The time response ranges from ms to s.

A particular case is represented by InSe . It has a direct bandgap of about 1.3 eV (bulk) and reducing its thickness to below $\sim 6 \text{ nm}$ leads to a transition to an indirect bandgap of higher energy. [96] The performance of photodetectors based on 10-nm-thick InSe flakes have been studied independently by Lei *et al.* [97] and Tamalampudi *et al.* [98]. In their detailed study, Lei and colleagues [97] report photocurrent spectra of 4-layer-thick InSe under excitation wavelength up to 800 nm. The tail of the photocurrent *vs.* wavelength spectra is well fitted by a parabolic relation, strongly suggesting the indirect nature of the bandgap in ultrathin InSe . The responsivity of these devices is about 35 mA W^{-1} and the response time is in the order of 0.5 ms. In their study, Tamalampudi and colleagues [98] fabricate photoFETs based on $\sim 12 \text{ nm}$ thick InSe on both an oxidized Si wafer and a bendable substrate. They measure gate tunable responsivities up to about 160 A W^{-1} and time response in the order 4 s. Both the larger responsivity and the much longer response time compared with the study of Lei *et al.* [97] indicate that long-lived trap states enhance the photoresponse in the devices studied by Tamalampudi [98].

Very recently, also IV-VI layered compounds have been used in photodetectors applications. Specifically, SnS_2 has attracted recent attention as semiconductor material for transistors and photodetector. Exfoliated flakes have been recently employed as

channel materials in FETs, showing mobility[109] of about $1 \text{ cm}^2 \text{ V}^{-1} \text{ s}^{-1}$ and ON/OFF ratios[109] exceeding 10^6 while chemically synthesized nanoparticle films of SnS_2 have already shown promising photoresponse.[110] Su *et al.*[111] have grown flakes of SnS_2 via a seeded CVD technique and used them as channel material for photoFET. SnS_2 -based photodetectors show gate-tunable responsivity up to about 8 mA W^{-1} and response time of $\sim 5 \mu\text{s}$, indicating a very fast photoresponse. Table 3.4 summarizes the main figures-of-merit of detectors based on III-VI and IV-VI materials.

In conclusion, III-VI and IV-VI compounds show responsivities that are comparable or larger than the one measured from TMDC based photoFETs. Moreover, their operation can be extended to the UV region of the spectrum, a feature that can enable them to be used in UV detectors. InSe shows a direct-to-indirect transition for the bandgap when its thickness is reduced below 6 nm, resulting in a parabolic absorption tail up to 1.4 eV photon energy. Thicker InSe flakes show large responsivity (about 160 A W^{-1}) and response time in the order of few seconds, indicating a strong effect of trap states on their photoresponse. Detectors based on SnS_2 can reach responsivity of about 8 mA W^{-1} and fast response time, making them promising as fast detectors.

3.6. FEW-LAYER BLACK PHOSPHORUS

The recently re-discovered few-layer black phosphorus (bP) is an interesting material for photodetection especially due to its intermediate bandgap between graphene and TMDCs; its reduced bandgap compared to TMDCs make few-layer bP a promising candidate to extend the detection range with sizable responsivity that is achievable with 2D materials. Black phosphorus is an elemental layered compound composed of phosphorus atoms arranged in a puckered unit cell. (Figure 3.11a,b) Its bulk form has been studied in the 80's[112] and, electronically, it behaves as a p-type semiconductor with mobilities[113] in the order of $10\,000 \text{ cm}^2 \text{ V}^{-1} \text{ s}^{-1}$ and a bandgap of about 0.35 eV. Once exfoliated to thin layers, it shows ambipolar transport [114–121], mobilities[117, 120] up to $1000 \text{ cm}^2 \text{ V}^{-1} \text{ s}^{-1}$ and absorption edge around 0.3 eV in agreement with its bulk bandgap.[117] The reduced symmetry of the puckered layer structure gives rise to strong anisotropy in the properties of few-layer bP, as evidenced by the anisotropic mobility and optical absorption. [117]

Calculations predict that the bandgap of bP depends strongly on the number of layers and it should reach more than 1 eV once exfoliated down to the single layer (see Figure 3.11c).[114, 118, 123] Black phosphorus can, thus, bridge the gap between the large-bandgap TMDCs and zero-bandgap graphene, completing the high-responsivity detection range that is achievable with 2D layered materials.

The research effort in bP-based photodetectors has been extensive in the past year.[115, 116, 124, 125] In Chapter 7 we present our results on photodetection in few-layer bP phototransistors and in Chapter 8 we showcase the realization of electrostatically defined PN-junctions in few-layer bP.

The thermoelectric effect plays a major role in the photocurrent generation of

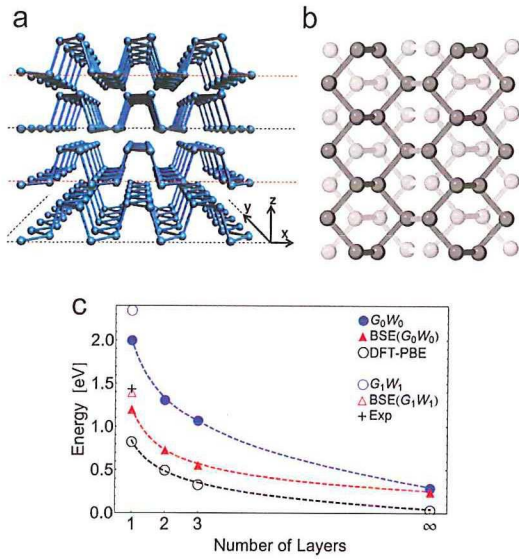


FIGURE 3.11: (a) Perspective view of the puckered structure of few-layer bP. (b) Top view of the puckered structure of few-layer bP. (c) Bandgap energy as a function of the number of layers calculated with different formalisms. The experimental point is taken from ref. [118]. Panel (a) is adapted from ref. [122]. Panel (b) is adapted from ref. [114]. Panel (c) is adapted from ref. [123]

3

ultrathin bP devices. Hong *et al.*[126] performed scanning photocurrent microscopy (SPCM) on a 8 nm high bP transistor with a diffraction limited $\lambda = 780$ nm laser spot as a function of polarization and gate bias. The authors find that both the PV effect (Schottky barriers) and the PTE effect contribute to the photocurrent generation.[126] In the OFF state, the electric field at the Schottky barriers separates the photogenerated electron-hole pairs. Applying a gate bias brings the device in the ON state and drastically reduces the contact resistance, allowing the PTE effect to contribute the photocurrent. By employing the Mott formalism (Equation 2.9) the authors estimate a maximum Seebeck coefficient of $\sim 100 \mu\text{V K}^{-1}$, which is reduced by a factor 10 with increasing gate bias.

In the OFF state, where the Schottky-Barrier induced PV is dominant, the photocurrent magnitude is modulated by incident light polarization. When the polarization is aligned with the low-effective-mass crystallographic axis (x-axis) the photocurrent is enhanced; conversely, aligning the polarization with the high-effective-mass axis (y-axis) suppresses the photocurrent. The polarization-dependent photocurrent is a direct result of the strongly asymmetric band structure of few-layer bP, highlighting a difference from the isotropic TMDCS.

The fast development of photodetectors based on bP has led to the realization of high performance devices for imaging[124, 127] and high-speed communication[125]. Engel *et al.*[124] have achieved high-resolution imaging with a phototransistor based on a 120 nm thick bP flake, working via the photo-bolometric effect.[124, 127] Figure 3.12a shows the geometry of the objects to be imaged: $4 \mu\text{m}$ wide metallic squares

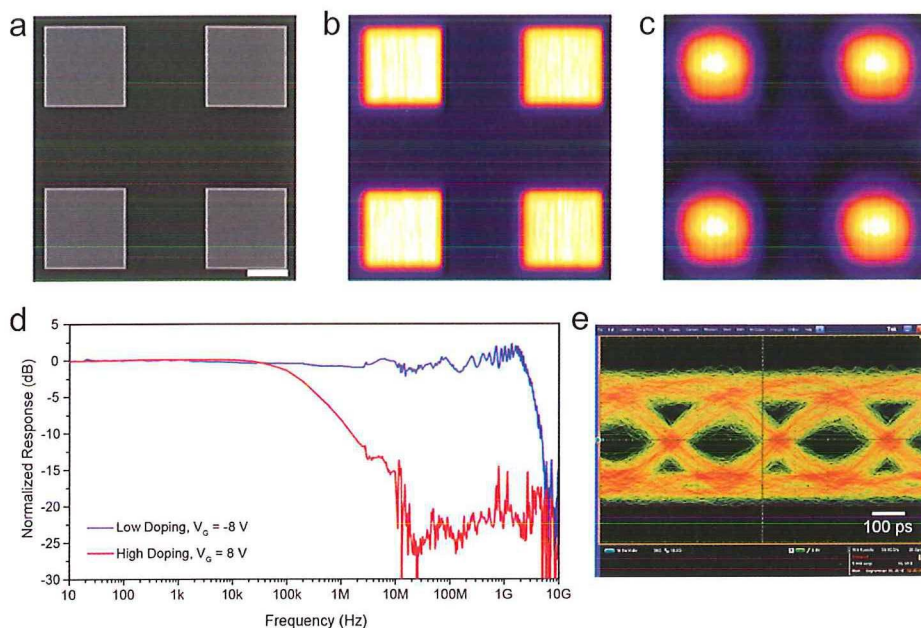


FIGURE 3.12: (a) Scanning electron micrograph of the target image object. The scale bar is $2\ \mu\text{m}$. (b) Image of the object in (a) obtained under focused illumination with $\lambda = 532\ \text{nm}$ and reading the reflected signal with a photodetector based on $120\ \text{nm}$ thick bP. (c) Image of the object in (a) obtained under focused illumination with $\lambda = 1550\ \text{nm}$ and reading the reflected signal with a photodetector based on $120\ \text{nm}$ thick bP. (d) Photoresponse as a function of modulation frequency at low doping (blue curve) and high doping (red curve). (e) Eye-diagram for 3 Gbits/s communication. Panels (a),(b),(c) are adapted from ref. [124]. Panels (d),(e) are adapted from ref. [125].

deposited on glass and separated by $2\ \mu\text{m}$. A focused laser spot is scanned over the surface of the object and the reflected signal is read by the bP phototransistor. Figure 3.12b,c show the images obtained by reading the electric signal from the bP photodetector at a wavelength of $532\ \text{nm}$ and $1550\ \text{nm}$, respectively. The large contrast allows for clear imaging of the features. Feature visibility is constant for sizes down to $1\ \mu\text{m}$ with $\lambda = 532\ \text{nm}$ and decreases by less than 20% with $\lambda = 1550\ \text{nm}$. [124]

Another study by Youngblood *et al.* [125] shows the photoresponse for a $\sim 11\ \text{nm}$ bP flake up to GHz frequencies. [125] The few-layer bP is embedded in an on-chip waveguide structure with a few-layer graphene top gate, allowing for optimal interaction with light and tunability of the carrier density. The DC responsivity reaches $130\ \text{mA W}^{-1}$. Figure 3.12d shows the photoresponse of the few-layer bP device as a function of modulation frequency for low doping (blue curve) and high doping (red curve). The response rolls off at about 3 GHz for low doping and at 2 MHz for

high doping. The authors ascribe this difference to a change of photocurrent generation mechanism induced by the doping. [125] Figure 3.12e shows an eye-diagram at 3 Gbits/s data rate (similar to the one reported for a graphene-based device in ref. [63]). The clean eye diagram indicates that the photodetector can operate well at this high data transfer rate. This study shows that few-layer bP phototransistors, embedded in engineered devices, can achieve data transfer speed similar to graphene photodetectors [7, 8] with larger responsivities.

Table 3.5 summarizes the principal figures of merit of bP based detectors. The reported responsivities for thin (~ 10 nm) bP are in between 0.5 mA W^{-1} and 130 mA W^{-1} while for thick bP can reach up to 700 mA W^{-1} , slightly lower compared with TMDCs. The response time is in the order of few ms for simple photo-FETs and the operation frequency can be pushed up to 3 GHz by device engineering, demonstrating a faster response to light excitation with respect to TMDC-based photodetectors.

Moreover, locally-gated bP PN junctions have demonstrated their use as photodiodes and solar cells also in the NIR part of the electromagnetic spectrum, making bP a promising material for photodetection and energy harvesting.

3.7. DEVICE COMPARISON

In the previous Sections we have reviewed photodetectors based on a large variety of semiconducting layered materials. In this Section, we summarize and compare the responsivity and response time of the devices we have so far reviewed.

Table 3.2 summarizes the responsivity, rise time and spectral range for photodetectors based on MoS_2 , MoSe_2 , WS_2 and WSe_2 . Within devices based on the same material, there is a large variability in the responsivity and rise time figures-of-merit, likely indicating that the device fabrication, measurement conditions and contact metals have a large effect on the photoresponse. It is worth mentioning that, in general, photodetectors based on MoS_2 present orders-of-magnitude larger responsivity and response times than photodetectors based on MoSe_2 or WS_2 , possibly indicating that trap states in MoS_2 are longer-lived than in the other compounds. All these compounds show a remarkable effect of the environment in which the measurements are performed, suggesting their potential application as light-sensitive gas detectors.

PN-junctions based on single-layer WSe_2 are also included in Table 3.2 even if their working principle is based on the photovoltaic effect, rather than photoconduction/photogating. Their responsivity is in the order of 1 to 10 mA W^{-1} when operated in the photovoltaic mode and shows a small increase when operated in the photoconductive mode. The reported responsivity for the WSe_2 PN junctions (see Table 3.2) is generally lower than photodetectors based on other TMDCs, especially in comparison with MoS_2 , indicating that the internal gain mechanism (trap states) is suppressed. This is expected for photodetectors working with the photovoltaic principles. However, locally-gated WSe_2 devices show versatile behavior, combining a photo-FET with a gate-controlled photodiode in a single device.

Table 3.3 summarizes the figures-of-merit for photodetectors based on trichalcogenide compounds. Devices based on TiS_3 ultrathin nanoribbons achieve both slightly higher responsivity and faster response than detectors based on MoS_2 . This good performance, coupled to the reduced dimensionality, make TiS_3 nanoribbons a promising material for nanostructured photodetection applications. On the other hand, both ZrS_3 - and HfS_3 -based detectors show poor responsivity and a slow response.

Both the semiconducting di- and tri-chalcogenides do not show photoresponse at telecommunication wavelengths. On the other hand, the newly (re)discovered black phosphorus demonstrates sizable responsivity (about 0.1 A W^{-1}) and response speed ($f_{3\text{dB}} \sim 3 \text{ GHz}$) under $\lambda = 1550 \text{ nm}$ excitation (see Table 3.5). Moreover, few-layer bP has shown ambipolar transport and the possibility of realizing versatile locally-gated devices, like in the case of single-layer WSe_2 . This makes few-layer bP a promising candidate for fast and broadband detection and light energy harvesting in the IR part of the spectrum. Compounds from elements in the III-VI groups are also attracting attention for photodetection applications. Devices based on multilayers of these materials show responsivities from tens to thousands A W^{-1} and response time between few and hundred ms. GaTe photodetectors outperform detectors based on single-layer MoS_2 reaching responsivities of $1 \cdot 10^4 \text{ A W}^{-1}$ and response time as short as 6 ms. Photodetectors based on In_2Se_3 , GaSe and GaS show responsivities and response times that are slightly better than most detectors based on MoS_2 . More consistency of device geometry, fabrication recipes and measurement conditions are needed for a proper benchmarking, but these materials have already demonstrated their promise for visible and UV detection.

To compare photodetectors based on different materials together, the data from Tables 1 to 5 is summarized in Figure 3.13. As a benchmark, also the responsivity and response time of a commercial silicon photodiode (black square) and a graphene photodetector (blue square) are shown. It is evident that photodetectors based on semiconducting layered materials display a large (about 10 orders of magnitude) variation in their responsivity. Regarding the response time, it appears that all but one of the reviewed devices show response times larger than $\sim 1 \cdot 10^{-2} \text{ ms}$. This long response time can be attributed to the presence of long-lived trap states (in devices with responsivity above $1 \cdot 10^3 \text{ mA W}^{-1}$) or to the limitation of the measurement electronics (RC time) likely induced by the large resistance of the device or input impedance of the current-to-voltage amplifier used in the read-out electronics.

The bP-based device presented in ref. [125] stands out from the rest of the devices by showing comparable performances to both a commercial silicon photodiode and a graphene-based detector. In particular, this device shows responsivity and response times (at telecommunications wavelengths) that are within one order of magnitude from a commercial silicon photodiode (in the visible), strongly indicating that bP-based photodetectors can already compete with traditional silicon detectors.

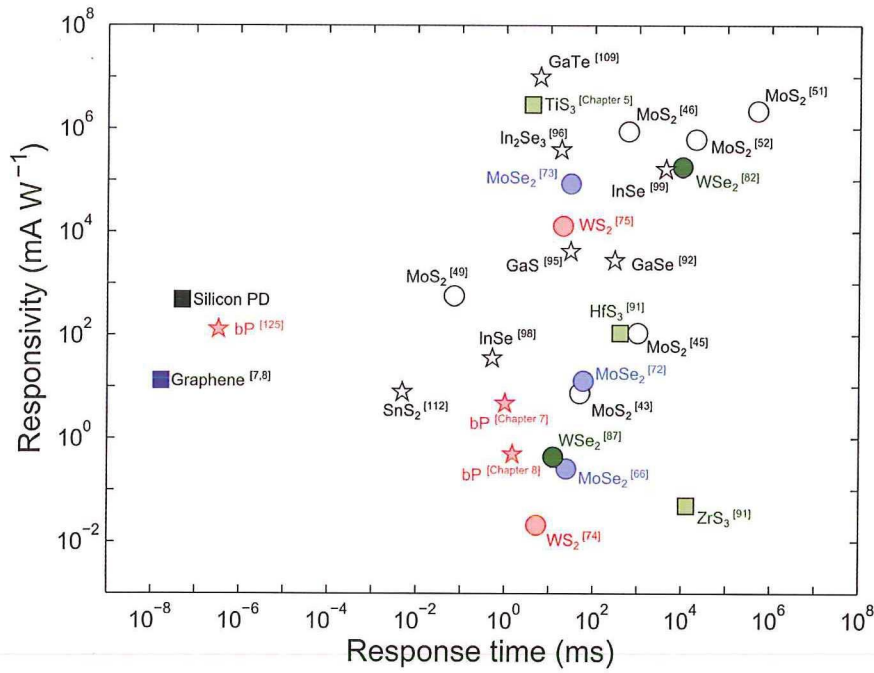


FIGURE 3.13: Responsivity against response time for the reviewed devices, for a commercial silicon photodiode (black square) and for graphene photodetectors (blue square).

In terms of absolute responsivity, half of the reviewed devices present values equal or larger than the Si photodiode. Especially, devices based on MoS₂, WSe₂, InSe, In₂Se₃, GaTe and TiS₃ present a responsivity which is three to four orders of magnitude above. The large responsivity supports the claim that layered semiconducting materials hold promise for ultrasensitive applications in the visible, for which the response times in the order of ms may be acceptable.

3.8. FUTURE DIRECTIONS

So far, we have reviewed photodetectors that are based on a single semiconducting material, used as channel material in a photo-transistor or a locally-gated PN junction. In this Section we will discuss one of the promising directions of photodetection with semiconducting layered materials: artificial heterostructures of different layered compounds.

3.8.1. ARTIFICIAL VAN-DER-WAALS HETEROSTRUCTURES.

Deterministic transfer techniques[10, 128–132] have opened the door to the realization of artificial heterostructures based on single- or few-layer semiconducting materials. These heterostructures can be built on conventional (3D) materials (like Si[133–135] and InAs[136]) or on other two dimensional materials and have triggered a great deal of experimental work on their electrical[137–148], optical[149–155] and mechanical properties.[156] In this Section, we review the recent experimental work aimed to establish the opto-electronic performances of devices based on these van-der-Waals heterostructures.

MoS₂/SI HETEROSTRUCTURES.

A device based on single-layer MoS₂ on p-doped Si has been fabricated by Lopez-Sanchez *et al.*[133, 134] and Li *et al.*[135]. Figure 3.14a shows a typical device geometry: single-layer MoS₂ is transferred on top of a highly p-doped Si substrate and charge transport occurs across the MoS₂/Si interface. In dark, the resulting I_{ds} - V_{ds} characteristics are diode-like (Figure 3.14b), evidencing the formation of a PN junction between the n-type MoS₂ and the p-doped Si.

Under illumination, the I_{ds} - V_{ds} curves show an increased reverse-bias current and I_{sc} (Figure 3.14b), strongly suggesting that the photogenerated carriers are separated by the electric field generated at the interface between the single-layer MoS₂ and the Si surface. The EQE of this device reaches about 4% in the visible and decreases to about 2.5% at $\lambda = 1000$ nm (see Figure 3.14c).[133] Compared with detectors based on only single-layer MoS₂, the EQE is much lower; however, the wavelength detection range is extended due to the lower bandgap of silicon, enabling detection of NIR photons.

To conclude, devices based on MoS₂/Si heterostructures show diode-like electrical characteristics, photovoltaic effect and electroluminescence, effects that strongly indicate an efficient charge transfer at the interface between the MoS₂ and the Si substrate.

GRAPHENE/TMDCs HETEROSTRUCTURES.

Figure 3.15a shows a schematic of a typical graphene/TMDC heterostructure; a layer of a semiconducting TMDC is covered with single-layer graphene which is contacted by metallic electrodes. In this geometry, charge is transported in the graphene layer and the TMDC serves as an additional gate dielectric with light-sensitizing properties. With this geometry, one layer of graphene over a multilayer MoS₂ resulted in photodetectors with drastically enhanced responsivity ($\sim 5 \cdot 10^8$ A W⁻¹) at the expense of an extremely slow response times ($> 1 \cdot 10^3$ s).[139] The large responsivity stems from a strong photogating effect on the single-layer graphene channel induced by the localized states in the MoS₂ layer. Under illumination, the photogenerated holes are trapped in localized states in the MoS₂ while the photogenerated electrons are transferred to the graphene, free to circulate. The trapped holes reside longer in the

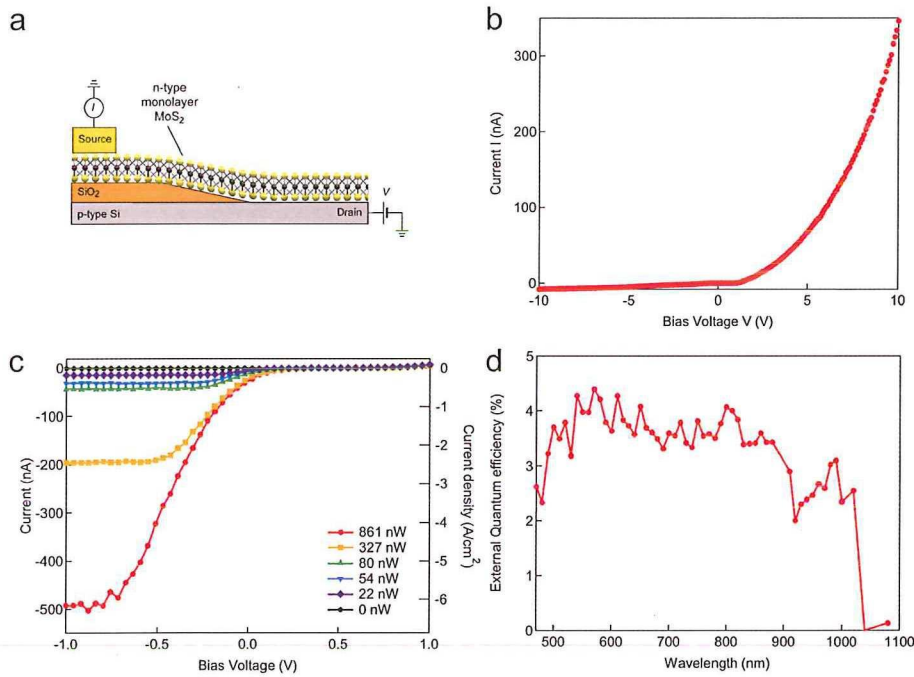


FIGURE 3.14: (a) Device schematics. (b) $I_{ds}-V_{ds}$ characteristic in dark showing diode-like behavior. (c) $I_{ds}-V_{ds}$ under illumination with $\lambda = 541$ nm and varying optical power, indicated in the panel. (d) External quantum efficiency as a function of excitation wavelength. All panels are adapted from ref. [133]

MoS₂ flake and thus act as a local gate on the graphene channel. Their long lifetime is responsible for the extremely large responsivity and long response times.

Photogating has also been observed in a hybrid detector composed of a single-layer MoS₂ covered by a single layer graphene, both grown by CVD techniques.[140] Under illumination, the $I_{ds}-V_g$ characteristics shift horizontally, clearly indicating that the photoresponse mechanism is dominated by the photogating effect (Figure 3.15b). Interestingly, the authors report a decrease of the magnitude of the photogating effect when the measurements are performed in vacuum. The smaller shift in vacuum is attributed to a reduction in the efficiency of the charge transfer between the MoS₂ and the graphene. In air, the graphene is slightly more p-type, increasing the electric field at the interface and, hence, increasing the charge transfer rate for electrons. In vacuum, the graphene is slightly more n-type, suppressing the electron transfer, thus reducing the generated photocurrent.[140] For this device, the responsivity is also very high (about $1 \cdot 10^7$ A W⁻¹) at low illumination power and response times from tens to hundreds of seconds (both values for the device in air).

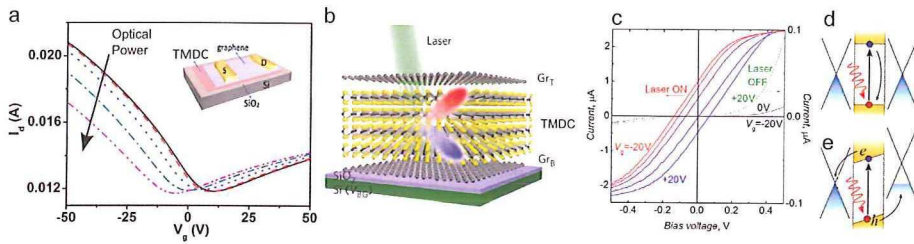


FIGURE 3.15: (a) Device schematics for graphene/TMDC heterostructures. Note that charge transport is measured across the graphene layer. (b) $I_{ds} - V_g$ characteristics for the device in panel (a) in dark (solid black line) and under varying illumination intensities ($\lambda = 650$ nm). (c) Device schematics for graphene/TMDC/graphene heterostructure. Note that electrical transport is measured across the two graphene layers, across the TMDC. (d) $I_{ds} - V_{ds}$ characteristics for device in panel (c) as a function of gate. The right (left) y-axis gives the current magnitude for measurements in dark, green traces (under illumination, blue to red traces). (e) Schematic band alignment in equilibrium. (f) Schematic band alignment under gate bias or chemical doping. Panels (a) and (b) are adapted from ref. [140] Panel (c) is adapted from ref. [138] Panels (d), (e) and (f) are adapted from ref. [137]

GRAPHENE/TMDCs/GRAPHENE HETEROSTRUCTURES.

In the previous Section, we have discussed two examples of graphene/TMDC heterostructures where charge transport was measured in the graphene layer and the TMDC flake served as sensitizing material to enhance the photoresponse. In this Section, we discuss devices based on vertical stacks of graphene/TMDCs/graphene where charge transport occurs through the TMDC layer. In other words, the graphene layers are used as transparent contacts to the photoactive TMDC layer.

In similar studies, Britnell *et al.*[137] and Yu *et al.*[138] fabricated vertical stacks of graphene, a ~ 50 nm thick TMDC and another graphene layer on various substrates, including SiO₂, indium-tin-oxide (ITO) and poly-(ethylene terephthalate) (PET, a flexible and transparent polymer). Figure 3.15c shows a schematic of a typical device. In the dark, such devices behave as tunnel transistors in which the current can be controlled by the gate electric field (see Figure 3.15d, green traces).[137, 138] Under illumination, the $I_{ds} - V_{ds}$ characteristics become linear (until saturation) and show a gate-tunable I_{sc} indicating that the photovoltaic effect dominates the photocurrent generation (see Figure 3.15d, blue to red traces).[137, 138]

The emergence of the photovoltaic effect can be understood by looking at the band diagram schematics presented in Figure 3.15e and Figure 3.15f. In an ideal case (Figure 3.15e) the band alignment between the graphene layers and the TMDC is symmetric. This symmetric alignment gives no preferential direction for the separation of the photogenerated electron-hole pairs, therefore leading to zero net photocurrent. On the other hand, a small difference in the doping level of the two graphene electrodes (induced by gating or chemical doping) will result a misalignment between the bands and, thus, in a built-in electric field. This built-in electric field separates the e-h pairs

and generates the I_{sc} (see Figure 3.15f). As a consequence, the sign and magnitude of I_{sc} are gate-tunable, as evidenced from the blue-to-red traces in Figure 3.15d. In both studies, SPCM measurements reveal that the photocurrent is generated only in the regions of the heterostructure where such an asymmetry is realized.

The responsivity of these devices is in the order of 0.2 A W^{-1} and the maximum electrical power that can be generated is in the order of a few μW , much larger than current PN junctions based on single-layer WSe_2 [78–80], making this type of devices very promising candidates for flexible solar cells.

TMDC/TMDC HETEROSTRUCTURES.

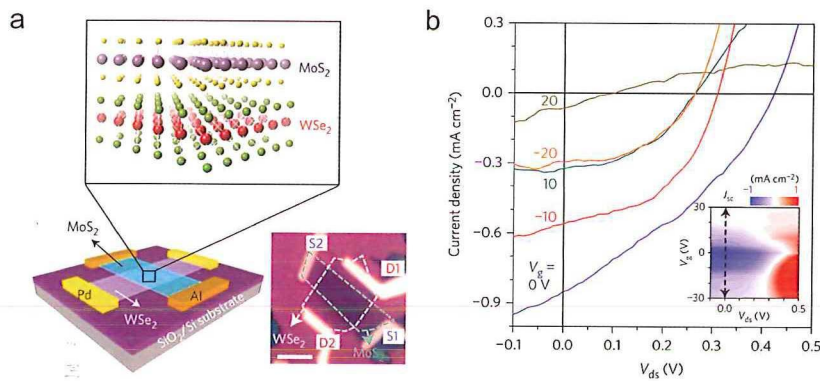


FIGURE 3.16: (a) Device schematic. Top: schematic representation of the single layers composing the heterostructure. Left: schematic of the contact geometry. Pd (Al) is used to contact the single-layer WSe_2 (MoS_2). Right: optical micrograph of the final device. D1 and D2 (S1 and S2) indicate the contacts to the WSe_2 (MoS_2). The scale bar is $2 \mu\text{m}$. (b) $I_{ds} - V_{ds}$ characteristics under illumination at different gate voltages. Inset: false color map of the current under illumination as a function of V_{ds} and V_g . Panels (a) and (b) are adapted from ref. [142]

Very recently, heterostructures based on single-layered semiconducting TMDCs have also been studied. For example, heterostructures of single-layer MoS_2 and single-layer WSe_2 have been fabricated by several groups. [141–144] Figure 3.16a shows an example of such a heterostructure from the Columbia group. [142] The WSe_2 and MoS_2 single layers have been chosen because of their natural tendency to display p- and n-type conduction respectively. In Figure 3.16a, single-layer MoS_2 and single-layer WSe_2 are crossed on top of each other and are contacted with Al and Pd to enhance the n-type and p-type character, respectively

In dark, $\text{WSe}_2/\text{MoS}_2$ heterostructures show gate-tunable rectifying behavior. [142, 143] Under illumination, these heterostructures show a gate-dependent photovoltaic effect as evidenced by the $I_{ds} - V_{ds}$ characteristics in Figure 3.16b. The I_{sc} and V_{oc} reach a maximum at $V_g = 0 \text{ V}$, the position at which the rectifying ratio is the highest. [142, 143] The inset of Figure 3.16b shows a colormap of the measured current as a function

of V_g and V_{ds} , highlighting the reduction of I_{sc} as the magnitude of the gate voltage increases. Through spatial photocurrent and photoluminescence maps the authors ascribe the origin of this photovoltaic effect to charge transfer between the WSe_2 and MoS_2 . [142–144]

Huo *et al.* [145] have recently fabricated heterostructures based on multilayer MoS_2 and WS_2 and measured the same qualitative behavior. [145] CVD techniques have also been used to grow both vertical and lateral heterostructures. [146] CVD-grown devices showed stronger interlayer interaction compared with their un-annealed transferred counterparts, [146] likely being caused by an even stronger charge transfer. An increase in the charge-transfer efficiency in CVD-grown MoS_2/WSe_2 heterostructure will likely lead to a larger rectification and stronger photovoltaic effect. In conclusion, TMDC/TMDC heterostructures present gate-tunable and strong photovoltaic power generation ($\sim 6 \mu W$) coupled to the possibility of direct CVD growth; these properties make them hold promise for large-area flexible and transparent solar cells.

BP/TMDC HETEROSTRUCTURES.

Also heterostructures comprising few-layer bP (p-type) and single layer MoS_2 (n-type) have recently shown gate-tunable photovoltaic effect, generating about 2 nW of electrical power. [147]

3.9. SUMMARY AND OUTLOOK

We have reviewed the current state-of-the-art in photodetection with layered semiconducting materials. Photodetectors based on TMDCs, especially MoS_2 , show large responsivity coupled to slow response times, indicating that these materials can be suitable for sensitive applications in the visible and when time response is not important. MoS_2 also possesses a large Seebeck coefficient, making it a promising material for thermal energy harvesting. Novel materials, such as tri-chalcogenides (TiS_3) nanoribbons, III-VI and IV-VI compounds (e.g. GaTe or SnS_2), show both large responsivities (larger than MoS_2 photodetectors) and fast response times, making them promising candidates for fast and sensitive photodetection applications. Few-layer black phosphorus and single-layer WSe_2 show ambipolar transport and have been employed in the realization of electrical devices that can be controlled via local electrostatic gating. Black phosphorus has shown sizable and very fast photoresponse at telecommunication wavelengths with orders-of-magnitude larger responsivity of graphene and comparable response speed, making it an interesting material for optical communications and energy harvesting.

A future direction is represented by the possibility of stacking different 2D materials to form artificial heterostructures, allowing to tailor the resulting opto-electronic properties for a specific application. This has led to ultra-high responsive photodetectors (albeit very slow) based on graphene/ MoS_2 vertical stacks. Moreover, heterostructures of different TMDCs and/or graphene show great potential for solar

energy harvesting in flexible and transparent solar cells. At this stage, a deeper understanding of the photocurrent and carrier recombination mechanisms is needed for optimization of device performance and large-area growth and transfer techniques will be fundamental for the realization of applications.

From an application perspective, the sizable variation in the figures-of-merit reported by different studies on the same material is an indication that device fabrication, contact metals and measurement environment play an important role in the photodetector performance. Furthermore, the fabrication process of these devices extensively relies on mechanical exfoliation. Both issues may be tackled by using CVD-grown materials, that provide large-area, uniform samples. Integration with current CMOS technology is also an important challenge. Especially the work from Lopez-Sanchez *et al.*[133, 134] demonstrates that coupling MoS₂ to silicon can be highly beneficial. Again, CVD growth may help in integrating MoS₂ and other TMDCs in CMOS fabrication.

3.10. ACKNOWLEDGMENTS

This work was supported by the Dutch organization for Fundamental Research on Matter (FOM). A.C-G. acknowledges financial support through the FP7-Marie Curie Project PIEF-GA-2011-300802 ('STRENGTHNANO').

3.11. APPENDIX: TABLES

Material	Measurement conditions				Responsivity R (mA W^{-1})	Rise time τ (ms)	Spectral range	Reference
	V_{ds} (V)	V_{g} (V)	λ (nm)	P (mW cm^{-2})				
1L MoS ₂	1	50	532	$8.0 \cdot 10^4$	7.5	$5 \cdot 10^1$	Visible	[43]
1L MoS ₂	8	-70	561	$2.4 \cdot 10^{-1}$	$8.8 \cdot 10^5$	$6 \cdot 10^2$	Visible	[46]
1L MoS ₂	1	41	532	$1.3 \cdot 10^{-1}$	$2.2 \cdot 10^6$	$5 \cdot 10^5$	-	[51]
>1L MoS ₂	1	-2	633	$5.0 \cdot 10^1$	$1.1 \cdot 10^2$	$1 \cdot 10^3$	Visible - NIR	[45]
2L MoS ₂	5	100	WL	5 nW	$6.2 \cdot 10^5$	$2 \cdot 10^4$	-	[52]
3L MoS ₂	10	0	532	$2.0 \cdot 10^3$	$5.7 \cdot 10^2$	$7.0 \cdot 10^{-2}$	$\lambda < 700$ nm	[49]
1L MoSe ₂	10	0	532	$1 \cdot 10^2$	$1.3 \cdot 10^1$	$6 \cdot 10^1$	-	[73]
1L MoSe ₂	1	0	650	$5.9 \cdot 10^2$	$2.6 \cdot 10^{-1}$	$2.5 \cdot 10^1$	-	[67]
20L MoSe ₂	20	0	532	4.8	$9.7 \cdot 10^4$	$3.0 \cdot 10^1$	-	[74]
1L WS ₂ a	30	0	458	2.0	$2.1 \cdot 10^{-2}$	5.3	Visible	[75]
1L WS ₂ b	30	0	633	$5.0 \cdot 10^{-2}$	$1.3 \cdot 10^4$	$2.0 \cdot 10^1$	-	[76]
1L WSe ₂	2	-60	650	$3.8 \cdot 10^{-1}$	$1.8 \cdot 10^5$	$1.0 \cdot 10^4$	-	[77]
1L WSe ₂	0	PN	WLc	$4.5 \cdot 10^1$	$1.0 \cdot 10^1$	-	-	[79]
1L WSe ₂	0	PN	522	$1 \cdot 10^{-2}$	$8.4 \cdot 10^{-1}$	-	$\lambda < 820$ nm	[78]
1L WSe ₂	0	PN	532	$8.4 \cdot 10^{-1}$	$4 \cdot 10^{-1}$	$1.0 \cdot 10^1$	$\lambda < (770 \pm 35)$ nm	[80]

a. Power in W. b. Data reported for the device in vacuum. c. WL = white light.

TABLE 3.2: Figures-of-merit for MoS₂, MoSe₂, WS₂ and WSe₂ based photodetectors

Stellingen

behorende bij het proefschrift

PHOTODETECTION WITH NOVEL MATERIALS:

COLLOIDAL QUANTUM DOTS, NANORIBBONS AND LAYERED MATERIALS

door

Michele BUSCEMA

1. Ultradunne, halfgeleidende gelaagde materialen voor fotodetectie van zichtbaar licht dagen commerciële siliciumfotodiodes uit, door hun vele malen grotere responsiviteit. (Hoofdstuk 3 en 5)
2. Enkel-laags MoS₂ laat een grote en varieerbare Seebeck coëfficiënt zien, wat het mogelijk maakt om stroom op te wekken door middel van een temperatuurverschil. (Hoofdstuk 6)
3. Lokale elektrostatische gating van atomair-dunne ambipolaire materialen maakt het mogelijk om een foto transistor, een zonnecel en een LED [1] in één enkel object te combineren. (Hoofdstuk 8)
4. Een opstelling waarin atoom-dikke materialen gehanteerd kunnen worden, kost geen fortuin. (Appendix A)
5. Groei en overdracht van enkellaagshalfgeleidende heterostructuren vormen de meest geschikte fabricagemethode voor het realiseren van transparante (en flexibele) zonnecellen.
6. Valleytronics is het nieuwe spintronics.
7. Een programmeertaal met een goede leesbaarheid van de code (b.v. Python) zorgt voor snellere instrumentintegratie en instrumentcontrole dan een graphische-objectgeoriënteerde programmeertaal (b.v. LabView).
8. Wedstrijdzeilen in ploegverband zou onderdeel van de opleiding moeten zijn voor jonge onderzoekers.
9. Fotografie (wetenschap) is de kunst om een verhaal in één foto (een paar figuren) te vangen.
10. In tegenstelling tot wat algemeen geloofd wordt, waarderen Italianen de Nederlandse snackbarcultuur.

Ref.

[1] Bauger BWH, *et al.*, Nature Nanotech. **9**, 262-267, 2014

[2] <http://nos.nl/artikel/2001380-friet-rukt-op-in-het-land-van-pizza-en-pasta.html> (accessed on 2/12/2014)

Deze stellingen worden oponeerbaar en verdedigbaar geacht en zijn als zodanig goedgekeurd door de promotor prof. dr. ir. H. S. J. van der Zant.

Propositions

accompanying the dissertation

PHOTODETECTION WITH NOVEL MATERIALS: COLLOIDAL QUANTUM DOTS, NANORIBBONS AND LAYERED MATERIALS

by

Michele BUSCEMA

1. Ultrathin, semiconducting layered materials for visible light photodetection challenge commercial silicon photodiodes with orders-of-magnitude larger responsivity. (Chapter 3 and 5)
 2. Single-layer MoS₂ shows a large and gate-tunable Seebeck coefficient, enabling the generation of current from temperature gradients. (Chapter 6)
 3. Local electrostatic gating of atomically-thin ambipolar materials allows to combine a photo-transistor, a solar cell and an LED [1] in a single device. (Chapter 8)
 4. A setup to manipulate one-atom-thick materials does not cost a fortune. (Appendix A)
 5. Growth and transfer of single-layer-semiconductor heterostructures are the best candidates for the realization of transparent (and flexible) solar cells.
-
6. Valleytronics is the new, rising spintronics.
 7. A programming language with high code readability (e.g. Python) allows faster instrument integration and control than a graphical-object-oriented one (e.g. LabView).
 8. Competitive crew-sailing should become an integral part of the education of a young researcher.
 9. Photography (science) is the art of framing a story into a picture (into few figures).
 10. Contrary to popular belief, Italians do appreciate Dutch street-food culture. [2]

Ref.

[1] Bauger BWH, *et al.*, Nature Nanotech. **9**, 262-267, 2014

[2] <http://nos.nl/artikel/2001380-friet-rukt-op-in-het-land-van-pizza-en-pasta.html> (accessed on 2/12/2014)

These propositions are regarded as opposable and defensible, and have been approved as such by the supervisor prof. dr. ir. H. S. J. van der Zant.

Material	Measurement conditions				Responsivity R (mA W ⁻¹)	Rise time τ (ms)	Spectral range	Reference
	V_{ds} (V)	V_g (V)	λ (nm)	P (mW cm ⁻²)				
TiS ₃	1	-40	640	$3 \cdot 10^{-1}$	$2.9 \cdot 10^6$	4	$\lambda < 940\text{nm}$	Chapter 5
ZrS ₃	5	-	405	$5 \cdot 10^{11}$	$5 \cdot 10^{-2}$	$13 \cdot 10^3$	$\lambda < 850\text{nm}$	[90]
HfS ₃	5	-	405	1.2	$1.1 \cdot 10^2$	$4 \cdot 10^2$	$\lambda < 650\text{nm}$	[89]

TABLE 3.3: Figures-of-merit for TiS₃, ZrS₃ and HfS₃ based photodetectors

Material	Measurement conditions				Responsivity R (mA W ⁻¹)	Rise time τ (ms)	Spectral range	Reference
	V_{ds} (V)	V_g (V)	λ (nm)	P (mW cm ⁻²)				
GaTe	5	0	532	$3.0 \cdot 10^{-5}$	$1 \cdot 10^7$	6	Visible	[108]
GaSe	5	0	254	1.0	$2.8 \cdot 10^3$	$3 \cdot 10^2$	UV - Visible	[91]
GaS	2	0	254	$2.6 \cdot 10^{-2}$	$4.2 \cdot 10^3$	$3 \cdot 10^1$	UV - Visible	[94]
In ₂ Se ₃	5	0	300	$2.1 \cdot 10^{-1}$	$3.9 \cdot 10^5$	$1.8 \cdot 10^1$	UV - NIR	[95]
InSe	10	80	633	$3.5 \cdot 10^2$	$1.6 \cdot 10^5$	$4.0 \cdot 10^3$	Visible - NIR	[98]
InSe	3	0	532	$2.5 \cdot 10^2$	$3.5 \cdot 10^1$	$5.0 \cdot 10^{-1}$	Visible - NIR	[97]
SnS ₂	3	0	457	$2 \cdot 10^3$	9	$5 \cdot 10^{-3}$	Visible - NIR	[111]

(a) P in mW

TABLE 3.4: Figures-of-merit for photodetectors based on III-VI compounds

Thickness (nm)	Measurement conditions				Responsivity R (mA W ⁻¹)	Rise time τ (ms)	Spectral range	Reference
	V_{ds} (V)	V_g (V)	λ (nm)	P (mW cm ⁻²)				
8	0.2	0	640	$1.6 \cdot 10^1$	4.8	1	Visible - NIR	Chapter 7
6	0	PN	532	$1.9 \cdot 10^3$	$5 \cdot 10^{-1}$	1.5	Visible - NIR	Chapter 8
6	-0.5	PN	532	$1.9 \cdot 10^3$	$2.8 \cdot 10^1$	-	Visible - IR	Chapter 8
120	0	0	1550	$3 \cdot 10^6$	5.0	-	Visible - IR	[122, 124]
120	0	0	532	$1 \cdot 10^7$	$2.0 \cdot 10^1$	-	Visible - NIR	[122, 124]
11.5	0.4	-8	1550	1.91	$1.3 \cdot 10^2$	a	Visible - NIR	[125]b

a. $f_{3dB} = 3$ GHz. Power in mW.

TABLE 3.5: Figures-of-merit for few-layer bP based photodetectors

REFERENCES

- [1] K. S. Novoselov, A. K. Geim, S. V. Morozov, D. Jiang *et al.*, *Electric Field Effect in Atomically Thin Carbon Films*, *Science* **306** 666 (2004), <http://www.sciencemag.org/content/306/5696/666.full.pdf>.
- [2] K. S. Novoselov, A. K. Geim, S. V. Morozov, D. Jiang *et al.*, *Two-dimensional gas of massless Dirac fermions in graphene*, *Nature* **438** 197 (2005).
- [3] K. S. Novoselov, D. Jiang, F. Schedin, T. J. Booth *et al.*, *Two-dimensional atomic crystals*, *Proceedings of the National Academy of Sciences of the United States of America* **102** 10451 (2005).
- [4] K. S. Novoselov, E. McCann, S. V. Morozov, V. I. Fal'ko *et al.*, *Unconventional quantum Hall effect and Berry's phase of 2π in bilayer graphene*, *Nat Phys* **2** 177 (2006).
- [5] K. S. Novoselov, Z. Jiang, Y. Zhang, S. V. Morozov *et al.*, *Room-Temperature Quantum Hall Effect in Graphene*, *Science* **315** 1379 (2007).
- [6] C. Lee, X. Wei, J. W. Kysar and J. Hone, *Measurement of the Elastic Properties and Intrinsic Strength of Monolayer Graphene*, *Science* **321** 385 (2008).
- [7] F. Xia, T. Mueller, Y.-m. Lin, A. Valdes-Garcia *et al.*, *Ultrafast graphene photodetector*, *Nat Nano* **4** 839 (2009).
- [8] T. Mueller, F. Xia and P. Avouris, *Graphene photodetectors for high-speed optical communications*, *Nature Photonics* **4** 297 (2010).
- [9] Q. H. Wang, K. Kalantar-Zadeh, A. Kis, J. N. Coleman *et al.*, *Electronics and optoelectronics of two-dimensional transition metal dichalcogenides*, *Nat Nano* **7** 699 (2012).
- [10] L. Wang, I. Meric, P. Y. Huang, Q. Gao *et al.*, *One-Dimensional Electrical Contact to a Two-Dimensional Material*, *Science* **342** 614 (2013).
- [11] J. N. Coleman, M. Lotya, A. O'Neill, S. D. Bergin *et al.*, *Two-Dimensional Nanosheets Produced by Liquid Exfoliation of Layered Materials*, *Science* **331** 568 (2011).
- [12] K. F. Mak, C. Lee, J. Hone, J. Shan *et al.*, *Atomically Thin MoS_2 : A New Direct-Gap Semiconductor*, *Phys. Rev. Lett.* **105** 136805 (2010).
- [13] K. F. Mak, K. He, J. Shan and T. F. Heinz, *Control of valley polarization in monolayer MoS_2 by optical helicity*, *Nat Nano* **7** 494 (2012).
- [14] K. F. Mak, K. He, C. Lee, G. H. Lee *et al.*, *Tightly bound trions in monolayer MoS_2* , *Nat. Mater.* **12** 207 (2013).
- [15] A. Ayari, E. Cobas, O. Ogundadegbe and M. S. Fuhrer, *Realization and electrical characterization of ultrathin crystals of layered transition-metal dichalcogenides*, *J. Appl. Phys.* **101** 014507 (2007).
- [16] B. Radisavljevic, A. Radenovic, J. Brivio, V. Giacometti *et al.*, *Single-layer MoS_2 transistors*, *Nature Nanotechnology* **6** 147 (2011).
- [17] A. Splendiani, L. Sun, Y. Zhang, T. Li *et al.*, *Emerging Photoluminescence in Monolayer MoS_2* , *Nano Letters* **10** 1271 (2010).
- [18] G. Eda, H. Yamaguchi, D. Voino, T. Fujita *et al.*, *Photoluminescence from Chemically Exfoliated MoS_2* , *Nano Lett.* **11** 5111 (2011).
- [19] W. S. Yun, S. W. Han, S. C. Hong, I. G. Kim *et al.*, *Thickness and strain effects on electronic structures of transition metal dichalcogenides: 2H-MX_2 semiconductors ($M = \text{Mo}, \text{W}$; $X = \text{S}, \text{Se}, \text{Te}$)*, *Phys. Rev. B* **85** 033305 (2012).
- [20] A. Castellanos-Gomez, M. Poot, G. A. Steele, H. S. van der Zant *et al.*, *Elastic properties of freely suspended MoS_2 nanosheets*, *Advanced Materials* **24** 772 (2012).
- [21] A. Castellanos-Gomez, V. Singh, H. S. van der Zant and G. A. Steele, *Mechanics of freely-suspended ultrathin layered materials*, *Annalen der Physik* (2014).
- [22] S. Bertolazzi, J. Brivio and A. Kis, *Stretching and Breaking of Ultrathin MoS_2* , *ACS Nano* **5** 9703 (2011).
- [23] R. C. Cooper, C. Lee, C. A. Marianetti, X. Wei *et al.*, *Nonlinear elastic behavior of two-dimensional molybdenum disulfide*, *Phys. Rev. B* **87** 035423 (2013).
- [24] A. Castellanos-Gomez, M. Poot, G. A. Steele, H. S. J. van der Zant *et al.*, *Elastic Properties of Freely Suspended MoS_2 Nanosheets*, *Adv. Mater.* **24** 772 (2012).
- [25] K. He, C. Poole, K. F. Mak and J. Shan, *Experimental Demonstration of Continuous Electronic Structure Tuning via Strain in Atomically Thin MoS_2* , *Nano Lett.* **13** 2931 (2013).

- [26] H. J. Conley, B. Wang, J. I. Ziegler, R. F. Haglund *et al.*, *Bandgap Engineering of Strained Monolayer and Bilayer MoS₂*, *Nano Lett.* **13** 3626 (2013).
- [27] C. R. Zhu, G. Wang, B. L. Liu, X. Marie *et al.*, *Strain tuning of optical emission energy and polarization in monolayer and bilayer MoS₂*, *Phys. Rev. B* **88** 121301 (2013).
- [28] J. Feng, X. Qian, C.-W. Huang and J. Li, *Strain-engineered artificial atom as a broad-spectrum solar energy funnel*, *Nat Photon* **6** 866 (2012).
- [29] A. Castellanos-Gomez, R. Roldán, E. Cappelluti, M. Buscema *et al.*, *Local strain engineering in atomically thin MoS₂*, *Nano Lett* **13** 5361 (2013).
- [30] J. M. Dawlaty, S. Shivaraman, J. Strait, P. George *et al.*, *Measurement of the optical absorption spectra of epitaxial graphene from terahertz to visible*, *Applied Physics Letters* **93** (2008).
- [31] P. R. Wallace, *The band theory of graphite*, *Physical Review* **71** 622 (1947).
- [32] A. Bostwick, T. Ohta, T. Seyller, K. Horn *et al.*, *Quasiparticle dynamics in graphene*, *Nat Phys* **3** 36 (2007).
- [33] M. Katsnelson, *Graphene: Carbon in Two Dimensions*, Cambridge University Press (2012).
- [34] L. Vicarelli, M. Vitiello, D. Coquillat, A. Lombardo *et al.*, *Graphene field-effect transistors as room-temperature terahertz detectors*, *Nature Materials* **11** 865 (2012).
- [35] M. Mittendorff, S. Winnerl, J. Kamann, J. Eroms *et al.*, *Ultrafast graphene-based broadband THz detector*, *Applied Physics Letters* **103** 021113 (2013).
- [36] E. J. H. Lee, K. Balasubramanian, R. T. Weitz, M. Burghard *et al.*, *Contact and edge effects in graphene devices*, *Nat Nano* **3** 486 (2008).
- [37] J. Park, Y. H. Ahn and C. Ruiz-Vargas, *Imaging of Photocurrent Generation and Collection in Single-Layer Graphene*, *Nano Lett.* **9** 1742 (2009).
- [38] Z. Sun and H. Chang, *Graphene and Graphene-Like Two-Dimensional Materials in Photodetection: Mechanisms and Methodology*, *ACS nano* (2014).
- [39] F. H. L. Koppens, T. Mueller, P. Avouris, A. C. Ferrari *et al.*, *Photodetectors based on graphene, other two-dimensional materials and hybrid systems*, *Nat Nano* **9** 780 (2014).
- [40] B. Radisavljevic and A. Kis, *Mobility engineering and a metal-insulator transition in monolayer MoS₂*, *Nature materials* **12** 815 (2013).
- [41] J. Pu, Y. Yomogida, K.-K. Liu, L.-J. Li *et al.*, *Highly Flexible MoS₂ Thin-Film Transistors with Ion Gel Dielectrics*, *Nano Lett.* **12** 4013 (2012).
- [42] Q. He, Z. Zeng, Z. Yin, H. Li *et al.*, *Fabrication of Flexible MoS₂ Thin-Film Transistor Arrays for Practical Gas-Sensing Applications*, *Small* **8** 2994 (2012).
- [43] Z. Yin, H. Li, H. Li, L. Jiang *et al.*, *Single-Layer MoS₂ Phototransistors*, *ACS Nano* **6** 74 (2012).
- [44] H. S. Lee, S.-W. Min, Y.-G. Chang, M. K. Park *et al.*, *MoS₂ Nanosheet Phototransistors with Thickness-Modulated Optical Energy Gap*, *Nano Lett.* **12** 3695 (2012).
- [45] W. Choi, M. Y. Cho, A. Konar, J. H. Lee *et al.*, *High-Detectivity Multilayer MoS₂ Phototransistors with Spectral Response from Ultraviolet to Infrared*, *Adv. Mater.* **24** 5832 (2012).
- [46] O. Lopez-Sanchez, D. Lembke, M. Kayci, A. Radenovic *et al.*, *Ultrasensitive photodetectors based on monolayer MoS₂*, *Nat Nano* **8** 497 (2013).
- [47] M. Buscema, M. Barkelid, V. Zwiller, H. S. J. van der Zant *et al.*, *Large and Tunable Photothermoelectric Effect in Single-Layer MoS₂*, *Nano Lett.* **13** 358 (2013).
- [48] M. Fontana, T. Deppe, A. K. Boyd, M. Rinzan *et al.*, *Electron-hole transport and photovoltaic effect in gated MoS₂ Schottky junctions*, *Scientific Reports* **3** (2013).
- [49] D.-S. Tsai, K.-K. Liu, D.-H. Lien, M.-L. Tsai *et al.*, *Few-Layer MoS₂ with High Broadband Photogain and Fast Optical Switching for Use in Harsh Environments*, *ACS Nano* **7** 3905 (2013).
- [50] C.-C. Wu, D. Jariwala, V. K. Sangwan, T. J. Marks *et al.*, *Elucidating the Photoresponse of Ultrathin MoS₂ Field-Effect Transistors by Scanning Photocurrent Microscopy*, *J. Phys. Chem. Lett.* **4** 2508 (2013).
- [51] W. Zhang, J.-K. Huang, C.-H. Chen, Y.-H. Chang *et al.*, *High-Gain Phototransistors Based on a CVD MoS₂ Monolayer*, *Adv. Mater.* **25** 3456 (2013).
- [52] M. M. Furchi, D. K. Polyushkin, A. Pospischil and T. Mueller, *Mechanisms of Photoconductivity in Atomically Thin MoS₂*, *Nano Lett.* – (2014).
- [53] P. Tonndorf, R. Schmidt, P. Böttger, X. Zhang *et al.*, *Photoluminescence emission and Raman response*

- of monolayer MoS₂, MoSe₂, and WSe₂*, Optics express **21** 4908 (2013).
- [54] H. R. Gutiérrez, N. Perea-López, A. L. Elías, A. Berkdemir *et al.*, *Extraordinary Room-Temperature Photoluminescence in Triangular WS₂ Monolayers*, Nano Lett. **13** 3447 (2012).
- [55] R. Kappera, D. Voiry, S. E. Yalcin, B. Branch *et al.*, *Phase-engineered low-resistance contacts for ultrathin MoS₂ transistors*, Nat Mater **advance online publication** (2014).
- [56] E. Schedin, A. K. Geim, S. V. Morozov, E. W. Hill *et al.*, *Detection of individual gas molecules adsorbed on graphene*, Nat Mater **6** 652 (2007).
- [57] H. Fang, S. Chuang, T. C. Chang, K. Takei *et al.*, *High-Performance Single Layered WSe₂ p-FETs with Chemically Doped Contacts*, Nano Lett. **12** 3788 (2012).
- [58] D. J. Late, B. Liu, H. S. S. R. Matte, V. P. Dravid *et al.*, *Hysteresis in Single-Layer MoS₂ Field Effect Transistors*, ACS Nano **6** 5635 (2012).
- [59] S. Tongay, J. Zhou, C. Ataca, J. Liu *et al.*, *Broad-Range Modulation of Light Emission in Two-Dimensional Semiconductors by Molecular Physisorption Gating*, Nano Lett. – (2013).
- [60] D.-S. Tsai, D.-H. Lien, M.-L. Tsai, S.-H. Su *et al.*, *Trilayered MoS₂ Metal-Semiconductor-Metal Photodetectors: Photogain and Radiation Resistance*, Selected Topics in Quantum Electronics, IEEE Journal of **20** 30 (2014).
- [61] D. Kufer, I. Nikitskiy, T. Lasanta, G. Navickaite *et al.*, *Hybrid 2D-0D MoS₂-PbS Quantum Dot Photodetectors*, Advanced Materials (2014).
- [62] G. Konstantatos, M. Badioli, L. Gaudreau, J. Osmond *et al.*, *Hybrid graphene-quantum dot phototransistors with ultrahigh gain*, Nature nanotechnology **7** 363 (2012).
- [63] T. Mueller, F. Xia, M. Freitag, J. Tsang *et al.*, *Role of contacts in graphene transistors: A scanning photocurrent study*, Phys. Rev. B **79** 245430 (2009).
- [64] N. Kaushik, A. Nipane, F. Basheer, S. Dubey *et al.*, *Schottky barrier heights for Au and Pd contacts to MoS₂*, Applied Physics Letters **105** (2014).
- [65] J. Wu, H. Schmidt, K. K. Amara, X. Xu *et al.*, *Large Thermoelectricity via Variable Range Hopping in Chemical Vapor Deposition Grown Single-Layer MoS₂*, Nano Lett. **14** 2730 (2014).
- [66] N. D. Boscher, C. J. Carmalt, R. G. Palgrave, J. J. Gil-Tomas *et al.*, *Atmospheric pressure CVD of molybdenum diselenide films on glass*, Chemical Vapor Deposition **12** 692 (2006).
- [67] Y.-H. Chang, W. Zhang, Y. Zhu, Y. Han *et al.*, *Monolayer MoSe₂ Grown by Chemical Vapor Deposition for Fast Photodetection*, ACS nano **8** 8582 (2014).
- [68] X. Lu, M. I. B. Utama, J. Lin, X. Gong *et al.*, *Large-Area Synthesis of Monolayer and Few-Layer MoSe₂ Films on SiO₂ Substrates*, Nano letters **14** 2419 (2014).
- [69] J. C. Shaw, H. Zhou, Y. Chen, N. O. Weiss *et al.*, *Chemical vapor deposition growth of monolayer MoSe₂ nanosheets*, Nano Research **7** 1 (2014).
- [70] G. W. Shim, K. Yoo, S.-B. Seo, J. Shin *et al.*, *Large-Area Single-Layer MoSe₂ and Its van der Waals Heterostructures*, ACS nano **8** 6655 (2014).
- [71] M. I. B. Utama, X. Lu, D. Zhan, S. T. Ha *et al.*, *Etching-free patterning method for electrical characterization of atomically thin MoSe₂ films grown by chemical vapor deposition*, Nanoscale **6** 12376 (2014).
- [72] X. Wang, Y. Gong, G. Shi, W. L. Chow *et al.*, *Chemical Vapor Deposition Growth of Crystalline Monolayer MoSe₂*, ACS nano **8** 5125 (2014).
- [73] J. Xia, X. Huang, L. Liu, M. Wang *et al.*, *CVD Synthesis of Large-area Highly Crystalline MoSe₂ Atomic Layers on Diverse Substrates and Photodetector Application*, Nanoscale (2014).
- [74] A. Abderrahmane, P. J. Ko, T. V. Thu, S. Ishizawa *et al.*, *High photosensitivity few-layered MoSe₂ back-gated field-effect phototransistors*, Nanotechnology **25** 365202 (2014).
- [75] N. Perea-López, A. L. Elías, A. Berkdemir, A. Castro-Beltran *et al.*, *Photosensor Device Based on Few-Layered WS₂ Films*, Adv. Funct. Mater. **23** 5511 (2013).
- [76] N. Huo, S. Yang, Z. Wei, S.-S. Li *et al.*, *Photoresponsive and Gas Sensing Field-Effect Transistors based on Multilayer WS₂ Nanoflakes*, Sci. Rep. **4** (2014).
- [77] W. Zhang, M.-H. Chiu, C.-H. Chen, W. Chen *et al.*, *Role of Metal Contacts in High-Performance Phototransistors Based on WSe₂ Monolayers*, ACS nano (2014).
- [78] B. W. H. Baugher, H. O. H. Churchill, Y. Yang and P. Jarillo-Herrero, *Optoelectronic devices based on*

- electrically tunable p-n diodes in a monolayer dichalcogenide*, Nat Nano **9** 262 (2014).
- [79] A. Pospischil, M. M. Furchi and T. Mueller, *Solar-energy conversion and light emission in an atomic monolayer p-n diode*, Nat Nano **9** 257 (2014).
- [80] D. J. Groenendijk, M. Buscema, G. A. Steele, S. Michaelis de Vasconcellos *et al.*, *Photovoltaic and Photothermoelectric Effect in a Double-Gated WSe₂ Device*, Nano Lett. **14** 5846 (2014).
- [81] V. Podzorov, M. E. Gershenson, C. Kloc, R. Zeis *et al.*, *High-mobility field-effect transistors based on transition metal dichalcogenides*, Applied Physics Letters **84** 3301 (2004).
- [82] S. Das and J. Appenzeller, *WSe₂ field effect transistors with enhanced ambipolar characteristics*, Applied Physics Letters **103** (2013).
- [83] J.-K. Huang, J. Pu, C.-L. Hsu, M.-H. Chiu *et al.*, *Large-Area Synthesis of Highly Crystalline WSe₂ Monolayers and Device Applications*, ACS Nano **8** 923 (2013).
- [84] M. Tosun, S. Chuang, H. Fang, A. B. Sachid *et al.*, *High-Gain Inverters Based on WSe₂ Complementary Field-Effect Transistors*, ACS Nano **8** 4948 (2014).
- [85] H.-J. Chuang, X. Tan, N. J. Ghimire, M. M. Perera *et al.*, *High Mobility WSe₂ p- and n-Type Field-Effect Transistors Contacted by Highly Doped Graphene for Low-Resistance Contacts*, Nano Lett. **14** 3594 (2014).
- [86] A. Allain and A. Kis, *Electron and Hole Mobilities in Single-Layer WSe₂*, ACS Nano **8** 7180 (2014).
- [87] J. S. Ross, P. Klement, A. M. Jones, N. J. Ghimire *et al.*, *Electrically tunable excitonic light-emitting diodes based on monolayer WSe₂ p-n junctions*, Nat Nano **9** 268 (2014).
- [88] J. O. Island, M. Buscema, M. Barawi, J. M. Clamagirand *et al.*, *Ultrahigh Photoresponse of Few-Layer TiS₃ Nanoribbon Transistors*, Advanced Optical Materials **2** 641 (2014).
- [89] W.-W. Xiong, J.-Q. Chen, X.-C. Wu and J.-J. Zhu, *Individual HfS₃ nanobelt for field-effect transistor and high performance visible-light detector*, J. Mater. Chem. C **2** 7392 (2014).
- [90] Y.-R. Tao, X.-C. Wu and W.-W. Xiong, *Flexible Visible-Light Photodetectors with Broad Photoresponse Based on ZrS₃ Nanobelt Films*, Small (2014).
- [91] P. Hu, Z. Wen, L. Wang, P. Tan *et al.*, *Synthesis of Few-Layer GaSe Nanosheets for High Performance Photodetectors*, ACS Nano **6** 5988 (2012).
- [92] D. J. Late, B. Liu, J. Luo, A. Yan *et al.*, *GaS and GaSe ultrathin layer transistors*, Advanced Materials **24** 3549 (2012).
- [93] H. Liu and P. Ye, *MoS₂ Dual-Gate MOSFET With Atomic-Layer-Deposited Al₂O₃ as Top-Gate Dielectric*, Electron Device Letters, IEEE **33** 546 (2012).
- [94] P. Hu, L. Wang, M. Yoon, J. Zhang *et al.*, *Highly Responsive Ultrathin GaS Nanosheet Photodetectors on Rigid and Flexible Substrates*, Nano Lett. **13** 1649 (2013).
- [95] R. B. Jacobs-Gedrim, M. Shanmugam, N. Jain, C. A. Durcan *et al.*, *Extraordinary Photoresponse in Two-Dimensional In₂Se₃ Nanosheets*, ACS Nano **8** 514 (2013).
- [96] G. W. Mudd, S. A. Svatek, T. Ren, A. Patané *et al.*, *Tuning the Bandgap of Exfoliated InSe Nanosheets by Quantum Confinement*, Adv. Mater. **25** 5714 (2013).
- [97] S. Lei, L. Ge, S. Najmaei, A. George *et al.*, *Evolution of the Electronic Band Structure and Efficient Photo-Detection in Atomic Layers of InSe*, ACS nano **8** 1263 (2014).
- [98] S. R. Tamalampudi, Y.-Y. Lu, R. Kumar U., R. Sankar *et al.*, *High Performance and Bendable Few-Layered InSe Photodetectors with Broad Spectral Response*, Nano Lett. **14** 2800 (2014).
- [99] V. Capozzi and M. Montagna, *Optical spectroscopy of extrinsic recombinations in gallium selenide*, Phys. Rev. B **40** 3182 (1989).
- [100] O. Alekperov, M. Godjaev, M. Zarbaliev and R. Suleimanov, *Interband photoconductivity in layer semiconductors GaSe, InSe and GaS*, Solid State Communications **77** 65 (1991).
- [101] M. Genut, L. Margulis, G. Hodes and R. Tenne, *Preparation and microstructure WS₂ thin films*, Thin Solid Films **217** 91 (1992).
- [102] L. Plucinski, R. L. Johnson, B. J. Kowalski, K. Kopalko *et al.*, *Electronic band structure of GaSe(0001): Angle-resolved photoemission and ab initio theory*, Phys. Rev. B **68** 125304 (2003).
- [103] C. H. Ho and S. L. Lin, *Optical properties of the interband transitions of layered gallium sulfide*, Journal of Applied Physics **100** (2006).
- [104] J. F. Sánchez-Royo, J. Pellicer-Porres, A. Segura, V. Muñoz Sanjosé *et al.*, *Angle-resolved photoemission*

- study and first-principles calculation of the electronic structure of GaTe*, Phys. Rev. B **65** 115201 (2002).
- [105] C. H. d. Groot and J. S. Moodera, *Growth and characterization of a novel In₂Se₃ structure*, Journal of Applied Physics **89** 4336 (2001).
- [106] J. F. Sánchez-Royo, A. Segura, O. Lang, E. Schaar *et al.*, *Optical and photovoltaic properties of indium selenide thin films prepared by van der Waals epitaxy*, Journal of Applied Physics **90** 2818 (2001).
- [107] R. Sreekumar, R. Jayakrishnan, C. Sudha Kartha, K. P. Vijayakumar *et al.*, *Enhancement of band gap and photoconductivity in gamma indium selenide due to swift heavy ion irradiation*, Journal of Applied Physics **103** (2008).
- [108] F. Liu, H. Shimotani, H. Shang, T. Kanagasekaran *et al.*, *High-Sensitivity Photodetectors Based on Multilayer GaTe Flakes*, ACS Nano **8** 752 (2013).
- [109] D. De, J. Manongdo, S. See, V. Zhang *et al.*, *High on/off ratio field effect transistors based on exfoliated crystalline SnS₂ nano-membranes*, Nanotechnology **24** 025202 (2013).
- [110] Y. Tao, X. Wu, W. Wang and J. Wang, *Flexible photodetector from ultraviolet to near infrared based on SnS₂ nanosheet microsphere film*, Journal of Materials Chemistry C (2014).
- [111] G. Su, V. G. Hadjiev, P. E. Loya, J. Zhang *et al.*, *Chemical Vapor Deposition of Thin Crystals of Layered Semiconductor SnS₂ for Fast Photodetection Application*, Nano Lett. – (2014).
- [112] A. Morita, *Semiconducting black phosphorus*, Applied Physics A **39** 227 (1986).
- [113] Y. Akahama, S. Endo and S.-i. Narita, *Electrical Properties of Black Phosphorus Single Crystals*, J. Phys. Soc. Jpn. **52** 2148 (1983).
- [114] A. Castellanos-Gomez, L. Vicarelli, E. Prada, J. O. Island *et al.*, *Isolation and characterization of few-layer black phosphorus*, 2D Materials **1** 025001 (2014).
- [115] M. Buscema, D. J. Groenendijk, S. I. Blanter, G. A. Steele *et al.*, *Fast and Broadband Photoresponse of Few-Layer Black Phosphorus Field-Effect Transistors*, Nano Lett. **14** 3347 (2014).
- [116] M. Buscema, D. J. Groenendijk, G. A. Steele, H. S. van der Zant *et al.*, *Photovoltaic effect in few-layer black phosphorus PN junctions defined by local electrostatic gating*, Nat Commun **5** (2014).
- [117] F. Xia, H. Wang and Y. Jia, *Rediscovering black phosphorus as an anisotropic layered material for optoelectronics and electronics*, Nat Commun **5** (2014).
- [118] H. Liu, A. T. Neal, Z. Zhu, Z. Luo *et al.*, *Phosphorene: An Unexplored 2D Semiconductor with a High Hole Mobility*, ACS Nano **8** 4033 (2014).
- [119] J. Qiao, X. Kong, Z.-X. Hu, F. Yang *et al.*, *High-mobility transport anisotropy and linear dichroism in few-layer black phosphorus*, Nat Commun **5** (2014).
- [120] L. Li, Y. Yu, G. J. Ye, Q. Ge *et al.*, *Black phosphorus field-effect transistors*, Nat Nano **9** 372 (2014).
- [121] S. P. Koenig, R. A. Doganov, H. Schmidt, A. H. Castro Neto *et al.*, *Electric field effect in ultrathin black phosphorus*, Applied Physics Letters **104** (2014).
- [122] T. Low, A. S. Rodin, A. Carvalho, Y. Jiang *et al.*, *Tunable optical properties of multilayer black phosphorus thin films*, Phys. Rev. B **90** 075434 (2014).
- [123] V. Tran, R. Soklaski, Y. Liang and L. Yang, *Layer-controlled band gap and anisotropic excitons in few-layer black phosphorus*, Phys. Rev. B **89** 235319 (2014).
- [124] M. Engel, M. Steiner and P. Avouris, *Black Phosphorus Photodetector for Multispectral, High-Resolution Imaging*, Nano Lett. – (2014).
- [125] N. Youngblood, C. Chen, S. J. Koester and M. Li, *Waveguide-integrated black phosphorus photodetector with high responsivity and low dark current*, arXiv preprint arXiv:1409.6412 (2014).
- [126] T. Hong, B. Chamlagain, W. Lin, H.-J. Chuang *et al.*, *Polarized photocurrent response in black phosphorus field-effect transistors*, Nanoscale **6** 8978 (2014).
- [127] T. Low, M. Engel, M. Steiner and P. Avouris, *Origin of photoresponse in black phosphorus phototransistors*, Physical Review B **90** 081408 (2014).
- [128] C. Dean, A. Young, I. Meric, C. Lee *et al.*, *Boron nitride substrates for high-quality graphene electronics*, Nature Nanotechnology **5** 722 (2010).
- [129] G. F. Schneider, V. E. Calado, H. Zandbergen, L. M. Vandersypen *et al.*, *Wedging transfer of nanostructures*, Nano letters **10** 1912 (2010).
- [130] X. Song, M. Oksanen, M. A. Sillanpää, H. Craighead *et al.*, *Stamp transferred suspended graphene mechanical resonators for radio frequency electrical readout*, Nano letters **12** 198 (2011).

- [131] P. Zomer, S. Dash, N. Tombros and B. Van Wees, *A transfer technique for high mobility graphene devices on commercially available hexagonal boron nitride*, Applied Physics Letters **99** 232104 (2011).
- [132] F. Bonaccorso, A. Lombardo, T. Hasan, Z. Sun *et al.*, *Production and processing of graphene and 2d crystals*, Materials Today **15** 564 (2012).
- [133] O. Lopez-Sanchez, E. Alarcon Llado, V. Koman, A. Fontcuberta i Morral *et al.*, *Light Generation and Harvesting in a van der Waals Heterostructure*, ACS Nano **8** 3042 (2014).
- [134] O. Lopez-Sanchez, D. Dumcenco, E. Charbon and A. Kis, *Avalanche photodiodes based on MoS₂/Si heterojunctions*, arXiv preprint arXiv:1411.3232 (2014).
- [135] Y. Li, C.-Y. Xu, J.-Y. Wang and L. Zhen, *Photodiode-Like Behavior and Excellent Photoresponse of Vertical Sil/Monolayer MoS₂ Heterostructures*, Sci. Rep. **4** (2014).
- [136] S. Chuang, R. Kapadia, H. Fang, T. C. Chang *et al.*, *Near-ideal electrical properties of InAs/WSe₂ van der Waals heterojunction diodes*, Applied Physics Letters **102** 242101 (2013).
- [137] L. Britnell, R. M. Ribeiro, A. Eckmann, R. Jalil *et al.*, *Strong Light-Matter Interactions in Heterostructures of Atomically Thin Films*, Science – (2013).
- [138] W. J. Yu, Y. Liu, H. Zhou, A. Yin *et al.*, *Highly efficient gate-tunable photocurrent generation in vertical heterostructures of layered materials*, Nat Nano **8** 952 (2013).
- [139] K. Roy, M. Padmanabhan, S. Goswami, T. P. Sai *et al.*, *Graphene-MoS₂ hybrid structures for multifunctional photoresponsive memory devices*, Nat Nano **8** 826 (2013).
- [140] W. Zhang, C.-P. Chuu, J.-K. Huang, C.-H. Chen *et al.*, *Ultrahigh-Gain Photodetectors Based on Atomically Thin Graphene-MoS₂ Heterostructures*, Sci. Rep. **4** (2014).
- [141] G.-H. Lee, C.-H. Lee, A. M. van der Zande, M. Han *et al.*, *Heterostructures based on inorganic and organic van der Waals systems*, APL Materials **2** (2014).
- [142] C.-H. Lee, G.-H. Lee, A. M. van der Zande, W. Chen *et al.*, *Atomically thin p-n junctions with van der Waals heterointerfaces*, Nat Nano **9** 676 (2014).
- [143] M. M. Furchi, A. Pospischil, F. Libisch, J. Burgdörfer *et al.*, *Photovoltaic Effect in an Electrically Tunable van der Waals Heterojunction*, Nano Lett. **14** 4785 (2014).
- [144] H. Fang, C. Battaglia, C. Carraro, S. Nemsak *et al.*, *Strong interlayer coupling in van der Waals heterostructures built from single-layer chalcogenides*, Proceedings of the National Academy of Sciences **111** 6198 (2014).
- [145] N. Huo, J. Kang, Z. Wei, S.-S. Li *et al.*, *Novel and Enhanced Optoelectronic Performances of Multilayer MoS₂-WS₂ Heterostructure Transistors*, Adv. Funct. Mater. n/a–n/a (2014).
- [146] Y. Gong, J. Lin, X. Wang, G. Shi *et al.*, *Vertical and in-plane heterostructures from WS₂/MoS₂ monolayers*, Nat Mater **advance online publication** (2014).
- [147] Y. Deng, Z. Luo, N. J. Conrad, H. Liu *et al.*, *Black Phosphorus-Monolayer MoS₂ van der Waals Heterojunction p-n Diode*, ACS Nano **8** 8292 (2014).
- [148] S. Wi, M. Chen, H. Nam, A. C. Liu *et al.*, *High blue-near ultraviolet photodiode response of vertically stacked graphene-MoS₂-metal heterostructures*, Applied Physics Letters **104** 232103 (2014).
- [149] C. H. Lui, Z. Ye, C. Ji, K.-C. Chiu *et al.*, *Observation of interlayer phonon modes in van der Waals heterostructures*, arXiv preprint arXiv:1410.4224 (2014).
- [150] H. Fang, C. Battaglia, C. Carraro, S. Nemsak *et al.*, *Strong interlayer coupling in van der Waals heterostructures built from single-layer chalcogenides*, Proceedings of the National Academy of Sciences **111** 6198 (2014).
- [151] J. He, N. Kumar, M. Z. Bellus, H.-Y. Chiu *et al.*, *Electron transfer and coupling in graphene-tungsten disulfide van der Waals heterostructures*, Nature communications **5** (2014).
- [152] Y. Yu, S. Hu, L. Su, L. Huang *et al.*, *Equally Efficient Interlayer Exciton Relaxation and Improved Absorption in Epitaxial and Non-epitaxial MoS₂/WS₂ Heterostructures*, Nano Lett. – (2014).
- [153] X. Hong, J. Kim, S.-F. Shi, Y. Zhang *et al.*, *Ultrafast charge transfer in atomically thin MoS₂/WS₂ heterostructures*, Nature nanotechnology (2014).
- [154] S. Tongay, W. Fan, J. Kang, J. Park *et al.*, *Tuning Interlayer Coupling in Large-area Heterostructures with CVD-grown MoS₂ and WS₂ monolayers*, Nano letters (2014).
- [155] F. Ceballos, M. Z. Bellus, H.-Y. Chiu and H. Zhao, *Ultrafast Charge Separation and Indirect Exciton Formation in a MoS₂-MoSe₂ van der Waals Heterostructure*, ACS nano (2014).

- [156] K. Liu, Q. Yan, M. Chen, W. Fan *et al.*, *Elastic Properties of Chemical-Vapor-Deposited Monolayer MoS₂, WS₂, and Their Bilayer Heterostructures*, *Nano Letters* **14** 5097 (2014).

CHAPTER 4

FAST AND EFFICIENT PHOTODETECTION IN NANOSCALE QUANTUM-DOT JUNCTIONS

Ferry Prins*, Michele Buscema, Johannes S. Seldenthuis, Samir Etaki,
Gilles Buchs, Maria Barkelid, Val Zwiller, Yunan Gao, Arjan J. Houtepen,
Laurens D. A. Siebbeles, Herre S. J. van der Zant*

We report on a photodetector in which colloidal quantum-dots directly bridge nanometer-spaced electrodes. Unlike in conventional quantum-dot thin film photodetectors, charge mobility no longer plays a role in our quantum-dot junctions as charge extraction requires only two individual tunnel events. We find an efficient photoconductive gain mechanism with external quantum-efficiencies of 38 electrons-per-photon in combination with response times faster than 300 ns. This compact device-architecture may open up new routes for improved photodetector performance in which efficiency and bandwidth do not go at the cost of one another.

Parts of this chapter have been published in Nano Letters 12, 5740 (2012) [1].

4.1. INTRODUCTION

Colloidal quantum dots (CQDs) profit from the quantum size effect,[2] which gives rise to a variety of unique phenomena such as size-tunability, multi-exciton processes[3–5] and slow carrier-relaxation.[6, 7] Moreover, they combine low-temperature synthetic methodology with solution processability, allowing for low-cost fabrication methods. [8, 9] To date, the use of CQDs as photosensitive material has been mainly focused on thin-film devices. [5, 8–10] In these systems, the extraction-efficiencies of photogenerated charge carriers are dominated by the charges mobility, which in CQD-films is generally described and limited by hopping through interparticle barriers. Techniques to enhance the electronic coupling between the CQDs and thus improve the film-mobility include the use of short linkers, [11] various surface passivation approaches [12, 13] and the use of CQDs with large Bohr-radii, in particular lead chalcogenide quantum dots. In addition, short channel-length detectors have shown promising performances.[14, 15]

An important advancement in the field of quantum-dot photodetectors has been the development of devices capable of photoconductive gain. [8, 10] In these devices, exciton generation is followed by the trapping of one of the charge carriers. If the trap life-time exceeds the transit time of the opposite carrier, many carriers worth of current can pass through the circuit before recombination takes place. The gain in efficiency does however go at the expense of an increase in the response time due to the slow trap-state dynamics, which is typically in the order of milliseconds.[8, 10]

Here, we present a photodetector which places a one-dimensional parallel array of quantum dots in direct contact with nanometer separated electrodes (see Figure 4.1a). In this CQD-junction, charge mobility no longer plays a role as the contact of both source and drain electrodes to each CQD allows for direct charge extraction, which is both fast and efficient.

4.2. FABRICATION AND ELECTRICAL CHARACTERIZATION

Nanometer-spaced electrodes are fabricated by a self-aligned fabrication scheme, consisting of a two-step lithography process.[16–18] On top of a Si/SiO₂ substrate, the first electrode is defined via electron-beam lithography and evaporation in high vacuum ($\sim 1 \cdot 10^{-8}$ mbar, consisting of a 2 nm thick Ti adhesive layer, with 24 nm Au on top as the electrode material, and 10 nm of Cr. Upon removal from the evaporation chamber, the Cr forms a natural Cr₂O₃ layer which overhangs the Au as a shadow mask. In the second step, the second electrode of 2 nm Ti with 20 nm Au on top is defined, overlaying the first Ti/Au/Cr/Cr₂O₃ electrode, while the shadow mask protects a few nanometers around the first electrode. In the third step, a selective wet Cr-etchant (Cyantek, Cr-10, 5 minutes immersion) is used to remove the shadowmask, exposing a nanometer sized separation between the first and second electrode (3 nm to 6 nm as determined from scanning electron microscopy, see inset Figure 4.1b).

Before use, the samples are O_2 -plasma cleaned.

An advantage of the self-alignment technique is that the nanometer-separated electrodes can be prepared over large widths, which allows contact to many particles in parallel (see Figure 4.1b). Here we use devices with an electrode separation of 4 nm, and with an electrode width of 10 μm . A single layer of PbSe quantum dots of 4 nm in size is placed on top of the electrodes using dipcoating [19] after which a subsequent ligand substitution step with 1,2-ethanedithiol increases the coupling to the electrodes. Electrical contact of the particles to the electrodes is confirmed by performing electrical characterization before and after deposition at room temperature in a vacuum probe station. Before deposition the resistance in all 300 devices studied is $> 100 \text{ G}\Omega$ at voltages up to 2.5 V, whereas after deposition of the PbSe QDs a clear onset of conductance is observed at approximately 1 V (see Figure 4.1c).

4.3. PHOTORESPONSE

In all devices, we found a strong photoconductive effect when irradiating them with visible light. Current-voltage ($I_{\text{ds}} - V_{\text{ds}}$) characteristics taken under laser light irradiation ($\lambda = 532 \text{ nm}$, and a power density, $P_{\text{d}} = 0.16 \text{ W cm}^{-2}$, see Figure 4.2a) display a linear dependence with the applied voltage in the low-bias regime; at higher bias the $I_{\text{ds}} - V_{\text{ds}}$ characteristics become non-linear at the onset of the dark current. Control experiments in which bare nanogaps without PbSe-QDs are illuminated, display no photoconductive response.

To spatially resolve the photoconductive response, we place a device in an optical scanning confocal-microscope setup. While scanning a diffraction limited laser spot ($\lambda = 532 \text{ nm}$, spot size of $\sim 800 \text{ nm}$) across the device, the current is measured as a function of the spot position. Conductance maps, recorded at 750 mV, show a high photoconductive response when the laser spot is placed directly on top of the nanogap area (see Figure 4.2b, data corrected for the dark current). The response along the gap is consistently above 2 nA, with some variations in the current (factor of two maximum). These variations are likely the result of non-uniformity in the distribution of PbSe QDs or in the electronic coupling of the particles to the electrodes. The full width at half maximum of the photoresponse is 805 nm measured perpendicular to the nanogap, consistent with the spot-size of our diffraction-limited laser beam (see Section 4.7).

The photoconductive response depends strongly on the wavelength of the incident light. For the device of Figure 4.2b, we fix the laser at the position of maximum response and measure the current at $V_{\text{ds}} = 750 \text{ mV}$ and constant optical power, $P = 15 \mu\text{W}$, for varying wavelengths between 850 nm and 1650 nm as shown in Figure 4.2c. The spectral dependence of the photoconductance closely resembles the absorption spectrum of a reference film of the same PbSe QDs on quartz (gray solid line in Figure 4.2c), including the peak absorption at the bandgap energy and the absence of response at longer wavelengths ($\lambda > 1600 \text{ nm}$). The correspondence to the

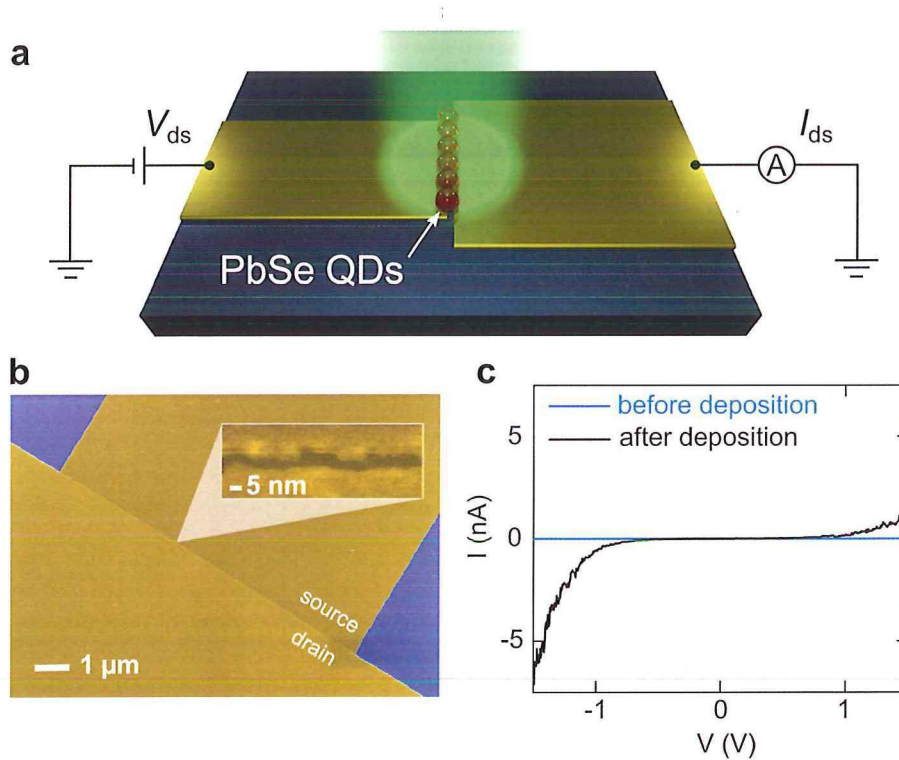


FIGURE 4.1: (a) Schematic of the device architecture and measurement circuitry, illustrating the one-dimensional CQD array geometry. The green shaded area represents the laser excitation impinging on the device. (b) Colorized scanning electron micrograph of an empty $10\ \mu\text{m}$ wide device fabricated by our self-aligned fabrication scheme. The inset shows a zoom-in of the nanogap area. (c) Room-temperature current-voltage characteristics before and after deposition of the PbSe CQDs. The device width is $10\ \mu\text{m}$. Measurements are performed in a vacuum probe-station at room temperature.

QD spectrum shows that the photoconductance is driven by optical excitations inside the QDs.

4.4. POWER DEPENDENCE

We have also recorded the photocurrent at $\lambda = 532\ \text{nm}$ at different optical powers (P_d between $2\ \text{W cm}^{-2}$ and $2000\ \text{W cm}^{-2}$, shown in Figure 4.3a). At low powers ($P_d < 50\ \text{W cm}^{-2}$), the current scales linearly with the laser power, while at higher powers ($P_d > 50\ \text{W cm}^{-2}$) the current saturates. The saturation at high powers is likely the result of the increasing Auger recombination rate. [19, 20] At lower powers the efficiency is highest. The external quantum efficiency (EQE), i.e. the number of extracted

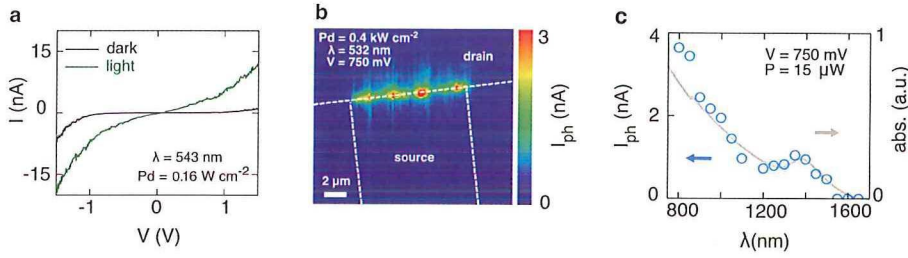


FIGURE 4.2: (a) $I_{ds} - V_{ds}$ characteristics in the dark (solid black line) and under laser illumination (solid green line), $\lambda = 532$ nm, and a power density, $P_d = 0.16$ W cm $^{-2}$, spot size = $150 \mu\text{m}$. (b) Photocurrent map of a different device (corrected for $I_{dark} = 0.8$ nA) as a function of the position of the diffraction-limited spot from a different setup with a spot size of about 800 nm ($\lambda = 532$ nm). Dashed white lines indicate the electrode edges determined from the reflection image. (c) Wavelength dependence of the photocurrent of the device in panel b at constant laser power (blue open circles). Photocurrent points are taken with the laser focused at the position of maximum response of the device. The optical absorption spectrum of a film of CQDs of the same thickness on quartz (solid gray line) is shown for comparison.

electrons (or holes) per photon incident on the device, can be calculated with

$$\text{EQE} = \frac{I_{ph}}{e} \frac{h\nu}{P_d \cdot A}, \quad (4.1)$$

where I_{ph} is the photocurrent ($I_{ph} = I_{illum.} - I_{dark}$) and A is the illuminated device area ($4 \times 800 \text{ nm}^2$). For the device in Figure 4.3a, the efficiency reaches 10.9 electrons per photon at 2 W cm^{-2} with a bias of 750 mV (see Section 4.7). At higher bias the photon-to-electron conversion is even more efficient; for example in the $I_{ds} - V_{ds}$ characteristic of Figure 4.2a, which is taken at low power, an EQE of 38 electrons per photon is observed at a bias of 1.5 V. In the calculation of the EQE it is assumed that all light incident on the gap area is absorbed by the one-dimensional array of quantum dots. If we do take the absorption probability of the single row of CQDs into account, [21] we can determine the internal quantum efficiency (IQE) of the detector. Assuming a maximum CQD coverage of 2000 4 -nm-sized particles across the $10 \mu\text{m}$ wide device of Figure 4.2a, we obtain IQEs as high as $5.9 \cdot 10^3$ electrons per photon (see supporting information).

The most striking feature of our device performance is the combination of high efficiency with fast response. Fig. 3b shows the temporal photoresponse of the device to a $1 \mu\text{s}$ laser pulse, measured using a low-noise amplifier and a 600 MHz oscilloscope. The observed rise and fall time of our device are approximately 200 and 300 ns, respectively, likely limited by the electronic bandwidth of the measurement circuit. Such fast response times combined with high efficiencies are crucial parameters in, for instance, video-rate laser-scanning microscopy where dwell-times in the order of

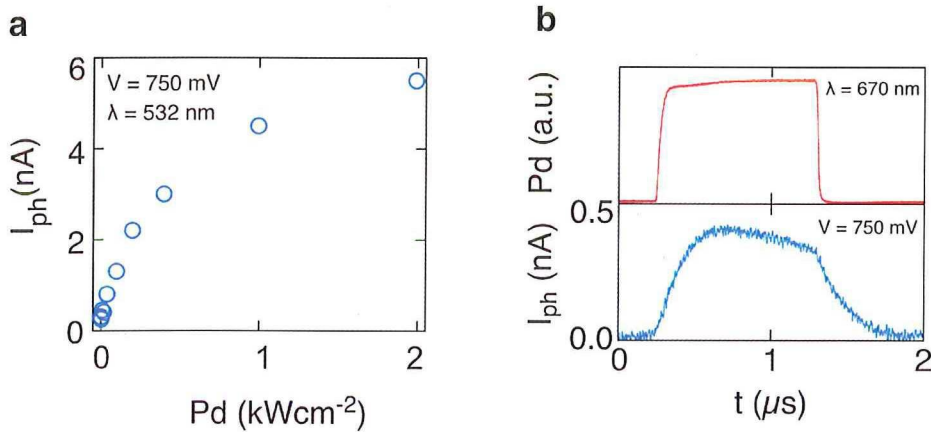


FIGURE 4.3: (a) Photocurrent I_{ph} as a function of surface power density (blue open circles) for the device in Figure 4.2b and c. (b) I_{ph} response (bottom panel) of a different device to a $1 \mu\text{s}$ square-wave pulsed laser illumination (top panel, $\lambda = 670 \text{ nm}$, 0.85 W cm^{-2} , spot size = $150 \mu\text{m}$). The rise and fall time of the laser signal is $< 20 \text{ ns}$.

100 ns are required. [22]

High efficiencies in CQD-photodetectors are usually achieved by trapping of one of the charge carriers, which is photoinduced by the incident light. If the lifetime of the trap state exceeds the carrier transit-time, the opposite charge carrier can circulate multiple times through the circuit before recombining with the trapped charge; the gain factor is then proportional to the ratio of the trap-life time over the transit time. For conventional CQD photoconductors, which have typical mobilities between $10^{-1} \text{ cm}^2 \text{ V}^{-1} \text{ s}^{-1}$ and $10^{-3} \text{ cm}^2 \text{ V}^{-1} \text{ s}^{-1}$ and channel lengths of about a micron, the transit time is hundreds of nanoseconds or longer. [13, 14]. Attaining an appreciable gain therefore requires trap-state life times as long as milliseconds, inevitably leading to the slow response times of these devices.

The orders-of-magnitude shorter rise and fall time of our device shows that if trap states are responsible for the gain they have to be short-lived, shorter than the observed 200 and 300 ns rise and fall time, and would thus require sub-nanosecond transit times in order to explain the observed IQE. Such short transit times are indeed feasible in our device as a direct result of the nanoscale geometry: the transit time is determined by the product of the tunneling probabilities of the two barriers that separate each CQD from source and drain electrodes. The interfacial electronic coupling energy for PbSe CQDs at or close to resonance is reported to be as high as 100 meV,[22] which corresponds to individual tunnel events at sub-picosecond timescales.[7] Taking this into consideration, only extremely short lived traps ($\ll 200 \text{ ns}$) could thus lead to considerable gain factors in our device, allowing for high

efficiency at short timescales.

For a possible explanation for the short-lived trap states, we take a closer look to the quantum dot junction. Since conduction through the CQD-device can only happen via tunneling through the barrier at the source and drain electrodes, the stochastic nature of the individual charge extraction events becomes important. [23–25] After creation of an exciton, either the electron or the hole will be extracted first, leaving the opposite carrier temporarily behind as if it was trapped. For instance, if the hole is left behind, the chemical potential of the QD electronic charge transitions is brought closer into resonance with the Fermi level as a result of the reduced Coulomb repulsion. This facilitates electron transport through the device until the hole recombines or is extracted, resulting in photoconductive gain, in the same manner as a *conventional* surface trap state at, for instance, the surface of a quantum dot. However, the crucial difference with *conventional* traps is that the life time of the charge in the trap state is only determined by the probabilistic nature of the tunnel events, which occur at sub-picosecond timescales. [7, 22] In the above discussion, we neglected plasmonic field enhancement effects that are known to increase light collection in nanogapped structures by effectively increasing the optical absorption cross section of the CQDs. [26–30]. If present, they would also contribute to the enhancement of the IQE number so that the gain is not solely determined by the ratio of the trap-life time over the transit time.

4.5. CONCLUSION AND OUTLOOK

In conclusion, the presented architecture offers a promising route towards solution processable, low-cost, nanoscale devices with ultrafast yet efficient detection performance. It moreover comprises a versatile platform to study the microscopic details of charge transfer at the metallic interface, not limited to colloidal quantum dots only, but applicable to a variety of nanomaterials. In addition, we expect that field enhancement may already play a role in the efficiency of our device, although the effect is expected to be small for the broad non-resonant electrodes. It will therefore be interesting to investigate devices with smaller widths which could profit from both efficient carrier extraction, as well as optimized light absorption by resonant plasmonic field enhancement.

4.6. ACKNOWLEDGMENTS

ACKNOWLEDGMENT We thank Gary A. Steele, Jos M. Thijssen, Yaroslav M. Blanter, Reinier W. Heeres and William A. Tisdale for discussions. We thank Mascha van Oossanen, Raymond Schouten and Ruud van Ooijik for technical assistance. This work was supported by Stichting FOM under the programs 86 and 111 and a FOM projectruimte, through the FP7-framework program ELFOS and a Marie Curie Intra European Fellowship (G.B.).

4.7. SUPPORTING INFORMATION

4.7.1. FABRICATION OF THE SELF-ALIGNED QD DEVICES

Lithography To obtain ~ 5 nm separation between the electrodes, we employ a self-aligned technique and selective wet etch of a sacrificial layer.[16, 18] Fabrication starts by spinning (3000 min^{-1}) and baking (175°C for 12 min) a double-layer resist* on a highly doped Si substrate covered with thermally grown SiO_2 . The first lithographic layer pattern consists of 32, $200 \times 300 \mu\text{m}$ pads arranged in a square; these pads will be one of the electrodes of the final device and provide the sacrificial layer to achieve the 5 nm separation by selective etching. After development in a solution of 1 MIBK : 3 IPA[†], a stack of metals is deposited in high vacuum (HV) conditions[‡] in the following order: 2 nm Ti as sticking layer, 20 nm Au as contact material, 10 nm Cr as sacrificial layer (see Figure 4.4a). As soon as the substrate is removed from the HV conditions, the top Cr layer oxidizes (Cr_xO_y) and slightly expands, jutting out from the rest of the metal stack (see Figure 4.4b).

The second layer defines the other electrodes composing the final devices, whose width ranges from 50 nm to $10 \mu\text{m}$. They are perpendicular to the short side of the pads and point towards the center of the design of the first layer. The resist used are identical to the first layer. After development and mild descum[§], 2 nm of Ti and 18 nm of Au are deposited. Since the metal deposition is performed in HV conditions, the small jutting structure provided by the chromium oxide acts a shadow mask and ensures no contact between the metals deposited in the first and second layer. This leads to the formation of a nanometric gap between the two metallic layers, covered by the small Cr_xO_y layer(see Figure 4.4c). After lift-off in warm (54°C) acetone, the gap is opened by removing of the Cr_xO_y layer by selective wet etch[¶] (see Figure 4.4d).

Deposition of the quantum dots Lead selenide (PbSe) colloidal quantum dots of ~ 4 nm in diameter were synthesized according to ref [31]. PbSe particles are deposited on the electrodes by a dipcoating technique under N_2 -atmosphere. First, the devices are immersed in a methanol (MeOH) solution of ethylenedithiol for 3 h to mediate a chemical linkage between the Au and the PbSe particles. The devices are subsequently immersed in MeOH (1 min) and a hexane solution of oleylamine-coated PbSe nanoparticles (1 min). Finally, the devices are once more immersed in a MeOH solution of ethylenedithiol (1 min, followed by 1 min in pure MeOH), to substitute the long oleylamine ligands and minimize the barrier between the particles and the

* 17.5 % in weight of a co-polymer methyl methacrylate (MMA):methacrylic acid (MAA) in ethyl-lactate - bottom, and poly-methyl methacrylate (PMMA) A2 950 kDa from Microchem - top

[†] MIBK is 4-methyl-2-pentanone, also called methyl isobutyl ketone

IPA is 2-propanol, also called iso-propyl-alcohol

[‡] AJA International electron beam evaporation, main chamber pressure about $5 \cdot 10^{-8}$ mbar

[§] 30 s O_2 plasma, flow = 50 mL min^{-1} , power = 50 W

[¶] Cyantek, Cr-10, ~ 5 min immersion

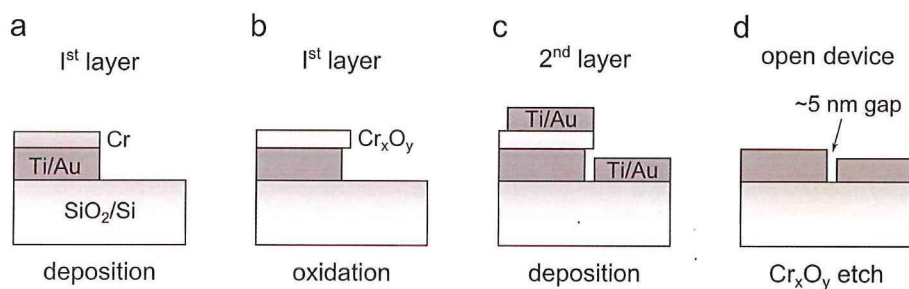


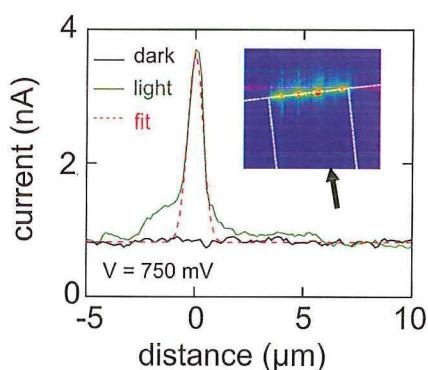
FIGURE 4.4: (a) First layer metal deposition: 2 nm Ti, 20 nm Au, 10 nm Cr. (b) Oxidation of Cr layer. Note the jutting part due to the expansion/growth oxide. (c) Second layer metal deposition: 2 nm Ti, 18 nm Au. (d) Device showing an open gap after the selective etching of the Cr_xO_y layer.

electrodes. The deposition results in a (sub-)monolayer coverage on the Au-electrodes as confirmed by AFM.

4.7.2. PHOTORESPONSE SPATIAL EXTENSION

Line traces taken perpendicular to the gap area in the conductance maps show the spatial distribution of the photoconductive response. The full width at half maximum of the conductance peak centered around the gap is 805 nm, consistent with the spot size of the diffraction limited spot (see Figure 4.5).

FIGURE 4.5: Line-cut of the conductance map taken perpendicular to the nanogap (see arrow in inset). Same device as Figure 4.2b. The red dashed line is a Gaussian fit to the photocurrent response at the gap area. The full width at half maximum of the fit equals 805 nm, closely matching the spot size of the diffraction limited spot of the scanning confocal microscope at $\lambda = 532$ nm. Slight deviations to the Gaussian fit are observed at larger distances from the gap.



4.7.3. QUANTUM EFFICIENCY CALCULATIONS

For the device in Figure 4.3, the external quantum efficiency (EQE) is calculated according to equation 4.1, taking the nanogap area within the spot size of 800 nm as the device area ($800 \times 4 = 3200 \text{ nm}^2$). The EQE reaches a maximum of reaches 10.9 electrons per photon at 2 W cm^{-2} , corresponding to a responsivity of 3.9 A W^{-1} (see

Figure 4.6). Similarly, the EQE for the device in Figure 4.2, in which the whole device is illuminated, can be calculated taking the full nanogap area into account ($10,000 \times 4 = 40 \cdot 10^3 \text{ nm}^2$), obtaining an EQE of 38 electrons per photon with a power density of 1.6 W cm^{-2} .

To determine the internal quantum efficiency (IQE) of the device we consider the optical cross-section of the sum of the maximum number of CQDs present in the gap area. For a $10 \mu\text{m}$ wide device and a particle diameter of 4 nm , the maximum number of CQDs that could be contacted in parallel is 2500. Taking the absorption cross-section of each particle to be 0.102 nm^2 at the excitation wavelength, as reported in ref. [20], we obtain a total optical cross section of a $10 \mu\text{m}$ wide device of $2500 \times 0.102 = 255 \text{ nm}^2$. With a surface power density of 1.6 W cm^{-2} (incident photon flux $\sim 4.5 \cdot 10^4 \text{ s}^{-1} \text{ nm}^{-2}$) and a photocurrent of 10.9 nA at 1.5 V (electron flux $68.1 \cdot 10^9 \text{ s}^{-1}$, corrected for the dark current) we obtain an IQE of $5.9 \cdot 10^3$ for the device in Figure 4.2a. It should be noted that the estimation of the number of particles is an upper limit and in reality is likely to be lower as a result of the distribution of the particles across the gap.

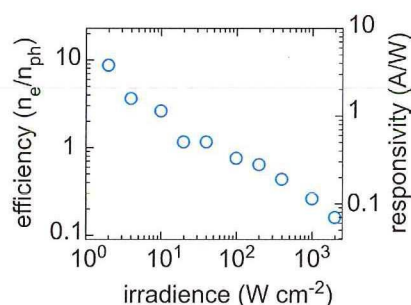


FIGURE 4.6: External quantum efficiency (EQE) and responsivity in terms of extracted electrons per photon incident on the illuminated device area ($800 \times 4 \text{ nm}$) of the device in Figure 4.2a as a function of the surface power density

REFERENCES

- [1] F. Prins, M. Buscema, J. S. Seldenthuis, S. Etaki *et al.*, *Fast and Efficient Photodetection in Nanoscale Quantum-Dot Junctions*, Nano Lett. **12** 5740 (2012).
- [2] L. E. Brus, *Electron-electron and electron-hole interactions in small semiconductor crystallites: The size dependence of the lowest excited electronic state*, The Journal of Chemical Physics **80** 4403 (1984).
- [3] M. C. Beard, *Multiple Exciton Generation in Semiconductor Quantum Dots*, J. Phys. Chem. Lett. **2** 1282 (2011).
- [4] R. D. Schaller and V. I. Klimov, *High Efficiency Carrier Multiplication in PbSe Nanocrystals: Implications for Solar Energy Conversion*, Phys. Rev. Lett. **92** 186601 (2004).
- [5] V. Sukhovatkin, S. Hinds, L. Brzozowski and E. H. Sargent, *Colloidal Quantum-Dot Photodetectors Exploiting Multiexciton Generation*, Science **324** 1542 (2009).
- [6] A. Pandey and P. Guyot-Sionnest, *Slow Electron Cooling in Colloidal Quantum Dots*, Science **322** 929 (2008).
- [7] W. A. Tisdale, K. J. Williams, B. A. Timp, D. J. Norris *et al.*, *Hot-Electron Transfer from Semiconductor Nanocrystals*, Science **328** 1543 (2010).

- [8] G. Konstantatos, I. Howard, A. Fischer, S. Hoogland *et al.*, *Ultrasensitive solution-cast quantum dot photodetectors*, *Nature* **442** 180 (2006).
- [9] G. Konstantatos and E. H. Sargent, *Nanostructured materials for photon detection*, *Nature nanotechnology* **5** 391 (2010).
- [10] J.-S. Lee, M. V. Kovalenko, J. Huang, D. S. Chung *et al.*, *Band-like transport, high electron mobility and high photoconductivity in all-inorganic nanocrystal arrays*, *Nat Nano* **6** 348 (2011).
- [11] D. Yu, C. Wang and P. Guyot-Sionnest, *n-Type Conducting CdSe Nanocrystal Solids*, *Science* **300** 1277 (2003).
- [12] Y. Liu, M. Gibbs, C. L. Perkins, J. Tolentino *et al.*, *Robust, Functional Nanocrystal Solids by Infilling with Atomic Layer Deposition*, *Nano Lett.* **11** 5349 (2011).
- [13] J. Tang, K. W. Kemp, S. Hoogland, K. S. Jeong *et al.*, *Colloidal-quantum-dot photovoltaics using atomic-ligand passivation*, *Nat Mater* **10** 765 (2011).
- [14] M. C. Hegg, M. P. Horning, T. Baehr-Jones, M. Hochberg *et al.*, *Nanogap quantum dot photodetectors with high sensitivity and bandwidth*, *Applied Physics Letters* **96** 101118 (2010).
- [15] L. J. Willis, J. A. Fairfield, T. Dadosh, M. D. Fischbein *et al.*, *Controlling Nanogap Quantum Dot Photoconductivity through Optoelectronic Trap Manipulation*, *Nano Lett.* **9** 4191 (2009).
- [16] A. Fursina, S. Lee, R. Sofin, I. Shvets *et al.*, *Nanogaps with very large aspect ratios for electrical measurements*, *Applied Physics Letters* **92** 113102 (2008).
- [17] F. Prins, M. Monrabal-Capilla, E. A. Osorio, E. Coronado *et al.*, *Room-Temperature Electrical Addressing of a Bistable Spin-Crossover Molecular System*, *Advanced Materials* **23** 1545 (2011).
- [18] J. Tang, E. De Poortere, J. Klare, C. Nuckolls *et al.*, *Single-molecule transistor fabrication by self-aligned lithography and in situ molecular assembly*, *Microelectronic engineering* **83** 1706 (2006).
- [19] E. Talgorn, Y. Gao, M. Aerts, L. T. Kunneman *et al.*, *Unity quantum yield of photogenerated charges and band-like transport in quantum-dot solids*, *Nat Nano* **6** 733 (2011).
- [20] I. Moreels, K. Lambert, D. De Muynck, F. Vanhaecke *et al.*, *Composition and Size-Dependent Extinction Coefficient of Colloidal PbSe Quantum Dots*, *Chem. Mater.* **19** 6101 (2007).
- [21] B. G. Saar, C. W. Freudiger, J. Reichman, C. M. Stanley *et al.*, *Video-Rate Molecular Imaging in Vivo with Stimulated Raman Scattering*, *Science* **330** 1368 (2010).
- [22] W. A. Tisdale and X.-Y. Zhu, *Artificial atoms on semiconductor surfaces*, *Proceedings of the National Academy of Sciences* **108** 965 (2011).
- [23] M. Galperin and A. Nitzan, *Molecular optoelectronics: the interaction of molecular conduction junctions with light*, *Phys. Chem. Chem. Phys.* **14** 9421 (2012).
- [24] L. Wang and V. May, *Charge transmission through single molecules: Effects of nonequilibrium molecular vibrations and photoinduced transitions*, *Chemical Physics* **375** 252 (2010).
- [25] L. Wang and V. May, *External field control of charge transmission through single molecules: Switching effects and transient currents*, *Journal of Electroanalytical Chemistry* **660** 320 (2011).
- [26] H. Im, K. C. Bantz, N. C. Lindquist, C. L. Haynes *et al.*, *Vertically Oriented Sub-10-nm Plasmonic Nanogap Arrays*, *Nano Lett.* **10** 2231 (2010).
- [27] T. Ishi, J. Fujikata, K. Makita, T. Baba *et al.*, *Si Nano-Photodiode with a Surface Plasmon Antenna*, *Japanese Journal of Applied Physics* **44** L364 (2005).
- [28] H. T. Miyazaki and Y. Kurokawa, *Squeezing Visible Light Waves into a 3-nm-Thick and 55-nm-Long Plasmon Cavity*, *Phys. Rev. Lett.* **96** 097401 (2006).
- [29] S.-F. Shi, X. Xu, D. C. Ralph and P. L. McEuen, *Plasmon Resonance in Individual Nanogap Electrodes Studied Using Graphene Nanoconstrictions as Photodetectors*, *Nano Lett.* **11** 1814 (2011).
- [30] D. R. Ward, N. J. Halas, J. W. Ciszek, J. M. Tour *et al.*, *Simultaneous Measurements of Electronic Conduction and Raman Response in Molecular Junctions*, *Nano Lett.* **8** 919 (2008).
- [31] M. V. Kovalenko, D. V. Talapin, M. A. Loi, F. Cordella *et al.*, *Quasi-Seeded Growth of Ligand-Tailored PbSe Nanocrystals through Cation-Exchange-Mediated Nucleation*, *Angewandte Chemie International Edition* **47** 3029 (2008).

CHAPTER 5

ULTRAHIGH PHOTORESPONSE OF FEW-LAYER TiS_3 NANORIBBON TRANSISTORS

Joshua O. Island*, Michele Buscema, Mariam Barawi, José M. Clamagirand, José R. Ares, Carlos Sánchez, Isabel J. Ferrer, Gary A. Steele, Herre S.J. van der Zant, and Andres Castellanos-Gomez*

Molybdenum- and tungsten-based dichalcogenides have recently received much attention due to their applications as semiconducting channel materials in field effect transistors and photodetectors. Although these atomically thin materials are promising for photodetection, a combination of high sensitivity and speed has yet to be shown. Here we explore the optoelectronic properties of TiS_3 ribbons, an almost unexplored layered material from the transition metal trichalcogenide family. TiS_3 ribbons present a direct band gap of 1.1 eV which is well-suited for detection all across the visible and the near-infrared spectrum. We isolate individual TiS_3 ribbons, exfoliate them down to few-layer thicknesses and use them as channel material for field effect phototransistors (FET). We measure mobilities up to $2.6 \text{ cm}^2 \text{ V}^{-1} \text{ s}^{-1}$ and ON/OFF ratios up to 104. Under illumination, the TiS_3 FETs present a high photoresponse of 2910 A W^{-1} and fast response times of 4 ms. In addition, we measure cutoff frequencies ($f_{3\text{dB}}$) up to 1000 Hz. The combination of large responsivity and fast response time all across the visible and near-infrared make layered TiS_3 a state-of-the-art material for photodetection.

Parts of this chapter have been published in *Advanced Optical Materials* 2, 641 (2014) [1].

5.1. INTRODUCTION

Transition metal chalcogenides have raised a huge interest in the nanoscience and material science communities.[2–5] The possibility of isolating ultrathin layers of these materials opens the door to new applications and phenomena derived from the reduced dimensionality. Within the large family of the semiconducting chalcogenides, the compounds based on Molybdenum Mo and Tungsten W have received the largest research effort because of their electronic and optical properties. [6–12] Nonetheless, there are many other semiconducting chalcogenide compounds whose electronic properties, in atomically thin form, are thus far unexplored.

TiS_3 , for instance, is one of the semiconducting members of the trichalcogenides family with a bulk optical bandgap of about 1 eV.[13] It has a structure, shown in Figure 5.1(a), composed of parallel sheets of one dimensional chains of stacked triangular prisms (TiS_3).[14] The sheets are held together by van der Waals forces and might be exfoliated in the same manner as graphene and other layered chalcogenide materials. [2–5] Although the bulk electronic properties have been studied in fair detail,[15–18] little is known of the properties of nanostructured TiS_3 . While Mo- and W- based dichalcogenides present a direct bandgap only at the single-layer limit, macroscopic films of TiS_3 ribbons (with thicknesses of hundreds of nanometers) show a direct bandgap of 1.1 eV and photocurrent response to white light illumination. [19, 20]

Here, we isolate individual few-layer TiS_3 nanoribbons (NR) by means of micromechanical exfoliation and use them as channel in field effect transistors (NR-FET). The electrical characteristics are studied finding an n-type behavior with current on/off ratios as high as 104 and mobilities up to $2.6 \text{ cm}^2 \text{ V}^{-1} \text{ s}^{-1}$. The photoresponse of the fabricated NR-FETs is studied at different illumination wavelengths and powers. The fabricated devices show a large photoresponse up to 2910 A W^{-1} and they respond to wavelengths across the visible spectrum. In addition, these devices present rise/fall times of about 4/9 ms and an $f_{3\text{dB}}$ frequency up to 1000 Hz. The excellent combination of FET characteristics, large photoresponse and high cutoff frequency make atomically thin TiS_3 NR-FETs superior to state-of-the-art phototransistors based on other semiconducting 2D materials.[7]

5.2. GROWTH AND CHARACTERIZATION

TiS_3 NRs are grown by sulfuration of bulk Ti disks at 500°C . [20] The morphology and stoichiometry of the sample can be accurately controlled by adjusting the process temperature and sulfur pressure. The growth results in gram-scale quantities of NR film. The resulting NR film is characterized by electron microscopy and X-ray diffraction. Figure 5.1(b) shows a bright field transmission electron microscopy (TEM) image of a single grown TiS_3 ribbon. The crystal planes are determined from the electron diffraction pattern (inset). The growth direction of the NRs is along the b-axis. Scanning electron microscopy (SEM) images of the film and a single NR are shown in

Figure 5.1(c) and Figure 5.1(d), respectively. As grown NRs have lengths of hundreds of microns, widths of a few microns, and thicknesses of hundreds of nanometers.

5.3. FET FABRICATION

To fabricate single ribbon devices, TiS_3 ribbons are transferred from the bulk disks onto degenerately doped silicon substrates with 285 nm of thermal SiO_2 using an all-dry viscoelastic stamping method.[21] During the transfer, the TiS_3 nanoribbons are mechanically exfoliated, leading to a decreased thickness of the transferred NR with respect to the as-grown ribbons.

To fabricate FET, ribbons with a thickness of 10 nm to 30 nm are selected due to their distinct optical contrast. Standard electron beam lithography and metal evaporation are used to deposit gold electrodes (50 nm) with a titanium sticking layer (5 nm). Finally, fabricated samples are annealed at 250 °C for 2 hours in a mixture of argon and hydrogen (5:1). Characteristics of 10 fabricated and measured devices can be found in Table 5.2. For consistency, all figures of the main text have been obtained from a single device.

5.4. ELECTRICAL CHARACTERIZATION

In Figure 5.2 we show the room temperature electrical characterization of a fabricated NR-FET device. An AFM micrograph of the device is presented in Figure 5.2(a). A line profile taken across the NR shows a thickness of 22 nm and a width of 195 nm. Measurements are made between two adjacent electrodes of the full device. Figure 5.2(b) plots the source-drain current as a function of the bias voltage ($I_{\text{ds}}-V_{\text{ds}}$) at different back-gate voltages (V_{g}). The $I_{\text{ds}}-V_{\text{ds}}$ characteristics are linear and symmetric with respect to V_{ds} and show a strong dependence on the back-gate voltage. This suggests that we can switch the device ON with the gate voltage and that the Ti/Au electrodes provide good contact to the TiS_3 NR.

Figure 5.2(c) shows the source-drain current versus back gate voltage ($I_{\text{ds}}-V_{\text{g}}$) at constant bias voltages. The device has a clear n-type behavior. At $V_{\text{ds}} = 1$ V, for negative V_{g} the current through the device is ~ 1.5 nA in the OFF state while for positive V_{g} the current reaches ~ 1.1 μA in the ON state giving an ON-OFF ratio of about 700.

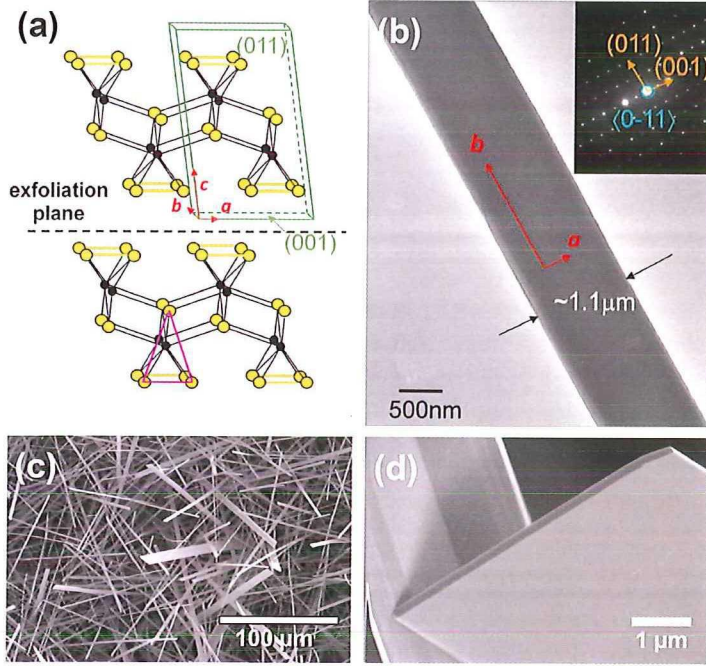


FIGURE 5.1: (a) TiS_3 nanoribbon structure composed of parallel sheets of one dimensional chains of stacked triangular prisms (TiS_3 , base shown in pink) that are held together by van der Waals forces across the exfoliation plane. (b) Bright field TEM micrograph and the corresponding electron diffraction pattern (inset) of a TiS_3 nanoribbon. (c) SEM image of TiS_3 nanoribbon film on the Ti growth disk. (d) FEG-SEM image of the edge of one TiS_3 nanoribbon.

From the calculated transconductance ($g = dI_{ds}/dV_g$), we estimate the mobility with

$$\mu_{\text{FE}} = g \cdot \frac{L}{Z} \cdot \frac{1}{C_{\text{ox}} V_{\text{ds}}}, \quad (5.1)$$

where L is the channel length, Z is the width of the nanoribbon, and C_{ox} is the oxide capacitance per unit area. The capacitance is calculated using finite element methods with COMSOL MULTIPHYSICS v4.3b to account for fringing effects derived from the reduced width of the TiS_3 ribbon channel (comparable to the dielectric thickness).[22] From Equation 5.1 we estimate a carrier mobility of $1.4 \text{ cm}^2 \text{ V}^{-1} \text{ s}^{-1}$ (up to $2.6 \text{ cm}^2 \text{ V}^{-1} \text{ s}^{-1}$ for other devices, see Table 5.2) which is an order of magnitude lower than the measured bulk value of $30 \text{ cm}^2 \text{ V}^{-1} \text{ s}^{-1}$. [15] Note that this estimate is likely a lower bound as it is obtained from a two terminal measurement. While the mobility estimates are modest, they compare well with recently fabricated MoS_2

photodetectors with mobilities of $4 \text{ cm}^2 \text{ V}^{-1} \text{ s}^{-1}$ and lower and may be improved by optimizing device geometry and dielectric material.[7, 8]

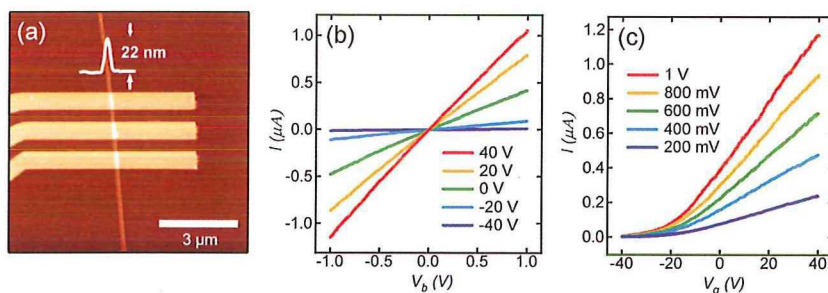


FIGURE 5.2: (a) AFM image of the FET device with electrodes spaced by 500 nm. The width of the TiS₃ NR is 195 nm. (b) Output characteristics ($I_{ds}-V_{ds}$) of the device at backgate voltages (V_g) from -40 V to $+40 \text{ V}$ in steps of 20 V . (c) Transfer characteristics ($I_{ds}-V_g$) at different bias voltages (V_{ds}) (from 200 mV to 1 V in steps of 200 mV).

5.5. PHOTORESPONSE

The photoresponse of the TiS₃ NR devices is studied by measuring their electrical characteristics upon illumination. The optoelectronic measurements are carried out in a vacuum probe station equipped with 5 lasers ($\lambda = 532 \text{ nm}$, 640 nm , 808 nm , 885 nm and 940 nm). Figure 5.3 shows the optoelectronic characterization of the same NR-FET device shown in Figure 5.2. Figure 5.3(a) shows $I_{ds}-V_g$ characteristics recorded at $V_{ds} = 500 \text{ mV}$ in dark (solid black line) and under 532 nm laser excitation (solid green line, $P = 500 \mu\text{W}$). The current increases steadily over the entire gate voltage range and, under illumination, the magnitude of the current is consistently larger than in dark. The photocurrent ($I_{\text{photo}} = I_{\text{illum.}} - I_{\text{dark}}$) starts at 40 nA in the OFF state ($V_g = -40 \text{ V}$) and reaches 100 nA at $V_g = 40 \text{ V}$. The inset shows the $I_{ds}-V_{ds}$ characteristics ($V_g = -40 \text{ V}$) recorded at the same power and wavelength as in the main panel, demonstrating linear and symmetric behavior.

In Figure 5.3(b) we plot the $I_{ds}-V_{ds}$ characteristics ($V_g = -40 \text{ V}$) measured with $\lambda 640 \text{ nm}$ for several excitation powers. The $I_{ds}-V_{ds}$ curves show a clear increase in the conductance of the NR-FET with increasing power, while maintaining the linear and symmetric behavior. The corresponding photocurrent, plotted in Figure 5.3(c), increases sublinearly with respect to the incident power, $I_{\text{ph}} \propto P^\alpha$ where $\alpha = 0.7$ suggesting a complex process of photocarrier generation, recombination, and trapping. [23, 24]

To evaluate the optical gain of the device, we calculate the responsivity from the

photocurrent,

$$R = \frac{I_{\text{ph}}}{P_{\text{d}}}, \quad (5.2)$$

where P_{d} is the power of the laser which has been scaled by the ratio of the area of the device ($195 \times 470 \text{ nm}$) to the area of the laser spot (diameter $200 \mu\text{m}$). Figure 5.3(d) plots the responsivity as a function of the laser power. The responsivity reaches 1030 A W^{-1} at a power of 100 nW and decreases with increasing power (the device with the best performance showed 2910 A W^{-1} , see Table 5.2).

This responsivity is several orders of magnitude larger than intrinsic graphene photodetectors and surprisingly larger than the most recent MoS₂ photodetectors which achieve a responsivity up to 880 A W^{-1} . [7, 25] Devices based on other materials, ZnO nanowire for example, have shown responsivities of $1 \cdot 10^4 \text{ A W}^{-1}$ however, unlike our TiS₃ NR-FETs, they operate outside the visible range of the spectrum. [26] Responsivities of our TiS₃ devices may be further improved by fabricating hybrid TiS₃-quantum dot devices as already demonstrated for graphene-quantum dot photodetectors. [27] The decrease in responsivity with increasing power could be attributed to filling of the long-lived trap states at higher powers which are responsible for high photoconductive gain. [28, 29] Using the responsivity of 1030 A W^{-1} , we estimate the external quantum efficiency (EQE) by

$$\text{EQE} = R \frac{hc}{e\lambda}. \quad (5.3)$$

The EQE for this device at wavelength of 640 nm reaches $2 \cdot 10^5 \%$ and is larger than the recent high gain In₂Se₃ nanosheet devices with an EQE of $1.6 \cdot 10^5 \%$. [30]

In Figure 5.3(e) we plot the photocurrent at $V_{\text{ds}} = 1 \text{ V}$ and $V_{\text{g}} = -40 \text{ V}$ for different excitation wavelengths. The photocurrent increases as the photon energy increases, likely related to an increase in the absorption of the material with higher photon energies. By linearly extrapolating the photocurrent vs. excitation wavelength, we can estimate an excitation energy for which the photocurrent would be zero, yielding a rough estimate of the bandgap. Following this methodology, we extract a bandgap energy of 1.2 eV (1010 nm) in close agreement with previous measurements on macroscopic TiS₃ thin films having a direct bandgap of 1.1 eV . [20]

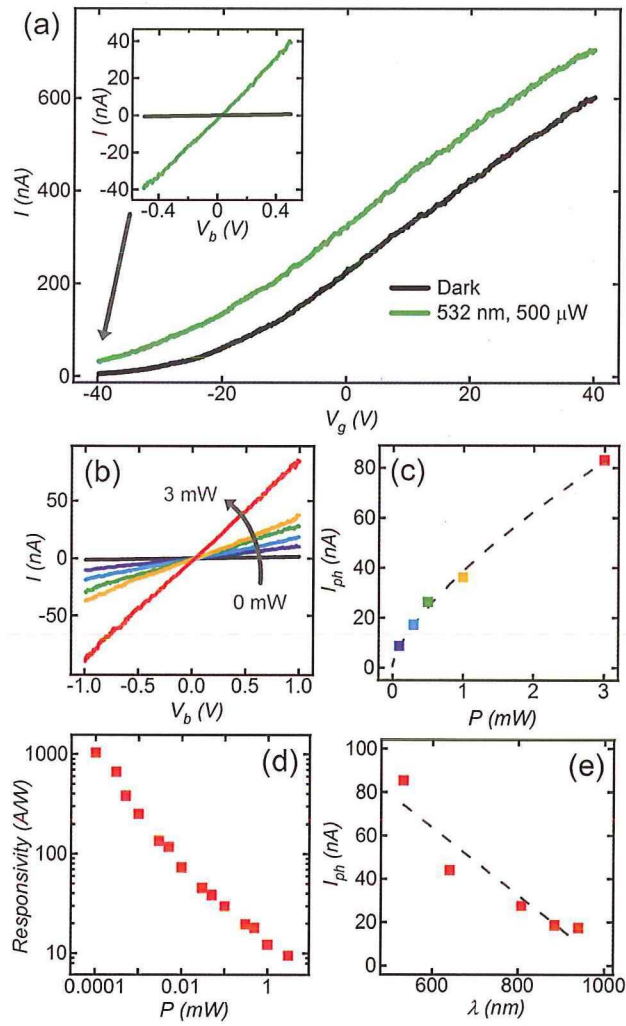


FIGURE 5.3: (a) $I_{ds}-V_g$ characteristics for $V_{ds} = 500$ mV in dark (black solid line) and under 532 nm, $500 \mu\text{W}$ excitation (green solid line). Inset shows the $I_{ds}-V_{ds}$ characteristics at $V_g = -40$ V for the same excitation. (b) $I_{ds}-V_{ds}$ characteristics at $V_g = -40$ V in dark (black solid line) and under 640 nm excitation for increasing laser powers up to 3 mW. (c) Photocurrent extracted from panel (b) for increasing powers. The dashed line is a power law fit. (d) Log-log plot of the responsivity as a function of excitation power ($\lambda = 640$ nm). (e) Photocurrent measured as a function of different laser wavelengths. Note that measurements for panels (c)-(e) are taken at $V_{ds} = 1$ V and $V_g = -40$ V.

5.6. TIME RESPONSE

The frequency response of the TiS_3 NR-FETs is characterized by modulating the intensity of the excitation laser in the time domain. In Figure 5.4, we show the photo-switching characteristics of our NR-FET by modulating the 640 nm ($P = 500 \mu\text{W}$) laser excitation with a mechanical chopper at $V_g = -40 \text{ V}$ and $V_{ds} = 1 \text{ V}$. Reliable, repeated cycling of the NR-FET at a frequency of 10 Hz is shown in Figure 5.4(a). In Figure 5.4(b), a zoom on one switching cycle is shown. The 10-90% rise time extracted is $\sim 4 \text{ ms}$ and the 10-90% fall time is $\sim 9 \text{ ms}$. The slower fall time is most likely related to the relaxation of deep trap states. These time scales are an order of magnitude faster than the lowest rise/fall times measured in MoS_2 devices and faster than the high gain ZnO nanowire devices.[8, 26] In Figure 5.4(c) we plot the device responsivity for increasing modulation frequency of the 640 nm laser at a power of $500 \mu\text{W}$. A cutoff frequency ($f_{3\text{dB}}$) of 1000 Hz is reached which is at the limit of our measurement set-up. This $f_{3\text{dB}}$ puts TiS_3 NR-FETs among the best nanostructured devices for photodetection. [31]

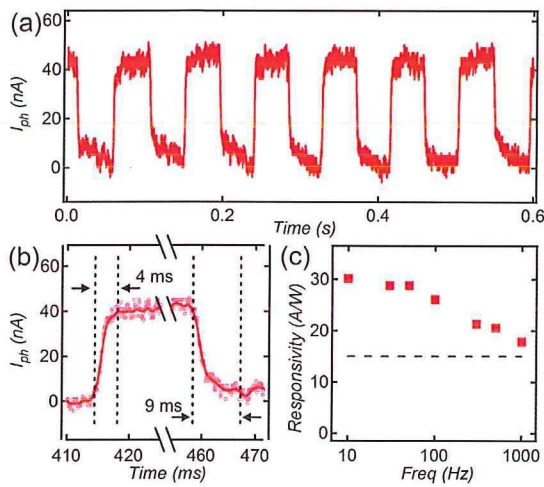


FIGURE 5.4: Photocurrent vs. time under a 10 Hz mechanically modulated optical excitation ($\lambda = 640 \text{ nm}$, $P = 500 \mu\text{W}$). (b) Zoom on a single switching cycle at 10 Hz frequency. Rise times taken at 10% and 90% of the maximum photocurrent are $\sim 4 \text{ ms}$ and fall times are $\sim 9 \text{ ms}$. The solid red curve is a moving average of the raw data (pink circles). (c) Responsivity versus modulation frequency for an excitation wavelength of 640 nm at $500 \mu\text{W}$. Note that all measurements are taken at $V_{ds} = 1 \text{ V}$ and $V_g = -40 \text{ V}$.

5.7. COMPARISON WITH LITERATURE

The direct bandgap (1.1 eV), high responsivity, and fast response make TiS_3 an ideal material for optoelectronic applications. Table 5.1 summarizes the latest high responsivity photodetectors. The TiS_3 NR-FETs have the best combination of responsivity and speed for visible and near-infrared light detection. The bandgap energy of 1.2 eV (cutoff wavelength of 1010 nm) makes them a suitable replacement to microstructured Si in applications where high gain is needed.

Material	Bandgap eV	λ_{cutoff} nm	Responsivity A W^{-1}	Rise time ms	Reference
TiS ₃ Nanoribbons	1.1	1130	$2.9 \cdot 10^3$	$4 \cdot 10^0$	This work
MoS ₂ Single Layer	1.8	690	$8.8 \cdot 10^2$	$4 \cdot 10^3$	[7]
WS ₂ Multilayer	1.96	635	$9.2 \cdot 10^{-5}$	$5 \cdot 10^0$	[12]
ZnO Nanowires	3.4	360	$4.7 \cdot 10^4$	–	[26]
In ₂ Se ₃ Nanosheets	1.3	955	$3.9 \cdot 10^2$	$1.8 \cdot 10^1$	[30]
GaTe Nanosheets	1.7	730	$1 \cdot 10^4$	$6 \cdot 10^0$	[32]
Si Microstructured	1.1	1130	$1.2 \cdot 10^2$	–	[33]
GaSe Nanosheets	2.11	590	$2.8 \cdot 10^0$	$2 \cdot 10^1$	[34]
Graphene Single Layer	–	–	$1 \cdot 10^{-2}$	$1.5 \cdot 10^{-9}$	[35]
InSe Nanosheets	1.4	885	$3.5 \cdot 10^{-2}$	$4.9 \cdot 10^{-1}$	[36]

TABLE 5.1: Figures-of-merit for recent high-responsivity photodetectors

5.8. CONCLUSIONS

In conclusion, this work represents one of the first characterizations of the photoreponse of nanostructured devices based TiS₃. Field-effect transistor based on few-layer TiS₃ have been fabricated and their electrical characteristic have been measured in dark and under illumination at room temperature. We find an n-type semiconducting behavior with mobilities of $2.6 \text{ cm}^2 \text{ V}^{-1} \text{ s}^{-1}$ and ON/OFF ratios up to 10^4 . The NR-FETs display an ultrahigh photoresponse up to 2910 A W^{-1} and fast switching times of about 4 ms with a cutoff frequency of 1000 Hz. The excellent combination of FET characteristics, high photoresponse and fast switching rates make ultrathin TiS₃ an interesting material for photodetection and photovoltaic applications. This work opens a new avenue to exploit the family of Ti-based trichalcogenides in 2D electronics and optoelectronics.

ACKNOWLEDGMENTS

This work was supported by the European Union (FP7) through the program RODIN and the Dutch organization for Fundamental Research on Matter (FOM). A.C-G. acknowledges financial support through the FP7-Marie Curie Project PIEF-GA-2011-300802 ('STRENGTHNANO'). Authors from MIRE Group acknowledge the support of the Ministry of Economy and Competitiveness (MINECO) for this research (contract MAT2011-22780). They also thank Dr. Garcés from CSIC-CENIM for the support at TEM and ED, Dr. Bodega for suggestions and discussions and technical support from Mr. F. Moreno.

Device	Thickness nm	ON/OFF	Mobility $\text{cm}^2 \text{V}^{-1} \text{s}^{-1}$	Responsivity A W^{-1}	Rise/fall time ms	$f_{3\text{dB}}$ Hz
J17B1	20	850	2.6	320		
J17B4	28	315	0.5	660	12/15	500
J19A2	22	730	1.4	1030	4/9	1000
J19A3	15	400	1.6			
J19A4	36	90	1.3	530		
J19A5	15	75	2.0	2590		
J19A6	19	725	0.8	430		
J19B3	22	740	1.5	2910		
J19B4	27	12 300	0.5	110		

TABLE 5.2: Summary of main characteristics of the measured devices.

REFERENCES

- [1] J. O. Island, M. Buscema, M. Barawi, J. M. Clamagirand *et al.*, *Ultra-high Photoresponse of Few-Layer TiS_3 Nanoribbon Transistors*, *Advanced Optical Materials* **2** 641 (2014).
- [2] K. S. Novoselov, D. Jiang, F. Schedin, T. J. Booth *et al.*, *Two-dimensional atomic crystals*, *Proceedings of the National Academy of Sciences of the United States of America* **102** 10451 (2005).
- [3] K. S. Novoselov, A. K. Geim, S. V. Morozov, D. Jiang *et al.*, *Electric Field Effect in Atomically Thin Carbon Films*, *Science* **306** 666 (2004), <http://www.sciencemag.org/content/306/5696/666.full.pdf>.
- [4] Q. H. Wang, K. Kalantar-Zadeh, A. Kis, J. N. Coleman *et al.*, *Electronics and optoelectronics of two-dimensional transition metal dichalcogenides*, *Nat Nano* **7** 699 (2012).
- [5] A. K. Geim and I. V. Grigorieva, *Van der Waals heterostructures*, *Nature* **499** 419 (2013).
- [6] G. Eda, H. Yamaguchi, D. Voiry, T. Fujita *et al.*, *Photoluminescence from Chemically Exfoliated MoS_2* , *Nano Lett.* **11** 5111 (2011).
- [7] O. Lopez-Sanchez, D. Lembke, M. Kayci, A. Radenovic *et al.*, *Ultrasensitive photodetectors based on monolayer MoS_2* , *Nat Nano* **8** 497 (2013).
- [8] Z. Yin, H. Li, H. Li, L. Jiang *et al.*, *Single-Layer MoS_2 Phototransistors*, *ACS Nano* **6** 74 (2012).
- [9] J. S. Ross, S. Wu, H. Yu, N. J. Ghimire *et al.*, *Electrical control of neutral and charged excitons in a monolayer semiconductor*, *Nat Commun* **4** 1474 (2013).
- [10] H. S. Lee, S.-W. Min, Y.-G. Chang, M. K. Park *et al.*, *MoS_2 Nanosheet Phototransistors with Thickness-Modulated Optical Energy Gap*, *Nano Lett.* **12** 3695 (2012).
- [11] R. S. Sundaram, M. Engel, A. Lombardo, R. Krupke *et al.*, *Electroluminescence in Single Layer MoS_2* , *Nano Lett.* **13** 1416 (2013).
- [12] N. Perea-López, A. L. Elías, A. Berkdemir, A. Castro-Beltran *et al.*, *Photosensor Device Based on Few-Layered WS_2 Films*, *Adv. Funct. Mater.* **23** 5511 (2013).
- [13] H. G. Grimmeis, A. Rabenau, H. Hann and P. Z. Neiss, *Elektrochem.* **9** 776 (1961).
- [14] M. Fleet, S. Harmer, X. Liu and H. Nesbitt, *Polarized X-ray absorption spectroscopy and XPS of TiS_3 : S K- and Ti L-edge XANES and S and Ti 2p XPS*, *Surface science* **584** 133 (2005).
- [15] E. Finkman and B. Fisher, *Electrical transport measurements in TiS_3* , *Solid state communications* **50** 25 (1984).
- [16] P.-L. Hsieh, C. Jackson and G. Grüner, *Disorder effects in the linear chain compound TiS_3* , *Solid state communications* **46** 505 (1983).
- [17] S. Kikkawa, M. Koizumi, S. Yamanaka, Y. Onuki *et al.*, *Electrical conductivity of TiS_3* , *physica status*

- solidi (a) **61** K55 (1980).
- [18] I. Gorlova, V. Y. Pokrovskii, S. Zytsev, A. Titov *et al.*, *Features of the conductivity of the quasi-one-dimensional compound TiS_3* , Journal of Experimental and Theoretical Physics **111** 298 (2010).
- [19] I. Ferrer, J. Ares, J. Clamagirand, M. Barawi *et al.*, *Optical properties of titanium trisulphide (TiS_3) thin films*, Thin Solid Films **535** 398 (2013).
- [20] I. Ferrer, M. Maciá, V. Carcelén, J. Ares *et al.*, *On the Photoelectrochemical Properties of TiS_3 Films*, Energy Procedia **22** 48 (2012).
- [21] A. Castellanos-Gomez, M. Buscema, R. Molenaar, V. Singh *et al.*, *Deterministic transfer of two-dimensional materials by all-dry viscoelastic stamping*, 2D Materials **1** 011002 (2014).
- [22] O. Wunnicke, *Gate capacitance of back-gated nanowire field-effect transistors*, Applied Physics Letters **89** 083102 (2006).
- [23] A. Rose, *Concepts in photoconductivity and allied problems*, Interscience Publishers (1963).
- [24] L. Li, P. S. Lee, C. Yan, T. Zhai *et al.*, *Ultrahigh-Performance Solar-Blind Photodetectors Based on Individual Single-crystalline $In_2Ge_2O_7$ Nanobelts*, Advanced Materials **22** 5145 (2010).
- [25] F. Xia, T. Mueller, R. Golizadeh-Mojarad, M. Freitag *et al.*, *Photocurrent Imaging and Efficient Photon Detection in a Graphene Transistor*, Nano Lett. **9** 1039 (2009).
- [26] W. Weng, S. Chang, C. Hsu and T. Hsueh, *A ZnO-nanowire phototransistor prepared on glass substrates*, ACS applied materials & interfaces **3** 162 (2011).
- [27] G. Konstantatos, M. Badioli, L. Gaudreau, J. Osmond *et al.*, *Hybrid graphene-quantum dot phototransistors with ultrahigh gain*, Nature nanotechnology **7** 363 (2012).
- [28] G. Konstantatos, J. Clifford, L. Levina and E. H. Sargent, *Sensitive solution-processed visible-wavelength photodetectors*, Nat Photon **1** 531 (2007).
- [29] N. Ai, Y. Zhou, Y. Zheng, H. Chen *et al.*, *Achieving high sensitivity in single organic submicrometer ribbon based photodetector through surface engineering*, Organic Electronics **14** 1103 (2013).
- [30] R. B. Jacobs-Gedrim, M. Shanmugam, N. Jain, C. A. Durcan *et al.*, *Extraordinary Photoresponse in Two-Dimensional In_2Se_3 Nanosheets*, ACS Nano **8** 514 (2013).
- [31] G. Konstantatos and E. H. Sargent, *Nanostructured materials for photon detection*, Nature nanotechnology **5** 391 (2010).
- [32] F. Liu, H. Shimotani, H. Shang, T. Kanagasekaran *et al.*, *High-Sensitivity Photodetectors Based on Multilayer GaTe Flakes*, ACS Nano **8** 752 (2013).
- [33] Z. Huang, J. E. Carey, M. Liu, X. Guo *et al.*, *Microstructured silicon photodetector*, Applied Physics Letters **89** 033506 (2006).
- [34] S. Lei, L. Ge, Z. Liu, S. Najmaei *et al.*, *Synthesis and Photoresponse of Large GaSe Atomic Layers*, Nano letters **13** 2777 (2013).
- [35] D. Sun, G. Aivazian, A. M. Jones, J. S. Ross *et al.*, *Ultrafast hot-carrier-dominated photocurrent in graphene*, Nature Nanotechnology **7** 114 (2012).
- [36] S. Lei, L. Ge, S. Najmaei, A. George *et al.*, *Evolution of the Electronic Band Structure and Efficient Photo-Detection in Atomic Layers of InSe*, ACS nano **8** 1263 (2014).

CHAPTER 6

PHOTO-THERMOELECTRIC EFFECT IN SINGLE-LAYER MoS_2

Michele Buscema*, Maria Barkelid, Val Zwiller, Herre S.J. van der Zant, Gary A. Steele* and Andres Castellanos-Gomez*

We study the photoresponse of single-layer molybdenum disulphide MoS_2 field-effect transistors by scanning photocurrent microscopy. We find that, unlike in many other semiconductors, the photocurrent generation in single-layer MoS_2 is dominated by the photo-thermoelectric effect and not by the separation of photoexcited electron-hole pairs across the Schottky barriers at the MoS_2 /electrode interfaces. We observe a large value for the Seebeck coefficient for single-layer MoS_2 that, by means of an external electric field, can be tuned between $-4 \cdot 10^4$ and $-1 \cdot 10^5 \mu\text{V K}^{-1}$. This large and tunable Seebeck coefficient of the single-layer MoS_2 paves the way to new applications of this material such as on-chip thermopower generation and waste thermal energy harvesting.

Parts of this chapter have been published in Nano Letters 13, 358 (2013) [1].

6.1. INTRODUCTION

THE experimental realization of graphene [2, 3] has opened the door not only to study exciting new phenomena but also to explore a whole new family of two-dimensional materials with complementary properties.[4, 5] For example, atomically thin semiconductor materials with a large bandgap are very interesting for electronic and optoelectronic applications where the lack of bandgap in graphene is hampering its applicability. Single-layer MoS₂ presents a large intrinsic bandgap (1.8 eV)[6–10] large in-plane mobility of about 200 to 500 cm² V⁻¹ s⁻¹ and remarkable mechanical properties.[11, 12] These properties are of great interest for sensors,[13] flexible circuits [14, 15] and optoelectronic devices. [16–18]

Recent works studying the optoelectronic properties of MoS₂ have shown that the photoresponse of externally biased MoS₂-based photo-transistors is driven by the change in conductivity upon illumination.[16–18] The photovoltaic effect in MoS₂ devices has also been reported with metallic electrodes that generate large Schottky barriers (SBs) and poor electrical contacts.[19, 20] These previous works made use of either an externally applied or a built-in electric field to separate the photogenerated carriers.

Here, we employ scanning photocurrent microscopy to study the photocurrent generation mechanism in single-layer MoS₂ transistors with no Schottky barriers and no external bias. We demonstrate that, in contrast to previous studies, the photo-thermoelectric effect dominates the photoresponse in our devices. From our observations, we estimate the electric-field modulation of the Seebeck coefficient for single-layer MoS₂, finding a large value that can be tuned by more than two orders of magnitude.

6.2. FABRICATION AND ELECTRICAL CHARACTERIZATION

The devices consist of a single-layer MoS₂ flake, deposited onto a Si/SiO₂ (285 nm) substrate by mechanical exfoliation.[4] Electrical contacts have been fabricated by standard electron-beam lithography and subsequent deposition of a Ti (5 nm)/Au (50 nm) layer. A combination of atomic force microscopy (AFM), Raman spectroscopy and optical microscopy [21] (see Section 6.6) has been used to characterize the MoS₂ samples. Figure 6.1(a) shows an AFM image of a field effect transistor (FET) fabricated with a single-layer MoS₂ flake. The line trace in Figure 6.1(b) shows that the height of the flake is around 0.9 nm in agreement with values previously reported in the literature. [21] Raman spectroscopy was also employed to further characterize the deposited MoS₂ layers. [22–24] As reported by C. Lee et al.[22] the frequency difference between the two most prominent Raman peaks depends monotonically on the thickness and it can therefore be used to accurately determine the number of MoS₂ layers. The Raman spectroscopy measurements confirm that our devices are single-layer MoS₂ (see Section 6.6). In order to increase the quality of the electrical contacts, the samples were annealed at 300 °C for two hours in a Ar/H₂ flow (500 sccm

/ 100 sccm).[7]

Figure 6.1(c) shows source-drain characteristics of the single-layer device at different gate voltages shown in Figure 6.1(a). The current vs. voltage relationship remains almost linear for a broad bias range, indicating that the conduction through the device is not dominated by Schottky barriers (SBs), in agreement with previous results by Radisavljevic et al. using similar electrode materials and annealing conditions.[7] Moreover, variable temperature transport experiments on MoS₂ using low work function electrodes (Ti and Sc) demonstrated a Schottky barrier height slightly larger than $k_B T$ at room temperature.[25]

This is also consistent with recent density functional theory (DFT) simulations and experimental work that demonstrate that Ti/MoS₂ interfaces provide ohmic contacts.[26, 27] Figure 6.1(d) shows various gate traces measured at different source-drain voltages. The device shows a pronounced n-type behavior, with a current on/off ratio exceeding $1 \cdot 10^3$ and a mobility of $\sim 0.85 \text{ cm}^2 \text{ V}^{-1} \text{ s}^{-1}$, that is characteristic of single-layer MoS₂ FETs fabricated on SiO₂ surfaces.[7, 13, 16, 27–29]

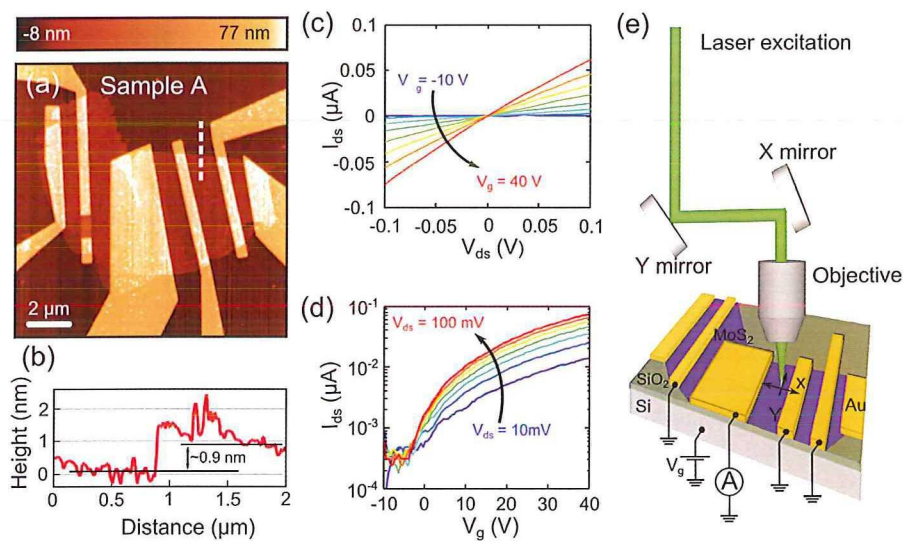


FIGURE 6.1: (a) Atomic force microscopy image of one of the studied devices, showing the MoS₂ flake and the electrodes used to make electrical contact. (b) Line profile over the dashed line in panel (a) showing the MoS₂ flake height. (c) Source-drain current vs. source-drain bias characteristics measured at different gate voltages. (d) Electrical transport characteristic of a MoS₂-based FET device (source-drain current vs. gate voltage) measured at different source-drain bias. For both panels (c) and (d) the channel length is 1.6 μm and width is 4.5 μm. (e) Schematic of the scanning photocurrent microscopy (SPCM) setup showing the excitation path and electric circuit used to perform SPCM measurements.

6.3. SCANNING PHOTOCURRENT MICROSCOPY

To spatially resolve the local photoresponse of the MoS_2 -FET device, we performed scanning photocurrent microscopy (SPCM) in a homebuilt scanning confocal microscope (see Figure 6.1(e)) with excitation provided by a continuous wave (CW) green laser ($\lambda = 532 \text{ nm}$) and a supercontinuum tuneable source at $\lambda = 750 \text{ nm}$, (see Section 6.6 for details). [30] In our experimental setup, we simultaneously record the intensity of the reflected laser light (Figure 6.2(a)) and the photocurrent (Figure 6.2(b)) generated in the device at every position along the scanning of the laser spot. It is thus possible to superimpose the two images to accurately determine where the photocurrent is generated (Figure 6.2(c)).

The gray-scale image in Figure 6.2(c) shows the reflection image and the color-scale shows the simultaneously measured current flowing through the device at zero bias (electrode 3 is connected to a current-to-voltage amplifier while all other electrodes are connected to ground). As it can be seen (e.g. by looking at electrode 3), there is photo-generated current at zero bias even when the laser spot is placed inside the area of the electrodes, microns away from the electrode edges, corresponding to distances up to 10 times larger than the full-width at half-maximum of the laser spot intensity profile. This is in striking contrast with several earlier findings on photocurrent on graphene [31, 32] which is localized at the interface between the graphene flake and the metal electrodes. In these previous works, the zero-bias photocurrent generation mechanism was attributed to the electron-hole separation at the SBs. This mechanism, however, cannot explain the presence of a photogenerated current when the laser is illuminating the metal electrodes, far from the electrode edges where SBs would be located.

The observation of photocurrent with the laser positioned deep inside the metal electrode suggests that the principal photocurrent generation mechanism in our device is different from photocurrent generation by the separation of photoexcited electron-hole pairs due to the localized electric field at the metal/semiconductor interface. This observation is also consistent with our conclusions from the data in Figure 6.1(b) that the SBs are not relevant for the transport characteristics of the device.

In order to gain a deeper insight into the photoresponse mechanism of single-layer MoS_2 FETs, we have performed scanning photocurrent measurements using different illumination wavelengths. Figure 6.3(a) shows a photoresponse map acquired with green ($\lambda = 532 \text{ nm}$, $h\nu = 2.33 \text{ eV}$) illumination. The photovoltage is obtained by dividing the measured photocurrent by the device resistance, measured under the same illumination conditions. A line profile of the photocurrent measured along the dashed green line in Figure 6.3 (a) is presented in Figure 6.3(b) as open blue circles. The solid red line is a Gaussian fit to the data corresponding to a diffraction limited laser spot. Notice that there is a significant photocurrent tail generated when the laser is scanned over the electrode (arrow in Figure 6.3(b)). This is again inconsistent

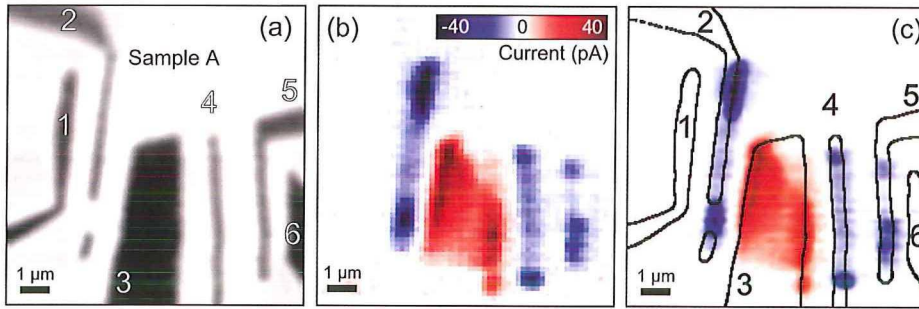


FIGURE 6.2: (a) Spatial map of the intensity of the reflected light from the device (white corresponds to low reflection). Electrodes have been numbered for clarity. (b) Photocurrent image of the MoS_2 FET. The colorscale in the inset gives the photocurrent value. (c) Superposition of the photocurrent map (from (b), same colorscale) and contours of the electrodes as obtained from the light reflection map. The scale bars are always $1 \mu\text{m}$. Reflection and photocurrent measurements are performed simultaneously with electrode number 3 connected to a current to voltage amplifier while the other electrodes are connected to ground. Excitation is given by a CW laser, $\lambda = 532 \text{ nm}$, $P = 1 \mu\text{W}$, spot waist radius $\sim 400 \text{ nm}$. The region of the flake from the right edge of electrode 2 to the right edge of electrode 3 is composed by multiple layers of MoS_2 . No current is seen flowing from electrode 1 or 6 because of poor contact between those with the underlying MoS_2 flake.

with a response shifted into the MoS_2 region, as would be expected for a photovoltaic response from Schottky barriers.

Figure 6.3(c) shows a photoresponse false-color map acquired with a red excitation wavelength ($\lambda = 750 \text{ nm}$, $h\nu = 1.65 \text{ eV}$). The photovoltage is calculated as in Figure 6.3(a). Note that the photovoltage under green illumination is larger because of the lower reflectance (and thus higher absorption) of the gold electrodes for this wavelength. The observation of photoresponse even for photon energies lower than the bandgap (Figure 6.3(c)) cannot be explained by separation of photoexcited electron-hole pairs (see Figure 6.3(e) - top panel). Moreover, previous photoconductivity measurements in MoS_2 transistors under large source-drain bias have not shown any significant photoresponse for excitation wavelength above 700 nm (or below 1.77 eV). [8, 16] This indicates that sub-bandgap impurity states are either not present or do not contribute to photocurrents, even in the presence of a large extraction bias, precluding sub-bandgap states as a possible source of photocurrent in Figure 6.3(c). From these considerations, we conclude that the generation of photocurrent with excitation energies below the bandgap cannot be ascribed to a photovoltaic effect.

Interestingly, for above-bandgap illumination, where photovoltaic effects could play a role, the photocurrent images show characteristics that are qualitatively very similar to those for below bandgap illumination. A line profile of the photocurrent measured along the dashed green line in Figure 6.3(c) is presented in Figure 6.3(d), in the same fashion as in Figure 6.3(b) to facilitate the comparison. The qualita-

tive agreement, and in particular the tail of photocurrent when the laser is focused over the metal, suggests that the photogeneration mechanism is not dominated by photovoltaic effects even for above-bandgap excitation.

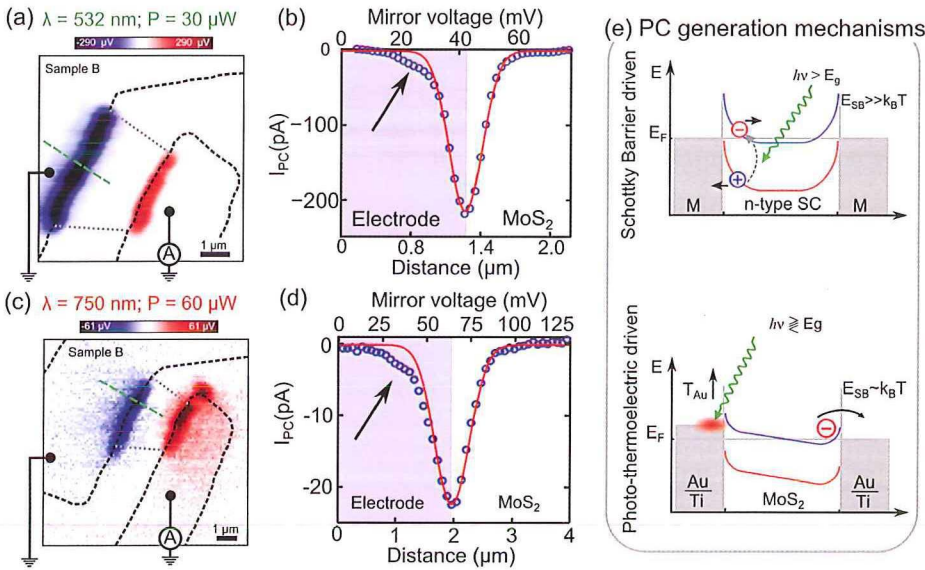


FIGURE 6.3: Photovoltage map of a single layer MoS_2 FET using an excitation wavelength of 532 nm (a) and 750 nm (c). (b)/(d) Photocurrent profile across the linecut in panel (a)/(b) (open blue circles). The solid red line is a Gaussian fit of the data and the arrow points at the photocurrent tail generated when the laser spot is scanned over the electrode. The shaded blue area represents the electrode area as determined by the reflection signal. (d) Schematic of photoresponse mechanism in a typical Metal-Semiconductor-Metal device. (e) Schematic of the photoresponse mechanism in a device dominated by photo-thermoelectric effect. The conduction band is drawn in blue while the valence band is drawn in red.

This hypothesis is also consistent with a lack of gate dependence of the SPCM images at above bandgap excitation energies ($\lambda = 532 \text{ nm}$). In particular, the position of the maximum photocurrent in the photovoltaic effect is expected to shift with the gate voltage, an effect also not observed in our devices. Figure 6.4(a) shows an SPCM map (at zero source-drain bias) of one of the studied devices acquired with the electrical circuit sketched in Figure 6.4(b). The SPCM map in Figure 6.4(a) is taken in a smaller area of the same device as in Figure 6.2. Since electrode 4 (not 3) is now connected to ground via the current amplifier, as shown in Figure 6.4(b), the strong photocurrent inside electrode 3 is now negative. By performing SPCM measurements with gate voltages ranging from +30 V to -30 V, displayed in Figure 6.4(c), we determine that the position of the photocurrent peaks does not change (within experimental resolution) with respect to gate voltage. This is in contrast with

earlier findings on devices in which the photocurrent is generated by the separation of photo-excited electrons and holes due to the electrostatic potential in p-n junctions or SBs whose extension depends on the charge carrier concentration. [31]

As the charge carrier density is reduced, the potential gradient of a p-n junction or SB would extend deeper into the material yielding a maximum photocurrent further and further away from the electrode edges, as sketched in Figure 6.4(d). [31–36] Therefore, the absence of shift in the position of the measured photocurrent (see Figure 6.4(c)) indicates that the dominant mechanism of photocurrent generation is not the separation of carriers by the built-in electrical potential along the SB near the electrodes and supports the proposed mechanism based on the photo-thermoelectric effect. As shown in Figure 6.4(e), the photo-induced temperature raise in the electrodes effectively generates a difference in the chemical potential of source and drain electrodes that can drive current through the device. This happens only when the laser is focused onto the electrode surface since the absorption of laser light by the MoS₂ flake is negligible. This also suggests that the main mechanism for photocurrent generation, even with above-bandgap illumination, is not the photovoltaic effect.

6.4. PHOTOTHERMOELECTRIC EFFECT

The negligible role of the SBs in the conductance of the devices, the strong measured photocurrent inside the area of the electrodes whose position is gate-independent and the observation of qualitatively identical photoresponse with below and above-bandgap illumination all suggest that photovoltaic effects cannot be responsible for the photoresponse observed here. Instead, we propose that the photoresponse in our device arises from a strong photo-thermoelectric effect. [37–41] In the photo-thermoelectric effect (Figure 6.3(e) - bottom panel), a temperature gradient arising from light absorption generates a photo-thermal voltage across a junction between two materials with different Seebeck coefficient. This photo-thermovoltage can drive current through the device. This mechanism is consistent with our observation of strong photocurrents when the laser is focused on the metallic electrodes and also explains the presence of localized and intense photocurrent spots at the edges of the electrodes where the laser absorption is increased and the heat dissipation is reduced. Moreover, it would also explain the stronger photocurrent in the electrode area in Figure 6.2 where the MoS₂ underneath the electrode is more than one layer thick which reduces the thermal coupling with the substrate and thus increases the local temperature of the electrode (see Figure 6.7 in Section 6.6).

The photo-thermoelectric generation of current can be understood as follows: the local absorption of the laser creates a local heating of the junction between the gold and the MoS₂ layer. This local heating of the junction is translated into a voltage difference (ΔV_{PTE}), which will drive current through the device, by the difference between the Seebeck coefficients of the MoS₂ flake (S_{MoS_2}) and the electrodes (S_{TiAu}) and the local increase of the junction temperature (ΔT) (see Section 2.4.1). This ΔT

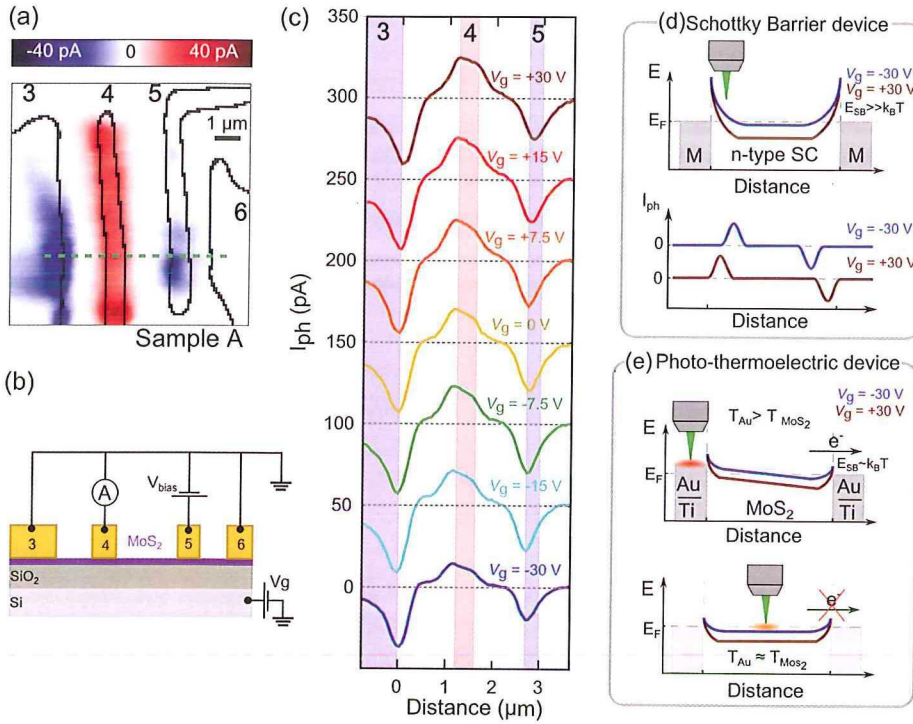


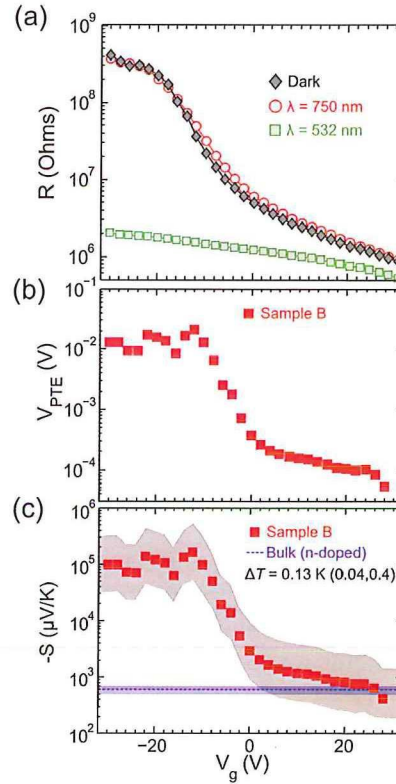
FIGURE 6.4: (a) Scanning photocurrent image of a single-layer MoS_2 FET taken at $\lambda = 532$ nm. Note that the current-to-voltage amplifier is connected to electrode 4, while electrode 3, 5 and 6 are connected to ground. (b) Schematic cross-section of the device, showing the electrical circuit used to perform the measurements. (c) Photocurrent line profiles (along the green dashed line in panel (a), $\lambda = 532$ nm) for gate voltages of +30 V, +15 V, +7.5 V, 0 V, -7.5 V, -15 V and -30 V from top to bottom. Consecutive lines are shifted by 50 pA for clarity. Shaded areas indicate the position and size of electrodes number 3, 4 and 5 as determined from the reflection signal; the colors of the shading indicates the sign of the photocurrent. (d) Schematic of the energy diagram of a typical Metal-Semiconductor-Metal device (top) and of the magnitude of a photocurrent line profile over such a device showing the expected gate-induced spatial shift in the photocurrent peak (bottom). (e) Schematic of the energy diagram of the single-layer MoS_2 device when the laser spot is incident on the electrode (top) and on the MoS_2 flake (bottom). In both panels (d) and (e) the conduction band is drawn at different gate voltages and the valence band is not shown for clarity.

can be modelled as the temperature difference of the locally heated gold electrode (T_{Au}) and a part of the MoS_2 flake which is distant from the junction (T_{MoS_2}).

$$\Delta V_{\text{PTE}} = \Delta S \cdot \Delta T = (S_{\text{MoS}_2} - S_{\text{TiAu}}) \cdot (T_{\text{MoS}_2} - T_{\text{TiAu}}) \quad (6.1)$$

We have further studied the gate dependence of the photo-thermoelectric effect

FIGURE 6.5: (a) Resistance of a single-layer MoS₂ device as a function of gate voltage in dark state and with the laser spot placed on the MoS₂/electrode interface. Two different illumination wavelengths have been used (532 nm and 750 nm). (b) Photo-thermoelectric voltage for a single-layer MoS₂ device measured with the laser spot ($\lambda = 750$ nm) placed on the MoS₂/electrode interface. (c) Estimated Seebeck coefficient vs. gate voltage. The values are calculated from eq. 6.1 using the measured photovoltage (symbols). The gray shaded area is the uncertainty due to the uncertainty in the estimation of the temperature gradient. The dashed light blue line corresponds to the Seebeck coefficient value of bulk MoS₂ with experimental uncertainty (shaded light blue area). The saturation effect at negative gate values is due to the high resistance of the device, leading to a current value below the noise floor of the current-to-voltage amplifier



in single layer MoS₂ by measuring the electrical transport characteristics of single MoS₂ devices while the laser spot is placed at a location with high photoresponse. For illumination wavelengths with a photon energy higher than the bandgap, the threshold voltage is shifted towards very negative values (see Figure 6.5(a)), not reachable without leading to gate leakage. It is therefore preferable to use illumination wavelengths with photon energy below the bandgap to minimize this photoconductive effect.

Figure 6.5(b) plots the measured the photothermoelectric voltage ΔV_{PTE} for a single-layer MoS₂ device at different gate voltages. The photo-thermoelectric voltage is the intercept with the voltage bias (V_{ds}) axis of the IV characteristic of the devices measured under sub-bandgap illumination. By decreasing the gate voltage below the threshold voltage, the photo-thermoelectric voltage shows a substantial increase. As the ΔV_{PTE} is proportional to the difference in the Seebeck coefficients and the temperatures of the AuTi electrodes and the MoS₂ flake (equation 6.1), the observed behavior can be attributed to the expected gate dependence of the Seebeck coefficient

of MoS₂.

As it is difficult to experimentally determine microscopic properties such as the energy dependent density of states in a given sample, the Seebeck coefficient is often parameterized in terms of the conductivity of the sample using the Mott relation: [42–45]

$$S = \frac{\pi^2 k_B^2 T}{3e} \left. \frac{d \ln(\sigma(E))}{dE} \right|_{E=E_F}, \quad (6.2)$$

where k_B is the Boltzmann constant, T the temperature, e the electron charge and $\sigma(E)$ is the conductivity as a function of energy (E), and the derivative is evaluated at the Fermi energy E_F . Using equation 6.2 we estimate the maximum Seebeck coefficient in our device to be in the order of $-2 \cdot 10^4 \mu\text{V K}^{-1}$, roughly an order of magnitude lower than the value we estimate from our measurements. This discrepancy could arise from the fact that equation 6.2 is based on the assumption that the conductor is a metal or a degenerate semiconductor, which is not the case for a single flake of MoS₂ near depletion.

According to equation 6.1 the Seebeck coefficient of MoS₂ can be determined from ΔV_{PTE} and the estimate of the temperature gradient across the AuTi/MoS₂ junction. Notice that the Seebeck coefficient of AuTi is negligible with respect to that of MoS₂ and no gate dependence is expected. To estimate the increase of temperature induced by the laser illumination, we have performed a finite elements analysis calculation, taking into account the reflections losses in the objective and at the surface of the sample and the absorbed intensity through the material according to $I = I_0 \cdot (1 - \exp(-\alpha \cdot d))$ where α is the absorption coefficient of the material and d is its thickness. With the employed laser excitation ($\lambda = 750 \text{ nm}$, $I_0 = 60 \mu\text{W}$ and $R_{\text{spot}} \approx 500 \text{ nm}$), if we assume that all the energy delivered by the laser is converted into heat, we obtain $\Delta T_{\text{AuTi/MoS}_2} \approx 0.13 \text{ K}$ (see Section 6.6). Figure 6.5(c) shows the estimated values: the experimental data are represented by squares while the shaded area represents the uncertainty in the estimation of the Seebeck coefficient deriving from an assumed uncertainty of a factor of 3 in the calculation of the temperature gradient (that is $\Delta T_{\text{AuTi/MoS}_2}$ in between 0.04 K and 0.4 K). The Seebeck coefficient value for bulk MoS₂ (between $-500 \mu\text{V K}^{-1}$ and $-700 \mu\text{V K}^{-1}$) is also plotted to facilitate the comparison.[46] A negative value of the Seebeck coefficient is expected for n-type semiconductors.

The obtained value for the Seebeck coefficient is remarkably large and varies strongly with the gate voltage from $-2 \cdot 10^2 \mu\text{V K}^{-1}$ at high doping levels (high positive gate) to $-3 \cdot 10^4 \mu\text{V K}^{-1}$ at low doping levels (high negative gate). Notice that at negative gate voltages, the Seebeck coefficient value saturates. This is due to the large resistance of the device at negative gate voltages which yields to a measured photocurrent that can be below the noise floor of the current amplifier (leading to the observed saturation in the estimated Seebeck coefficient).

The Seebeck coefficient that we observe for single-layer MoS₂ is orders-of-magnitude larger than that of graphene (± 4 to $\pm 100 \mu\text{V K}^{-1}$) [37, 38, 47–49] semiconducting carbon nanotubes ($\sim -300 \mu\text{V K}^{-1}$) [50], organic semiconductors ($\sim 1 \cdot 10^3 \mu\text{V K}^{-1}$) [51] and even than materials regularly employed for thermopower generation such as Bi₂Te₃ ($\pm 150 \mu\text{V K}^{-1}$) [52, 53]. On the other hand the presented Seebeck coefficient is comparable with other materials such as MnO₂ powder ($20 \cdot 10^3 \mu\text{V K}^{-1}$) [54] and Fe₂O₃ ($\pm 1 \cdot 10^4 \mu\text{V K}^{-1}$) [55]. In addition, the wide gate tunability of the Seebeck coefficient can be useful for applications such as on-chip power generation and thermoelectric nanodevices. These applications include, but are not limited to, energy harvesting of waste thermal energy of other processes, [56, 57] and to the possibility of developing autonomously powered devices. [58, 59] In all these applications, the tunability of the Seebeck coefficient represents an efficient way of optimizing device performances. [58, 59]

6.5. CONCLUSION AND OUTLOOK

Using sub-bandgap illumination, we have demonstrated a clear and strong photothermoelectric effect arising from the large mismatch between the Seebeck coefficients of the MoS₂ and of the electrodes. Furthermore, the identical qualitative characteristics of the photocurrent images for above bandgap illumination suggests that the photothermal effect is also the dominant mechanism for photocurrent generation here as well, and that photovoltaic effects seem not to play a significant role. We estimated the Seebeck coefficient for single-layer MoS₂, finding a large value which can be tuned by an external electric field between $-4 \cdot 10^2 \mu\text{V K}^{-1}$ and $-1 \cdot 10^5 \mu\text{V K}^{-1}$. This value is 70-25000 times larger than the values reported for graphene. From these results, we expect that single-layer MoS₂ could be an interesting complement to graphene in applications requiring a material with a large and tunable Seebeck coefficient, such as thermoelectric nanodevices or energy harvesting.

We acknowledge the support from the European Union (FP7) through the program RODIN and the Dutch organization for Fundamental Research on Matter (FOM).

6.6. SUPPORTING INFORMATION

6.6.1. MATERIALS AND METHODS

We prepare MoS₂ nanosheets on SiO₂/Si substrates by mechanical exfoliation of natural MoS₂ (SPI Supplies, 429ML-AB) with blue Nitto tape (Nitto Denko Co., SPV 224P). For a detailed description of the fabrication procedures see Appendix A

To increase the charge carrier mobility in the flakes prior to electrical characterization, the samples were annealed at 300 °C for two hours in an Ar/H₂ flow (with a flow rate of 500 sccm/100 sccm). The basic electronic transport characterization of the MoS₂ FETs is performed at room temperature under high vacuum ($< 1 \cdot 10^{-5}$ mbar) in a Lakeshore Cryogenics probestation. The scanning photocurrent microscopy is

carried out in vacuum at room temperature in a homebuilt confocal microscope setup with an objective with $\text{NA}=0.8$ and a telecentric optical system, equipped with electrically movable mirrors. The excitation was provided by a continuous wave (CW) solid state laser ($\lambda = 532 \text{ nm}$) and by a supercontinuum white-light source (Fianium Ltd) equipped with an acousto-optical tuneable filter (AOTF).

6.6.2. RAMAN SPECTROSCOPY DATA

To confirm the number of layers in the selected MoS_2 flakes, Raman microscopy is performed with a micro-Raman spectrometer (Renishaw in via RM 2000) in backscattering configuration excited with a visible laser ($\lambda = 514 \text{ nm}$) as in ref [28]. Figure 6.6(a) shows a collection of the Raman spectra recorded for different MoS_2 flakes deposited on the chip and bulk MoS_2 . As expected, the difference between the energy of the peaks labeled E_{2g}^1 and A_{1g}^1 increases monotonically with thickness of the flake, and, therefore, it has been employed to estimate the number of layers in the flake. Figure 6.6(b) and (c) show optical images of the FETs characterized in the present work. The circles in Figure 6.6(b) indicate the positions where the Raman spectra were recorded. The spectra designated by 1L and 2L show a difference in the energies of the E_{2g}^1 and A_{1g}^1 peaks of 19 cm^{-1} and 21 cm^{-1} respectively. These values are in agreement, respectively, with single-layer and bilayer-layer MoS_2 spectra previously reported in literature.[22]

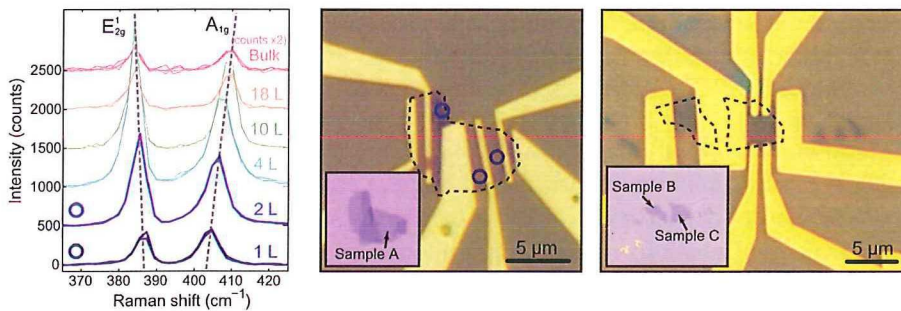


FIGURE 6.6: (a) Raman spectra of various MoS_2 flakes deposited on the chip. The blue circles refer to the location in panel (b) (traces in lighter color have been obtained in other MoS_2 flakes, not used to fabricate the devices studied in this work). (b,c) Optical image of the fabricated FETs. The circles indicate the location where the indicated Raman spectra in panel (a) were collected.

6.6.3. LASER-INDUCED TEMPERATURE INCREASE ESTIMATION

To calculate the Seebeck coefficient with equation 6.1, it is necessary to estimate the temperature difference between the Au electrode and the MoS_2 flake induced by the laser heating. The heat transfer process was simulated using a commercially available

Finite Element Method (FEM) software package. The system is modelled as presented (out of scale for clarity) in Figure 6.7(a): a cross section of a single-layer MoS₂ FET which is symmetric around the axis of the incident laser beam (z axis). The axial symmetry allows one to reduce the amount of mesh elements needed for a precise solution, while ensuring a reasonable solution time.

Note that the roughness of the electrode, as determined with Atomic Force Microscopy is around 5 nm, much smaller than the excitation wavelength, and therefore does not play a role in the laser absorption by the electrodes. The material properties used for the simulation are listed in Table S1. The incident laser power density is calculated from the measured power assuming a diffraction limited spot ($R_{\text{spot}} \sim 500$ nm for $\lambda = 750$ nm), a 68% transmission through the objective and the absorption through the thickness of the material according to $I = I_0 \cdot (1 - \exp(-\alpha d))$ where α is the absorption coefficient of the Au/Ti electrode and d is its thickness ($\alpha \sim 5.5 \cdot 10^5 \text{ cm}^{-1}$ and $d = 55$ nm). We assume that all the incident laser power is converted into heat. The boundary conditions are as follows: symmetry around the z axis ($r = 0$), incoming heat flux density on the area of the spot size equal to the optical power density calculated above, free heat outlet for the SiO₂ and Si free boundaries (as their in-plane size is much bigger than the one of the MoS₂ and the electrodes), room temperature fixed at the bottom of the silicon chip. This is reasonable since the bottom is in good thermal contact with the chip carrier and the cryostat that can be modelled as a thermal bath at constant temperature due to the much bigger mass. Radiation from the other surfaces is neglected.

The calculations are performed in the time domain and the results are presented in Figure 6.7(b) for the two points highlighted by the green circles in Figure 6.7(a): one on top of the gold electrode and one on top of the MoS₂ layer far from the gold electrode. After 10 ms the system is in steady state and the temperature difference between the electrode and the MoS₂ flake is around 0.13 K. The time to reach steady state is lower than the laser spot dwell time during the SPCM measurements, therefore the system can be considered to be in steady state when the measurements are performed. Figure 6.7(c) shows the result of FEM simulations of the temperature difference between the top of the Au electrode and the MoS₂ flake as a function of the flake thickness. The temperature difference increases linearly with the flake thickness. Referring to equation 6.1 in the main text, the potential difference ΔV_{PTE} is proportional to the temperature difference. In Figure 6.2(b,c), the MoS₂ underneath the electrode number 3 is multi-layered, which would explain the increased measured photocurrent when the laser is scanned over the electrode. Moreover, this can explain why the photocurrent inside electrode 3 in Figure 6.2(c) is larger than the one measured in Figure 6.3(a,c) where the flake is a single layer.

We also perform a simulation without the MoS₂ flake, therefore allowing direct contact between the Au/Ti electrode and the SiO₂ substrate. The temperature difference is calculated between the top of the Au electrode and a point on the surface of

	d (nm)	ρ (J m^{-3})	C ($\text{J kg}^{-1} \text{K}^{-1}$)	k ($\text{W m}^{-1} \text{K}^{-1}$)
Au	50	19300	128.74	315
Ti	5	4500	540	21.9
MoS ₂	1	5000	400	1.8
SiO ₂	285	2650	1000	1.38
Si	500000	2330	710	149

TABLE 6.1: Material properties values employed for thermal gradient estimation

the SiO₂ at the same distance of the edge of the flake. The temperature difference in this configuration is around 2 mK lower, indicating the thermal sinking effect of the SiO₂ substrate.

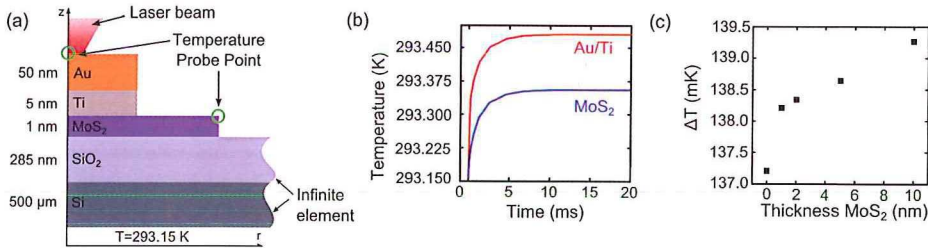


FIGURE 6.7: (a) Schematic of the modelled system. The system is a 2D cross section of a single layer MoS₂ device and is symmetric around the z axis which is the center of the incoming laser beam. The drawing is out of scale for clarity. (b) Results of the FEM simulation in the time domain for two points: one over the Au electrode, one over the MoS₂ flake. (c) Difference in temperature between the Au electrode and the MoS₂ flake in steady state as a function of the MoS₂ flake thickness

REFERENCES

- [1] M. Buscema, M. Barkelid, V. Zwiller, H. S. J. van der Zant *et al.*, *Large and Tunable Photothermoelectric Effect in Single-Layer MoS₂*, *Nano Lett.* **13** 358 (2013).
- [2] K. S. Novoselov, A. K. Geim, S. V. Morozov, D. Jiang *et al.*, *Electric Field Effect in Atomically Thin Carbon Films*, *Science* **306** 666 (2004), <http://www.sciencemag.org/content/306/5696/666.full.pdf>.
- [3] K. S. Novoselov, A. K. Geim, S. V. Morozov, D. Jiang *et al.*, *Two-dimensional gas of massless Dirac fermions in graphene*, *Nature* **438** 197 (2005).
- [4] K. S. Novoselov, D. Jiang, F. Schedin, T. J. Booth *et al.*, *Two-dimensional atomic crystals*, *Proceedings of the National Academy of Sciences of the United States of America* **102** 10451 (2005).
- [5] J. N. Coleman, M. Lotya, A. O'Neill, S. D. Bergin *et al.*, *Two-Dimensional Nanosheets Produced by Liquid Exfoliation of Layered Materials*, *Science* **331** 568 (2011).
- [6] A. Ayari, E. Cobas, O. Ogundadegbe and M. S. Fuhrer, *Realization and electrical characterization of ultrathin crystals of layered transition-metal dichalcogenides*, *J. Appl. Phys.* **101** 014507 (2007).
- [7] B. Radisavljevic, A. Radenovic, J. Brivio, V. Giacometti *et al.*, *Single-layer MoS₂ transistors*, *Nature Nanotechnology* **6** 147 (2011).

- [8] K. F. Mak, C. Lee, J. Hone, J. Shan *et al.*, *Atomically Thin MoS₂: A New Direct-Gap Semiconductor*, Phys. Rev. Lett. **105** 136805 (2010).
- [9] A. Splendiani, L. Sun, Y. Zhang, T. Li *et al.*, *Emerging Photoluminescence in Monolayer MoS₂*, Nano Letters **10** 1271 (2010).
- [10] G. Eda, H. Yamaguchi, D. Voiry, T. Fujita *et al.*, *Photoluminescence from Chemically Exfoliated MoS₂*, Nano Lett. **11** 5111 (2011).
- [11] S. Bertolazzi, J. Brivio and A. Kis, *Stretching and Breaking of Ultrathin MoS₂*, ACS Nano **5** 9703 (2011).
- [12] A. Castellanos-Gomez, M. Poot, G. A. Steele, H. S. J. van der Zant *et al.*, *Elastic Properties of Freely Suspended MoS₂ Nanosheets*, Adv. Mater. **24** 772 (2012).
- [13] H. Li, Z. Yin, Q. He, H. Li *et al.*, *Fabrication of Single- and Multilayer MoS₂ Film-Based Field-Effect Transistors for Sensing NO at Room Temperature*, Small **8** 63 (2012).
- [14] J. Pu, Y. Yomogida, K.-K. Liu, L.-J. Li *et al.*, *Highly Flexible MoS₂ Thin-Film Transistors with Ion Gel Dielectrics*, Nano Lett. **12** 4013 (2012).
- [15] Q. He, Z. Zeng, Z. Yin, H. Li *et al.*, *Fabrication of Flexible MoS₂ Thin-Film Transistor Arrays for Practical Gas-Sensing Applications*, Small **8** 2994 (2012).
- [16] Z. Yin, H. Li, H. Li, L. Jiang *et al.*, *Single-Layer MoS₂ Phototransistors*, ACS Nano **6** 74 (2012).
- [17] H. S. Lee, S.-W. Min, Y.-G. Chang, M. K. Park *et al.*, *MoS₂ Nanosheet Phototransistors with Thickness-Modulated Optical Energy Gap*, Nano Lett. **12** 3695 (2012).
- [18] W. Choi, M. Y. Cho, A. Konar, J. H. Lee *et al.*, *High-Detectivity Multilayer MoS₂ Phototransistors with Spectral Response from Ultraviolet to Infrared*, Adv. Mater. **24** 5832 (2012).
- [19] M. Fontana, T. Deppe, A. K. Boyd, M. Rinzan *et al.*, *Electron-hole transport and photovoltaic effect in gated MoS₂ Schottky junctions*, Scientific Reports **3** (2013).
- [20] M. Shanmugam, C. A. Durcan and B. Yu, *Layered semiconductor molybdenum disulfide nanomembrane based Schottky-barrier solar cells*, Nanoscale – (2012).
- [21] A. Castellanos-Gomez, N. Agrait and G. Rubio-Bollinger, *Optical identification of atomically thin dichalcogenide crystals*, Appl. Phys. Lett. **96** 213116 (2010).
- [22] C. Lee, H. Yan, L. E. Brus, T. F. Heinz *et al.*, *Anomalous Lattice Vibrations of Single- and Few-Layer MoS₂*, ACS Nano **4** 2695 (2010).
- [23] T. Korn, S. Heydrich, M. Hirmer, J. Schmutzler *et al.*, *Low-temperature photocarrier dynamics in monolayer MoS₂*, Applied Physics Letters **99** (2011).
- [24] D. J. Late, B. Liu, H. S. S. R. Matte, C. N. R. Rao *et al.*, *Rapid Characterization of Ultrathin Layers of Chalcogenides on SiO₂/Si Substrates*, Adv. Funct. Mater. **22** 1894 (2012).
- [25] S. Das, H.-Y. Chen, A. V. Penumatcha and J. Appenzeller, *High Performance Multilayer MoS₂ Transistors with Scandium Contacts*, Nano Lett. – (2012).
- [26] I. Popov, G. Seifert and D. Tománek, *Designing Electrical Contacts to MoS₂ Monolayers: A Computational Study*, Phys. Rev. Lett. **108** 156802 (2012).
- [27] S. Ghatak, A. N. Pal and A. Ghosh, *Nature of Electronic States in Atomically Thin MoS₂ Field-Effect Transistors*, ACS Nano **5** 7707 (2011).
- [28] A. Castellanos-Gomez, M. Barkelid, A. M. Goossens, V. E. Calado *et al.*, *Laser-Thinning of MoS₂: On Demand Generation of a Single-Layer Semiconductor*, Nano Lett. **12** 3187 (2012).
- [29] H. Liu and P. Ye, *MoS₂ Dual-Gate MOSFET With Atomic-Layer-Deposited Al₂O₃ as Top-Gate Dielectric*, Electron Device Letters, IEEE **33** 546 (2012).
- [30] G. Buchs, M. Barkelid, S. Bagiante, G. A. Steele *et al.*, *Imaging the formation of a p-n junction in a suspended carbon nanotube with scanning photocurrent microscopy*, Journal of Applied Physics **110** (2011).
- [31] F. Xia, T. Mueller, R. Golizadeh-Mojarad, M. Freitag *et al.*, *Photocurrent Imaging and Efficient Photon Detection in a Graphene Transistor*, Nano Lett. **9** 1039 (2009).
- [32] J. Park, Y. H. Ahn and C. Ruiz-Vargas, *Imaging of Photocurrent Generation and Collection in Single-Layer Graphene*, Nano Lett. **9** 1742 (2009).
- [33] Y. Ahn, J. Dunning and J. Park, *Scanning Photocurrent Imaging and Electronic Band Studies in Silicon Nanowire Field Effect Transistors*, Nano Lett. **5** 1367 (2005).
- [34] Y. H. Ahn, A. W. Tsen, B. Kim, Y. W. Park *et al.*, *Photocurrent Imaging of p-n Junctions in Ambipolar*

- Carbon Nanotube Transistors*, Nano Lett. 7 3320 (2007).
- [35] K. Balasubramanian, M. Burghard, K. Kern, M. Scolari *et al.*, *Photocurrent imaging of charge transport barriers in carbon nanotube devices*, Nano letters 5 507 (2005).
- [36] M. Freitag, J. C. Tsang, A. Bol, D. Yuan *et al.*, *Imaging of the Schottky barriers and charge depletion in carbon nanotube transistors*, Nano letters 7 2037 (2007).
- [37] X. Xu, N. M. Gabor, J. S. Alden, A. M. van der Zande *et al.*, *Photo-Thermoelectric Effect at a Graphene Interface Junction*, Nano Lett. 10 562 (2009).
- [38] N. M. Gabor, J. C. W. Song, Q. Ma, N. L. Nair *et al.*, *Hot Carrier Assisted Intrinsic Photoresponse in Graphene*, Science 334 648 (2011).
- [39] J. C. W. Song, M. S. Rudner, C. M. Marcus and L. S. Levitov, *Hot Carrier Transport and Photocurrent Response in Graphene*, Nano Lett. 11 4688 (2011).
- [40] B. C. St-Antoine, D. Mènard and R. Martel, *Photothermoelectric effects in single-walled carbon nanotube films: Reinterpreting scanning photocurrent experiments* 5 73 (2012).
- [41] D. Sun, G. Aivazian, A. M. Jones, J. S. Ross *et al.*, *Ultrafast hot-carrier-dominated photocurrent in graphene*, Nature Nanotechnology 7 114 (2012).
- [42] N. Mott and H. Jones, *The theory of the properties of metals and alloys*, The Clarendon Press (1936).
- [43] Bhushan, *Springer Handbook of Nanotechnology* – (2007).
- [44] J. P. Heremans, V. Jovic, E. S. Toberer, A. Saramat *et al.*, *Enhancement of Thermoelectric Efficiency in PbTe by Distortion of the Electronic Density of States*, Science 321 554 (2008).
- [45] G. Nolas, J. Sharp and H. Goldsmid, *Thermoelectrics: Basic Principles and New Materials Developments*, Springer (2001).
- [46] R. Mansfield and S. A. Salam, *Electrical Properties of Molybdenite*, Proceedings of the Physical Society, Section B 66 377 (1953).
- [47] J. H. Seol, I. Jo, A. L. Moore, L. Lindsay *et al.*, *Two-Dimensional Phonon Transport in Supported Graphene*, Science 328 213 (2010).
- [48] K. L. Grosse, M.-H. Bae, F. Lian, E. Pop *et al.*, *Nanoscale Joule heating, Peltier cooling and current crowding at graphene-metal contacts*, Nat Nano 6 287 (2011).
- [49] Z. Wang, R. Xie, C. T. Bui, D. Liu *et al.*, *Thermal Transport in Suspended and Supported Few-Layer Graphene*, Nano Lett. 11 113 (2010).
- [50] J. P. Small, K. M. Perez and P. Kim, *Modulation of Thermoelectric Power of Individual Carbon Nanotubes*, Phys. Rev. Lett. 91 256801 (2003).
- [51] K. P. Pernstich, B. Rossner and B. Batlogg, *Field-effect-modulated Seebeck coefficient in organic semiconductors*, Nat Mater 7 321 (2008).
- [52] J. Fleurial, L. Gailliard, R. Triboulet, H. Scherrer *et al.*, *Thermal properties of high quality single crystals of bismuth telluride—Part I: Experimental characterization*, Journal of Physics and Chemistry of Solids 49 1237 (1988).
- [53] A. L. Bassi, A. Bailini, C. S. Casari, F. Donati *et al.*, *Thermoelectric properties of Bi-Te films with controlled structure and morphology*, J. Appl. Phys. 105 124307 (2009).
- [54] F. Song, L. Wu and S. Liang, *Giant Seebeck coefficient thermoelectric device of MnO₂ powder*, Nanotechnology 23 085401 (2012).
- [55] R. Gardner, F. Sweett and D. Tanner, *The electrical properties of alpha ferric oxide (II): Ferric oxide of high purity*, Journal of Physics and Chemistry of Solids 24 1183 (1963).
- [56] L. E. Bell, *Cooling, Heating, Generating Power, and Recovering Waste Heat with Thermoelectric Systems*, Science 321 1457 (2008).
- [57] I. Chowdhury, R. Prasher, K. Lofgreen, G. Chrysler *et al.*, *On-chip cooling by superlattice-based thin-film thermoelectrics*, Nat Nano 4 235 (2009).
- [58] W. Liang, A. I. Hochbaum, M. Fardy, O. Rabin *et al.*, *Field-Effect Modulation of Seebeck Coefficient in Single PbSe Nanowires*, Nano Lett. 9 1689 (2009).
- [59] H. Ohta, Y. Masuoka, R. Asahi, T. Kato *et al.*, *Field-modulated thermopower in SrTiO₃-based field-effect transistors with amorphous [12 CaO] · [7 Al₂O₃] glass gate insulator*, Appl. Phys. Lett. 95 113505 (2009).

CHAPTER 7

FAST AND BROADBAND PHOTORESPONSE OF FEW-LAYER BLACK PHOSPHOROUS PHOTO TRANSISTORS

Michele Buscema*, Dirk J. Groenendijk, Sofya I. Blanter, Gary A. Steele,
Herre S.J. van der Zant and Andres Castellanos-Gomez*

Few-layer black phosphorus, a new elemental 2D material recently isolated by mechanical exfoliation, is a high-mobility layered semiconductor with a direct bandgap that is predicted to strongly depend on the number of layers, from 0.35 eV (bulk) to 2.0 eV (single-layer). Therefore, black phosphorus is an appealing candidate for tunable photodetection from the visible to the infrared part of the spectrum. We study the photoresponse of field-effect transistors (FETs) made of few-layer black phosphorus (3 nm to 8 nm thick), as a function of excitation wavelength, power and frequency. In the dark state, the black phosphorus FETs can be tuned both in hole and electron doping regimes allowing for ambipolar operation. We measure mobilities in the order of $100 \text{ cm}^2 \text{ V}^{-1} \text{ s}^{-1}$ current ON/OFF ratio larger than $1 \cdot 10^3$. Upon illumination, the black phosphorus transistors show response to excitation wavelengths from the visible up to 940 nm and rise time of about 1 ms, demonstrating broadband and fast detection. The responsivity reaches 4.8 mA W^{-1} . The ambipolar behavior coupled to the fast and broadband photodetection make few-layer black phosphorus a promising 2D material for photodetection across the visible and near-infrared part of the electromagnetic spectrum.

Parts of this chapter have been published in Nano Letters 14, 3347 (2014) [1].

7.1. INTRODUCTION

Since the discovery of graphene,[2, 3] the research effort on 2D materials has rapidly increased, driven by their extraordinary optical, electrical and mechanical properties.[4, 5] In fact, graphene, a single layer of carbon atoms arranged in a honeycomb lattice, has shown extremely high mobilities and impressively high breaking strength.[6, 7] However, the absence of a bandgap in graphene reduces its applicability in semiconducting and optoelectronic devices. This has triggered substantial research interest in other 2D materials with an intrinsic bandgap.[4] Silicene, a 2D layer of silicon atoms, has been considered as semiconducting counterpart of graphene but its environmental stability represents a key issue for further studies and its applicability.[8]

Among the studied 2D semiconductors, the large family of the transition metal dichalcogenides (TMDCs) shows promising properties for optoelectronic applications due to the direct bandgap and strong absorption.[9–13] However, these materials have demonstrated relatively slow photoresponse and, because of the large bandgap of Mo- and W-based compounds, they are suited for applications in only part of the visible range of the electromagnetic spectrum. A material with a direct and small bandgap together with fast photoresponse is needed to extend the detection range accessible with 2D materials.

Recently, a new elemental 2D material has been isolated by mechanical cleavage of black phosphorus crystals, a layered allotrope of the element phosphorus.[14–17] In bulk, black phosphorus is a semiconductor with a direct bandgap of 0.35 eV and mobilities in the order of $10\,000\text{ cm}^2\text{ V}^{-1}\text{ s}^{-1}$. [18] Exfoliated black phosphorus flakes have been recently used as channel material in field-effect transistors (FETs) showing mobility values up to $1000\text{ cm}^2\text{ V}^{-1}\text{ s}^{-1}$. [14, 17] Moreover, the small and direct bandgap opens the door to application of black phosphorus for broadband photodetection where TMDCs are limited because of their large bandgap.

In this Chapter, we fabricate few-layer black phosphorus (b-P) field-effect transistors and study their optoelectronic properties as photodetectors. In the dark state, the b-P FETs present ambipolar behavior with mobilities of about $100\text{ cm}^2\text{ V}^{-1}\text{ s}^{-1}$ and current ON/OFF ratios larger than $1 \cdot 10^3$ for holes and $0.5\text{ cm}^2\text{ V}^{-1}\text{ s}^{-1}$ and 10 for electrons. Upon illumination, the b-P FETs show photoresponse reaching 4.8 mA W^{-1} in the visible and extending up to wavelengths in the near-infrared (940 nm). Furthermore, the b-P photodetector shows time response of 1 ms (rise) and 4 ms (fall). These properties make few-layer black phosphorus a promising active 2D material in broadband and fast photodetectors across the visible and near-infrared.

7.2. FABRICATION AND ELECTRICAL CHARACTERIZATION

We isolate few-layer b-P on a SiO_2 (285 nm)/Si substrate via a modified version of the mechanical exfoliation method.[19] We fabricate b-P based FETS by standard e-beam

lithography, metal deposition (Ti/Au 5/50 nm) and lift-off in warm acetone. In Figure 7.1a we show an optical micrograph of the fabricated b-P FET. The metallic leads were patterned after selection of thin regions in the flake by optical contrast.[20] The topography of the fabricated devices is studied by atomic force microscopy (Figure 7.1b). The measured height of the flake shown in Figure 7.1b is 8 nm, corresponding to 15 layers of b-P. Figure 7.1c shows a Raman spectrum of the flake in which the three peaks characteristic for pristine black phosphorus can clearly be identified.[21] We performed electrical characterization in dark and under light excitation in a probe station at room temperature and in vacuum ($1 \cdot 10^{-5}$ mbar). Figure 7.1d shows a schematic of the b-P FET and the measurement circuit.

In Figure 7.2 we present the electrical characterization (dark) of the device shown in Figure 7.1. The six studied devices display similar behavior. The two-terminal transfer characteristics ($I_{ds} - V_g$ at different fixed V_{ds}) in Figure 7.2a show large currents at negative gate values that decrease to a minimum value at small positive gate voltages and followed by a shallow increase as the gate is swept toward more positive voltages. The inset of Figure 7.2a shows the data in a linear scale. The measured transfer characteristics describe the typical behavior of an ambipolar transistor and demonstrate that b-P FETs can operate in both holes and electron doping regimes by simply controlling the gate electric field, unlike MoS_2 -based transistors.[22, 23]

The current minimum (flatband condition, V_{FB}) is reached at $V_g \sim 10$ V, indicating that the natural doping of this b-P device is p-type and that the bands at $V_g = 0$ V are curved upwards at the contacts, facilitating hole conduction. In the hole doping regime, the current levels can be tuned by more than 3 orders of magnitude, displaying OFF currents around hundreds of pA and ON currents of a few hundreds of nA. Lower values of ON currents are achieved for electron injection. The difference in current levels between p- and n-type operation can be explained by the band alignment imposed by the work function of the contacts that generates a small (large) Schottky barrier for hole (electron) injection (Figure 7.2d). From the measured transconductance, by employing the formula

$$\mu_{FE} = \frac{dI_{ds}}{dV_g} \frac{L}{W} \frac{1}{C_{ox} \cdot V_{ds}}, \quad (7.1)$$

where L and W are the channel length and width respectively and C_{ox} is the capacitance of the gate oxide,[24] we extract mobilities (μ_{FE}) of about $100 \text{ cm}^2 \text{ V}^{-1} \text{ s}^{-1}$ for hole transport and $0.5 \text{ cm}^2 \text{ V}^{-1} \text{ s}^{-1}$ for electron transport without performing any cleaning or annealing process after fabrication. We note that these values represent a lower bound as the measurements were performed in two-terminal configuration, thus including the contact resistance.

The mobility values compare well with recent measurements on similar, ultra-thin b-P samples.[14–17, 25] Figure 7.2b and Figure 7.2c display the measured output characteristics ($I_{ds} - V_{ds}$ curves at fixed V_g) for hole and electron doping, respectively.

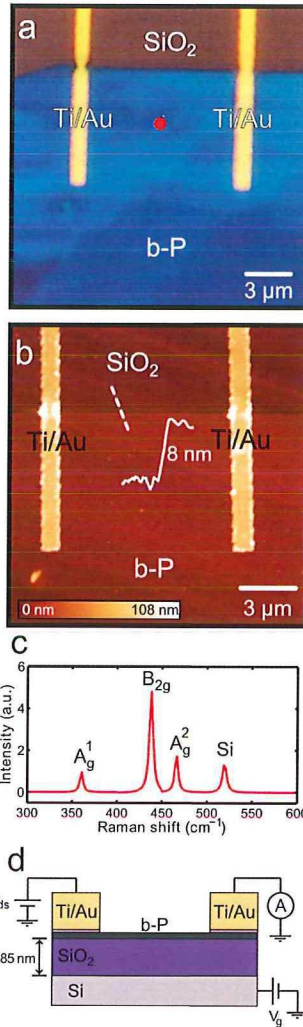


FIGURE 7.1: (a) Optical image of the black-phosphorus (b-P) based FET. The flake is located on a SiO_2/Si substrate and is contacted by Au electrodes with Ti adhesion layer. (b) Atomic force microscopy (AFM) topography of the b-P based FET presented in panel (a). (c) Raman spectrum of the few-layer b-P taken at the position of the red dot in panel (a). (d) Schematics of the b-P based FET and the circuit used to perform two-terminal electrical measurements.

The $I_{ds} - V_{ds}$ curves are linear and symmetric in both cases, indicating that the Ti/Au electrodes make ohmic contact to the b-P flake. In the p-doped region ($V_g < V_{FB}$), a large current flows when applying a small bias voltage. This can be explained by having a small and thin Schottky barrier at the metal/b-P interface (Figure 7.2e). For electron doping ($V_g > V_{FB}$), only a small current flows through the device under bias, indicating a larger contact resistance (Figure 7.2f). We note that the transfer characteristics are shifted towards more positive V_g values by either performing consecutive gate sweeps

(Figure S2a) or applying a constant gate voltage in time (Figure S2b). Moreover, the devices relax toward their pristine behavior if the gate is grounded for a long time (Figure S2b). These signatures suggest that the gate electric field is also promoting a slowly decaying charge transfer from either charged states at the $\text{SiO}_2/\text{b-P}$ interface or adsorbates on the b-P flake, as also observed in other nanodevices.[26–29] In the remainder of this Letter, we will discuss measurements performed at $V_g = 0$ V so that the gate-induced stress will not affect the measured data.

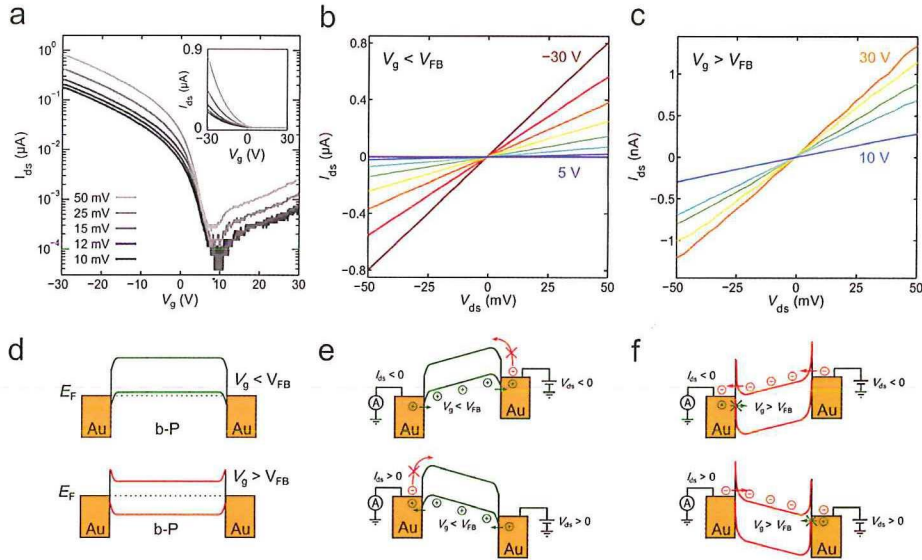


FIGURE 7.2: (a) Semi-log plot of the source-drain current (I_{ds}) versus gate voltage (V_g) characteristics of the b-P based FET measured at the indicated source-drain voltages (V_{ds}). The inset shows the same measurements on a linear scale. (b) I_{ds} versus V_{ds} characteristics measured at gate voltages below the flatband condition ($V_{FB} \sim 10$ V) in steps of 5 V. (c) Source-drain current versus source-drain voltage characteristics measured above the flatband condition ($V_{FB} \sim 10$ V) in steps of 5 V. (d) Band diagram at zero source-drain bias showing a cartoon of the Schottky barriers at the contacts for gate voltages below and above the flatband condition. E_F denotes the Fermi energy. The bands are drawn for $V_g < V_{FB}$ (green lines) and for $V_g > V_{FB}$ (red line). (e) Band diagram at $V_g < V_{FB}$ for negative (top) and positive (bottom) source-drain voltage. (f) Band diagram at positive $V_g > V_{FB}$ for negative (top) and positive (bottom) source-drain voltage.

7.3. PHOTORESPONSE

We now turn our attention to the photoresponse of the fabricated b-P FETs. The measurements are carried out by mechanically modulating the intensity of the incoming light and recording the current under constant $V_{ds} = 200$ mV and zero gate bias. The laser spot waist is 230 ± 8 μm for all wavelengths and covers the whole device area.

Figure 7.3(a) shows the measured current for 940 nm, 885 nm and 640 nm excitation. The photocurrent is in phase with the excitation modulation and decreases with increasing wavelength. The clear response to excitation wavelengths up to 940 nm shows that it is still possible to photoexcite carriers over the b-P bandgap with low energy photons (1.34 eV) and extract them with a small bias voltage. Moreover, this demonstrates that b-P based devices can be operated in the near-infrared (NIR) part of the spectrum, unlike photodetectors based on other layered materials that are usually operated in the visible or ultraviolet due to their larger bandgap. [9, 11, 30–34]

The responsivity (R) is calculated by dividing the photocurrent (I_{photo} , $I_{\text{photo}} = I_{\text{illum.}} - I_{\text{dark}}$) by the power incident on the device area (P_{d} , $P_{\text{d}} = P_{\text{in}} \cdot \frac{A_{\text{device}}}{A_{\text{spot}}}$, where P_{in} is the total optical power, A_{device} is the area of the device and A_{spot} is the area of the laser spot). Figure 7.3b shows that the responsivity increases as the excitation wavelength is decreased. The other measured devices show similar behavior (Figure S6). Since the measurements were conducted at the same incident power for all the different wavelengths, the increase in responsivity could be due to an increase in the optical absorption of the material at shorter wavelengths. By linearly fitting the data, we can estimate the wavelength where the responsivity is zero; we find this cut-off wavelength ($\lambda_{\text{cut-off}}$) to be around 997 nm (1.24 eV). The $\lambda_{\text{cut-off}}$ value is larger than previously reported photodetectors based on MoS_2 , [9, 30, 35] WS_2 , [36] GaSe [37] and GaS [33] indicating that b-P can be used as active material for broadband photodetection. Moreover, the bandgap predicted by DFT calculations (from 0.33 eV to 0.81 eV) [15, 38] for this thickness of b-P is much smaller than our estimate of the cut-off wavelength. Further studies with excitation by lower energy photons should be carried out to measure the photoresponse up to the b-P optical absorption edge.

We further characterize the b-P based phototransistor by varying the excitation power at a fixed excitation wavelength ($\lambda = 640$ nm, Figure 7.3c). The photocurrent increases sublinearly with increasing intensity and it reaches a few nA at high excitation powers (Figure S7). We measure responsivities (R) up to 4.8 mA W^{-1} with small source-drain bias ($V_{\text{ds}} = 200$ mV). The measured responsivity decreases with increasing excitation power (Figure 7.3d). The responsivity vs. incident optical power relationship can be modeled by a power law of the following type

$$R \propto P_{\text{d}}^{(\alpha-1)}. \quad (7.2)$$

By fitting the data with equation 7.2, we extract $\alpha \sim 0.7$, indicating that the recombination kinetics of photocarriers involves both trap states and interactions between the photogenerated carriers. [39, 40] The decrease in responsivity with incident optical power is commonly observed in photodetectors based on other nanostructured materials, such as MoS_2 , [11, 30] and colloidal quantum dots. [41, 42] This effect can be associated with a reduction of the number of photogenerated carriers available for extraction under high photon flux due to Auger processes or the saturation of recombination/trap states that influence the lifetime of the generated carriers. [40]

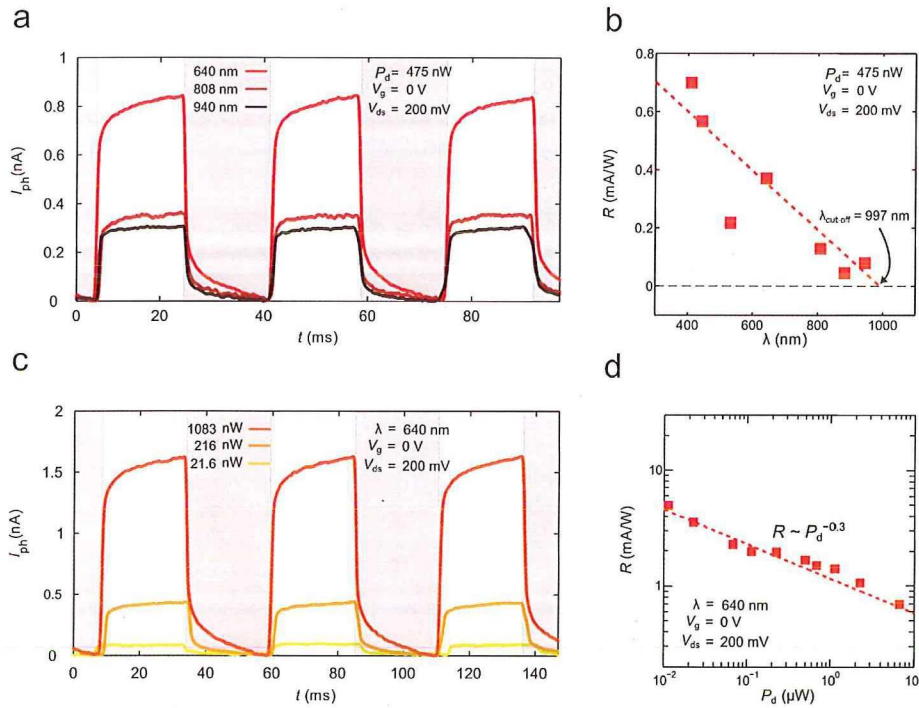


FIGURE 7.3: (a) Photocurrent as a function of time under modulated light excitation (~ 20 Hz) with different wavelengths. The shaded areas indicate the time when the light beam is blanketed by the mechanical chopper. Measurements are taken at the experimental conditions indicated in the panel. (b) Responsivity (R) vs. excitation wavelength (λ) at constant power (red squares). The dashed red line is a linear fit to the data. (c) Photocurrent as a function of time under modulated light excitation (~ 20 Hz) with different powers. (d) Responsivity (R) vs. power incident on the device P_d . The red squares represent the measured values while the dashed red line is a power law fit to the data.

7

7.4. TIME RESPONSE

By mechanically modulating the light intensity and recording the magnitude of I_{ds} as a function of time, we measure the speed of the device response to the incoming excitation. The b-P FETs show a remarkably fast response: from one period of light excitation (Figure 7.4a), we measure the 10-90 % rise and fall time to be 1 ms and 4 ms, respectively. We measure the amplitude of the photocurrent as a function of modulation frequency and power (Figure 7.4b). For the highest incident power ($P_d = 6.49 \mu$ W), the photocurrent amplitude decreases with increasing modulation frequency and reaches the -3 dB point at 3 kHz (experimental limit). Furthermore, as the incident power is reduced, the photocurrent decreases more slowly with the

modulation frequency, possibly indicating that the $f_{3\text{dB}}$ of the device is larger for lower excitation power. The reduction of $f_{3\text{dB}}$ at higher incident photon flux could be related to an increase in the rate of the recombination processes between photogenerated charge carriers, which is also consistent with the measured sublinear increase of the photocurrent with power.

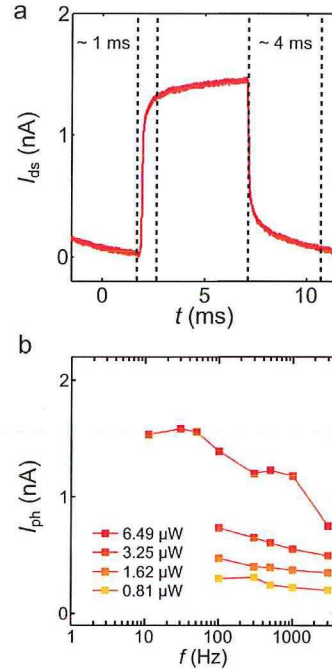


FIGURE 7.4: (a) Photocurrent measured in one period of modulation of the light intensity ($\lambda = 640$ nm, $P_{\text{d}} = 6.49$ μW , $V_{\text{ds}} = 100$ mV). We can estimate a rise (fall) time of 1 ms (4 ms). (b) Photocurrent as a function of the modulation frequency for different incident power levels.

7.5. COMPARISON WITH LITERATURE

In order to assess the performance of the fabricated b-P photodetector, we summarize in Table 7.1 the relevant figures of merit reported in literature for other devices based on semiconducting layered materials. The experimental conditions are also listed for ease of comparison. The measured small-bias responsivity of the fabricated b-P transistors is much larger than detector based on multilayer WS_2 . Other materials show higher responsivity values but much slower response times and limitation in the detection range. The combination of sizable ($R = 4.8$ mA W^{-1}), broadband ($\lambda_{\text{cut-off}} \sim 997$ nm) and fast ($\tau_{\text{rise}} \sim 1$ ms) photoresponse makes b-P a very promising material for photodetection with room for improvement through further device engineering.

Material	Measurement conditions				Responsivity R (mA W ⁻¹)	Rise time τ (ms)	Spectral range	Reference
	V_{ds} (V)	V_g (V)	λ (nm)	P (mW cm ⁻²)				
>1L b-P	0.2	0	640	$1.6 \cdot 10^1$	4.8	1	Visible - NIR	This work
1L MoS ₂	1	50	532	$8.0 \cdot 10^4$	7.5	$5 \cdot 10^1$	Visible	[9]
1L MoS ₂	8	-70	561	$2.4 \cdot 10^{-1}$	$8.8 \cdot 10^5$	$6 \cdot 10^2$	Visible	[30]
>1L MoS ₂	1	-2	633	$5.0 \cdot 10^1$	$1.1 \cdot 10^2$	$1 \cdot 10^3$	Visible - NIR	[35]
>1L WS ₂ (a)	30	0	458	2.0	$2.1 \cdot 10^{-2}$	5.3	Visible	[36]
>1L In ₂ Se ₃	5	0	300	$2.1 \cdot 10^{-1}$	$3.9 \cdot 10^5$	$1.8 \cdot 10^1$	UV - NIR	[34]
>1L GaTe	5	0	532	$3.0 \cdot 10^{-5}$	$1 \cdot 10^7$	6	Visible	[43]
>1L GaSe	5	0	254	1.0	$2.8 \cdot 10^3$	$3 \cdot 10^2$	UV - Visible	[37]
>1L GaS	2	0	254	$2.6 \cdot 10^{-2}$	$4.2 \cdot 10^3$	$3 \cdot 10^1$	UV - Visible	[33]

(a) P in mW

TABLE 7.1: Figures-of-merit for 2D-material-based photodetectors

7.6. CONCLUSION AND OUTLOOK

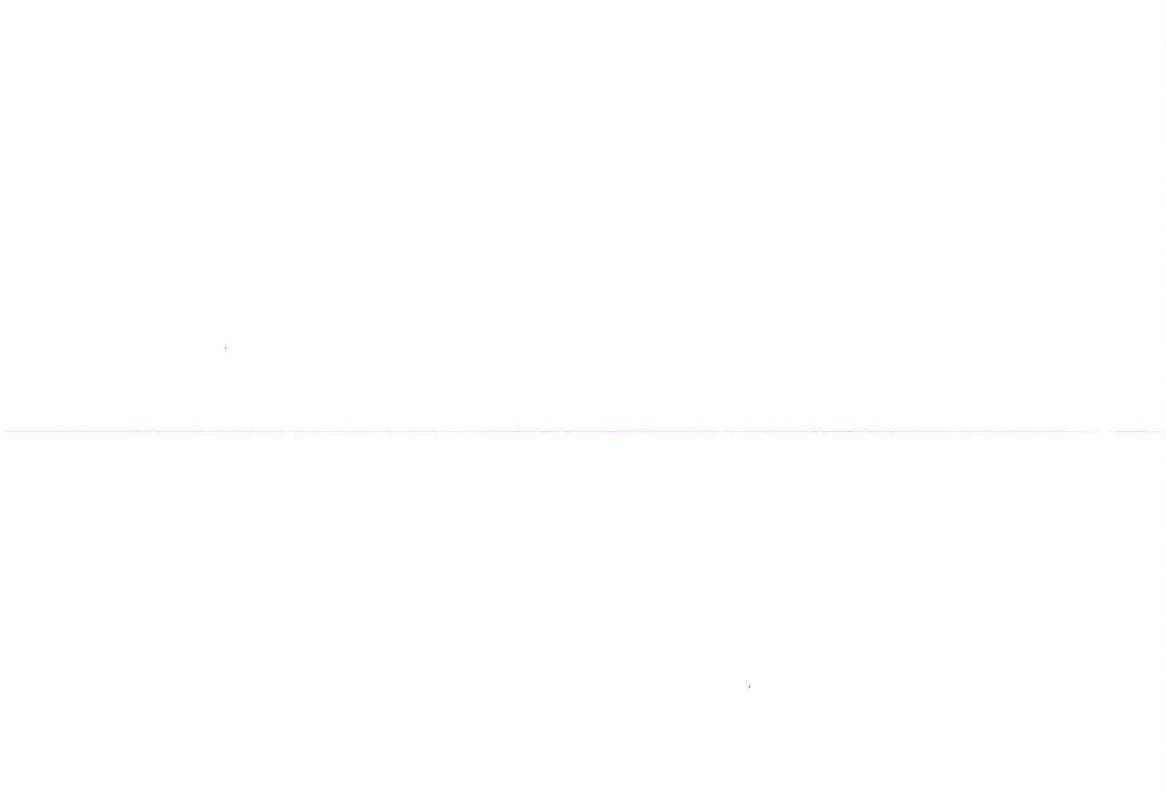
In conclusion, we have characterized the opto-electronic properties of b-P based FETs. In the dark state, the b-P FETs show ambipolar behavior and good mobility values in the hole doping regime. The ambipolarity opens the door to the realization of electrostatically defined PN junctions with great promise for both electronics and optoelectronics. We measure a broadband response to light excitation from the visible up to the NIR region, in contrast to photodetectors based on TMDCs and other semiconducting layered materials that are limited to the visible part of the spectrum. Our results show the potential of black phosphorus as active material for high-speed NIR detectors.

We acknowledge support by the European Union (FP7) through the program 9 RODIN and the Dutch organization for Fundamental Research on Matter (FOM). A.C-G. acknowledges financial support through the FP7-Marie Curie Project PIEF-GA-2011-300802 ('STRENGTHNANO').

REFERENCES

- [1] M. Buscema, D. J. Groenendijk, S. I. Blanter, G. A. Steele *et al.*, *Fast and Broadband Photoresponse of Few-Layer Black Phosphorus Field-Effect Transistors*, *Nano Lett.* **14** 3347 (2014).
- [2] K. S. Novoselov, A. K. Geim, S. V. Morozov, D. Jiang *et al.*, *Electric Field Effect in Atomically Thin Carbon Films*, *Science* **306** 666 (2004), <http://www.sciencemag.org/content/306/5696/666.full.pdf>.
- [3] K. S. Novoselov, A. K. Geim, S. V. Morozov, D. Jiang *et al.*, *Two-dimensional gas of massless Dirac fermions in graphene*, *Nature* **438** 197 (2005).
- [4] K. S. Novoselov, D. Jiang, F. Schedin, T. J. Booth *et al.*, *Two-dimensional atomic crystals*, *Proceedings of the National Academy of Sciences of the United States of America* **102** 10451 (2005).
- [5] Q. H. Wang, K. Kalantar-Zadeh, A. Kis, J. N. Coleman *et al.*, *Electronics and optoelectronics of two-dimensional transition metal dichalcogenides*, *Nat Nano* **7** 699 (2012).
- [6] L. Wang, I. Meric, P. Y. Huang, Q. Gao *et al.*, *One-Dimensional Electrical Contact to a Two-Dimensional Material*, *Science* **342** 614 (2013).
- [7] C. Lee, X. Wei, J. W. Kysar and J. Hone, *Measurement of the Elastic Properties and Intrinsic Strength of Monolayer Graphene*, *Science* **321** 385 (2008).
- [8] P. Vogt, P. De Padova, C. Quaresima, J. Avila *et al.*, *Silicene: Compelling Experimental Evidence for Graphenelike Two-Dimensional Silicon*, *Phys. Rev. Lett.* **108** 155501 (2012).
- [9] Z. Yin, H. Li, H. Li, L. Jiang *et al.*, *Single-Layer MoS₂ Phototransistors*, *ACS Nano* **6** 74 (2012).
- [10] M. Shanmugam, C. A. Durcan and B. Yu, *Layered semiconductor molybdenum disulfide nanomembrane based Schottky-barrier solar cells*, *Nanoscale* – (2012).
- [11] H. S. Lee, S.-W. Min, Y.-G. Chang, M. K. Park *et al.*, *MoS₂ Nanosheet Phototransistors with Thickness-Modulated Optical Energy Gap*, *Nano Lett.* **12** 3695 (2012).
- [12] M. Buscema, M. Barkelid, V. Zwiller, H. S. J. van der Zant *et al.*, *Large and Tunable Photothermoelectric Effect in Single-Layer MoS₂*, *Nano Lett.* **13** 358 (2013).
- [13] M. Fontana, T. Deppe, A. K. Boyd, M. Rinzan *et al.*, *Electron-hole transport and photovoltaic effect in gated MoS₂ Schottky junctions*, *Scientific Reports* **3** (2013).
- [14] F. Xia, H. Wang and Y. Jia, *Rediscovering black phosphorus as an anisotropic layered material for optoelectronics and electronics*, *Nat Commun* **5** (2014).
- [15] H. Liu, A. T. Neal, Z. Zhu, Z. Luo *et al.*, *Phosphorene: An Unexplored 2D Semiconductor with a High Hole Mobility*, *ACS Nano* **8** 4033 (2014).
- [16] J. Qiao, X. Kong, Z.-X. Hu, F. Yang *et al.*, *High-mobility transport anisotropy and linear dichroism in*

- few-layer black phosphorus*, Nat Commun 5 (2014).
- [17] L. Li, Y. Yu, G. J. Ye, Q. Ge *et al.*, *Black phosphorus field-effect transistors*, Nat Nano 9 372 (2014).
- [18] Y. Akahama, S. Endo and S.-i. Narita, *Electrical Properties of Black Phosphorus Single Crystals*, J. Phys. Soc. Jpn. 52 2148 (1983).
- [19] A. Castellanos-Gomez, M. Buscema, R. Molenaar, V. Singh *et al.*, *Deterministic transfer of two-dimensional materials by all-dry viscoelastic stamping*, 2D Materials 1 011002 (2014).
- [20] A. Castellanos-Gomez, E. Navarro-Moratalla, G. Mokry, J. Quereda *et al.*, *Fast and reliable identification of atomically thin layers of TaSe₂ crystals* 6 191 (2013).
- [21] A. Morita, *Semiconducting black phosphorus*, Applied Physics A 39 227 (1986).
- [22] B. Radisavljevic, A. Radenovic, J. Brivio, V. Giacometti *et al.*, *Single-layer MoS₂ transistors*, Nature Nanotechnology 6 147 (2011).
- [23] Y. J. Zhang, J. T. Ye, Y. Yomogida, T. Takenobu *et al.*, *Formation of a Stable p-n Junction in a Liquid-Gated MoS₂ Ambipolar Transistor*, Nano Lett. 13 3023 (2013).
- [24] S. Ghatak, A. N. Pal and A. Ghosh, *Nature of Electronic States in Atomically Thin MoS₂ Field-Effect Transistors*, ACS Nano 5 7707 (2011).
- [25] S. P. Koenig, R. A. Doganov, H. Schmidt, A. H. Castro Neto *et al.*, *Electric field effect in ultrathin black phosphorus*, Applied Physics Letters 104 (2014).
- [26] H. Wang, Y. Wu, C. Cong, J. Shang *et al.*, *Hysteresis of Electronic Transport in Graphene Transistors*, ACS Nano 4 7221 (2010).
- [27] R. B. M. Cross and M. De Souza, *The Effect of Gate-Bias Stress and Temperature on the Performance of ZnO Thin-Film Transistors*, Device and Materials Reliability, IEEE Transactions on 8 277 (2008).
- [28] A. Suresh and J. F. Muth, *Bias stress stability of indium gallium zinc oxide channel based transparent thin film transistors*, Applied Physics Letters 92 (2008).
- [29] D. Knipp, R. A. Street, A. Völkel and J. Ho, *Pentacene thin film transistors on inorganic dielectrics: Morphology, structural properties, and electronic transport*, Journal of Applied Physics 93 347 (2003).
- [30] O. Lopez-Sanchez, D. Lembke, M. Kayci, A. Radenovic *et al.*, *Ultrasensitive photodetectors based on monolayer MoS₂*, Nat Nano 8 497 (2013).
- [31] A. Pospischil, M. M. Furchi and T. Mueller, *Solar-energy conversion and light emission in an atomic monolayer p-n diode*, Nat Nano 9 257 (2014).
- [32] B. W. H. Baugher, H. O. H. Churchill, Y. Yang and P. Jarillo-Herrero, *Optoelectronic devices based on electrically tunable p-n diodes in a monolayer dichalcogenide*, Nat Nano 9 262 (2014).
- [33] P. Hu, L. Wang, M. Yoon, J. Zhang *et al.*, *Highly Responsive Ultrathin GaS Nanosheet Photodetectors on Rigid and Flexible Substrates*, Nano Lett. 13 1649 (2013).
- [34] R. B. Jacobs-Gedrim, M. Shanmugam, N. Jain, C. A. Durcan *et al.*, *Extraordinary Photoresponse in Two-Dimensional In₂Se₃ Nanosheets*, ACS Nano 8 514 (2013).
- [35] W. Choi, M. Y. Cho, A. Konar, J. H. Lee *et al.*, *High-Detectivity Multilayer MoS₂ Phototransistors with Spectral Response from Ultraviolet to Infrared*, Adv. Mater. 24 5832 (2012).
- [36] N. Perea-López, A. L. Elías, A. Berkdemir, A. Castro-Beltran *et al.*, *Photosensor Device Based on Few-Layered WS₂ Films*, Adv. Funct. Mater. 23 5511 (2013).
- [37] P. Hu, Z. Wen, L. Wang, P. Tan *et al.*, *Synthesis of Few-Layer GaSe Nanosheets for High Performance Photodetectors*, ACS Nano 6 5988 (2012).
- [38] A. Castellanos-Gomez, L. Vicarelli, E. Prada, J. O. Island *et al.*, *Isolation and characterization of few-layer black phosphorus*, 2D Materials 1 025001 (2014).
- [39] A. Rose, *Concepts in photoconductivity and allied problems*, Interscience Publishers (1963).
- [40] R. Bube, *Photoelectronic Properties of Semiconductors*, Cambridge University Press (1992).
- [41] G. Konstantatos, J. Clifford, L. Levina and E. H. Sargent, *Sensitive solution-processed visible-wavelength photodetectors*, Nat Photon 1 531 (2007).
- [42] F. Prins, M. Buscema, J. S. Seldenthuis, S. Etaki *et al.*, *Fast and Efficient Photodetection in Nanoscale Quantum-Dot Junctions*, Nano Lett. 12 5740 (2012).
- [43] F. Liu, H. Shimotani, H. Shang, T. Kanagasekaran *et al.*, *High-Sensitivity Photodetectors Based on Multilayer GaTe Flakes*, ACS Nano 8 752 (2013).



CHAPTER 8

PHOTOVOLTAIC EFFECT IN FEW-LAYER BLACK PHOSPHORUS PN JUNCTIONS DEFINED BY LOCAL ELECTROSTATIC GATING

Michele Buscema,[†] Dirk J. Groenendijk,[†] Gary A. Steele, Herre S.J. van der Zant and Andres Castellanos-Gomez*

In conventional photovoltaic solar cells, photogenerated carriers are extracted by the built-in electric field of a semiconductor PN-junction, defined by ionic dopants. In atomically thin semiconductors, the doping level can be controlled by the field-effect, enabling the implementation of electrically tunable PN-junctions. However, most 2D semiconductors do not show ambipolar transport, necessary to realize PN-junctions. Few-layer black phosphorus (b-P) is a recently isolated 2D semiconductor with direct bandgap, high mobility, large current on/off ratios, and ambipolar operation.

Here, we fabricate few-layer b-P field-effect transistors with split gates and hexagonal boron nitride dielectric. We demonstrate electrostatic control of the local charge carrier type and density in the device. Illuminating a gate-defined PN-junction, we observe zero-bias photocurrents and significant open-circuit voltages due to the photovoltaic effect. The small bandgap of the material allows power generation for illumination wavelengths up to 940 nm, attractive for energy harvesting in the near-infrared.

[†] These authors contributed equally. Parts of this chapter have been published in Nature Communications 5, 4651 (2014) [1].

8.1. INTRODUCTION

In the past few years the research effort on two-dimensional (2D) materials has increased rapidly, driven by the great variety of layered materials and their exceptional properties when reduced to few atomic layers.[2–4] Due to their remarkable mechanical, [5, 6] electrical [7, 8] and optical properties [9–11] layered materials have proven to be promising candidates for many applications such as mass sensing,[12] transistor operation,[8] optical communication[13] and photodetection.[14–17]

The field of electronics now has access to a large library of 2D materials, ranging from elemental gapless semiconductors (graphene), semiconducting and superconducting chalcogenides (e.g. transition metal dichalcogenides, TMDCs) to large bandgap insulators (e.g. hexagonal boron nitride, h-BN). The combined use of their exceptional properties has recently been made possible due to advancements in transfer techniques.[7, 18, 19] Different 2D materials can now be used as components of a single device such as a field-effect transistor, where a gate dielectric and a semiconducting channel material are needed.

Due to its atomically flat surface and its disorder-free interface with other 2D materials, h-BN is well-suited to be used as a gate dielectric material.[7, 20, 21] Few-layer black phosphorus (b-P), a recently isolated 2D material, has shown promising characteristics for its use as channel material, such as high mobility, good current ON/OFF ratios and ambipolarity. [22–29] Especially the ambipolarity and the direct bandgap (optimum for visible and near-infrared applications) make b-P an interesting candidate for electrostatically tuneable optoelectronic devices.

Here, we transfer h-BN and few-layer black phosphorus onto a pair of local gates to define PN junctions. The electrostatic control of the charge carrier type in different regions of a few-layer b-P flake allows us to tune the electronic behavior from metallic to diode-like. Under illumination, the PN junctions show photovoltaic effect, demonstrating that a large internal electric field can be obtained by local gating. Beyond fabricating a locally-gated PN junction based on a van der Waals heterostructure of 2D materials, our results set the ground for further research towards photodetection and energy harvesting based on few-layer black phosphorus devices.

8.2. FABRICATION OF LOCALLY GATED DEVICES

To efficiently control the doping level in different regions of the b-P flake, we fabricate a pair of local gates (Ti/AuPd, 5 nm/25 nm) separated by a 300 nm gap on a SiO₂/Si substrate by standard e-beam lithography and metal deposition techniques (Figure 8.1a). The schematics below each panel of Figure 1 show a cross section of the device after each fabrication step. On top of the local gates, we first transfer a thin (~ 20 nm) h-BN flake for use as gate dielectric (Figure 8.1b).

We select, by optical inspection, h-BN flakes free of large wrinkles and folds that could hamper subsequent transfer and fabrication steps. Then, we transfer a

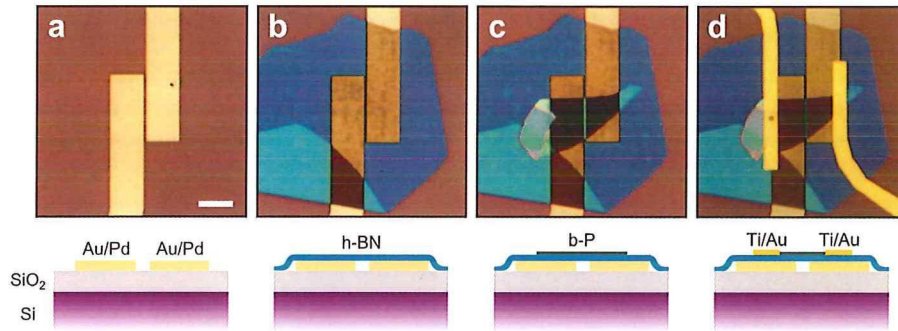


FIGURE 8.1: (a) Local gates (Au/Pd) patterned on the surface of a SiO_2/Si substrate. The gap between the gates is 300 nm wide. (b) After the transfer of a thin h-BN flake on top of the split gates. (c) After the transfer of a thin b-P flake on top of the h-BN and the split gate region. (d) The final device after fabrication of the contacts (Ti/Au). The schematics below each panel show a cross section of the device after each fabrication step. The scale bar is 5 μm for all panels.

few-layer (6 to 7 nm) b-P flake on top of the thin h-BN such that it is well centered with respect to the local gates (Figure 1c). Both transfer steps are performed via a recently developed deterministic dry-transfer method.[19] The b-P flake is then contacted with two leads (Ti/Au 2 nm/60 nm), fabricated by e-beam lithography, metal deposition and lift-off (Figure 8.1d). All electrical measurements are performed in a probe station in vacuum ($1 \cdot 10^{-5}$ mbar) to minimize degradation of the b-P flakes in ambient conditions.[25, 30]

8.3. TRANSISTOR OPERATION

Figure 8.2a shows the electrical transfer characteristics of a locally gated b-P flake; the source-drain current (I_{ds}) is recorded at constant source-drain bias (V_{ds}) while the two local gates act as a single back-gate ($V_{\text{lg}} = V_{\text{rg}} = V_{\text{g}}$). The inset shows the data on a linear scale. The source-drain current is strongly modulated as V_{g} is swept from negative to positive voltages: I_{ds} varies from a few μA at $V_{\text{g}} = -10$ V to a minimum of ~ 100 pA at $V_{\text{g}} = 5$ V and increases to tens of nA for larger V_{g} values. The non-monotonic transfer curve is a clear signature of ambipolar transport, indicating that both hole and electron doping can be achieved, as expected for few-layer b-P.[27, 30]

From the Figure, we derive that the b-P transistor on h-BN is naturally P-doped with an unintentional doping level larger than devices fabricated on SiO_2 . [22–27, 30] The field-effect mobility is in the order of $25 \text{ cm}^2 \text{ V}^{-1} \text{ s}^{-1}$ and the current modulation is more than a factor $1 \cdot 10^4$ for holes ($0.12 \text{ cm}^2 \text{ V}^{-1} \text{ s}^{-1}$ and $1 \cdot 10^2$ for electrons). We observe similar behavior in three fabricated locally gated b-P devices (See Figures 8.7 and 8.8). Interestingly, the current values in the hole- and electron-doped regimes at

the same carrier concentration differ less than one order of magnitude for all devices. This stronger ambipolar behavior is most likely due to a more efficient gate coupling provided by the high quality (i.e. high breakdown voltage) of the ultrathin h-BN.

Figure 8.2b and Figure 8.2c show the conductance of the device in P- and N-type operation respectively. The measured $I_{ds} - V_{ds}$ curves are linear for both operation modes over a wide range of gate voltages, indicating that the Schottky barriers do not dominate the transport and that the Ti/Au leads make good ohmic contact to the b-P flake. The current in the hole-doped regime is higher than in the electron-doped regime, indicating that the Fermi energy of the contacts is closer to the valence band of b-P, similar to previous devices contacted with the same metals.[27]

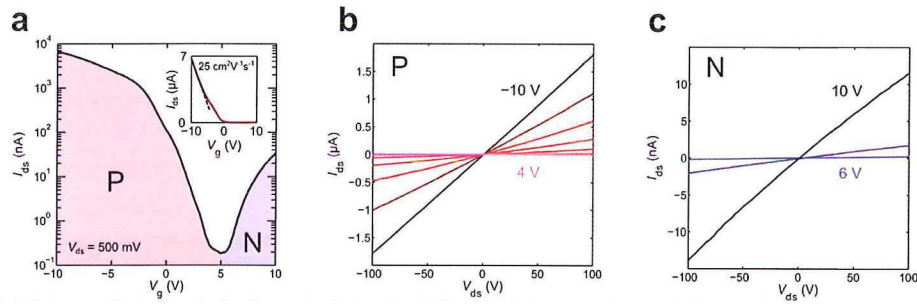


FIGURE 8.2: Transfer characteristic at $V_{ds} = 500$ mV. The inset shows the data in linear scale. (b) Output characteristics for V_g from -10 to 4 V in steps of 2 V. (c) Output characteristics for V_g from 6 to 10 V in steps of 2 V.

8.4. PN JUNCTION OPERATION

The multiple gates in our device allow us not only to make an ambipolar transistor, as in Figure 8.2a, but also to locally induce hole and electron doping in different parts of the channel. Figure 8.3a and Figure 8.3b show false-color maps of the magnitude of I_{ds} at a fixed bias voltage as the split gates are independently swept from 7 to 12 V. The gate voltage values are chosen to be close to the flatband condition as determined from the transfer characteristics measured in single back-gate configuration (Figure 8.2a). In both maps, it is possible to distinguish four distinct regions where current flows, separated by regions where only a small current is measured (the OFF state of the device). The previously reported effect of gate-induced stress for devices on SiO_2 is drastically reduced by choosing a h-BN flake as gate dielectric because it provides a more stable dielectric environment. Moreover, the shift in the gate voltage is constant over several days, in contrast with the much shorter time scales (minutes) of devices fabricated on SiO_2 . [27]

The cross of suppressed conductance allows us to identify four distinct regions of doping, indicating the good control of the gates over the doping type and concen-

tration in the b-P flake. In Figure 3a, the NN ($V_{\text{lg}} = V_{\text{rg}} = 12 \text{ V}$) and PP ($V_{\text{lg}} = V_{\text{rg}} = 7 \text{ V}$) quadrants show the highest current values, as expected from the transfer characteristics in Figure 8.2a. On the other hand, the measured current in the NP ($V_{\text{rg}} = 7 \text{ V}$, $V_{\text{lg}} = 12 \text{ V}$) region is much higher than in the PN ($V_{\text{rg}} = 12 \text{ V}$, $V_{\text{lg}} = 7 \text{ V}$) region, suggesting the formation of a junction diode when the gates are biased with opposite polarities. To confirm that the asymmetry in the current is due to the formation of a PN or NP junction, we repeat the measurement at negative bias (Figure 8.3b). Again, the NN and PP region show the highest current. However, the current in the NP configuration is now much smaller than the current in the PN configuration, confirming the formation of a junction diode as different type of charge carriers are accumulated in the channel.

The origin of the strong current modulation induced by the local gates can be explained by the band diagrams in Figure 8.3c. In the NN and PP regions, the electric field generated by the two gates is homogeneous and favors either electron (NN) or hole (PP) conduction. As the gates are biased in opposite polarities (PN or NP configuration), a strong horizontal electric field is also present in the b-P region bridging the gates. This large horizontal electric field contributes to charge accumulation in the two different regions of the b-P flake, giving rise to an asymmetric energy landscape. Therefore, the horizontal electric field generated by the local gates and the charge accumulation in the different regions of the b-P flake generate a PN or NP junction, which is then responsible for the measured rectifying output characteristics. This is similar to a PN junction in bulk-doped materials in which the dopant charges are now located at the surface of the gates rather than in the bulk of the semiconductor itself.

The control of the electrical response of the device with the local gates is even more evident by looking at the measured output characteristics in the different doping configurations (Figure 8.3d). In the NN and PP configuration, the $I_{\text{ds}} - V_{\text{ds}}$ curves are linear, as expected from Figure 8.2b and 8.2c. In the PN and NP configuration, the $I_{\text{ds}} - V_{\text{ds}}$ curves are highly non-linear and the device shows rectifying behavior, whose direction can be controlled by the gate bias polarity. In the PN configuration, the reverse-bias current is in the order of 1 nA ($V_{\text{ds}} = -500 \text{ mV}$), while the reverse-bias current in the NP configuration is around 5 nA ($V_{\text{ds}} = +500 \text{ mV}$).

To extract the diode parameters, we fit the $I_{\text{ds}} - V_{\text{ds}}$ curves to a modified version of the Shockley equation which includes parasitic resistances in parallel and in series to the junction (see Section 8.7.2). [31] The results are summarized in Figure 8.9 and Table 8.2. The ideality factors and the series resistances are comparable with PN junctions based on single layer WSe₂. [32, 33] However, our devices show lower values for the parallel resistance that model the non-zero reverse-bias current. We can attribute this to leakage current due to thermally excited carriers. Given the small bandgap of few-layer b-P, the leakage current is higher than in PN junctions based on larger-bandgap single layer WSe₂. [21, 32, 33]

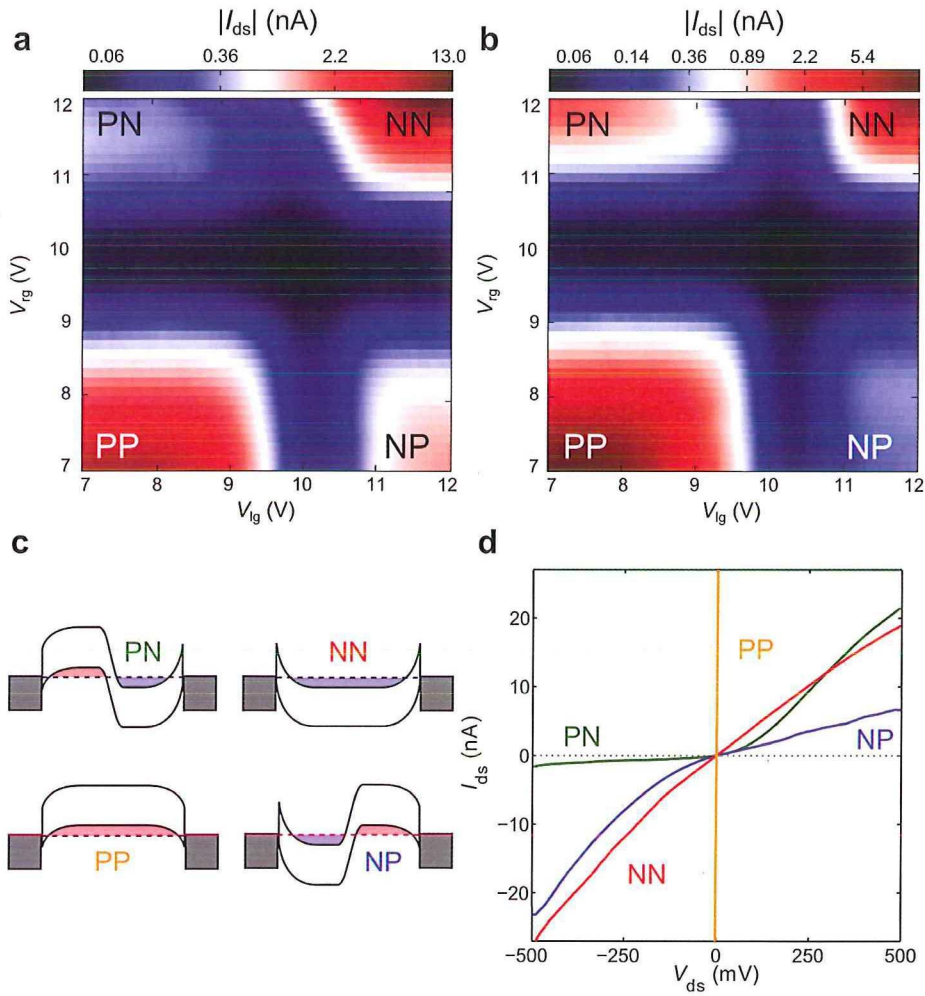


FIGURE 8.3: (a) False color map of the magnitude of the source-drain current at constant bias voltage (+100 mV) as the voltage on the two local gates is changed independently. (b) False color map of the magnitude of the source-drain current at constant bias voltage (-100 mV) as the voltage on the two local gates is changed independently. (c) Band diagrams corresponding to the different device configurations (d) Output characteristics of the device in different gate configurations (PP: $V_{lg} = V_{rg} = -10$ V, NN: $V_{lg} = V_{rg} = 10$ V, NP: $V_{lg} = 10$ V, $V_{rg} = -10$ V, PN: $V_{lg} = -10$ V, $V_{rg} = 10$ V).

8.5. PHOTOVOLTAIC EFFECT

A characteristic feature of PN junctions is the large built-in electric field that can be used to separate photoexcited carriers via the photovoltaic effect. [32–34] Upon

illumination, the internal electric field at the junction separates photogenerated carriers and gives rise to a photocurrent at zero external bias (short-circuit current, I_{sc}) and a photovoltage with no current flowing (open circuit voltage, V_{oc}). Figure 8.4a shows a false-color map of I_{sc} of the device under illumination ($\lambda = 640 \text{ nm}$, $P = 3.9 \mu\text{W}$) as the gates voltages are swept independently. Four regions are clearly visible: high photocurrent in PN and NP configuration and no photocurrent in the PP and NN configuration. Figure 8.4b displays the measured photovoltage (V_{oc}); again four distinct regions appear: large V_{oc} in PN and NP configuration and zero V_{oc} in PP and NN configuration.

The photocurrent and photovoltage are only generated when the local gates are oppositely biased, indicating that the mechanism is photovoltaic originating from the formation of a PN or NP junction in the channel. Figure 8.4c shows schematically that when the gates are biased in opposite polarities, the internal electric field in the b-P channel separates the photogenerated carriers under above-bandgap illumination, generating a photocurrent. If the circuit is kept open, the photogenerated carriers accumulate in distinct parts of the flake, giving rise to a photovoltage. This demonstrates that the b-P PN junction can be used for energy harvesting.

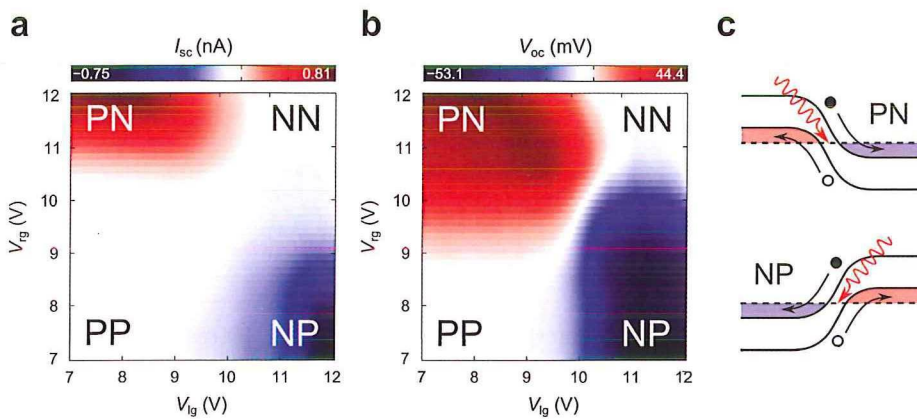


FIGURE 8.4: (a) False color map of the short circuit current (I_{sc} , $V_{ds} = 0 \text{ V}$) as the voltages on the two local gates are changed independently. (b) False color map of the open circuit voltage (V_{oc} , $I_{ds} = 0 \text{ A}$) as the voltages on the two local gates are changed independently. (c) Band diagrams illustrating the photovoltaic mechanism in PN and NP configuration: an impinging photon (red arrow) generates an electron-hole pair that is swept away from the junction region by the built-in electric field.

In Figure 8.5a, we characterize the optoelectronic properties of few-layer b-P junction diodes by measuring the output characteristics under illumination with varying incident power. As the power is increased, the $I_{ds} - V_{ds}$ characteristics shift towards more negative current values. This is consistent with a photocurrent generation mech-

anism where the separation of the electron-hole pairs is driven by the internal electric field at the junction region: the photocurrent has the same sign as the reverse-bias current; therefore, under illumination and reverse-bias, the total measured current is larger than in dark. Thus, an additional forward-bias is required to compensate the photogenerated reverse-current, giving rise to a non-zero open-circuit voltage. The measured I_{SC} is in the order of 1 nA and $V_{OC} \sim 50$ mV at the highest incident power and both I_{SC} and V_{OC} are linear as function of the incident power (Figure 8.6).

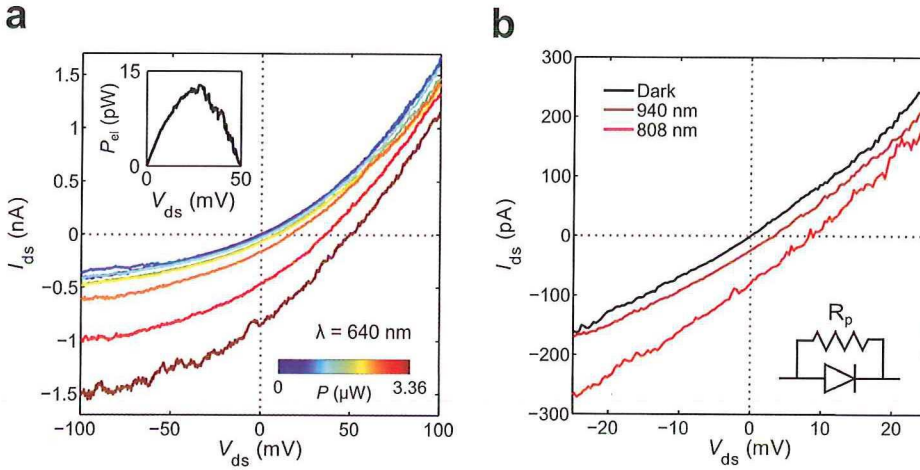


FIGURE 8.5: (a) $I_{ds} - V_{ds}$ curves in the PN configuration as a function of the incident optical power ($\lambda = 640$ nm). The inset shows the electrical power that can be harvested at the maximum employed illumination power. (b) Output characteristics in the PN configuration in dark (black solid line) and under illumination of different wavelengths excitation wavelength at fixed power ($P = 0.33$ μ W). The inset shows the schematics of the equivalent circuit.

Moreover, we can evaluate the electrical power harvested by the b-P PN junction by $P_{el} = V_{ds} \cdot I_{ds}$ (Figure 8.5a, inset) and find that the maximum P_{el} is in the order of 13 pW, in good comparison with other electrostatically defined PN junctions based on WSe_2 . [32, 33] While the photocurrent is in the same order of magnitude as similar devices realized with single layer WSe_2 [32, 33], the open circuit voltage is lower, due to the smaller bandgap of few-layer b-P. We note that the measured V_{oc} is significantly lower than the predicted bandgap of few-layer b-P (~ 300 meV). We attribute this to a resistance in parallel (R_p) to the junction (see inset of Figure 8.5b) which limits V_{oc} by leakage of photogenerated carriers across the junction. The slope of the $I_{ds} - V_{ds}$ curve at $V_{ds} = 0$ V (in dark, Figure 8.5b) is a signature of this parallel resistance.

The b-P PN junctions show photovoltaic effect up to the near-infrared (NIR) part of the electromagnetic spectrum. Figure 8.5b plots the $I_{ds} - V_{ds}$ curves in PN configuration in dark (solid black line) and with excitation wavelengths of 808 nm, 885 nm and 940 nm ($P_{device} = 0.33$ μ W). Under illumination, the output characteristics con-

firm that the photocurrent generation mechanism is dominated by the photovoltaic effect. As the photon energy is increased, both I_{sc} and V_{oc} increase, consistent with increased absorption in the b-P flake at shorter wavelengths.

The measured photovoltaic effect up to 940 nm illumination indicates that the bandgap of the b-P flake is smaller than 1.31 eV and demonstrates energy harvesting in NIR part of the spectrum. This constitutes a strong advantage with respect to other 2D semiconductors such as Mo- or W- chalcogenides whose large bandgap (> 1.6 eV) limits their applicability in the NIR.[14, 32, 33]

Figure 8.6 plots the V_{oc} (left vertical axis) and I_{sc} (right vertical axis) against the total optical power incident on the device. I_{sc} is linear with the excitation power for the whole range of incident optical power, indicating that the recombination rate of the photogenerated carriers is not related the rate of incoming photons. This is usually associated with monomolecular recombination processes: the recombination rate is linearly proportional to the density of photogenerated carriers.[32, 35] Also V_{oc} increases linearly with the incident optical power. In an ideal case, the open-circuit voltage should increase logarithmically with the optical power incident on the device. The deviation from the ideal behavior can be attributed to parasitic resistive losses in our device (see Figure 8.9 and Table 8.2).

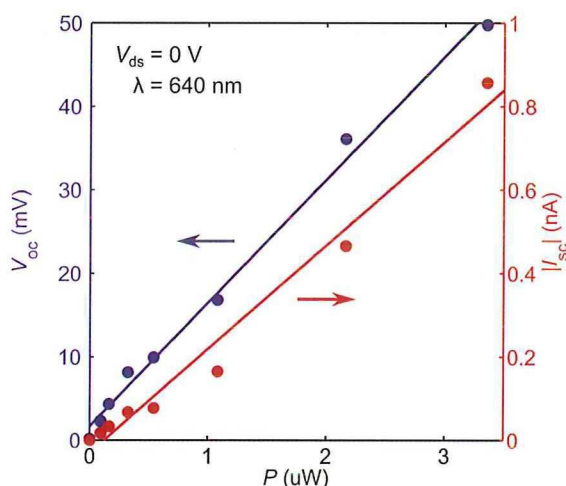


FIGURE 8.6: Open circuit voltage (left axis, blue dots) and short-circuit current (right axis, red dots) as function of total incident excitation power.

We measure I_{sc} under modulated excitation ($\lambda = 640$ nm, $P 2.7 \mu\text{W}$) in the time domain. We find a short response time of about 2 ms coupled to a high signal to noise ratio provided by the extremely small dark current (~ 100 pA), making few-layer b-P PN junctions promising as fast and sensitive photodetectors.

λ (nm)	V_{oc} (mV)	I_{sc} (nA)	P_{el}^{max} (pW)	FF (-)	EQE (%)
532	11	0.090	0.28	0.283	0.064
640	16	0.168	0.80	0.298	0.102
808	8	0.080	0.19	0.295	0.038
885	3	0.025	0.03	0.333	0.011
940	2.8	0.021	0.02	0.391	0.009

TABLE 8.1: Figures-of-merit for bp PN junction.

To further evaluate the performance of the devices, we calculate figures-of-merit such as the external quantum efficiency (EQE) and the fill factor ($FF = P_{el}^{max}/(V_{oc} \cdot I_{sc})$) as a function of wavelength (see Table 8.1). We compare the EQE values to those of PN junctions based on single layer WSe_2 [33] and find that the EQE for our devices is lower for 532 nm illumination and larger for longer wavelengths.

8.6. DISCUSSION

We have fabricated PN junctions based on van der Waals heterostructures of two different 2D materials: h-BN as gate dielectric and b-P as ambipolar semiconducting channel material. We demonstrate full electrostatic control of the device by means of local gating which allows us to tune the electrical behavior of the device from metallic to rectifying. We observe a strong photocurrent and a significant open-circuit photovoltage, which we attribute to electron-hole separation at the PN junction from the photovoltaic effect, which extends even up to the NIR. Our work sets the ground for further research towards broad-band energy harvesting devices based on few-layer black-phosphorus.

ACKNOWLEDGMENT

We acknowledge support by the European Union (FP7) through the program 9 RODIN and the Dutch organization for Fundamental Research on Matter (FOM). A.C-G. acknowledges financial support through the FP7-Marie Curie Project PIEF-GA-2011-300802 ('STRENGTHNANO').

8.7. SUPPORTING INFORMATION

8.7.1. TWO OTHER FABRICATED DEVICES

We measured two other locally gated b-P devices. Figure 8.7a shows an optical micrograph of the second device, highlighting the similar geometry to the device in the main part of this Chapter. Figure 8.7b displays the measured $I_{ds} - V_g$ traces at fixed V_{ds} . The two local gates are linked together, so they act as a single backgate (V_g). This

second device also displays strong ambipolar behavior, with I_{ds} varying from a few μA with $V_g = -15\text{ V}$ to $\sim 500\text{ nA}$ at with $V_g = 15\text{ V}$. The inset shows the data in a linear scale. We extract a field effect mobility of $17\text{ cm}^2\text{ V}^{-1}\text{ s}^{-1}$. The $I_{ds}-V_{ds}$ curves of the device in different gate configurations are shown in Figure 8.7c. The $I_{ds}-V_{ds}$ curves are linear in PP ($V_{lg} = V_{rg} = -15\text{ V}$) and NN ($V_{lg} = V_{rg} = 15\text{ V}$) configuration and strongly rectifying behavior when the gates are biased at different polarities (PN and NP configurations).

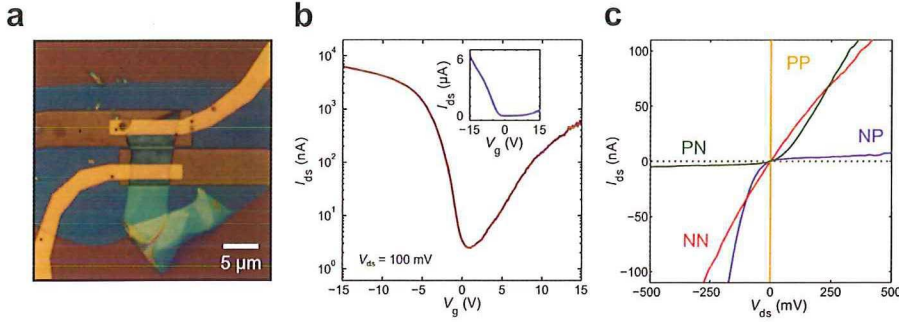


FIGURE 8.7: (a) Optical micrograph of the device. (b) Transfer characteristic at $V_{ds} = 100\text{ mV}$. The inset shows the data in a linear scale. (c) Output characteristics of the device in different gate configurations (PP: $V_{lg} = V_{rg} = -15\text{ V}$, NN: $V_{lg} = V_{rg} = 15\text{ V}$, NP: $V_{lg} = 15\text{ V}$, $V_{rg} = -15\text{ V}$, PN: $V_{lg} = -15\text{ V}$, $V_{rg} = 15\text{ V}$).

Figure 8.8a shows an optical micrograph of the third locally gated PN junction. The lighter diagonal line across the channel is a part of the flake which is folded or elevated from the hBN. Figure 8.8b displays the measured $I_{ds}-V_g$ traces at fixed V_{ds} . The two local gates are linked together, so they act as a single backgate (V_g). The inset shows the data in a linear scale. We extract a field effect mobility of $0.27\text{ cm}^2\text{ V}^{-1}\text{ s}^{-1}$ for holes. Figure 8.8c shows the $I_{ds}-V_{ds}$ characteristics for different gate configurations. The PP and NN configuration show linear behavior, whereas the PN configuration shows diode-like behavior. In the NP configuration, the rectifying behavior is suppressed; this might be related to imperfections of the b-P flake that can be seen in Figure 8.8a.

8.7.2. DETERMINATION OF THE DIODE PARAMETERS WITH SHOCKLEY MODEL

In this Section, we model the $I_{ds}-V_{ds}$ characteristics in the PN and NP configuration of all the measured devices with a modified form of the Shockley equation. In an ideal case, the relationship between the current (I_{ds}) and the voltage bias (V_{ds}) across a PN diode is described by the Shockley model:

$$I_{ds} = I_s \left\{ \exp\left(\frac{V_{ds}}{nV_T}\right) - 1 \right\}, \quad (8.1)$$

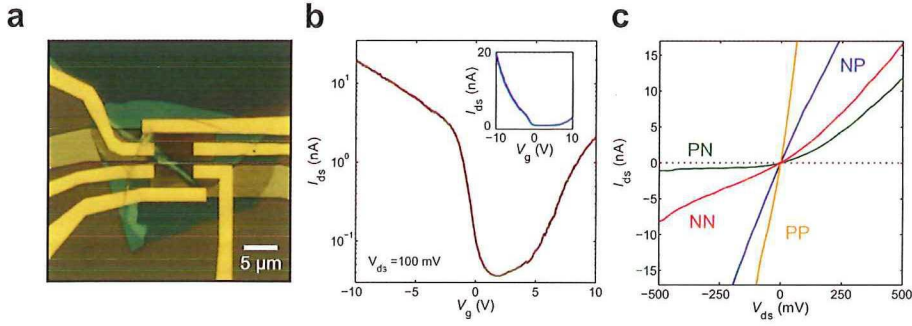


FIGURE 8.8: (a) Optical micrograph of the device. (b) Transfer characteristic at $V_{ds} = 100$ mV. The inset shows the data in a linear scale. (c) Output characteristics of the device in different gate configurations (PP: $V_{lg} = V_{rg} = -10$ V, NN: $V_{lg} = V_{rg} = 10$ V, NP: $V_{lg} = 10$ V, $V_{rg} = -10$ V, PN: $V_{lg} = -10$ V, $V_{rg} = 10$ V).

		I_s (nA)	n	R_s (M Ω)	R_p (M Ω)
Device 1	PN	0.998	1.288	13.3	347.8
	NP	0.279	1.960	11.6	67.7
Device 2	PN	1.95	1.019	2.2	124.3
	NP	6.39	1.87	0.327	∞^a
Device 3	PN	0.539	2.459	25.5	989.6
	NP	1.211	0.203	9.8	6.5

a: $R_p > 1 \cdot 10^5$ M Ω

TABLE 8.2: Diode parameters of the measured devices determined from fitting to equation 8.3.

8

where I_s is the saturation current, n is the ideality factor, $V_T = k_B T$ (k_B is the Boltzmann constant in eV K $^{-1}$ and T is the temperature in K) is the thermal voltage. The ideality factor is related to the carrier recombination mechanisms at the PN junction; $n = 1$ indicates that there is only band-to-band recombination of minority carriers, which is the ideal case. A more realistic model should include current losses due to parasitic resistances in parallel (R_p) and in series (R_s) with the junction. A schematic of the model circuit is presented in Figure 8.9. The series resistance R_s models the voltage losses due to e.g. contact resistance and the resistance of the degenerately doped regions of the b-P flake. The parallel resistance R_p models additional carrier recombination mechanisms that drain current from the junction. The slope of the measured $I_{ds} - V_{ds}$ curves at $V_{ds} = 0$ V (see Figure 8.9) indicates a non-infinite R_p . To

include these effects, we can rewrite equation 8.1 as

$$I_{ds} = I_s \left\{ \exp \left(\frac{V_{ds} - I_{ds} R_s}{n V_T} \right) - 1 \right\} + \frac{V_{ds} - I_{ds} R_s}{R_p}. \quad (8.2)$$

An analytical expression can be obtained in the following form:[31]

$$I_{ds} = \frac{n V_T}{R_s} \mathcal{W} \left\{ \frac{I_s R_s R_p}{n V_T (R_s + R_p)} \exp \left(\frac{R_p (V_{ds} + I_s R_s)}{n V_T (R_s + R_p)} \right) \right\} + \frac{R_p (V_{ds} - I_s R_p)}{R_s + R_p}, \quad (8.3)$$

where \mathcal{W} is the Lambert \mathcal{W} -function.

The measured $I_{ds} - V_{ds}$ curves and the model described in expression 8.3 are in good agreement (Figure 8.9). We summarized the extracted model parameters in Table 8.2.

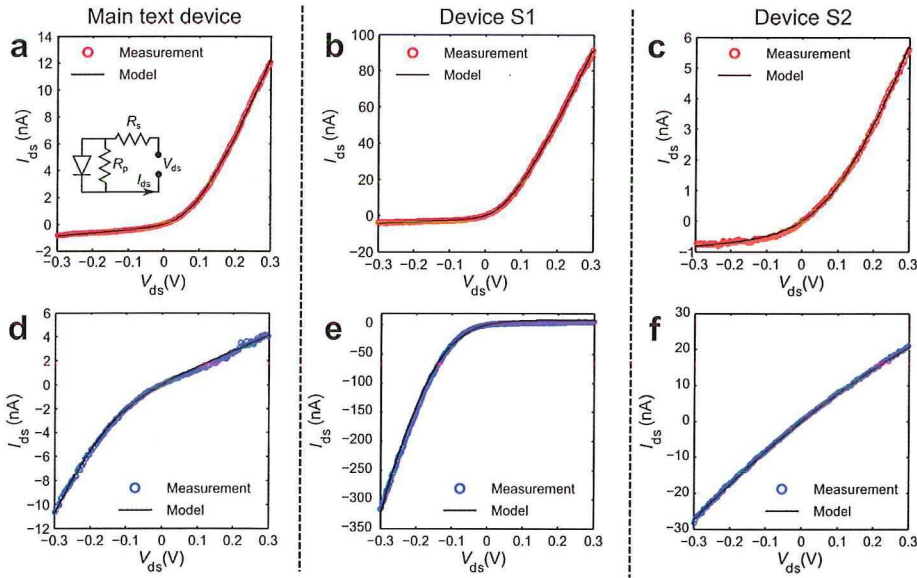


FIGURE 8.9: Shockley fits of the IV-characteristics in PN and NP configuration for the measured devices. (a-c) $I_{ds} - V_{ds}$ curves in PN configuration (red dots) and model (black solid line). The inset of (a) shows the circuit model schematics. (d-f) $I_{ds} - V_{ds}$ curves in the NP configuration (blue dots) and model (black solid line)

REFERENCES

- [1] M. Buscema, D. J. Groenendijk, G. A. Steele, H. S. van der Zant *et al.*, *Photovoltaic effect in few-layer black phosphorus PN junctions defined by local electrostatic gating*, Nat Commun 5 (2014).

- [2] K. S. Novoselov, D. Jiang, F. Schedin, T. J. Booth *et al.*, *Two-dimensional atomic crystals*, Proceedings of the National Academy of Sciences of the United States of America **102** 10451 (2005).
- [3] K. S. Novoselov, A. K. Geim, S. V. Morozov, D. Jiang *et al.*, *Electric Field Effect in Atomically Thin Carbon Films*, Science **306** 666 (2004), <http://www.sciencemag.org/content/306/5696/666.full.pdf>.
- [4] Q. H. Wang, K. Kalantar-Zadeh, A. Kis, J. N. Coleman *et al.*, *Electronics and optoelectronics of two-dimensional transition metal dichalcogenides*, Nat Nano **7** 699 (2012).
- [5] C. Lee, X. Wei, J. W. Kysar and J. Hone, *Measurement of the Elastic Properties and Intrinsic Strength of Monolayer Graphene*, Science **321** 385 (2008).
- [6] A. Castellanos-Gomez, M. Poot, G. A. Steele, H. S. J. van der Zant *et al.*, *Elastic Properties of Freely Suspended MoS₂ Nanosheets*, Adv. Mater. **24** 772 (2012).
- [7] L. Wang, I. Meric, P. Y. Huang, Q. Gao *et al.*, *One-Dimensional Electrical Contact to a Two-Dimensional Material*, Science **342** 614 (2013).
- [8] B. Radisavljevic, A. Radenovic, J. Brivio, V. Giacometti *et al.*, *Single-layer MoS₂ transistors*, Nature Nanotechnology **6** 147 (2011).
- [9] K. F. Mak, C. Lee, J. Hone, J. Shan *et al.*, *Atomically Thin MoS₂: A New Direct-Gap Semiconductor*, Phys. Rev. Lett. **105** 136805 (2010).
- [10] K. F. Mak, K. He, J. Shan and T. F. Heinz, *Control of valley polarization in monolayer MoS₂ by optical helicity*, Nat Nano **7** 494 (2012).
- [11] K. F. Mak, K. He, C. Lee, G. H. Lee *et al.*, *Tightly bound trions in monolayer MoS₂*, Nat. Mater. **12** 207 (2013).
- [12] C. Chen, S. Rosenblatt, K. I. Bolotin, W. Kalb *et al.*, *Performance of monolayer graphene nanomechanical resonators with electrical readout*, Nat Nano **4** 861 (2009).
- [13] F. Xia, T. Mueller, Y.-m. Lin, A. Valdes-Garcia *et al.*, *Ultrafast graphene photodetector*, Nat Nano **4** 839 (2009).
- [14] O. Lopez-Sanchez, D. Lembke, M. Kayci, A. Radenovic *et al.*, *Ultrasensitive photodetectors based on monolayer MoS₂*, Nat Nano **8** 497 (2013).
- [15] M. Buscema, M. Barkelid, V. Zwiller, H. S. J. van der Zant *et al.*, *Large and Tunable Photothermoelectric Effect in Single-Layer MoS₂*, Nano Lett. **13** 358 (2013).
- [16] Z. Yin, H. Li, H. Li, L. Jiang *et al.*, *Single-Layer MoS₂ Phototransistors*, ACS Nano **6** 74 (2012).
- [17] H. S. Lee, S.-W. Min, Y.-G. Chang, M. K. Park *et al.*, *MoS₂ Nanosheet Phototransistors with Thickness-Modulated Optical Energy Gap*, Nano Lett. **12** 3695 (2012).
- [18] L. Britnell, R. M. Ribeiro, A. Eckmann, R. Jalil *et al.*, *Strong Light-Matter Interactions in Heterostructures of Atomically Thin Films*, Science – (2013).
- [19] A. Castellanos-Gomez, M. Buscema, R. Molenaar, V. Singh *et al.*, *Deterministic transfer of two-dimensional materials by all-dry viscoelastic stamping*, 2D Materials **1** 011002 (2014).
- [20] C. Dean, A. Young, I. Meric, C. Lee *et al.*, *Boron nitride substrates for high-quality graphene electronics*, Nature Nanotechnology **5** 722 (2010).
- [21] J. S. Ross, P. Klement, A. M. Jones, N. J. Ghimire *et al.*, *Electrically tunable excitonic light-emitting diodes based on monolayer WSe₂ p-n junctions*, Nat Nano **9** 268 (2014).
- [22] F. Xia, H. Wang and Y. Jia, *Rediscovering black phosphorus as an anisotropic layered material for optoelectronics and electronics*, Nat Commun **5** (2014).
- [23] H. Liu, A. T. Neal, Z. Zhu, Z. Luo *et al.*, *Phosphorene: An Unexplored 2D Semiconductor with a High Hole Mobility*, ACS Nano **8** 4033 (2014).
- [24] J. Qiao, X. Kong, Z.-X. Hu, F. Yang *et al.*, *High-mobility transport anisotropy and linear dichroism in few-layer black phosphorus*, Nat Commun **5** (2014).
- [25] L. Li, Y. Yu, G. J. Ye, Q. Ge *et al.*, *Black phosphorus field-effect transistors*, Nat Nano **9** 372 (2014).
- [26] S. P. Koenig, R. A. Doganov, H. Schmidt, A. H. Castro Neto *et al.*, *Electric field effect in ultrathin black phosphorus*, Applied Physics Letters **104** (2014).
- [27] M. Buscema, D. J. Groenendijk, S. I. Blanter, G. A. Steele *et al.*, *Fast and Broadband Photoresponse of Few-Layer Black Phosphorus Field-Effect Transistors*, Nano Lett. **14** 3347 (2014).
- [28] J. Dai and X. C. Zeng, *Bilayer Phosphorene: Effect of Stacking Order on Bandgap and its Potential*

- Applications in Thin-Film Solar Cells*, arXiv:1403.6189 – (2014).
- [29] V. Tran, R. Soklaski, Y. Liang and L. Yang, *Layer-Controlled Band Gap and Anisotropic Excitons in Phosphorene and Few-Layer Black Phosphorus*, arXiv:1402.4192 – (2014).
- [30] A. Castellanos-Gomez, L. Vicarelli, E. Prada, J. O. Island *et al.*, *Isolation and characterization of few-layer black phosphorus*, *2D Materials* **1** 025001 (2014).
- [31] A. Ortiz-Conde, F. J. García Sánchez and J. Muci, *Exact analytical solutions of the forward non-ideal diode equation with series and shunt parasitic resistances*, *Solid-State Electronics* **44** 1861 (2000).
- [32] A. Pospischil, M. M. Furchi and T. Mueller, *Solar-energy conversion and light emission in an atomic monolayer p-n diode*, *Nat Nano* **9** 257 (2014).
- [33] B. W. H. Baugher, H. O. H. Churchill, Y. Yang and P. Jarillo-Herrero, *Optoelectronic devices based on electrically tunable p-n diodes in a monolayer dichalcogenide*, *Nat Nano* **9** 262 (2014).
- [34] S. M. Sze and K. K. Ng, *Physics of semiconductor devices*, John Wiley & Sons (2006).
- [35] R. Bube, *Photoelectronic Properties of Semiconductors*, Cambridge University Press (1992).

CHAPTER A

EXPERIMENTAL METHODS

The fabrication of the devices used in this thesis is introduced, with a special focus on the method used to transfer the different two dimensional layered materials on a variety of substrates. The setups used to characterize both the materials and the devices are described, briefly highlighting their working principle.

Parts of this chapter have been published in 2D Materials, 2014, 1 011002 [1].

A.1. FABRICATION TECHNIQUES

A.1.1. ELECTRON BEAM LITHOGRAPHY

Electron beam lithography is used to fabricate the majority of the devices presented in this thesis. In electron beam lithography, an electron beam patter generator (EBPG) scans a focused beam of electrons onto a substrate covered with an electron-sensitive resist (*exposure*, see Figure A.1a). The scanning of the electron beam follows a user-defined pattern. The EBPG used in this thesis is a Vistec EBPG5000+ with an acceleration voltage of 100 kV. The chemical modifications induced in the resist by the electron beam allow the pattern to be transferred on the substrate. We use a positive tone resist: the exposed resist can be selectively dissolved in certain solvents, exposing the surface of the substrate only along the pattern followed by the electron beam (*development*, see Figure A.1b). Then, metals are deposited (*deposition*, see Figure A.1c) and the unexposed resist is dissolved in warm (54 °C) acetone, lifting off the metal layer on top (*lift-off*, see Figure A.1d). Effectively, the unexposed resist is a mask, allowing metal deposition only where the pattern has been written. Therefore, after lift-off, the pattern written by the electron beam is covered with metal. This sequence can be repeated several times (lithographic layers) to fabricate complex devices. To ensure that every lithographic layer is well-aligned with the first, alignment markers need to be deposited in the first layer. These markers will then be recognized by the EBPG and used to align the patterns.

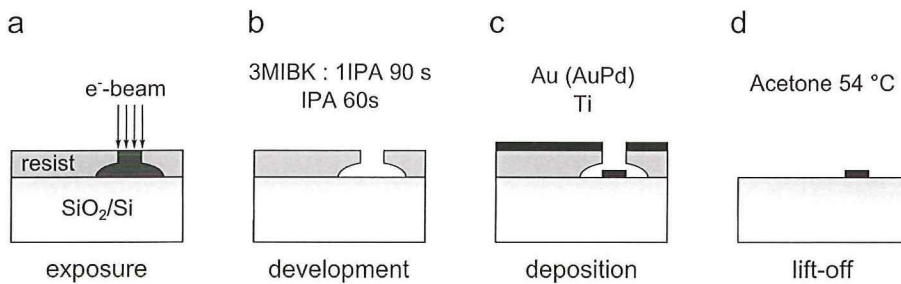


FIGURE A.1: (a) Exposure. The bi-layer resist stack is exposed by the electron beam. The shape of the exposed area is due to the backscattered electrons from the SiO_2/Si surface. (b) Development. The exposed resist is removed with organic solvents (positive tone development). (c) Metal deposition. A thin layer of metals is deposited via electron-beam deposition in high vacuum conditions. Ti is used as sticking layer, on top of which either Au or AuPd are deposited. (d) Lift-off. The unexposed resist is removed in warm (54 °C) acetone, leaving the deposited structure on the substrate surface.

A.1.2. EXFOLIATION

Micromechanical exfoliation represents the starting point of the research on two dimensional materials, as pioneered by Novoselov et al [2]. We use blue Nitto tape* to peel off flakes from bulk crystals, either natural or synthetic†. The lateral dimensions of the crystal are in the order of few millimeters. We start exfoliation by preparing about 10 small strips 2 × 5 cm of blue Nitto tape. With one strip, we peel off flakes from the bulk crystal (see Figure A.2a). Afterwards, we use the other clean strips to successively peel off flakes from the first strip, until the density of material on the strip is reduced and uniform (see Figure A.2b-c). The two strips are carefully brought in contact (Figure A.2b), slight pressure is applied with a cotton swab (Figure A.2c) and the two strips are peeled off from each other (Figure A.2d). Usually, five to six exfoliation times are enough to achieve the correct material density.

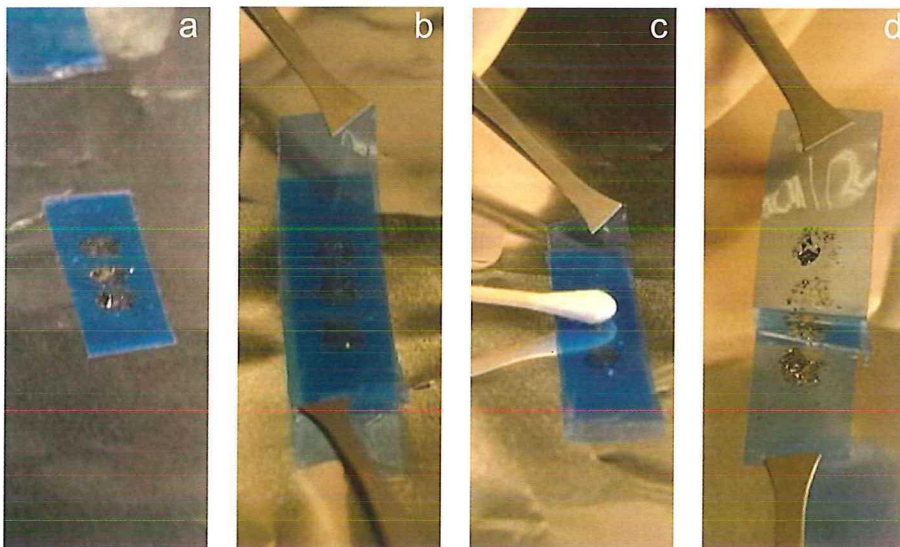


FIGURE A.2: (a) Strip of blue Nitto tape after repeated peeling off from a natural layered crystal. (b) Two strips of blue Nitto tape are brought in contact. (c) Slight pressure is applied with a cotton swab on the two joined strips. (d) The two strips are peeled off each other. Note the material transfer to the clean strip.

To deposit the material on the SiO_2/Si sample, the strip prepared at last is brought into contact with a freshly cleaned ‡ 4 × 4 mm piece of Si (covered with 285 nm thermally grown SiO_2), pressure is applied with a cotton swab and the strip is peeled

*Nitto Denko Corporation, SPV 224P

†various suppliers, including SPI and webelements.com

‡sonication in HNO_3 for several minutes and ~ 30 min in an ozone cleaner right before exfoliation

off relatively fast. The amount of pressure applied and the speed of removal of the strip affect the yield of monolayers present on the surface of the SiO₂/Si piece. Every material studied in this thesis presents its own optimal amount of exfoliation cycles, pressure and removal speed. Empirically, we noted a decrease in the yield of single layers once the surface of strip containing the material looked dull or the substrate was not properly cleaned.

The exfoliated flakes are inspected via optical microscopy*. For MoS₂, we routinely find single layers of about 5 to 20 μm. The optical contrast of the flakes with respect to the substrate is enhanced by the thin-film interference effect given by the thickness of the SiO₂ layer on top of the Si. As shown already for the case of graphene [3] and other layered compound[4, 5], a thickness of 285 nm provides about 12 % contrast difference at $\lambda = 550$ nm, enough to rapidly locate single layers.

The devices studied in this thesis are fabricated on substrates diced from 100 mm wafers of B-doped Si with 285 nm thermally grown, dry chlorinated SiO₂†.

A.1.3. FABRICATION OF ELECTRICAL DEVICES BASED ON 2D MATERIALS

The fabrication of electrical devices based on 2D materials starts with micromechanical exfoliation (see section A.1.2) of the selected material on the 285 nm SiO₂/Si substrates with optical markers defined by e-beam lithography. The reference markers will be used to accurately locate the flakes with the right characteristics for device fabrication and to design the electrical connections.

The reference markers are written together with large bonding pads with a standard double-layer resist‡ on the 285 nm SiO₂/Si substrates. A dose of 900 μC cm⁻², beam currents of ~ 250 nA and beam spot size of ~ 100 nm are typically used. The pattern is then developed in a solution of 1 MIBK : 3 IPA for 90 s and rinsed in pure IPA for at least a minute. Before metal deposition in high vacuum, a short O₂ descum is performed. We usually deposit thick (> 80 nm) bonding pads of AuPd with a ~ 5 nm Ti sticking layer. Both the metal alloy and the thickness are chosen to improve the wire-bonding success of the final device. After lift-off, the substrate is sonicated in HNO₃ and ozone cleaned just before exfoliation.

The electrical connections (leads) to the selected flakes are patterned following a similar recipe with a smaller beam spot size (about 20 nm) and higher dose (1200 μC cm⁻²). The metals used as contact materials provide low contact resistance with the studied materials; usually a stack of ~ 2 nm of Ti as sticking layer and ~ 60 nm of Au is used.

*Olympus BX 51 equipped with a Canon 600D digital camera

†Resistivity 0.01 to 0.05 Ω cm⁻¹ NOVA electronic materials

‡PMMA A3 495 kDa - bottom and PMMA A3 950 kDa - top, both from MicroChem, previously spun (3000 min⁻¹) and baked (175 °C for 12 min)



A.1.4. ALL DRY, DETERMINISTIC TRANSFER METHOD

The micromechanical exfoliation method outlined in Section A.1.2, coupled to the possibility of fast and reliable optical identification, represents the starting point of the entire 2D material research field.[2, 4, 6–13] This simple method enables the reliable fabrication of electrical devices based on layered materials with thickness down to the single layer. However, the scotch-tape exfoliation is intrinsically limited by the random location of the deposited flakes, hampering the realization of more complex devices, such as locally bottom-gated transistors and vertical heterostructures of different 2D materials. The probability of creating artificial heterostructures by randomly exfoliating 2D crystals onto the same substrate is vanishingly small.

Deterministic transfer techniques overcome this limitation and allow for controlled positioning of the exfoliated flakes to fabricate devices with complex geometries. [14–17] All these methods involve a wet chemical step, namely the dissolution of a sacrificial layer with solvents after the flake of interest has been successfully transferred. This step can leave residues on the transferred flake and does not allow the fabrication of freely suspended structures due to the capillary forces.

In this section, we present a deterministic transfer method based on a viscoelastic stamp that does not require any wet chemistry step. We transfer atomically thin 2D flakes on arbitrary substrates and fabricate freely suspended devices.

The main components of the setup used to accomplish the dry deterministic transfer are a zoom lens attached to a camera, an XYZ micromanipulator, an XY Θ sample stage all fixed to a magnetic optical breadboard (see Figure A.3 and Table A.1 for a full list of components and part numbers). The viscoelastic stamp used to transfer the flakes is obtained from a commercially available PDMS-based polymer (Gelfilm from GelPack - WF-30-X4 or PF-30-X4) and it is placed at the end of a clean glass slide to allow handling.

The two-dimensional flakes to be transferred are exfoliated onto the viscoelastic stamp (Figure A.2 and Figure A.4a). The prepared stamp is inspected under an optical microscope* in reflection and transmission. Both optical contrast and transmission are used to determine the number of layers and select the flake(s) to be transferred. Raman spectroscopy can be also carried out on the surface of the stamp to confirm the thickness of the flake.[12, 18] Once a thin flake has been identified, the acceptor substrate (sample) is fixed in the center of the XY Θ sample stage using double sided tape. Placing the acceptor substrate in the center of the sample stage allows to use the rotation degree of freedom to facilitate alignment. The glass slide containing the stamp is then mounted onto the XYZ micromanipulator upside down, so that the top surface of the viscoelastic stamp - carrying the flakes - faces the sample (Figure A.4b). The sample and the stamp are then aligned under the zoom lens (Figure A.4c). While keeping the focus on the surface of the sample, the stamp is slowly lowered. As the stamp is transparent, it is possible to align the selected flake on the desired location

*Olympus BX51 with a Canon 600D camera

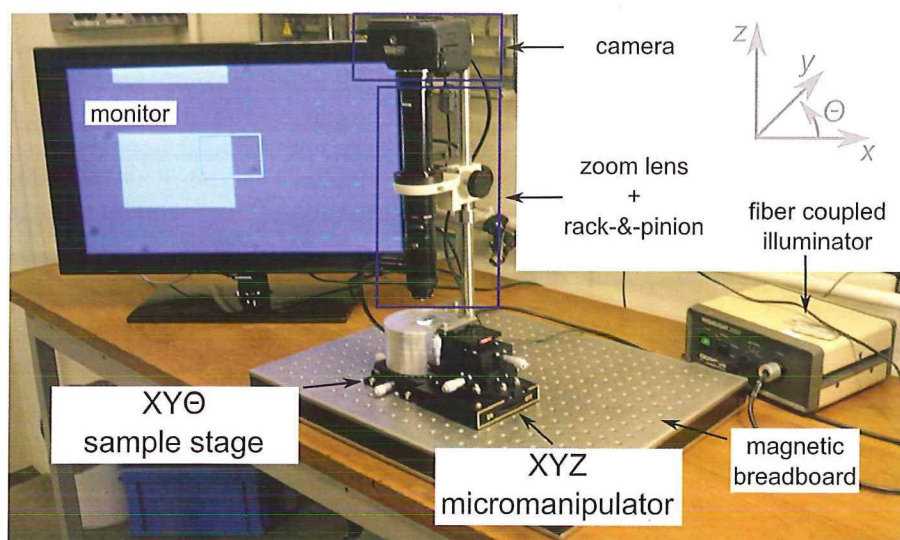


FIGURE A.3: Picture of the setup used for the dry transfer of two dimensional materials with indication of the main components.

of the acceptor surface with sub-micrometer resolution. This is facilitated by the extended depth of field (DOF) provided by the low numerical aperture of the zoom lens. The large DOF allows to have both the desired location and flake in focus before they are in contact. This allows to refine the in-plane alignment. Another benefit of a zoom lens is the possibility to smoothly change the size of the field of view of the transfer area and correcting for focus shifts without affecting the sample-flake distance.

Once the selected flake is precisely aligned on and very close to the desired location, the transfer is initiated by slowly lowering the stamp and pressing it against the sample surface (Figure A.4d). The working principle of the transfer is based on viscoelasticity: the stamp behaves as an elastic solid at short timescales while it can slowly flow at long timescales.[19] As the stamp slowly come in contact with the sample surface, it will start flowing over it. The contact area will change color and a clear boundary with the non-contact area will be formed. This boundary and the color changes are used to monitor the extent of the contact area as the position of the stamp is adjusted during the stamping process. The stamp is lowered with the micromanipulator until the desired flake is fully in contact with sample surface. Then, the stamp is slowly peeled off (A.4e). During the slow removal of the stamp, a small shear strain is imparted by a small adjustment of the XY micrometric screws. A slow releasing speed prevents the formation of bubbles and wrinkles in the transferred

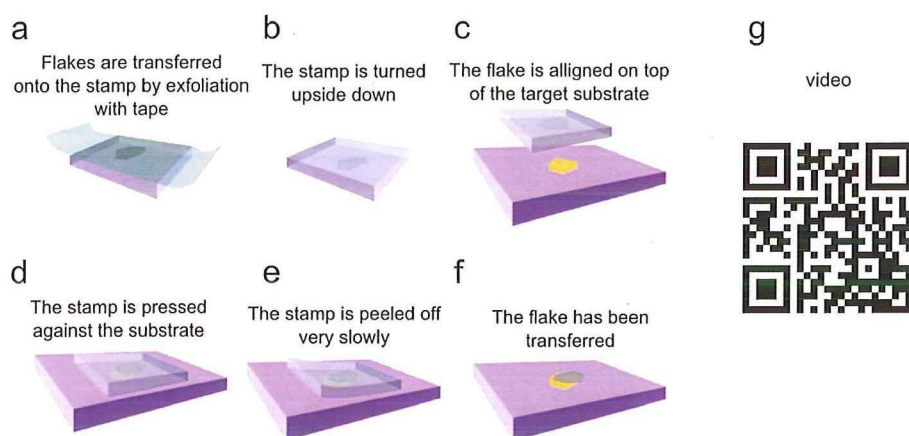


FIGURE A.4: (a) Flakes are exfoliated on the viscoelastic stamp. (b) The stamp is turned upside down and affixed to the XYZ micromanipulator. (c) The flake on the stamp is aligned with the target area on the substrate (in this case another 2D flake). (d) The stamp is pressed onto the target surface. (e) The stamp is slowly released. (f) Schematic of the obtained heterostructure. (g) QR code linking to a real-time video of the dry transfer process explained in panels a-f. Video link <http://goo.gl/tNZQmN>

flake. The release of the flake is monitored by the change in its optical contrast and apparent color. After the desired flake is transferred, the stamp can be peeled off quickly, leaving the desired flake on the acceptor surface (Figure A.4f). A real-time video of the dry transfer process is available at <http://goo.gl/tNZQmN> which can be quickly accessed by scanning the QR code in Figure A.4g.

This procedure is used to fabricate the devices studied in Chapter 8 by sequential transfer of hexagonal boron nitride (hBN) and few-layer black-phosphorous (bP), see Figure 8.1.

We also fabricated heterostructures based on MoS_2 and other layered compounds. Figure A.5a shows a vertical stack of single and few-layer MoS_2 on a few-layer graphene (FLG) flake on the 285 nm SiO_2/Si substrate. Figure A.5b shows a vertical stack of single and bilayer MoS_2 on a mica flake, on the usual SiO_2/Si substrate. These heterostructures are just examples that confirm the possibility of transferring MoS_2 flakes on top of arbitrary substrates and have been used to study the effect of the substrate on the Raman and luminescence of single and few-layer MoS_2 . [20] Fabrication of suspended structure is also possible, allowing the study of their properties as mechanical resonators both at room temperature [21] and at low temperature, approaching the quantum limit (see Figure A.6). [22] The transfer method can be applied to all exfoliable layered crystals, opening the door to the realization of artificially engineered materials.

	Description	Part number	Supplier
Lens and vision	Zoom lens	MVL12X3Z	Thorlabs
	Extension tube	MVL20FA	Thorlabs
	Magnification lens	MVL12X20L	Thorlabs
	DSRL Camera	Canon EOS600D	Canon
	Canon to F-mount	-	eBay
	32-inch TV screen	-	Samsung
	HDMI cable	-	Samsung
Mechanics	Magnetic breadboard	55-227	Edmund Optics
	Magnetic clamp	62-272	Edmund Optics
	Table clamp	54-262	Edmund Optics
	Steel bar	39-353	Edmund Optics
	Rack and pinion	03-609	Edmund Optics
	Steel bar	39-353	Edmund Optics
	Post bases (2x)	BA2/M	Thorlabs
Manipulation	XY θ sample stage	XYR1/M	Thorlabs
	XYZ micromanipulator	RB13M/M	Thorlabs

TABLE A.1: Full list of components of the setup for the dry transfer of 2D materials. Notes:

The fiber-coupled illuminator and M6 capped screws were already present in the lab.

An adaptor for the zoom-lens to fit in the rack-and-pinion mount and an adaptor for the sample stage were machined in the faculty workshop by Ing. Ron Hoogeheinde.

Extra M6-threaded holes were machined in the post bases to allow mounting of the steel clamp and centering of the zoom lens.

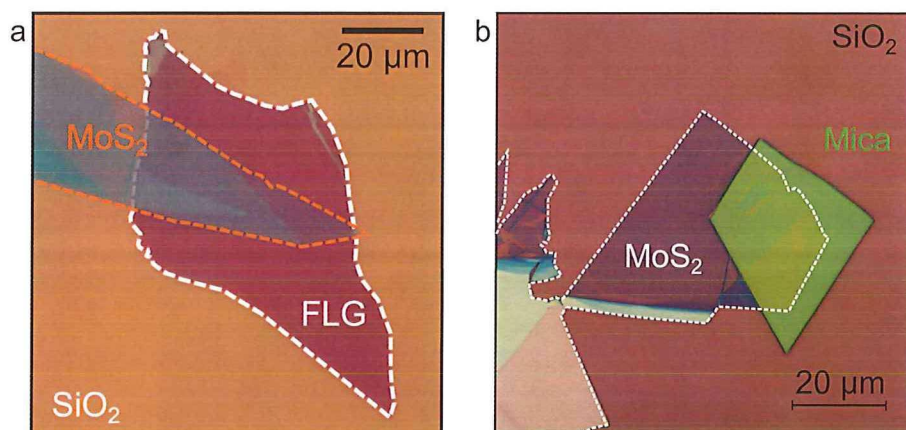


FIGURE A.5: (a) Heterostructure composed of a MoS_2 flake on top of few-layer graphene (FLG) flake on the 285 nm SiO_2/Si substrate. (b) Heterostructure composed of a single and bi-layer MoS_2 flake on top of Mica flake on 285 nm SiO_2/Si substrate. In both panels, the contours of the flakes are highlighted for clarity.

A.2. CHARACTERIZATION TECHNIQUES

A.2.1. ATOMIC FORCE MICROSCOPY

Atomic force microscopy (AFM) is used to characterize the height profiles of . The AFM used in this work is a Veeco D3100 with a Nanoscope IIIa controller or a Veeco Multimode with a Nanoscope IIIa controller. The cantilever used in this Thesis are standard Si cantilevers for tapping mode (Olympus, OMCL-AC160TS-R3, $f_{\text{resonance}} = 300 \text{ kHz}$, $k_{\text{spring}} = 26.1 \text{ N m}^{-1}$) Usually, the AFM is operated in amplitude modulation (tapping mode): the cantilever is kept in oscillation close to its resonant frequency and the oscillation amplitude of the cantilever is used as feedback variable. A change in the amplitude is directly related to a topographic feature. A simple introduction to the working principle of AFM and over scanning probe techniques can be found at <http://www.ntmdt.com/spm-principles>.

A.2.2. RAMAN MICROSCOPY

Raman microscopy is extensively used to reliably determine the number of layers in flakes of the transition metal dichalcogenides.[18, 23–25] Raman spectroscopy is based on inelastic scattering of an incoming photon and the lattice of material under study. The small momentum of the incoming photons allows only momentum-preserving (vertical) transitions of the excited electrons, to either a virtual or a real electronic state. The excited electron exchanges energy with allowed vibrational modes (phonons) and then radiatively recombines, emitting a photon of a different

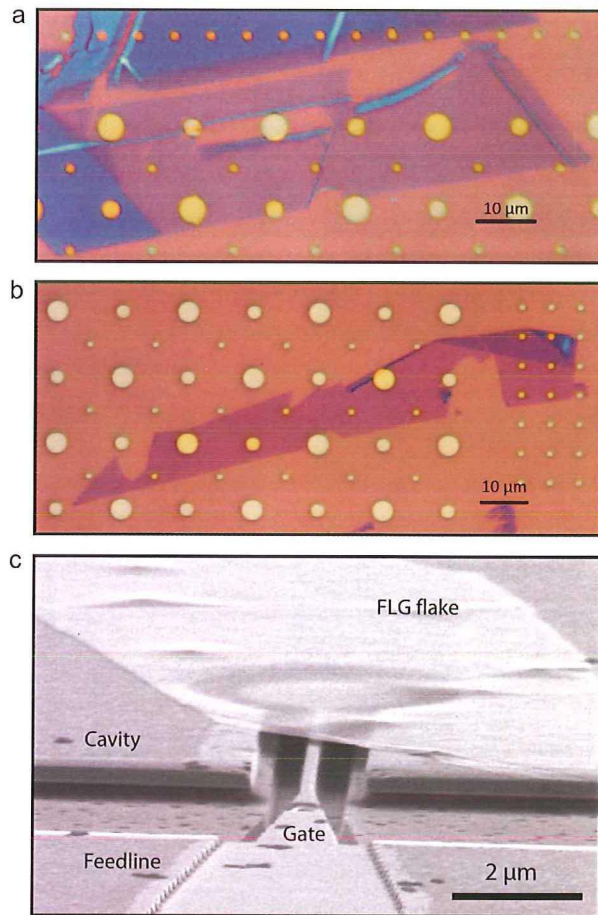


FIGURE A.6: (a) and (b) Optical micrographs of single and few-layer MoS₂ transferred on holes etched in a 285 nm SiO₂/Si substrate. Image courtesy of Andres Castellanos-Gomez.[21] (c) Tilted-angle SEM image of a multilayer (10 nm) graphene flake embedded in a microwave cavity. Image courtesy of Vibhor Singh. [22]

energy compared with the excitation photon. The energy difference between the emitted photon and the excitation photon is the energy of the vibrational mode. The most probable process is that the excited electron loses energy to phonons, resulting in the emission of a lower energy photon (Stokes process). However, the electron can also gain energy from the phonon bath and emit a higher energy photon (anti-Stokes process). Stokes Raman emission is more intense and the ratio between Stokes and anti-Stokes emission is related to the population of the phonon bath, given by the

lattice temperature.

A

A.2.3. OPTO-ELECTRONIC CHARACTERIZATION SETUP

We have developed a setup to perform electrical characterization under excitation at optical frequencies. The setup is sketched in Figure A.7 and the components/part numbers are listed in Table A.2.

The optical excitation is provided by nine diode pumped solid state lasers (DPSSL), mounted on a vibrationally damped optical table, emitting from 405 nm to 940 nm. A system of mirrors in kinematic mounts allows for rapid wavelength selection. The laser light is directed onto a parabolic mirror which focuses it into a multimode fiber. The free space coupling scheme allows to easily control the light intensity via neutral density filters and frequency modulation by mechanical chopper, before coupling the light to the fiber. We chose a parabolic mirror as a coupler since its reflected focal length is independent of the wavelength. At the end of the fiber, an identical parabolic mirror collimates the light into the viewing system of the probe station and, ultimately, on the sample space through the cryostat window. The spot diameter on the sample is about 230 μm .

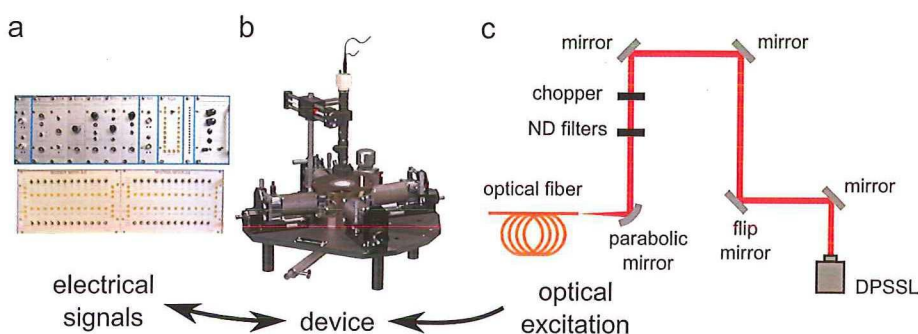


FIGURE A.7: (a) Home-built measurement electronics. (b) Schematic of a Lakeshore probe station (from lakeshore.com). (c) Schematic of the laser setup used to provide optical excitation. The main components are defined in the panel.

The design principle of the system providing optical excitation is to balance the optical power and the coverage of the visible-infrared part of the electromagnetic spectrum. The current solution provides power densities of about 10 W cm^{-2} on sample and covers the electromagnetic spectrum with eight wavelengths. Using a monochromator coupled to a white light source would allow to continuously cover the UV-visible-NIR region of the electromagnetic spectrum but offer significantly lower power densities, especially after fiber coupling. Employing supercontinuum generation coupled with acousto-optical tuneable filters would provide a higher power

A densities (compared with the monochromator design) but limits the shortest wavelength to about 500 nm and considerably increases the cost of the setup.

Electrical measurements are performed using home built electronics (IVVI-rack and modules) that allow to apply and read analog currents and voltages. The digital conversion is performed by an Adwin, operated as both a digital to analog converter (DAC) to apply the input signal and as a analog to digital converter (ADC) to read the output signal from the device. The Adwin is computer controlled via Labview routines.

The measurements are usually performed in vacuum (pressure $\sim 10^{-5}$ mbar) and at room temperature. The noise floor is in the order of tenths of picoamperes.

	Description	Part number	Supplier
Lasers	$\lambda = 405$ nm, Power = 20 mW	MDL-III-405-20mW	CNI Lasers
	$\lambda = 442$ nm, Power = 20 mW	MDL-III-442-20mW	CNI Lasers
	$\lambda = 473$ nm, Power = 20 mW	MBL-III-473-20mW	CNI Lasers
	$\lambda = 532$ nm, Power = 20 mW	MGL-III-532-20mW	CNI Lasers
	$\lambda = 640$ nm, Power = 20 mW	MRL-III-640-20mW	CNI Lasers
	$\lambda = 808$ nm, Power = 20 mW	MDL-III-808-20mW	CNI Lasers
	$\lambda = 885$ nm, Power = 20 mW	MDL-III-885-20mW	CNI Lasers
	$\lambda = 940$ nm, Power = 20 mW	MDL-III-940-20mW	CNI Lasers
Optics	Circular flat mirrors (18x) $\varnothing = 25.4$ mm	PF10-03-P01	Thorlabs
	90° off-axis parabolic mirrors (2x) $\varnothing = 12.7$ mm , RFL = 25.4 mm	MPD127127-90-P01	Thorlabs
	Graded index multimode optical fiber $\varnothing = 62.5$ μ m, NA = 0.275, length = 5 m	M31L05	Thorlabs
	Mounted round variable ND filter	NDC-50C-4M	Thorlabs
Mechanics	Optical table, 1.2 \times 2 \times 0.21 m	T1220CK	Thorlabs
	Aluminum breadboard, 200 \times 900 \times 12.7 mm	MB2090/M	Thorlabs
	Kinematic mount for $\varnothing = 25.4$ mm optics (18x)	KM100	Thorlabs
	Flip mount adapter (8x)	FM90/M	Thorlabs
	6-Axis kinematic optic mount	K6X	Thorlabs
	30-mm cage rotation mount for $\varnothing = 25.4$ mm optics (2x)	CRM1/M	Thorlabs
	SM1-threaded fiber adapters (2x)	SM1FC	Thorlabs

TABLE A.2: Key components of optical excitation setup. Note that posts, post holders, cage rods and M6/M4 screws are not listed. The mechanical chopper was already present in the lab.



REFERENCES

- [1] A. Castellanos-Gomez, M. Buscema, R. Molenaar, V. Singh *et al.*, *Deterministic transfer of two-dimensional materials by all-dry viscoelastic stamping*, *2D Materials* **1** 011002 (2014).
- [2] K. S. Novoselov, A. K. Geim, S. V. Morozov, D. Jiang *et al.*, *Electric Field Effect in Atomically Thin Carbon Films*, *Science* **306** 666 (2004), <http://www.sciencemag.org/content/306/5696/666.full.pdf>.
- [3] P. Blake, E. W. Hill, A. H. Castro Neto, K. S. Novoselov *et al.*, *Making graphene visible*, *Applied Physics Letters* **91** (2007).
- [4] A. Castellanos-Gomez, E. Navarro-Moratalla, G. Mokry, J. Quereda *et al.*, *Fast and reliable identification of atomically thin layers of TaSe₂ crystals* **6** 191 (2013).
- [5] M. M. Benameur, B. Radisavljevic, J. S. Héron, S. Sahoo *et al.*, *Visibility of dichalcogenide nanolayers*, *Nanotechnology* **22** 125706 (2011).
- [6] K. S. Novoselov, A. K. Geim, S. V. Morozov, D. Jiang *et al.*, *Two-dimensional gas of massless Dirac fermions in graphene*, *Nature* **438** 197 (2005).
- [7] A. C. Ferrari, J. C. Meyer, V. Scardaci, C. Casiraghi *et al.*, *Raman Spectrum of Graphene and Graphene Layers*, *Phys. Rev. Lett.* **97** 187401 (2006).
- [8] M. Y. Han, B. Özyilmaz, Y. Zhang and P. Kim, *Energy band-gap engineering of graphene nanoribbons*, *Physical review letters* **98** 206805 (2007).
- [9] A. K. Geim and K. S. Novoselov, *The rise of graphene*, *Nature materials* **6** 183 (2007).
- [10] C. Lee, X. Wei, J. W. Kysar and J. Hone, *Measurement of the Elastic Properties and Intrinsic Strength of Monolayer Graphene*, *Science* **321** 385 (2008).
- [11] B. Radisavljevic, A. Radenovic, J. Brivio, V. Giacometti *et al.*, *Single-layer MoS₂ transistors*, *Nature Nanotechnology* **6** 147 (2011).
- [12] A. C. Ferrari and D. M. Basko, *Raman spectroscopy as a versatile tool for studying the properties of graphene*, *Nature nanotechnology* **8** 235 (2013).
- [13] G. Fiori, F. Bonaccorso, G. Iannaccone, T. Palacios *et al.*, *Electronics based on two-dimensional materials*, *Nat Nano* **9** 768 (2014).
- [14] G. F. Schneider, V. E. Calado, H. Zandbergen, L. M. Vandersypen *et al.*, *Wedging transfer of nanostructures*, *Nano letters* **10** 1912 (2010).
- [15] C. Dean, A. Young, I. Meric, C. Lee *et al.*, *Boron nitride substrates for high-quality graphene electronics*, *Nature Nanotechnology* **5** 722 (2010).
- [16] X. Song, M. Oksanen, M. A. Sillanpää, H. Craighead *et al.*, *Stamp transferred suspended graphene mechanical resonators for radio frequency electrical readout*, *Nano letters* **12** 198 (2011).
- [17] P. Zomer, S. Dash, N. Tombros and B. Van Wees, *A transfer technique for high mobility graphene devices on commercially available hexagonal boron nitride*, *Applied Physics Letters* **99** 232104 (2011).
- [18] C. Lee, H. Yan, L. E. Brus, T. F. Heinz *et al.*, *Anomalous Lattice Vibrations of Single- and Few-Layer MoS₂*, *ACS Nano* **4** 2695 (2010).
- [19] M. A. Meitl, Z.-T. Zhu, V. Kumar, K. J. Lee *et al.*, *Transfer printing by kinetic control of adhesion to an elastomeric stamp*, *Nat Mater* **5** 33 (2006).
- [20] M. Buscema, G. Steele, H. van der Zant and A. Castellanos-Gomez, *The effect of the substrate on the Raman and photoluminescence emission of single-layer MoS₂* **7** 1 (2014).
- [21] A. Castellanos-Gomez, R. van Leeuwen, M. Buscema, H. S. van der Zant *et al.*, *Single-Layer MoS₂ Mechanical Resonators*, *Advanced Materials* **25** 6719 (2013).
- [22] SinghV, B. J., S. H., B. M. *et al.*, *Optomechanical coupling between a multilayer graphene mechanical resonator and a superconducting microwave cavity*, *Nat Nano* **9** 820 (2014).
- [23] A. Castellanos-Gomez, M. Barkelid, A. M. Goossens, V. E. Calado *et al.*, *Laser-Thinning of MoS₂: On Demand Generation of a Single-Layer Semiconductor*, *Nano Lett.* **12** 3187 (2012).
- [24] P. Tonndorf, R. Schmidt, P. Böttger, X. Zhang *et al.*, *Photoluminescence emission and Raman response of monolayer MoS₂, MoSe₂, and WSe₂*, *Optics express* **21** 4908 (2013).
- [25] M. Buscema, M. Barkelid, V. Zwiller, H. S. J. van der Zant *et al.*, *Large and Tunable Photothermoelectric Effect in Single-Layer MoS₂*, *Nano Lett.* **13** 358 (2013).

SUMMARY

This Thesis describes explorative experimental work on the opto-electronic properties of novel, nano-scale semiconducting materials. The reduced dimensionality of these semiconductors makes them interesting from a fundamental as well as from an applied standpoint.

Chapter 1 introduces the field of opto-electronics and photodetection, giving a short overview of the current limitations of silicon and III-V technologies, motivating the need for the study of novel materials.

Chapter 2 gives a brief overview of the principal photocurrent generation mechanisms. We first review the mechanisms that are based on the separation of a photo-generated electron-hole pair by an electric field (photoconduction and photovoltaic). Then, we review the mechanisms based on a gradient or change in temperature (photo-thermoelectric and photo-bolometric).

In **Chapter 3** the state-of-the-art photodetectors based on two-dimensional layered materials are reviewed. Graphene-based photodetectors reach responsivities in the order of few mA W^{-1} , a bandwidth of a few tens of GHz and absorb very-low-energy photons. Semiconducting transition metal dichalcogenides (TMDCs) have a large (> 1.5 eV) and direct bandgap once exfoliated to a single layer. Photodetectors based on TMDCs can achieve responsivities up to thousands of A W^{-1} , orders-of-magnitude higher compared to graphene, silicon and InGaAs detectors. This large photoresponse stems from (i) efficient absorption due to the direct bandgap and (ii) trap states with long decay time, providing a large optical gain. Other layered semiconductors, such as GaS and TiS_3 , are also being explored for photodetection applications and show characteristics that are similar to the TMDCs. Few-layer black phosphorus (bP) has already shown both sizable responsivity and high bandwidth. A future research direction is represented by the fabrication of artificial heterostructures by using deterministic transfer methods to stack several layers of different materials.

Chapter 4 shows the fast and efficient photoresponse of a detector based on a single row of colloidal quantum dots (PbSe). The electrical characteristics of the fabricated devices show signatures of blockaded transport, which is lifted under illumination. Scanning photocurrent spectroscopy measurements reveal that (i) the photoresponse is located at the separation between the electrodes and (ii) the photoresponse spectra follow the absorption spectra of the PbSe quantum dots. Under pulsed light excitation, the devices show a fast rise time of about 200 ns.

Chapter 5 is dedicated to the study of the photoresponse of single, ultrathin TiS_3 nanoribbons (NR). Mechanical exfoliation and deterministic transfer allow us to

reduce the NR thickness down to 15 nm. Without illumination, the fabricated NR-transistors show mobilities of about $2.6 \text{ cm}^2 \text{ V}^{-1} \text{ s}^{-1}$ and an ON/OFF ratio of $1 \cdot 10^4$. Under illumination, the responsivity reaches values larger than $1 \cdot 10^3 \text{ A W}^{-1}$ in the OFF state and a photoresponse up to 940 nm. Even though trap states are involved in the photoresponse, the devices show response times in the ms range.

In **Chapter 6** we study the photocurrent generation mechanism in mechanically exfoliated single-layer MoS_2 . Under zero external bias, we measure the photocurrent while scanning a diffraction-limited laser spot over the device. We observe that (i) the photocurrent is generated when the laser spot is placed within the area of the electrodes, (ii) the photocurrent location shows no gate dependence and (iii) the photocurrent persists under below-bandgap illumination. These three main findings strongly suggest that the photothermoelectric effect is the main photocurrent generation mechanism. From these measurements, we can derive the Seebeck coefficient of single-layer MoS_2 which can be tuned from $-4 \cdot 10^4 \text{ } \mu\text{VK}^{-1}$ to $-1 \cdot 10^5 \text{ } \mu\text{VK}^{-1}$ with an applied gate electric field.

Chapter 7 and **Chapter 8** are dedicated to the study of few-layer black phosphorus (bP), a novel layered semiconductor. We first study the photoresponse of phototransistors based on few-layer bP (Chapter 7). Without illumination, few-layer bP devices show mobilities in the order of $100 \text{ cm}^2 \text{ V}^{-1} \text{ s}^{-1}$, an ON/OFF ratio of about $1 \cdot 10^3$ and ambipolar behavior. Under illumination, few-layer bP demonstrates sizable responsivities (4.8 mA W^{-1}) and fast response times ($\sim 1 \text{ ms}$).

Next, motivated by the ambipolarity and strong field effect, we define PN junctions in few-layer bP by local electrostatic gating (Chapter 8). The bP channel is separated from two bottom split gates by a thin hexagonal boron nitride (h-BN) layer. Both the bP and the h-BN flakes have been deterministically transferred on top of the gates. Without illumination, the devices display a versatile electrical behaviour, controlled by the gates' electric field. When the gates are biased in the same polarity, the devices show linear IVs. With opposite gate polarity, the devices show rectifying IVs, suggesting the formation of a PN junction. In PN gate configuration, illuminating the devices up to $\lambda = 940 \text{ nm}$ results in a sizable short-circuit current and open-circuit voltage, clear signatures of photovoltaic photocurrent generation mechanism.

At last, **Appendix A** describes in detail the experimental methodologies and setups.

SAMENVATTING

Dit Proefschrift beschrijft exploratief experimenteel werk aan de opto-elektronische eigenschappen van nieuwe halfgeleidende materialen op nanoschaal. De gereduceerde dimensionaliteit van deze halfgeleiders maakt hen interessant vanuit zowel fundamenteel als toegepast standpunt.

Hoofdstuk 1 introduceert verschillende opto-elektronica en fotodetectie-technieken. Daarnaast wordt een kort overzicht gegeven van de huidige beperkingen van silicium en III-V technologie, hetgeen de noodzaak voor de studie van nieuwe materialen motiveert.

Hoofdstuk 2 geeft een kort overzicht van de belangrijkste fotostroom-generatie mechanismen. We bespreken eerst de mechanismen die gebaseerd zijn op de scheiding van een fotogegenereerd elektron-gat paar door middel van een elektrisch veld (fotogeleiding en het fotovoltaïsch effect). Hierna bespreken we mechanismen die gebaseerd zijn op een verloop of op een verandering in temperatuur (foto thermoelectrisch en foto-bolometrisch).

In **Hoofdstuk 3** bespreken we de huidige generatie fotodetectoren gebaseerd op gelaagde twee-dimensionale materialen. Grafeen fotodetectoren bereiken een responsiviteit in de orde van enkele mA W^{-1} en een bandbreedte van enkele tientallen GHz. Daarnaast reageren ze op fotonen met een zeer lage energie. Halfgeleidende overgangsmetaal dichalcogenides (OMDCs), geëxfolieerd tot een enkele laag, hebben een grote ($> 1.5 \text{ eV}$) en directe bandgap. Photodetectoren gebaseerd op OMDCs kunnen een responsiviteit bereiken tot duizenden A W^{-1} die velen malen groter is dan grafeen, silicium en InGaAs detectoren. Deze grote fotoresponse komt voort uit (i) de efficiënte absorptie van licht als gevolg van de directe bandgap en (ii) *trap states* met een lange verval tijd, die zorgen voor een grote optische versterking.

Andere gelaagde halfgeleiders, zoals GaS en TiS_3 , worden ook onderzocht voor fotodetectie toepassingen. Ze tonen eigenschappen die vergelijkbaar zijn met de OMDCs; bijvoorbeeld, multi-laag zwart fosfor (bP) – een nieuw type gelaagde halfgeleider – heeft al een meetbare responsiviteit en hoge bandbreedte laten zien. Een toekomstige onderzoeksrichting zal de fabricage van kunstmatige heterostructuren zijn, gebruikmakend van deterministische overdrachtsmethoden om verscheidene lagen van verschillende materialen op elkaar te stapelen.

Hoofdstuk 4 behandelt de snelle en efficiënte fotorespons van een detector op basis van een enkele rij van PbSe quantum dots. De elektrische eigenschappen van de gefabriceerde structuur tonen een blokkade van de stroom, die opgeheven kan worden indien beschonen met licht. Uit plaatsafhankelijke fotostroom spectroscopie metingen blijkt dat (i) de fotorespons zijn oorsprong vindt in het gebied tussen de

electroden en (ii) dat het fotorespons spectrum het absorptiespectrum van de PbSe quantum dots volgt. Onder gepulseerde lichtexcitatie laten de devices een snelle verandering van de stroom zien, op een tijdschaal van ongeveer 200 ns.

In **Hoofdstuk 5** wordt de fotorespons van enkele, ultradunne TiS_3 nanolinten behandeld. Door middel van exfoliatie en deterministische overdracht is de nanolindikte verkleind tot 15 nm. Zonder lichtexcitatie vertonen nanolint-transistors een mobiliteit van $2.6 \text{ cm}^2 \text{ V}^{-1} \text{ s}^{-1}$ en een ON/OFF verhouding van $1 \cdot 10^4$. Onder invloed van lichtexcitatie, bereiken de nanolint-transistors reactiewaarden groter dan $1 \cdot 10^3 \text{ A W}^{-1}$ in de *OFF state* en een fotorespons tot golflengtes van 940 nm. Ondanks de aanwezigheid van *trap states*, tonen de devices reactietijden van rond de millieconde.

In **Hoofdstuk 6** bestuderen we het ontstaan van fotostromen in mechanisch geëxfolieerd enkellaags MoS_2 . Zonder een externe spanning aan te leggen, meten we de fotostroom terwijl het device gescand wordt met een diffractie gelimiteerde laserstraal. We zien dat (i) een fotostroom gegenereerd wordt wanneer de laserstraal op de electrodes schijnt (ii) de fotostroom geen *gate* afhankelijkheid vertoont en (iii) dat de fotostroom stand houdt onder excitatie van fotonen met een energie lager dan de bandgap. Deze drie bevindingen laten zien dat fotothermoelectrische effecten het belangrijkste mechanisme van fotostroomgeneratie zijn. Door het elektrische veld van de *gate* te variëren, kan de Seebeck coëfficiënt van enkel-laags MoS_2 ingesteld worden van $-4 \cdot 10^4 \mu\text{VK}^{-1}$ tot $-1 \cdot 10^5 \mu\text{VK}^{-1}$.

Hoofdstuk 7 en **Hoofdstuk 8** zijn gewijd aan het bestuderen van enkele lagen zwart fosfor (bP). Eerst bestuderen we de fotoreactie van fototransistors gebaseerd op enkele lagen bP (Hoofdstuk 7). Zonder belichting vertonen de bP devices een mobiliteit van rond de $100 \text{ cm}^2 \text{ V}^{-1} \text{ s}^{-1}$, een ON/OFF verhouding van $1 \cdot 10^3$ en ambipolair gedrag. Onder belichting laat enkel-laags bP een meetbare responsiviteit (4.8 mA W^{-1}) en snelle reactietijden ($\sim 1 \text{ ms}$) zien.

We hebben ook een PN junctie in enkellaags bP ontworpen gebruikmakend van het ambipolaire gedrag en het sterke elektrische veld effect (Hoofdstuk 8). Het bP kanaal wordt gescheiden van de twee afzonderlijke gates door middel van een dunne laag hexagonaal boron nitride (h-BN). Zowel het bP als het h-BN zijn deterministisch geplaatst op de gates. Zonder belichting laten de devices verschillend elektrisch gedrag zien, afhankelijk van het elektrische veld op de *gates*. Wanneer dezelfde spanning op de *gates* wordt aangelegd, laat het device lineaire stroom-voltage karakteristieken (IVs) zien. Bij een tegengestelde polariteit van het aangelegde veld op de *gates*, zijn de IVs asymmetrisch met een duidelijk rectificerend karakter. Dit duidt op de formatie van een PN junctie. Belichting van deze PN junctie tot golflengtes van 940 nm levert een meetbare kortsluitstroom en een open klemspanning. Dit zijn duidelijke indicaties van een photovoltaïsche fotostroom generatiemechanisme.

Ten slotte, **Appendix A** beschrijft de experimentele methoden en opstellingen.

CURRICULUM VITÆ

Michele BUSCEMA

02-10-1986 Born in La Spezia, Italy.

EDUCATION

2000–2005 High School
Liceo Scientifico Statale '*Antonio Pacinotti*'
La Spezia, Italy

2005–2008 Bachelor of Science in Materials Engineering
Politecnico di Milano, Milano, Italy

2008–2010 Master of Science in Materials Engineering
Politecnico di Milano, Milano, Italy

2009–2010 UNITECH exchange programme
Delft University of Technology, Delft, the Netherlands

Thesis: Charge transport in molecular systems through
self-aligned nanogaps

Supervisors: Prof. dr. ir. H.S.J. van der Zant and dr. Ferry Prins

2010–2011 Intern (4 months) in the Evonik Industries
Nanotronics Science-to-Business Center Marl, Marl, Germany

2011–2015 Ph.D. in Applied Physics
Delft University of Technology, Delft, the Netherlands

Thesis: Photodetection with novel materials:
colloidal quantum dots, nanoribbons and layered
materials

Promotor: Prof. dr. ir. H.S.J. van der Zant

Supervisor: dr. A. Castellanos-Gomez

LIST OF PUBLICATIONS

- [15] **Buscema M**, Island JO, Groenendik DJ, Blanter SI, Steele GA, van der Zant HSJ and Castellanos-Gomez A, *Photocurrent generation with two-dimensional van der Waals semiconductors*, under review.
- [14] Velez S,[†] Ciudad D,[†] Island JO, **Buscema M**, Txoperena O, Parui S, Steele GA, Casanova F, van der Zant HSJ, Castellanos-Gomez A and Hueso LE, *Gate-tunable diode and photovoltaic effect in an organic-2D layered material p-n junction*, submitted
- [13] Plechinger G, Castellanos-Gomez A, **Buscema M**, van der Zant HSJ, Steele GA, Kuc A, Heine T, Schueller C and Korn T, *Control of biaxial strain in single-layer MoS₂ using local thermal expansion of the substrate*, accepted in 2D Materials
- [12] Tonndorf P, Schmidt R, Kern J, **Buscema M**, Steele GA, Castellanos-Gomez A, van der Zant HSJ, Michaelis de Vasconcellos S and Bratschitsch R, *Single photon emission from localized excitons in an atomically thin semiconductor*, under review.
- [11] Groenendijk DJ, **Buscema M**, Steele GA, Michaelis de Vasconcellos S, Bratschitsch R, van der Zant HSJ and Castellanos-Gomez A, *Photovoltaic and Photothermoelectric Effect in a Double-Gated WSe₂ Device*, Nano Letters **14** 5846 (2014).
- [10] **Buscema M**,[†] Groenendijk DJ,[†] Steele GA, van der Zant HSJ and Castellanos-Gomez A, *Photovoltaic effect in few-layer black phosphorus PN junctions defined by local electrostatic gating*, Nature Communications **5** (2014).
- [9] **Buscema M**, Groenendijk DJ, Blanter SI, Steele GA, van der Zant HSJ and Castellanos-Gomez A, *Fast and Broadband Photoresponse of Few-Layer Black Phosphorus Field-Effect Transistors*, Nano Letters **14** 3347 (2014).

-
- [8] Castellanos-Gomez A, Vicarelli L, Prada E, Island JO, Narasimha-Acharya KL, Blanter SI, Groenendijk DJ, **Buscema M**, Steele GA, Alvarez JV, Zandbergen HW, Palacios JJ and van der Zant HSJ, *Isolation and characterization of few-layer black phosphorus*, 2D Materials **1** 025001 (2014).
- [7] Island JO, **Buscema M**, Barawi M, Clamagirand JM, Ares JR, Sánchez C, Ferrer IJ, Steele GA, van der Zant HSJ and Castellanos-Gomez A, *Ultrahigh Photoresponse of Few-Layer TiS_3 Nanoribbon Transistors*, Advanced Optical Materials **2** 641 (2014).
- [6] **Buscema M**, Steele G, van der Zant HSJ and Castellanos-Gomez A, *The effect of the substrate on the Raman and photoluminescence emission of single-layer MoS_2* Nano Research **7** 1 (2014).
- [5] Castellanos-Gomez A, **Buscema M**, Molenaar R, Singh V, Janssen L, van der Zant HSJ and Steele GA, *Deterministic transfer of two-dimensional materials by all-dry viscoelastic stamping*, 2D Materials **1** 011002 (2014).
- [4] Castellanos-Gomez A, van Leeuwen R, **Buscema M**, van der Zant HSJ, Steele GA and Venstra WJ, *Single-Layer MoS_2 Mechanical Resonators*, Advanced Materials **25** 6719 (2013).
- [3] Castellanos-Gomez A, Roldan R, Cappelluti E, **Buscema M**, Guinea F, van der Zant HSJ and Steele GA *Local strain engineering in atomically thin MoS_2* , Nano Letters, **13** 5361 (2013).
- [2] **Buscema M**, Barkelid M, Zwiller V, van der Zant HSJ, Steele GA and Castellanos-Gomez A, *Large and Tunable Photothermoelectric Effect in Single-Layer MoS_2* , Nano Letters **13** 358 (2013).
- [1] Prins F, **Buscema M**, Seldenthuis JS, Etaki S, Buchs G, Barkelid M, Zwiller V, Gao Y, Houtepen AJ, Siebbeles LDA and van der Zant HSJ, *Fast and Efficient Photodetection in Nanoscale Quantum-Dot Junctions*, Nano Letters **12** 5740 (2012).

PATENTS

- [1] Surdeanu R, **Buscema M**, Cox M, Koenderink F, *Solid state lighting element, peak wavelength estimation method and binning method*, EP Patent Publication number EP 2746792 A1.

ACKNOWLEDGMENTS

This 4-year-long experience changed my life and it would not have been possible without the following people. To start with, my advisor: Herre. During these years, you taught me many things, in every formal and informal occasion: how to communicate *to the point* and without *smoesjes*, being independent while collaborating with others, strive for realizing my own ideas, delegate and take responsibility and, of course, how to work on a myriad of parallel projects in a focused way ...I'll always have your example to follow. Even more importantly, I want to thank you for having allowed me to change research topic on-the-go. I will never forget my first annual review meeting (were you made very clear that shorter feedback loops were needed) and your first question when I told you about a job offer (*is this really what you want?*), asked with a genuine interest in my motivation. For all this (and more that I cannot remember now) I am indebted to you.

Next in line is Andres. Without your support and guidance I would not have achieved much of what is in this Thesis. I remember the first time you approached me with the idea of making a phototransistor out of MoS₂. I was still measuring some PbSe devices and you came in the lab showing a paper that, in retrospect, had already done much of what we could have done at that moment. I did not understand – I was still a stubborn freshman – so I let your offer pass by. Few months later there was a faculty seminar about layered materials for phase change applications...after that talk, I came to you to look for a collaboration (or help?). The day after you taught me how to exfoliate and keep my personal materials' library, and that was really the start of a new part of my Ph.D. You taught me that every paper is *almost done*, that its central part is called *el turron*, that *four figures is all you need* and that the drawer below the desk is always full of publishable results or interesting materials. On the serious side, among many other things, you taught me how to be organized, with my thoughts and my files. I really appreciate that. Your pragmatic, creative and positive attitude made sure we never run out of ideas to develop and publish, maybe too many in certain points. I will never forget when we were addressed as “the Delft group” at conferences: little did they know that, back then, it was only you and me...I will also never forget some basic Spanish wisdom (especially regarding the weight of a chicken...) learnt from the awesome trip to Madrid you arranged with Ferry, Samir, Jos and Ronald...THANK YOU, Andres!

I started in MED as a master student and then got “upgraded” to Ph.D. In that time, I was supervised by Ferry. You introduced me to MED and its spirit, to the electronics and how to measure, to the cleanroom and nanofabrication in general. You also introduced me to Dutch directness and you made me understand what a

critical spirit means, two very valuable qualities for a Ph.D. I still remember the many times we had drinks together with other MEDers (especially Samir) and the few times we ended up at “de Kurk”. I really appreciate the time we worked together and the time you spent teaching and mentoring me, also “remotely”. Dankjewel, Ferry.

During the past 4 years, I shared the office with some of MED’s finest members. One was Ferry (see above). The next was Harold: thank you for your positive, supportive, open and genuine spirit. You helped me going through the rough times of the first year(s) of my Ph.D. You taught me how to shape my working habits, like making 2D mind maps – no exfoliation involved there... That one time I sang with your band (and realized I cannot sing) it was a lot of fun! Having been your paranyph at your defense has been an honor... I’m happy that our friendship continues after the MED time, fed by swimming+pizza evenings. Thanks, Harold!

The next who joined the office mate has been Anna. For the first part of your Ph.D. you were in the office for a small part of your day, due to the hard (forced) work in the STM dungeon...The moments you were with Harold and me, we had lots of laughs and nice talks. Then, Sander got more helpers and you were finally free to *waste* your time with me and Harold in the office! Jokes apart, thanks for cheerful and deeply Roman spirit.

I also want to thank the other components of the old-school MED for their help and support: Edgar (thanks for teaching me how to cool down a 1K probe in an evening), Menno (thanks for the tips on the AFM/Adwin connection), Jos (thanks for trying to teach me how to make simulations based on master equations), Alexander (thanks for the help with the QT bonder), Christian (thanks for nice discussion about the motivation to start a Ph.D. and its consequences to ones life), Hidde and Ben.

Before transitioning to the current and newer generation MEDers, I still want to thank a very important person of the old-school MED: Samir. You have been an example of the constant and extreme dedication it takes to succeed in a Ph.D. You have taught me the art of “shopping” for electronics modules and the art of high frequency electrical measurements. I will never forget the extraordinary Madrid trip.

Next, there are Mickael and Ronald. We had the same trajectory, the three of us started as master students before leveling-up to Ph.Ds. We also started in MED almost at the same date, and so we are graduating close together...thanks for sharing the load (and some tips) of completing the thesis through an unexpected rule change. Mickael: thanks for the teaching me how to use the ALD and etcher and for the translation of the summary to Dutch. Ronald: thanks for preserving the old MED spirit of having lunch all together and for placing your defense two days before mine... aahahaha ;)

The new MED is a much different ambient to work in. To start with, it got way more Italian during the years, thanks to the addition of Anna, Riccardo, Rocco, Andrea, Giordano and, at last, Nicola. Thank you all guys for the coffee breaks, lunches and all the little pauses, at which we self-assemble into a little Italian corner...You made MED feel more like home! Riccardo: thanks for the very nice parties at your place,

with all the special Italian delicacies and thanks for taking pictures at my defence! Rocco: many thanks for your positive and forward-looking spirit: after every time I talk with you, I feel more positive. Andrea: thanks for all the discussion we had about science and life as a scientist...and good luck with your baby! Giordano: you surprised me for the speed at which you integrated in the group and learnt about fabrication, the electronics and the systems we use...And Nicola, we did not speak so much but thanks for bringing another piece of Liguria in the Netherlands!

Many thanks to Joshua for the time we spent together working on the nanoribbons devices. I will never forget your comment when I wanted to do some extra measurements...you were right, man! Keep on pushing, it's almost done (to quote our common mentor)!

Enrique, I want to thank you for your calm approach to the job and for the many coffee breaks we had in the mornings, to start the day by talking about something else than physics. Sal, you deserve a special mention. I remember the first time we talked. I was exfoliating some MoS₂ with Andres in the microscope room. You came in and I asked you to explain your project...I did not understand a word of your answer but you were so enthusiast and passionate. Keep that up man! And enjoy the rest of your Ph.D. Thanks for your advices on job hunting, as well!

I also would like to thank the students that helped me in these 4 years. Many thanks to the students who endured my supervision in my first two years: Fokko, Margeaux and Reyu. A special thank note goes to Andrew, Sofya and Dirk. With the three of you we formed the so-called "Buscema Lab". It was a really enjoyable experience. I'm very happy that all of you completed your respective theses with good grades. Andrew: thanks for having taken care of a very high-risk, difficult project. Sofya: I'm sure you'll be very successful in Regensburg! Dirk: thank you for your constant effort, motivation and very good work. I fondly remember the hours spent in the cleanroom or setting up the "godfather" setup or at the probe station. With your critical spirit, you pointed out the mistakes I made as mentor, giving me a clear direction to further improve myself.

I would like to extend the acknowledgments to all MED members that I had the pleasure to meet. In random order: Venkatesh (thanks for your job-searching tips and for your calm view on the world), Max (good luck with your measurement automation idea!), Shun-san, Santiago (how's the Montana setup? ahahah), Mingyun (good luck with your baby!), Sander (thanks for the help in the Dutch translation of my summary), Simon, Richard, Gary (thanks for the intensive toughening-up course), Teun (thanks for the revision of my propositions), Vibhor, Warner, Dejan (thanks for the help with the CVD growth and for having pushed me to apply for the Casimir Entrepreneurship course. Without that, I would not have found my future employer. I owe you a proper Italian dinner!), Peter (thanks for spreading my CV at NXP!), Alexandra, Mafalda, Wiel (keep on trying to measure those nanoparticles!), Julien (you too: keep on trying to measure those nanoparticles!), Vera, Robin, Floris, Emre (keep going strong and enjoy

your Ph.D. man!), Ben B., Ranko, Nandini, Ignacio and all the new members I did not have time to talk to before printing the thesis.

All the technical support within MED: Mascha, Ron, Tino and Allard. Thanks for all the little mechanical pieces/modifications you made for me and for the help in setting up (and make safe) my laser setup. Thanks to Maria, Irma and Dorine for all the forms and orders that handled for me. Technical support in the cleanroom: Arnold, Anja, Roel, Ewan, Marco (2x), Marc and Charles: Many thanks for keeping the machine running as swiss clocks, so that we can use (and abuse) them for our fabrications. Lots of thanks to the DEMO guys: Raymond, Jack, Ruud and Rogier!

Outside MED I want to thank the other Italians in the building: Gabriele (and Maria), Pasquale (thanks for the helpful discussion about the QDs in black phosphorus), Diego (Enjoy Boston), Alessandro (never change!) and Leonardo (thanks for the TEM help). Thank you guys for all the nice discussions at the departmental social half hour and at the several parties we have been together. Within QT, I'd like to thank Victor and Srijit for their interesting discussion over 2D materials and Maria B. for her help using her setup.

I'd like to thank the people I shared a house with in the first year of my Ph.D: Julien, Laurens, Frank and Vincent. Thanks for the many parties (and regular evenings) we had in the house. Vincent: enjoy your Ph.D. in San Francisco and thanks for the awesome time we spent playing with the evergreen Mario Kart in the old Super Nintendo system.

Voglio ringraziare i miei genitori e la mia famiglia, per il loro costante supporto attraverso questi 4 anni di dottorato di ricerca. Qualche volta é stato difficile capirsi, sia nel contenuto sia nelle motivazioni del mio impegno continuo e costante (forse troppo). Abbiamo superato queste difficoltà insieme e ora guardiamo avanti. Grazie. Alessia ed Alessandro: grazie per non avermi mai fatto sentire il peso di questi anni di assenza...

Thanks to the family of my girlfriend for having having accepted me as a son or sibling for the past years.

The last paragraph is for a special person. Without you, I would not have reached this point. You really supported me and helped me go through the most difficult parts of the past years. Now there is going to be a new chapter in our life, let's make it beautiful together.

*Michele Buscema
Delft, March 2015*